ELASTIC WAVEFIELD MIGRATION AND TOMOGRAPHY

by

Yuting Duan

© Copyright by Yuting Duan, 2016

All Rights Reserved

A thesis submitted to the Faculty and the Board of Trustees of the Colorado School of Mines in partial fulfillment of the requirements for the degree of Doctor of Philosophy (Geophysics).

Golden, Colorado

Date _____

Signed: _____
Yuting Duan

Signed: _____
Dr. Paul C. Sava
Thesis Advisor

Golden, Colorado

Date _____

Signed: _____
Dr. Roel Snieder
Professor and Head
Department of Geophysics

ABSTRACT

Wavefield migration and tomography are well-developed under the acoustic assumption; however, multicomponent recorded seismic data include shear waves (S-modes) in addition to the compressional waves (P-modes). Constructing multicomponent wavefields and considering multiparameter model properties make it possible to utilize information provided by various wave modes, and this information allows for better characterization of the subsurface. In my thesis, I apply popular wavefield imaging and tomography to elastic media, and propose methods to address challenges posed by elastic multicomponent wavefields and multiparameter models. The key novelty of my research consists of new elastic imaging conditions, which generate elastic images with improved qualities and clear physical meaning. Moreover, I demonstrate an elastic wavefield tomography method to obtain realistic elastic models which benefits elastic migration.

Migration techniques, including conventional RTM, extended RTM, and least-squares RTM (LSRTM), provide images of subsurface structures. I propose one imaging condition that computes potential images (PP, PS, SP, and SS). This imaging condition exploits pure P- and S-modes obtained by Helmholtz decomposition and corrects for the polarity reversal in PS and SP images. Using this imaging condition, I propose methods for conventional RTM and extended RTM. The extended imaging condition makes it possible to compute angle gathers for converted waves. The amplitudes of the scalar images indicate reflectivities, which can be used for amplitude verse offset (AVO) analysis; however, this imaging condition requires knowledge of the geologic dip. I propose a second imaging condition that computes perturbation images, i.e., P and S velocity perturbations. Because these images correspond to perturbations to material properties that are angle-independent, they do not have polarity reversals; therefore, they do not need dip information for polarity correction. I use this perturbation imaging condition for LSRTM to increases the image resolution and attenuates

artifacts.

Since the quality of the wavefield-based migration image greatly depends on the accuracy of the material property models, I also propose elastic waveform inversion methods for multiparameter model estimation. Waveform inversion solves a non-linear problem and aims to obtain a model that best matches the predicted and observed data. My contribution to elastic waveform inversion is a petrophysical constraint term in the objective function, which imposes plausible relations between model parameters; this feasible region is assumed to be prior information which can be obtained from laboratory measurements or well logs. Such petrophysical constraint term enforces appropriate physical relationships between the model parameters. With the constraint term, I obtain realistic models that can be used for migration and reservoir characterization.

TABLE OF CONTENTS

ABSTRACT iii

LIST OF FIGURES viii

LIST OF ABBREVIATIONS xviii

ACKNOWLEDGMENTS xix

DEDICATION xxi

CHAPTER 1 INTRODUCTION 1

CHAPTER 2 SCALAR IMAGING CONDITION FOR ELASTIC REVERSE TIME MIGRATION 8

2.1 Introduction 8

2.2 Theory 11

2.3 Examples 22

2.4 Discussions 32

2.4.1 Estimation of the reflector normal 34

2.4.2 Imaging from opposite sides of a reflector 40

2.5 Conclusions 42

2.6 Acknowledgments 45

CHAPTER 3 3D ANGLE DECOMPOSITION FOR ELASTIC REVERSE TIME MIGRATION 46

3.1 Introduction 47

3.2 Elastic scalar imaging condition 49

3.3 Moveout analysis 50

3.3.1 Angle decomposition using CIPs . . . 55
3.3.2 Angle decomposition using τCIGs . . . 61
3.3.3 Angle decomposition using λCIG . . . 70
3.4 Examples . . . 71
3.4.1 SEG/EAGE example . . . 71
3.4.2 Volve data example . . . 75
3.5 Conclusions . . . 79
3.6 Acknowledgments . . . 79
CHAPTER 4 ELASTIC LEAST-SQUARES REVERSE TIME MIGRATION . . . 81
4.1 Introduction . . . 81
4.2 Theory . . . 83
4.3 Examples . . . 86
4.3.1 Layered model . . . 86
4.3.2 Marmousi model . . . 94
4.3.3 Volve OBC data . . . 99
4.4 Conclusions . . . 108
4.5 Acknowledgments . . . 109
CHAPTER 5 ELASTIC WAVEFIELD TOMOGRAPHY WITH PHYSICAL MODEL CONSTRAINTS . . . 110
5.1 Introduction . . . 110
5.2 Elastic wavefield modeling . . . 112
5.3 Objective function . . . 113
5.4 Objective function gradient . . . 115

5.5 Example 117
5.5.1 Borehole model 117
5.5.2 Marmousi model 122
5.6 Conclusion 135
5.7 Acknowledgments 136
CHAPTER 6 CONCLUSION 137
6.1 Scalar imaging condition for elastic reverse-time migration 137
6.2 Angle decomposition 137
6.3 Elastic least-squares reverse time migration 138
6.4 Elastic wavefield tomography with physical model constraints 139
REFERENCES CITED 140
APPENDIX - PERMISSION OF PAPERS 150
A.1 Permission from publisher 150
A.2 Permission from co-author 150
A.3 Permission for field data 151

LIST OF FIGURES

Figure 1.1 Schematic representations of for (a) RTM, (b) LSRTM, and (c) FWI. Symbols d_s and d_r represent the source wavelet and recorded data, respectively. Symbol I is the computed image. u_s and u_r are constructed source and receiver wavefield, respectively, by using model material property m. Squares highlight the domain used to construct the objective function. Circles indicate the components that are updated through inversion in order to minimize the objective function. . . 4

Figure 2.1 (a) 3D synthetic model with one horizontal reflector in a constant velocity medium, at depth $z = 0.2$ km. The source is located at $(0.2, 0.2, 0.02)$ km; the 2D network of receivers is at $z = 0.03$ km. (b) A snapshot of source P wavefield. 12

Figure 2.2 Snapshots of (a) x-, (c) y-, and (e) z-component of the receiver S wavefield and the corresponding (b) x-, (d) y-, and (f) z-component of the PS image. The S wavefields are decomposed from the displacement wavefield using Helmholtz decomposition. Polarity reversal occurs as a function of azimuth in the wavefield which leads to polarity change in three components of the PS image shown. Z-component of the S wavefield is much weaker than x- and y-component. 13

Figure 2.5 1D images obtained by (a) crosscorrelation of source and receiver wavefields, (b) crosscorrelation followed by spatial derivative, and (c) source integral prior to crosscorrelation, followed by spatial derivative. . . 19

Figure 2.8 (a) Source P wavefield and (b) receiver S wavefield for a single shot. Both source and recievers are on the surface of the model. 23

Figure 2.9 (a) Source S wavefield and (b) receiver P wavefield for a single shot. Both source and recievers are on the surface of the model. 24

Figure 2.10 PS stacked images obtained using (a) the conventional imaging condition and (b) our new imaging condition. The image in panel (b) at $(1.0, 1.0)$ km is stronger, in contrast with the image in panel (a) which suffers from cancellation due to polarity reversal. 25

Figure 2.11 SP images obtained using (a) the conventional imaging condition and (b) our new imaging condition. The image in panel (b) at $(1.0, 0.7)$ km is stronger, in contrast with the image in panel (a) which suffers from cancellation due to polarity reversal. 26

Figure 2.12 PS common image gather at $x = 1.5$ km obtained from (a) the conventional imaging condition. From left to right, the horizontal events change sign at normal incidence. (b) Using the new imaging condition, we obtain the PS common image gather without polarity change. 27

Figure 2.13 SP common image gather at $x = 1.5$ km obtained from (a) the conventional imaging condition. From left to right, the horizontal events change sign at normal incidence. (b) Using the new imaging condition, we obtain the SP common image gather without polarity changes. 27

Figure 2.15 PS common image gather at $x = 2.5$ km obtained from (a) the conventional imaging condition, (b) the conventional imaging condition with the simple correction that flips the sign of the image at negative offset, and (c) the new imaging condition. 29

Figure 2.16 PS image from a single shot using (a) the conventional imaging condition, (b) the conventional imaging condition with simple correction that flips the sign of the image at negative offset, and (c) the new imaging condition. Source is located at $(1.85, 0)$ km. 30

Figure 2.17 PS stacked image using (a) the conventional imaging condition, (b) the conventional imaging condition with simple correction that flips the sign of the image at negative offset, and (c) the new imaging condition. . 31

Figure 2.18 (a) 3D SEG/EAGE salt model, the density model. (b) The PS image obtained using the new imaging condition. 33

Figure 2.20 (a) The PP image computed by crosscorrelating P-waves in source and receiver wavefields. (b) The reflector normal estimated using the PP image. (c) The PS image computed using the dip field in panel (b). Note that the image of the reflector incorrectly changes polarity at around (0.7,0.6) km. 35

Figure 2.21 (a) The PS image obtained by crosscorrelating the source P wavefield and receiver S wavefield. (b) The reflector dip estimated using PS image. (c) The PS image computed using the dip field from panel (b). This PS image has no polarity change. 36

Figure 2.23 (a) The stacked PP image computed by crosscorrelating P-waves in source and receiver wavefields. (b) The reflector normal estimated using the PP image. (c) The PS image computed using the dip field from panel (b). The reflectors highlighted by the boxes are not continuous and poorly imaged. 37

Figure 2.24 (a) The stacked PS image computed by crosscorrelating P-waves in the source wavefield and S-waves in the receiver wavefield. The PS image polarity for individual shots are corrected by reversing the image at negative offsets. (b) The reflector dip estimated using PS image. (c) The PS image computed using the dip field. The reflectors highlighted by the boxes are better imaged compared to the PS image in Figure 2.23(c). 38

Figure 2.25 Schematic representation of reflections at an interface for (a)down-going and (b)up-going PS converted-modes. Compared to (a), vector ∇P changes sign in (b), resulting in the sign change of $\nabla P \times \mathbf{n}$. 40

Figure 2.26 PS imaging of a horizontal interface for various source/receiver configurations. The left panels are the models with the acquisition geometry, and the right panels are the corresponding PS images. The dots are the locations of the sources and lines are the locations of the receivers. The arrow indicates the reflector normal for PS migration. Note that the polarities of the PS images are the same in experiments (a) and (d), but different from experiments (b) and (c). 43

Figure 2.28 (a) The stacked PS image using conventional imaging condition. The reflectors around $z = 1.2$ km are not imaged. (b) The stacked PS image using the scalar imaging condition. The reflectors around $z = 1.2$ km are well-imaged. The left panels are the stacked PS images and the right panels are common image gathers at $x = 0.8$ km. Note that for Figure (a), the polarities of the events in the common image gather are inconsistent from left to right, while for Figure (b), the events have consistent polarities in all experiments. 44

Figure 3.2 Cartoon describing source and receiver planes intersecting in the reflection plane (a) at location $\mathbf{x}_o$ at time t_o, and (b) at location $\mathbf{x}$ after moving both planes along time- and space-axises. Vectors $\mathbf{n}_s$ and $\mathbf{n}_r$ define the propogation directions of the incident and reflected waves in space, respectively. 53

Figure 3.4 (a) PP and (b) PS images computed for one shot at $(0.4, 0.4, 0.02)$ km. The flat reflector is at $z = 0.2$ km. 58

Figure 3.5 PP extended CIP and wide-azimuth angle gathers of (a) a picked image point at coordinates $(0.33, 0.33, 0.2)$ km for one shot at coordinates $(0.4, 0.4, 0.02)$ km and (b) a picked image point at coordinates $(0.4, 0.4, 0.2)$ km for eight shots. The dot represents the analytical estimation of the opening and azimuth angle using the acquisition geometry. 59

Figure 3.6 PS extended CIP and wide-azimuth angle gathers of (a) a picked image point at coordinates $(0.2, 0.2, 0.2)$ km for one shot at coordinates $(0.4, 0.4, 0.02)$ km and (b) a picked image point at coordinates $(0.4, 0.4, 0.2)$ km for eight shots. The dot represents the analytical estimation of the opening and azimuth angle using the acquisition geometry. 60

Figure 3.7 (a) PP image computed from one shot gather. The reflector is horizontal at $z = 0.0$ km. The star represents the source location, and the white line represents the receiver locations. (b) Predicted spatial shift of a horizontal reflector for $\gamma = 1$. The star at coordinates $x = -0.6$ km, $z = -0.6$ km, and $\tau = 0$ s represents the source location, and the white line at $z = -0.6$ km and $\tau = 0$ s represents the receiver locations. The dotted line at $z = 0.0$ km and $\tau = 0$ s shows the zero-lag image. The line at $x = 0.0$ km illustrates the spatial shift for the image point at $\{0.0, 0.0\}$ km. The colors on the surface indicate the contour of the spacial shifts for different image points. 62

Figure 3.8 (a) Computed extended image gathers at several x-locations, indicated by the number below each image. The shape of the image in each panel matches the corresponding horizontal slice of the surface plot in Figure 3.7(b). Computed angles for all samples on the reflector by applying (b) a line slant-stack along the vertical trace, and (c) the method described in Algorithm 2, which applies a slant-stack along the surface shown in Figure 3.7(b). The two methods generate the same angle gathers, and they are the same for PP reflections with flat reflectors. 63

Figure 3.9 (a) PP image computed from one shot gather. The reflector is dipping. (b) Predicted spatial shift of a dipping reflector for $\gamma = 1$. The star at coordinates $x = -0.6$ km, $z = -0.6$ km, and $\tau = 0$ s represents the source location, and the white line at $z = -0.6$ km and $\tau = 0$ s represents the receiver locations. The dotted line at $\tau = 0$ s shows the zero-lag image. The dashed line illustrates the spatial shift for image point at $(0.0, -0.6)$ km. The solid line at $x = 0.0$ km illustrates the extended image for a time-lag gather at a fixed horizontal position. Note that these two lines do not overlay. The colors on the surface indicate the contour of the spacial shifts for different image points. . . . 66

Figure 3.10 (a) Computed extended image gathers at several x-locations, indicated by the number below each image. The shape of the image in each panel matches the corresponding horizontal slice of the surface plot in Figure 3.9(b). Computed angles for all samples on the reflector by applying (b) a line slant-stack along the vertical trace and (c) the method described in Algorithm 2, which applies a slant-stack along the surface shown in Figure 3.9(b). The angle gathers in (c) are more focused and accurate than those in (b). 67

Figure 3.11 (a) PS image computed from one shot gather. The reflector is horizontal at $z = 0.0$ km. (b) Predicted spatial shift of a horizontal reflector for $\gamma = 1.8$. The star at coordinates $x = -0.6$ km, $z = -0.6$ km, and $\tau = 0$ s represents the source location, and the white line at $z = -0.6$ km and $\tau = 0$ s represents the receiver locations. The dotted line at $z = 0.0$ km and $\tau = 0$ s shows the zero-lag image. The dashed line illustrates the spatial shift for the image point at $(0.0, -0.6)$ km, The solid line illustrates the extended image for a time-lag gather at a fixed horizontal position ($x = 0.0$ km). Note that these two lines do not overlay. The colors on the surface indicate the contour of the spacial shifts for different image points. 68

Figure 3.12 (a) Computed extended image gathers at several x-locations, indicated by the number below each image. The shape of image in each panel matches the corresponding horizontal slice of the surface plot in Figure 3.11(b). Computed angles for all samples on the reflector by applying (b) a line slant-stack along the vertical trace and (c) the method described in Algorithm 2, which applies a surface slant-stack along the surface shown in Figure 3.11(b). The angle gathers in (c) are more focused than those in (b), and they have higher resolutions at larger opening angles. 69

Figure 3.13 (a) SEG/EAGE model. The dots show the source locations. (b) Relative position of the image point at coordinates $(0.3, 0.4, 0.3)$ km and the salt body. 72

Figure 3.16 Volve data example. (a) PP and (b) PS images computed using 142 receiver gathers. The dots show locations of all the receivers, and the stars show locations of four receivers. The reflectors in the PS image are less continuous than those in the PP image. 76

Figure 3.17 PP extended CIP and wide-azimuth angle gathers for four receiver gathers. The receivers are at (a) $(4.1, 4.0, 0.1)$, (b) $(8.6, 4.0, 0.1)$, (c) $(4.1, 2.8, 0.1)$, and (d) $(8.6, 2.8, 0.1)$ km. The angle gathers show that this image point is illuminated by the four receivers from various directions with PP reflections. 77

Figure 3.18 PS extended CIP and wide-azimuth angle gathers for four receiver gathers. The receivers are at (a) $(4.1, 4.0, 0.1)$, (b) $(8.6, 4.0, 0.1)$, (c) $(4.1, 2.8, 0.1)$, and (d) $(8.6, 2.8, 0.1)$ km. The angle gathers show that this image point is illuminated by the four receivers from various directions with PS reflections. 78

Figure 4.1 Synthetic layered model example. (a) α model with a horizontal reflector at $z = 0.45$ km, and (b) β model with a horizontal reflector at $z = 0.62$ km. 87

Figure 4.2 Synthetic layered model example. Snapshots of an elastic wavefield, for a source at coordinates $(0.76, 0.06)$ km: (a) x- and (b) z-components of the wavefield at $t = 0.2$ s; (c) x- and (d) z-components of the wavefield at $t = 0.3$ s; (e) x- and (f) z-components of the wavefield at $t = 0.4$ s. Two horizontal lines indicate the locations of reflectors in α and β models. P waves generate reflections only at the top reflector; S waves generate reflections only at the bottom reflector; 88

Figure 4.3 Synthetic layered model example. For the source at $(0.76, 0.06)$ km, (a) x- and (b) z-components of the recorded data (c) x- and (d) z-components of the predicted data using the inverted model. The direct arrivals are removed in the shot gathers. Note that the predicted data match the recorded data in both phase and amplitude. 89

Figure 4.4 Synthetic layered model example. (a) $\delta\alpha$ and (b) $\delta\beta$ images after first iteration. In addition to the event at the correct depth, there are two strong horizontal events in the $\delta\beta$ image, which are crosstalk artifacts. (c) $\delta\alpha$ and (d) $\delta\beta$ images after 10 iterations. Compare to the $\delta\alpha$ and $\delta\beta$ images after the first iteration, the artifacts have been attenuated. 90

Figure 4.5 Synthetic Marmousi model example. Background (a) α and (b) β models. The receivers are at depth $z = 0.025$ km, and the sources are at depth $z = 0.013$ km. The top layer is homogeneous for both background models. 91

Figure 4.6 Synthetic Marmousi model example. True (a) $\delta\alpha$ and (b) $\delta\beta$ perturbation models. The perturbation models are not identical, e.g., a reflector with negative value at $(2, 0.4)$ km is presents only in the $\delta\alpha$ model. 92

Figure 4.7 Synthetic Marmousi model example. For the source location at $(1.54, 0.013)$ km, (a) z-component of one shot gather. The highlighted arrival is the reflection from the bottom of the homogeneous layer, and its amplitude is much stronger than other arrivals in the recorded data. (b) The data weighting function generated from the recorded data. The same weighting function is applied to horizontal and vertical components of the shot gather. 93

Figure 4.9 Synthetic Marmousi model example. (a) $\delta\alpha$ and (b) $\delta\beta$ RTM images with illumination compensation based on the source wavefield. 95

Figure 4.10 Synthetic Marmousi model example. Updated (a) $\delta\alpha$ and (b) $\delta\beta$ images after 100 iterations. Note that the reservoir near coordinates $(2.0, 0.4)$ km is correctly recovered in the updated $\delta\alpha$ image, without any leakage in the updated $\delta\beta$ image. 96

Figure 4.11 Synthetic Marmousi model example. The z component of (a) the predicted shot gather and (b) the data difference using the updated models (Figures 4.10(a) and 4.10(b)). 97

Figure 4.12 Volve data example. (a) one PP shot gather at $x = 6$ km, which is assumed to be a vertical displacement gather. (b) Weighting matrix for this shot gather. The weighting function mutes the direct arrivals, attenuates the predicted shear waves, and boosts later reflections. . . . 100

Figure 4.13 Volve data example. Background (a) α and (b) β models. The top water layer is from $z = 0$ to 90 m. 101

Figure 4.14 Volve data example. (a) $\delta\alpha$ and (b) $\delta\beta$ RTM images. The chalk layer is from $z = 2.5$ to 3.0 km. Note that the events above the chalk layer in the $\delta\beta$ are weak and discontinuous. 102

Figure 4.15 Volve data example. (a) $\delta\alpha$ and (b) $\delta\beta$ LSRTM images after 12 iterations. Compared to the RTM images (Figure 4.14(a) and 4.14(b)), the LSRTM images have higher resolution and better balanced amplitudes. The reflectors above 1.5 km appear in the $\delta\beta$ image after inversion with larger lateral extent along the x-direction than those in the $\delta\alpha$ image. 103

Figure 4.16 Volve data example. The weighted (a) observed data, (b) predicted data, and (c) data residual after 12 iterations. The predicted data accurately reproduces the dominant reflection energy seen in the observed data. The data residual contains mostly noise and some weaker reflection events. 104

Figure 4.17 Volve data example. Predicted shot gathers using only (a) $\delta\alpha$ and (b) $\delta\beta$ LSRTM images. The $\delta\alpha$ image predicts most of the arrivals in the observation with correct amplitudes. The $\delta\beta$ image compensates for the AVO effect of the PP reflections at far offsets (e.g., $x = 8.5$ km, $t = 3.0$ s). 105

Figure 5.2 Horizontal (left panels) and vertical (right panels) components of a shot gather with the source at $z = 3.5$ km. First arrival is the P wave and second arrival is the S wave. (a) The original data. (b) Processed data for inversion with P waves only from $z = 0$ to 3.5 km and S waves only from $z = 3.5$ to 7 km. We window selected portions of the original data to simulate partial illumination for different wave modes. 118

Figure 5.3 Updated α models after 21 iterations using (a) objective function $\mathcal{J}_D$ and (b) $\mathcal{J}_D + \mathcal{J}_C$. Note that the Gaussian anomaly in (b) at $(1.5, 5)$ km is better recovered, and its amplitude and shape are closer to the true model compared to that in (a). 119

Figure 5.4 Updated β models after 21 iterations using (a) objective function $\mathcal{J}_D$ and (b) $\mathcal{J}_D + \mathcal{J}_C$. Note that the Gaussian anomaly in (b) at $(1.5, 2)$ km is better recovered, and its amplitude and shape are closer to the true model compared to that in (a). 120

Figure 5.5 Model updates for the Gaussian model in Figure 5.1 as a function of iterations at (a) $(1.5, 2)$ km and (b) $(1.5, 5)$ km. Stars and dots are the updated models with and without constraints, respectively. Note that without constraints, the α and β models update toward the boundaries, while with constraints, the relationship of α and β models is enforced to be close to the true model indicated by the median line in the underlying physical constraint. 121

Figure 5.6 (a) True α model, (b) true β model, and (c) the crossplot of α and β models. The α and β models are computed from the original Marmousi P and S velocity models, respectively. 123

Figure 5.7 (a) Starting α model, (b) starting β model, and (c) crossplot of α and β models for Marmousi example. The α and β models are computed from the true model with smoothing mainly along the horizontal axis to eliminate detailed structures in the true model. 124

Figure 5.8 (a) Vertical and (b) horizontal components of the difference between a recorded shot gather and the corresponding predicted data for the first frequency band ($0-5$ Hz). The predicted data are computed using the initial model shown in Figures 5.7(a) and 5.7(b); (c) vertical and (d) horizontal components of the difference between the recorded and predicted data for the first frequency band. The predicted data are computed using the final model for the first frequency band. 125

Figure 5.9 (a) Vertical and (b) horizontal components of the difference between a recorded shot gather and the corresponding predicted data for the second frequency band ($0-7$ Hz). The predicted data are computed using the final model from the first frequency band; (c) vertical and (d) horizontal components of the difference between the recorded and predicted data for the second frequency band. The predicted data are computed using the final model for the second frequency band. 126

Figure 5.10 Recovered (a) α and (b) β models after the inversion of the second frequency band. (c) Crossplot of recovered α and β models using objective function $\mathcal{J}_D$. Note that the recovered β model contains more details than the α model. 127

Figure 5.11 Recovered (a) α and (b) β models after the inversion of the second frequency band. (c) Crossplot of recovered α and β models using objective function $\mathcal{J}_D + \mathcal{J}_C$. The upper and lower boundaries are indicated by the two solid lines. Note that the recovered α and β models contain similar details. 128

Figure 5.12 Recovered (a) α and (b) β models after the inversion of the second frequency band. (c) Crossplot of recovered α and β models using objective function $\mathcal{J}_D + \mathcal{J}_C$. The upper and lower boundaries are indicated by the two solid lines. 129

Figure 5.13 Recovered (a) α and (b) β models after the inversion of the second frequency band. (c) Crossplot of recovered α and β models using objective function $\mathcal{J}_D + \mathcal{J}_C$. The upper and lower boundaries are indicated by the two solid lines. 130

Figure 5.14 Comparison between initial or recovered models (solid lines) and true models (dashed lines) from the well at $x = 2.4$ km. Row one: Solid lines are the α profiles of (a) initial model; (b) updated models using objective function $\mathcal{J}_D$; (c) updated models using objective function $\mathcal{J}_D + \mathcal{J}_C$; (d) updated models using objective function $\mathcal{J}_D + \mathcal{J}_C$, where $\mathcal{J}_C$ is defined with a wider feasible region; (e) updated models using objective function $\mathcal{J}_D + \mathcal{J}_C$, where $\mathcal{J}_C$ is defined with a shifted feasible region. Row two: Solid lines are the β profiles of (f) initial model; (g) updated models using objective function $\mathcal{J}_D$; (h) updated models using objective function $\mathcal{J}_D + \mathcal{J}_C$; (i) updated models using objective function $\mathcal{J}_D + \mathcal{J}_C$, where $\mathcal{J}_C$ is defined with a wider feasible region; (j) updated models using objective function $\mathcal{J}_D + \mathcal{J}_C$, where $\mathcal{J}_C$ is defined with a shifted feasible region. In (c), (d), (g), (h), and (i), the recovered model profiles match the true models. 131

LIST OF ABBREVIATIONS

Reverse Time Migration . . . . . RTM

Least-squares Reverse Time Migration . . . . . LSRTM

Full Waveform Inversion . . . . . FWI

Migration Velocity Analysis . . . . . MVA

Center for Wave Phenomena . . . . . CWP

Amplitude Versus Offset . . . . . AVO

ACKNOWLEDGMENTS

Undertaking this PhD has been a truly life-changing experience for me. This thesis has been kept on track and been seen through to completion with the support , guidance, and encouragement of numerous people. I would like to thank all of them who made this thesis possible and an unforgettable experience for me.

Firstly, I would like to thank my advisor Dr. Paul Sava who accepted me as his PhD student. Thereafter, he offered me the continuous support of my PhD study and related research with his patience, motivation, and immense knowledge. In addition to the research projects, I have learned a lot from him. He taught me presentation skills and habits of scientific thinking, which will be beneficial for my future career and life.

Besides my advisor, I would like to thank the rest of my thesis committee and other CWP professors, Roel Snieder, Ilya Tsvankin, Antoine Guitton, Ken Larner, and John Stockwell for their insightful comments and encouragement, but also for the questions which inspired me to widen my research from various perspectives. Dave introduced his impressive thoughts of geophysical computing and digital signal processing to me through his courses, and I enjoyed working on the homework and having discussions in his class. I greatly appreciate the support received through the collaborative work with Antoine. He helped me go through the difficulties in the applications of my method on field data.

My sincere thanks also goes to Dr. Lee Bell, Dr. Marianne Houbiers, Dr. Jan Douma, Dr. Seth Haines, who provided me an opportunity to who gave access to field datasets. Without they precious support it would not be possible to conduct this research. I would like to thank Dr. Paul Fowler and Dr. Tariq Alkhalifah for their excellent advises and detailed suggestions during the preparation of this thesis.

I would like to thank my fellow teammates in A-team, I-team, C-team, and S-team, for the stimulating discussions, for the sleepless nights we were working together before deadlines,

and for all the fun we have had in the past four years. I enjoyed talking to Esteban Díaz, Nishant Kamath, Francesco Perrone, Nori Nakata, Vladimir Li, Oscar Jarillo Michel, Hui Wang, Ivan Chen Ning Lim and many others. My special appreciation goes to my friend Jing Wu for her friendship and encouragement.

Special thanks are given to Pamela Kraus, Shingo Ishida, and Michelle Szobody, who were always there when I really needed help. I thank Diane Witters as a writing consultant for her tremendous help on my writing skills, and also as a friend for the encouragement and inspirations from her.

Last but not the least, I would like to thank my family. They form the backbone and origin of my happiness. Their love and support without any complaint or regret has enabled me to complete this PhD project.

To my parents

CHAPTER 1

INTRODUCTION

Seismic techniques extract information from the basic inputs and place reflections at their correct locations with correct relative amplitudes, which can then be interpreted. In seismic exploration, the inputs are the recorded data $d_r(e, \mathbf{x}, t)$, which are a function of the experiment index e, space $\mathbf{x}$ and time t. With source estimation techniques (Bube et al., 1988; Pratt, 1999; Lee and Kim, 2003), one is able to obtain the input source signal $d_s(e, \mathbf{x}, t)$. With the recorded data and estimated source signals, the two biggest goals for seismic processing techniques are to reveal the underground geologic structures and to recover the material properties.

The first goal is related to imaging, which is a widely-used processing technique to obtain the geologic structures (Claerbout and Doherty, 1972; Schneider, 1978; Červenỳ et al., 1982; Whitmore et al., 1983). For reverse time migration (RTM) (Baysal et al., 1983; McMechan, 1983; Etgen et al., 2009; Zhou et al., 2006; Fletcher et al., 2008; Chang and McMechan, 1994), constructs source wavefield $u_s(e, \mathbf{x}, t)$ and receiver wavefield $u_r(e, \mathbf{x}, t)$ by using the estimated source d_s and recorded data d_r, respectively. Different from one-way wave equation approaches such as Kirchhoff and Beam migration, RTM uses a numerical solution of two-way wave equation, which allows the waves to travel both up and down if the velocity model is complex or exhibits strong velocity gradients. Therefore, this imaging technique has no dip limitation and handles all complex waveform multipathing, and it becomes the preferred seismic imaging tool for challenging seismic exploration projects. Conventional RTM consists of two steps: wavefield extrapolation followed by application of an imaging condition (Claerbout, 1971), as illustrated in Figure 1.1(a). The accuracy in terms of both amplitude and location of images $I(\mathbf{x})$ is important to interpretation and drilling.

For migration, it is usually assumed that material properties are known, however, in practice, the material property models for wavefield construction are usually not accurate enough. Moreover, migration suffers from insufficient data, e.g., limited acquisition, and from certain assumptions about the wave equation, e.g., isotropic acoustic. All these limitations lead to imaging artifacts and unfocused images that hamper geologic interpretation, both qualitative and quantitative. Compared to conventional RTM, least-squares reverse time migration (LSRTM) is a more promising approach designed to minimize imaging artifacts and to increase image resolution. As shown in Figure 1.1(b), the objective of LSRTM is to optimize the image I in order to match the recorded data with data generated from Born modeling using the image (Schuster et al., 1993; Nemeth et al., 1999; Aoki and Schuster, 2009; Dai et al., 2011). For LSRTM, material properties $m(\mathbf{x})$ are assumed known and are not updated.

Imaging conditions for conventional RTM represent special cases, i.e., zero-lag crosscorrelation, of more general forms of extended imaging conditions (Rickett and Sava, 2002; Sava and Fomel, 2006; Sava and Vasconcelos, 2009), which define the image as a function of space and cross-correlation lags in space and time. Compared to the conventional image, the extended images contain information which provides a straightforward way to analyze the image quality, e.g., by measurement of the reflection energy focussing in the extended space domain. The extended image distortions caused by velocity model errors can be used to design velocity model building algorithms (Biondi and Sava, 1999; Shen et al., 2003; Sava and Biondi, 2004a,b). Moreover, the extensions can be converted to reflection angles, thus enabling analysis of amplitude variation with angle (Sava and Fomel, 2003; Sava et al., 2005; Sava and Vlad, 2011; Sava and Alkhalifah, 2013).

Another goal for seismic processing techniques is to recover the material properties. Wavefield tomography is a commonly used tool for building models of subsurface parameters from recorded seismic data. Although computationally more expensive compared to ray-based tomography, wavefield tomography is more effective in recovering model param-

eters that are sensitive to waveform amplitudes (Tarantola, 1986; Mora, 1988; Pratt, 1999; Prieux et al., 2010), and has greater capability to accurately recover parameters at large depths (Bae et al., 2012; McNeely et al., 2012). The various approaches to wavefield tomography generally fall into two categories: waveform inversion and wave-equation migration velocity analysis. The waveform inversion technique, generally known as full waveform inversion (FWI), aims to match the predicted and observed data by inverting for physical properties (Claerbout, 1971; Tarantola, 1984; Pratt, 1999; Operto et al., 2004; Biondi and Almomin, 2014). Given an initial guess of the subsurface parameters, the data are predicted by solving a wave-equation. The model m is updated in order to reduce the misfit between the observed data d_r and predicted data, which can also be described as the source wavefield u_s restricted to the known receiver positions (Figure 1.1(c)). Compared to LSRTM, which is a linearized inversion problem, FWI solves a non-linear inversion problem, where the forward modeling operator changes with model m at each iteration.

Wavefield migration and tomography are well-developed under the acoustic assumption (Claerbout, 1971; Tarantola, 1984; Pratt, 1999; Operto et al., 2004; Biondi and Almomin, 2014); however, recorded seismic data, either in scalar d_r or vector $\mathbf{d}_r$ forms, may include shear waves in addition to the compressional waves. Because all wave modes contain material property and structural information about the subsurface, the elastic wavefield allows for better characterization of the subsurface (Tarantola, 1986; Pratt, 1990; Guasch et al., 2012; Vigh et al., 2012). For example, elastic wavefields are sensitive to S velocity change in the model in addition to changes in P velocity and density. The contribution of my thesis is in applying migration, and waveform inversion methods to multicomponent wavefields $\mathbf{u}$ for elastic material properties, vector $\mathbf{m}$, which can provide shear wave related lithological information. I propose new imaging conditions for different types of elastic images, which illustrate certain aspects of the elastic media, for example, images indicating perturbations in P and S velocity models. For elastic waveform inversion, I propose improved methods to invert for realistic P and S velocity models simultaneously. With my proposed meth-

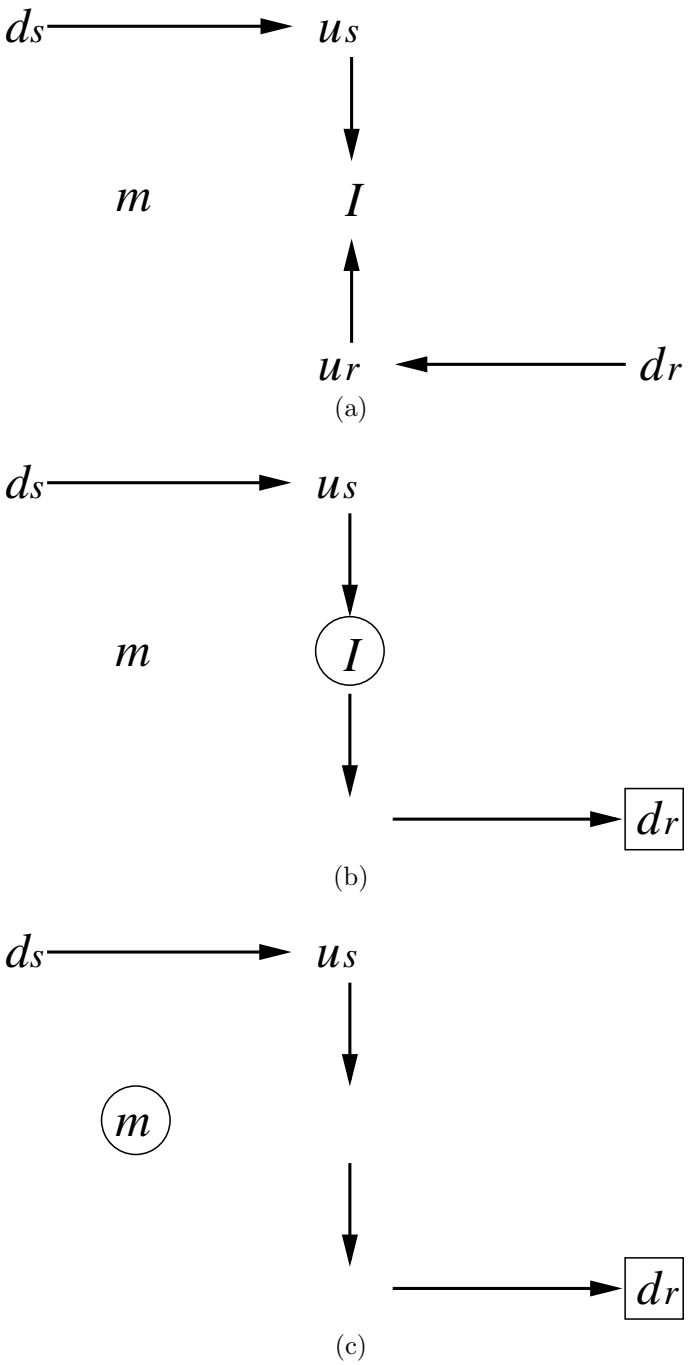

Figure 1.1: Schematic representations of for (a) RTM, (b) LSRTM, and (c) FWI. Symbols d_s and d_r represent the source wavelet and recorded data, respectively. Symbol I is the computed image. u_s and u_r are constructed source and receiver wavefield, respectively, by using model material property m. Squares highlight the domain used to construct the objective function. Circles indicate the components that are updated through inversion in order to minimize the objective function.

ods, I obtain elastic images or models with improved amplitude information that facilitates reservoir characterization.

In Chapter 2 of my thesis, I propose an imaging condition for converted waves obtained using multi-component data. For elastic migration, I use an elastic wave-equation-based wavefield propagation operator to construct source and receiver vector wavefields. Following wavefield extrapolation, I apply an imaging condition by combining the source and receiver wavefields to obtain images of subsurface structures. Multi-component wavefields allow for a variety of imaging conditions that provide multiple images by cross-correlating different wave modes present in the source and receiver wavefields (Dellinger and Etgen, 1990b; Yan and Sava, 2008; Yan and Xie, 2012). In this case, the migrated images correspond to reflectivity for different combinations of incident and reflected P- and S-modes, e.g. PP, PS, SP and SS reflectivity. One difficulty when imaging multi-component wavefields is that the PS and SP images change sign at certain incidence angles. For example, in isotropic media, polarity reversal occurs at normal incidence (Balch and Erdemir, 1994). This sign change can lead to destructive interference when multiple experiments of a seismic survey are stacked for a final image. Another difficulty is that the PS and SP images are vectors in 3D case, and it is difficult to combine the three components of each image and find the physical meaning of the combinations. I address this problem by designing an imaging condition for converted waves to correct the image polarity and produce scalar PS and SP images. This imaging condition exploits pure P- and S-modes obtained by Helmholtz decomposition. The PS and SP images are generated using geometrical relationships between the propagation directions for the P and S wavefields, the reflector orientation, and the S-mode polarization direction.

In Chapter 3 of my thesis, I extend the elastic images derived in Chapter 2 to time- and space-lag domains to compute common image gathers (CIG) and common image point (CIP) gathers. Wavefield-based migration velocity analysis using the semblance principle requires computation of images in an extended space in which we can evaluate the imaging consistency as a function of overlapping experiments. One approach is to assemble those seismic

images in CIGs that represent image attributes indicating inaccurate model properties, e.g., angle domain CIGs (Biondi and Symes, 2004; Sava and Biondi, 2004a) and offset domain CIGs (Mulder and Ten Kroode, 2002). The angle domain CIGs describe the reflectivity as a function of reflection angles and a space axis, typically the depth axis, which is not computationally efficient for analysis that only needs to focus on the most relevant locations. An alternative approach is to use CIP gathers instead of CIGs constructed as a function of both space and time-lag extensions at sparse and irregularly distributed points in the image (Yan et al., 2010; Yang et al., 2010; Sava and Vlad, 2011). In this chapter, I discuss an extended imaging condition developed from the potential imaging condition proposed in Chapter 2. Similar to RTM images computed using the proposed potential imaging condition, the extended RTM images are scalars and have no polarity changes at normal incidence. I propose methods to apply angle decomposition to both space-/time-lag CIGs and CIP gathers. The angle gathers depict reflectivity as a function of reflection angles. Such images highlight the subsurface illumination patterns and therefore could be used for image postprocessing for amplitude variation with angle (AVA) analysis, or for tomographic velocity updates.

In Chapter 4, I propose an least-squares reverse time migration (LSRTM) algorithm. A key component for elastic LSRTM is the imaging condition, and many different types of imaging conditions have been proposed for elastic media. For example, Yan and Sava (2008) propose a displacement imaging condition that crosscorrelates each component of source and receiver displacement wavefields. They also propose a potential imaging condition that crosscorrelates P- and S-wave modes in source and receiver wavefields. One issue with this potential imaging condition is that the image components for converted waves change polarity at normal incidence. Stanton and Sacchi (2015) use a LSRTM method based on this imaging condition, including an additional polarity correction in the angle domain. In Chapter 2, I show a scalar imaging condition for converted waves that produces scalar images without polarity reversal; however, this imaging condition requires knowledge of the geologic dip. Here I propose an elastic LSRTM method based on another new perturbation imaging

condition, which is derived for squared P and S velocities. Images computed using this new imaging condition can be simply related to physical subsurface properties, and do not suffer from polarity changes; Using the perturbation imaging condition, one is able to obtain elastic LSRTM images with higher resolution and reduced migration artifacts, including cross-talks of different wave modes.

In Chapters 5 of my thesis, I propose tomographic methods for elastic full waveform inversion. For elastic tomography, there are many possible model parameterizations, which lead to different inversion schemes. For example, Tarantola (1986) shows wavefield tomography for compressional (P) impedance, shear (S) impedance, and density, while Mora (1988) and Guasch et al. (2012) compute P- and S-velocity models using wavefield tomography. Moreover, although inversion for multi-parameters adds more physical information to the updated model compared to single-parameter inversion, different parameters in the updated model may not be physically realistic (Plessix, 2006), i.e., inversion might not be able to resolve the model parameters while preserving their intrinsic physical relationships. I propose to address this problem by introducing a petrophysical constraint term in the objective function, which explicitly sets the relationships between model parameters. Such physical relationships need to be enforced explicitly because their action on the inverted model differs from the alternative constraints provided by data or by shaping model regularizations (Tarantola, 1987; Hale, 2007; Guitton et al., 2012). Physical relationships between model parameters in elastic media can be derived from well logs, seismic data, and laboratory measurements, but they can also be derived based on first-principle physical relationships (Tsuneyama, 2006; Compton and Hale, 2013). In Chapter 5, I perform FWI using the isotropic elastic wave-equation, and the mathematical derivation shows that the simplest approach is to invert for the squared velocities of P- and S-waves. I include the petrophysical constraint term into the objective functions, which sets the relationships between parameters based on petrophysical prior information. Examples demonstrate that this physical constraint yields models that are more physically plausible, compared to models obtained using only the data misfit ob-

jective function. In the last chapter, I draw general conclusions and suggest possible future work directions.

CHAPTER 2

SCALAR IMAGING CONDITION FOR ELASTIC REVERSE TIME MIGRATION

Modified from a paper published[1] in *Geophysics*

Yuting Duan[2,3] and Paul Sava[3]

Polarity changes in converted-wave images constructed by elastic reverse-time migration cause destructive interference after stacking over the experiments of a seismic survey. This polarity reversal is due to PS and SP reflectivities reversing sign at certain incidence angles, e.g. at normal incidence in isotropic media. Many of the available polarity correction methods are complex and require costly transformations, e.g. to the angle domain. We derive a simple imaging condition for converted waves in order to correct the image polarity and reveal the conversion strength from one wave mode to another. Our imaging condition exploits pure P- and S-modes obtained by Helmholtz decomposition. Instead of correlating Cartesian components of the vector S-mode with the P-mode, we exploit all three components of the S wavefield at once to produce a unique image. We generate PS and SP images using geometrical relationships between the propagation directions for the P and S wavefields, the reflector orientation, and the S-mode polarization direction. Compared to alternative methods for correcting the polarity reversal of PS and SP images, our imaging condition is simple and robust and does not significantly increase the cost of reverse-time migration. Several numerical examples demonstrate the effectiveness of our new imaging condition using simple and complex models.

2.1 Introduction

Advances in seismic acquisition and ongoing improvements in computational capability have made imaging using multi-component elastic waves increasingly feasible. Elastic mi-

[1]Reprinted with permission of *Geophysics*, 2015, 80, No. 4, S127-S136

[2]Author for correspondence.
[3]Center for Wave Phenomena, Colorado School of Mines, 924 16th Street, Golden, CO 80401.

gration with multi-component seismic data can provide additional subsurface structural information compared to conventional acoustic migration using single-component data. Multi-component seismic data can be used, for example, to estimate fracture distributions as well as elastic properties. Such data can also provide broader illumination of the subsurface, thus reducing potential P-wave shadow zones.

In complex geologic environments, it is desirable to use wavefield-based imaging methods, e.g. reverse-time migration (RTM). Conventional reverse-time migration consists of two steps: wavefield extrapolation followed by the application of an imaging condition (Claerbout, 1971). Wavefield extrapolation requires constructing source and receiver wavefields using an estimated wavelet and the recorded data, respectively. In elastic media, source and receiver wavefields are constructed using different forms of elastic (vector) wave equations corresponding to different parametrizations of the subsurface model parameters.

Following wavefield extrapolation, an imaging condition is applied by combining the source and receiver wavefields to obtain images of subsurface structures. Multi-component wavefields allow for a variety of imaging conditions (Yan and Sava, 2008; Denli and Huang, 2008; Artman et al., 2009; Wu et al., 2010). A simple imaging condition for multi-component wavefields is the crosscorrelation of the Cartesian components of the displacement vectors characterizing the source and receiver wavefields (Yan and Sava, 2008). In 3D, this results in 9 images for different combinations of source and receiver displacement vector components. One limitation of this method is that P- and S-modes are mixed in the extrapolated wavefields; therefore, cross-talk between P- and S-modes creates artifacts that make interpretation difficult. Another imaging condition for multi-component wavefields first requires the decomposition of wavefields into different wave modes, for example, P- and S-modes. For isotropic elastic wavefields far from the source, P- and S-modes correspond to the compressional and transverse components of the wavefield, respectively (Aki and Richards, 2002). Similar to the imaging condition using displacement vector components, this imaging condition provides multiple images by cross-correlating different wave modes present in the source

and receiver wavefields (Dellinger and Etgen, 1990b; Yoon et al., 2004; Yan and Sava, 2008; Yan and Xie, 2012). However, in this case, images correspond to reflectivity for different combinations of incident and reflected P- and S-modes, e.g. PP, PS, SP and SS reflectivity, and therefore are more useful in geological interpretation.

One difficulty when imaging multi-component wavefields is that the PS and SP images change sign at certain incidence angles. For example, in isotropic media, polarity reversal occurs at normal incidence (Balch and Erdemir, 1994). This sign change can lead to destructive interference when multiple experiments of a seismic survey are stacked for a final image. A simple way to correct the polarity reversal in PS and SP images is based on the assumption that the polarity change occurs at zero offset and can be corrected based on the acquisition geometry. However, this assumption fails if the reflectors are not horizontal (Du et al., 2012b). An alternative method to correct for the polarity change requires that we compute the incidence angles at each image point and then reverse the polarity based on this estimated angle under the assumption that polarity reverses at normal incidence. There are various techniques to compute the reflection angles. One possibility is to use ray theory to simulate the incident wavefield direction, and apply this direction to the reflected wave extrapolated from the surface to every imaging point (Balch and Erdemir, 1994). This method is limited by the ray approximation and may become impractical when applied to elastic RTM in media characterized by complex multipathing. Another method to correct for polarity changes is to image in the angle domain, and then reverse the image polarity as a function of angle (Yan and Sava, 2008; Rosales et al., 2008; Yan and Xie, 2012). Constructing angle-domain common image gathers is accurate and robust, but can also be expensive. Finally, another possibility for polarity correction is to reverse the polarity in source and receiver wavefields based on the sign of the reflection coefficient, which is computed from the directions of the incident and reflected waves (Sun et al., 2006; Du et al., 2012a). These directions are typically computed using Poynting vectors, which may be inaccurate in complicated models characterized by multipathing (Dickens and Winbow, 2011; Patrikeeva and

Sava, 2013).

In this paper, we propose an alternative 3D imaging condition for elastic reverse-time migration. Our new imaging condition exploits geometric relationships between incident and reflected wave directions, reflector orientation, and rotation directions of S wavefields . Using our new imaging condition, we are able to obtain PS and SP images without polarity reversal. The method is simple and robust and operates on separated wave modes obtained, for example, using Helmholtz decomposition (Yan and Sava, 2008). Our method is also computationally efficient to apply since it does not require complex operations such as angle or directional decomposition. We begin by discussing the theory underlying our method and then illustrate it using simple and complex synthetic examples.

2.2 Theory

Our proposed imaging condition is meant to automatically compensate for the polarity reversal characterizing conventional converted-wave images. Our method builds on existing techniques which first decompose elastic wavefields into pure P- and S-modes. However, in contrast with more conventional methods, our imaging condition does not simply correlate the P-mode with different components of the vector S-mode. We explain the logic of our method next.

Reconstructed source and receiver elastic wavefields can be separated into P- and S-modes prior to imaging (Dellinger and Etgen, 1990b; Yan and Sava, 2008). In isotropic media, this separation can be performed using Helmholtz decomposition (Aki and Richards, 2002), which describes the compressional component P and transverse component $\mathbf{S}$ of the wavefield using the divergence and curl of the displacement vector field $\mathbf{u}$:

$$P\left(e,\mathbf{x},t\right) = \nabla\cdot\mathbf{u}\left(e,\mathbf{x},t\right), \tag{2.1}$$

$$\mathbf{S}\left(e,\mathbf{x},t\right) = \nabla\times\mathbf{u}\left(e,\mathbf{x},t\right). \tag{2.2}$$

PS and SP images can then be obtained by cross-correlating the P wavefield with each component of the $\mathbf{S}$ wavefield (Yan and Sava, 2008). Images produced in this way have

three independent components at every location in space, i.e., PS and SP images are vector images. The method discussed here is applicable to wavefields reconstructed in isotropic media, but can be adapted to anisotropic media, for example using the method discussed by Yan and Sava (2008).

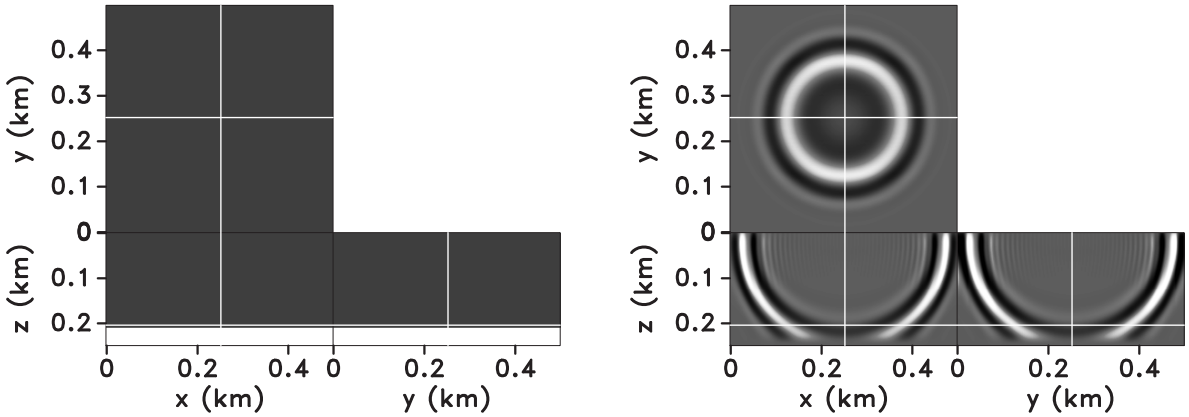

(a) (b)

Figure 2.1: (a) 3D synthetic model with one horizontal reflector in a constant velocity medium, at depth $z = 0.2$ km. The source is located at $(0.2, 0.2, 0.02)$ km; the 2D network of receivers is at $z = 0.03$ km. (b) A snapshot of source P wavefield.

We illustrate this conventional imaging condition with the 3D synthetic model shown in Figure 2.1(a), which contains one horizontal reflector embedded in a constant velocity medium. A single pressure source is at $(0.2, 0.2, 0.02)$ and the source function is a Ricker wavelet with a peak frequency of 30 Hz. Figure 2.1(b) shows a snapshot of the source P wavefield for a single source indicated in Figure 2.1(a). The x-, y- and z-components of the receiver S wavefield are shown in Figures 2.2(a), 2.2(c), and 2.2(e), respectively. P and S wavefields are decomposed from the displacement wavefield using Helmholtz decomposition. The z-component of the receiver S wavefield corresponds to S waves propagating in the xy-plane, which are weaker than the x- and y-component shown in 2.2(e). In Figures 2.2(a) and 2.2(c), another S wave appearing at $z = 0.1$ km is converted from P waves in the recorded data. Such waves produce artifacts in the migrated images, as seen in Figures 2.2(b), 2.2(d), and 2.2(f). As the artifacts are generally inconsistent with each other between different

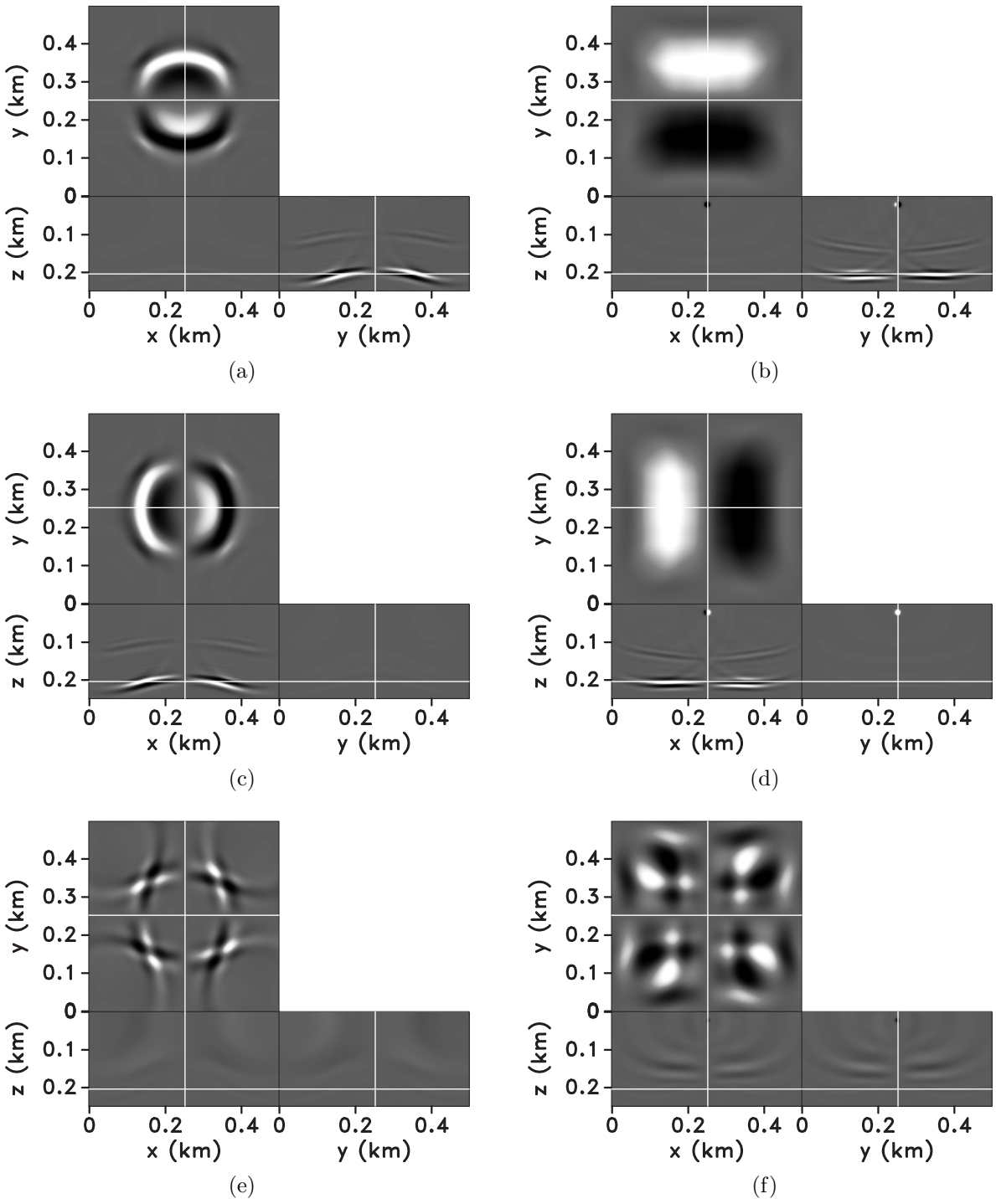

Figure 2.2: Snapshots of (a) x-, (c) y-, and (e) z-component of the receiver S wavefield and the corresponding (b) x-, (d) y-, and (f) z-component of the PS image. The S wavefields are decomposed from the displacement wavefield using Helmholtz decomposition. Polarity reversal occurs as a function of azimuth in the wavefield which leads to polarity change in three components of the PS image shown. Z-component of the S wavefield is much weaker than x- and y-component.

shots, they are attenuated in stacked images (Duan and Sava, 2014). Notice that polarity reversal occurs as a function of azimuth, which leads to the polarity change in the three components of the PS image shown in Figures 2.2(b), 2.2(d), and 2.2(f).

Another problem of the conventional imaging condition is that it is difficult to find the physical meaning of the various constructed images. We seek to avoid vector PS and SP images by combining all components of the S wavefield with the P wavefield into a single image representing the energy conversion strength from one wave-mode to another at an interface.

To formulate the imaging condition, I define the following quantities, shown in Figures 2.3 and 2.4 :

- Vector $\mathbf{n}$ which is the local normal to the interface represented by plane $\mathcal{I}$
- Vector $\mathbf{S}$ indicating the curl direction of the S-mode particle displacement

According to Snell's law, propagation directions of incident and reflected waves, and $\mathbf{n}$ belong to the reflection plane $\mathcal{R}$. Vector $\mathbf{S}$ is orthogonal to the propagation direction of the S-mode. In the following, I assume that I know the normal vector $\mathbf{n}$, e.g., from a prior PP or PS stacked images obtained using other methods, such as PS Kirchhoff migration.

Both incident P- and S-modes generate reflected S-modes; therefore, the receiver wavefield vector $\mathbf{S}$ is complicated and in general not orthogonal to the plane $\mathcal{R}$, and can be decomposed into vectors $\mathbf{S}_\perp$ and $\mathbf{S}_\parallel$ such that

$$\mathbf{S} = \mathbf{S}_\perp + \mathbf{S}_\parallel \ . \tag{2.3}$$

Vectors $\mathbf{S}_\perp$ and $\mathbf{S}_\parallel$ are orthogonal and parallel to plane $\mathcal{R}$, respectively. The S-modes reflected from incident P- and SV-modes are SV-modes and confined to the vector field $\mathbf{S}_\perp$. The S-modes reflected from incident SH-modes are also SH-modes and confined to the vector field $\mathbf{S}_\parallel$.

As indicated earlier, the signs of the PS and SP reflection coefficients change across normal incidence in every plane, which causes the polarity of the reflected waves to change

at normal incidence. Since normal incidence depends on the acquisition geometry and the geologic structure, this polarity reversal can occur at different positions in space, thus making it difficult to stack images for an entire multicomponent survey.

In order to address this challenge, we propose the following imaging conditions for I^{PS} and I^{SP} components in image $I = \begin{bmatrix} I^{PP} & I^{PS} & I^{SP} & I^{SS} \end{bmatrix}^T$:

$$I^{PP}(\mathbf{x}) = \sum_{e,t} P_s(e,\mathbf{x},t)\, P_r(e,\mathbf{x},t) \ , \tag{2.4}$$

$$I^{PS}(\mathbf{x}) = \sum_{e,t} (\nabla P_s(e,\mathbf{x},t) \times \mathbf{n}(\mathbf{x})) \cdot \mathbf{S}_r(e,\mathbf{x},t) \ , \tag{2.5}$$

$$I^{SP}(\mathbf{x}) = \sum_{e,t} ((\nabla \times \mathbf{S}_s(e,\mathbf{x},t)) \cdot \mathbf{n}(\mathbf{x}))\, P_r(e,\mathbf{x},t) \ . \tag{2.6}$$

$$I^{SS}(\mathbf{x}) = \sum_{e,t} \mathbf{S}_s(e,\mathbf{x},t) \cdot \mathbf{S}_r(e,\mathbf{x},t) \ . \tag{2.7}$$

Here, P and $\mathbf{S}$ are functions of the experiment index e, space $\mathbf{x}$ and time t, and represent the scalar P- and vector S-modes after Helmholtz decomposition, respectively. $I^{PS}(\mathbf{x})$ and $I^{SP}(\mathbf{x})$ are the PS and SP scalar images, respectively. This expression contains summation over time as well as summation over experiments. Subscripts s and r indicate source- and receiver-side wavefields, respectively. We assume that we know the normal vector $\mathbf{n}$ which can be obtained in practice, for example, from a prior computed PP image. Note that waves with small incidence angles contribute to PS and SP images much less than those with larger incidence angles because the PS and SP reflectivities approach zero as the incidence angle decreases to zero. Thus a small error in the estimation of normal vector $\mathbf{n}$ would affect only the polarity correction at small incidence angles, and this effect can be neglected in the stacked image. In fact, for the examples shown in this paper, we use a smoothed version of the true normal vectors and obtain satisfactory results.

The geometrical interpretation of our new imaging condition, equations 2.4 - 2.7, is as follows:

PP imaging (equation 2.4): The decomposed incident P-mode and the corresponding reflected P-mode are scalars, and their propagation directions are in the reflection plane $\mathcal{R}$.

Similar to an acoustic RTM image, which is the crosscorrelation of the source and receiver scalar wavefields, the PP image is defined as the crosscorrelation the source and receiver scalar P wavefields.

PS imaging (equation 2.5): The vector ∇P_s characterizes the propagation direction of the incident P-mode and can be calculated directly on the separated P wavefield. The cross product with the normal vector $\mathbf{n}$ constructs a vector orthogonal to the reflection plane $\mathcal{R}$; as indicated earlier, this direction is parallel with the reflected SV-mode $\mathbf{S}_{r\perp}$ and orthogonal to other SH-modes $\mathbf{S}_{r\parallel}$ in the wavefield. Therefore, the dot product of $(\nabla P \times \mathbf{n})$ and $\mathbf{S}$ is just a projection of the vector $\mathbf{S}_{r\perp}$ wavefield on a vector which depends on the incidence angle of the P wavefield. For a P-mode incident in the opposite direction, the vector $\nabla P \times \mathbf{n}$ reverses direction, thus compensating for the opposite direction of the S-mode. Consequently, the PS imaging condition has the same sign regardless of the incidence direction, and therefore PS images can be stacked without canceling each-other at various positions in space.

SP imaging (equation 2.6): The reflected P-mode is generated by the incident SV-mode $\mathbf{S}_{s\perp}$. Vector $\nabla \times \mathbf{S}_{s\perp}$ is orthogonal to the reflection plane. The dot product with the normal vector $\mathbf{n}$ produces a scalar field characterizing the magnitude of the S-mode, but is signed according to its relation with respect to the normal $\mathbf{n}$. This scalar quantity can be simply correlated with the scalar reflected P wavefield, thus leading to a single image without sign change as a function of the incidence direction. Thus, SP images produced in this fashion can also be stacked without canceling each other at various positions in space.

SS imaging (equation 2.7): The incident $\mathbf{S}_s$ contains components $\mathbf{S}_{s\perp}$ (SV-mode) and $\mathbf{S}_{s\parallel}$ (SH-mode), generating reflected $\mathbf{S}_{r\perp}$ (SV-mode) and $\mathbf{S}_{r\parallel}$ (SH-mode), respectively. The cross product of incident $\mathbf{S}_s$ and $\mathbf{S}_r$ for the SS imaging condition can be expanded as $\mathbf{S}_{s\perp} \cdot \mathbf{S}_{r\perp} + \mathbf{S}_{s\parallel} \cdot \mathbf{S}_{r\parallel}$, because vectors $\mathbf{S}_{s\perp}$ and $\mathbf{S}_{s\parallel}$ are orthogonal to each other and $\mathbf{S}_{s\perp} \cdot \mathbf{S}_{r\parallel} = \mathbf{S}_{s\parallel} \cdot \mathbf{S}_{r\perp} = 0$. Therefore, the SS image I^{SS} is a combination for the SH image and SV image.

In 2D, the scalar imaging conditions from equations 2.5 and 2.6 are simplified. The $\mathbf{S}$ has only one non-zero component, S_y, since the vector $\mathbf{S}$ is orthogonal to the local reflection

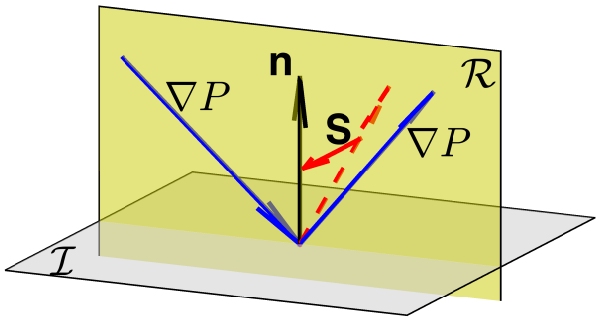

Figure 2.3: Schematic representation of P and SV reflections for an incidence P-mode. $\mathcal{I}$ and $\mathcal{R}$ are the interface plane and reflection planes, respectively. Vector **n** indicates the normal to the interface $\mathcal{I}$, vector ∇P is parallel to the propagation direction of the incident P-mode. The vectors represented by the dashed lines indicate the propagation directions of the S-modes, and vector **S** is orthogonal to its propagation direction. ∇P and **n** are both contained within the reflection plane $\mathcal{R}$. Vector **S** representing the reflected SV-mode is orthogonal to the reflection plane $\mathcal{R}$.

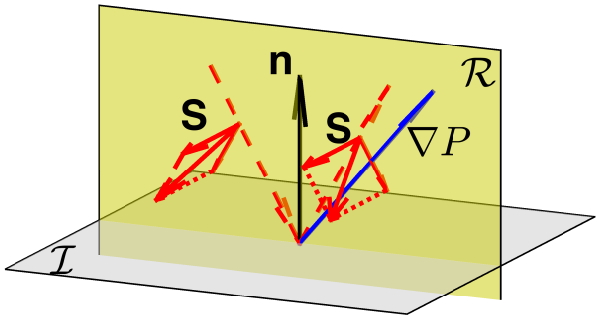

Figure 2.4: Schematic representation of P and S reflections for an incidence S-mode. Both incidence and reflected S-modes can be decomposed in to components orthogonal to the reflection plane (SV-modes) and components in the reflection plane (SH-modes). The incidence SH-mode generates reflected SH-mode, while the incidence SV-mode generates reflected P and SV-mode.

plane $\mathcal{R}$. Therefore, the PS and SP imaging conditions are

$$I^{PS} = - \sum_e \sum_t \left(\frac{\partial P}{\partial x} n_z - \frac{\partial P}{\partial z} n_x \right) S_y \, , \tag{2.8}$$

$$I^{SP} = \sum_e \sum_t \left(\frac{\partial S_y}{\partial x} n_z - \frac{\partial S_y}{\partial z} n_x \right) P \, , \tag{2.9}$$

where $I = I\,(x,z)$, $P = P\,(e,x,z,t)$, $S_y = S_y\,(e,x,z,t)$, $n_z = n_z\,(x,z)$ and $n_x = n_x\,(x,z)$. For a horizontal reflector, i.e. $\mathbf{n} = \{0,0,1\}$, we can write

$$I^{PS} = - \sum_e \sum_t \frac{\partial P}{\partial x} S_y \, , \tag{2.10}$$

$$I^{SP} = \sum_e \sum_t \frac{\partial S_y}{\partial x} P \, , \tag{2.11}$$

which simply indicates that in the new imaging condition, we correlate the P or S wavefields with the x derivative of the S or P wavefields, respectively. That is, of course, just a special case of the more general relation in equations 2.5 and 2.6.

We interpret the propagation direction of the P-mode and the polarization direction of the S-mode as the gradient and curl of the displacement vector field, respectively. For a plane wave, ∇P and $\nabla \times \mathbf{S}$ are equivalent to $i\mathbf{k}P$ and $i\mathbf{k} \times \mathbf{S}$, respectively, where $\mathbf{k}$ is the wavenumber vector indicating the propagation direction. However, while the spatial derivatives contained in the gradient and curl provide information regarding the directionality of the wavefield, the application of the gradient and curl operators also distorts the amplitude spectrum as well as the phase of the wavefield, and implicitly it distorts the phase of the migrated images. The distortion of the amplitude and phase is undesirable and must be avoided because it can lead to incorrect stratigraphic interpretation.

To correct for a similar distortion of images resulting from the application of a Laplacian filter designed to remove backscattering artifacts in reverse-time migration, Zhang and Sun (2009) apply a v^2/ω^2 filter that compensates for the k^2 representing the Laplacian. Here v is velocity and ω is the angular frequency. To apply this filter, Zhang and Sun (2009)

propose a two-step approach: first, divide the source function by ω^2 prior to reconstructing the source wavefield, and second, scale the image by v^2 following migration. The ω^2 filtering is equivalent to a double time integral. We follow their approach and use a similar filter to correct for the distortion of the amplitude and phase of the image. Notice that we can write $i\mathbf{k} = \frac{i\omega}{v}\frac{\mathbf{k}}{|\mathbf{k}|}$, where the unit vector $\frac{\mathbf{k}}{|\mathbf{k}|}$ is the propagation direction. Hence, to correct the imaging condition in equation 2.5, we apply a $1/i\omega$ filter by integrating the source function over time prior to source wavefield reconstruction, and then we multiply the image in the space domain by the P-wave velocity v. A similar transformation is applicable for the imaging condition in 2.6 except that in this case, we scale by the S-wave velocity.

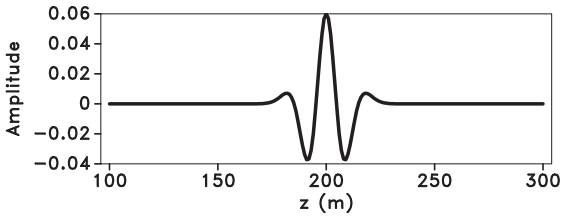

(a)

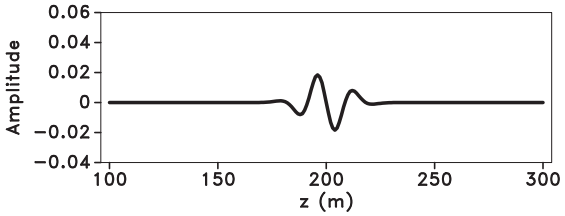

(b)

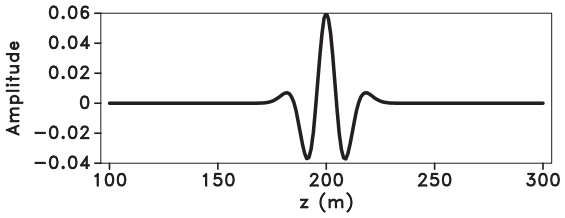

(c)

Figure 2.5: 1D images obtained by (a) crosscorrelation of source and receiver wavefields, (b) crosscorrelation followed by spatial derivative, and (c) source integral prior to crosscorrelation, followed by spatial derivative.

Figure 2.5(a) shows a 1D image obtained by crosscorrelation of source and receiver wavefields. After applying a gradient filter, which is simply a spatial derivative in 1D, the amplitude and phase of the image change, Figure 2.5(b). To allow for application of the gradient filter while preserving the amplitude and phase, we follow the flow discussed above to obtain the image shown in Figure 2.5(c), which is identical to the image shown in Figure 2.5(a).

Using the same $v/(i\omega)$ filter, we are also able to correct for the amplitude and phase distortion resulting from Helmholtz decomposition, which involves computation of the divergence and curl of the displacement wavefields. In this case, we apply the filter $v/(i\omega)$ to both the source and receiver wavefields except that the meaning of the velocity is different, depending on whether we operate with the P or S mode. Similar to the correction for our proposed imaging condition, we apply a $1/i\omega$ filter by integrating over time the source function prior to source wavefield reconstruction, and by integrating the recorded data prior to receiver wavefield reconstruction. Then, we multiply the PS and SP images by the product of the velocities for the source and receiver wavefields.

In summary, to correct for the amplitude and phase distortion resulting from both Helmholtz decomposition and our new imaging condition, we combine the two corrections discussed earlier by (1) integrating the source function over time twice, prior to source wavefield reconstruction; (2) integrating the recorded data over time once, prior to receiver wavefield reconstruction; and (3) multiplying the PS image by $v_p^2 v_s$ and the SP image by $v_p v_s^2$.

The units of the original displacement wavefield are meters, and the units of the spatial derivative of the wavefield are 1. The application of a $v/(i\omega)$ filter, in order to correct for the amplitude and phase distortion caused by the spatial derivative, changes the units of the spatial derivative of the wavefield back to meters. Therefore, the units of the image computed from the new imaging condition with the filter are meters squared.

For the 3D example in Figure 2.1(a), our new imaging condition leads to the PS image in Figure 2.6. In this figure, we apply the filters to correct for image spectrum and

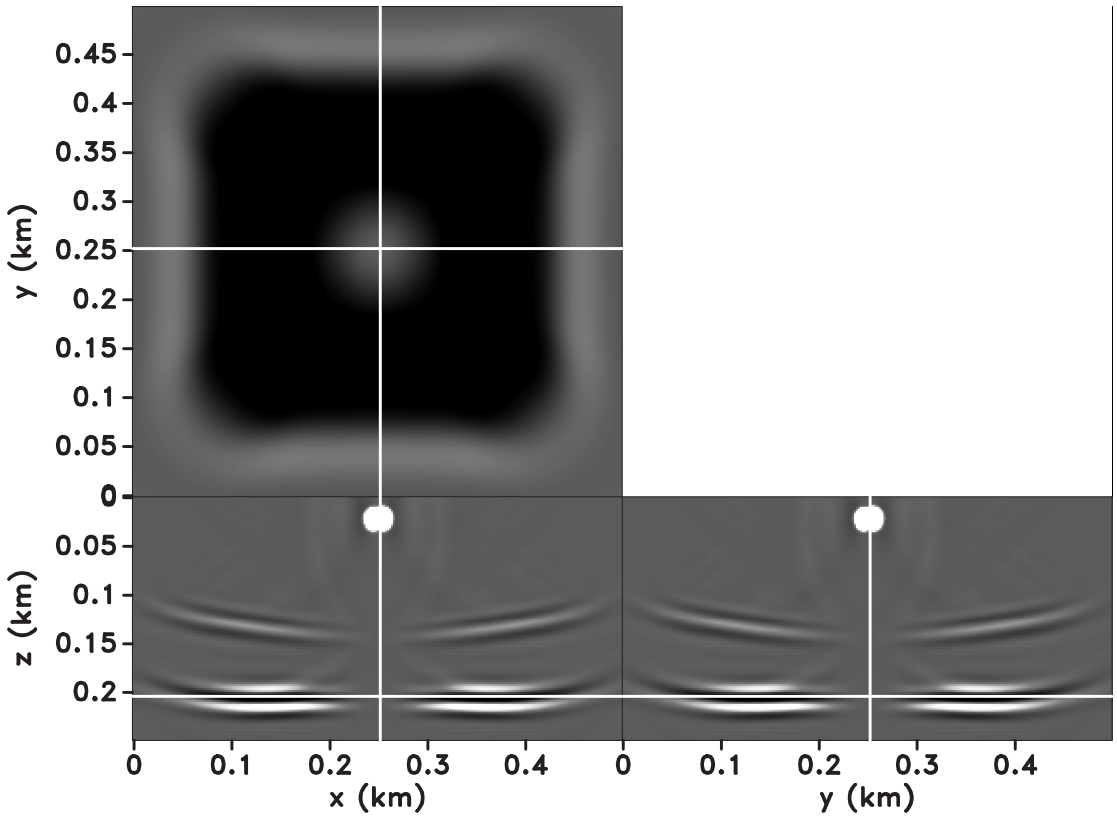

Figure 2.6: The PS image computed using the new imaging condition. Compared to the three components of the vector image shown in Figure 2.2(b), 2.2(d) and 2.2(f), this PS image is a scalar without polarity reversal.

amplitude distortions due to Helmholtz decomposition and our new imaging condition. In contrast to the vector PS image characterized by polarity reversal obtained by using the conventional imaging condition, the PS image obtained using our new imaging condition is a scalar without polarity reversal. This correction allows us to stack multiple elastic images over experiments without cancellation due to opposite polarity of the images constructed from different experiments.

2.3 Examples

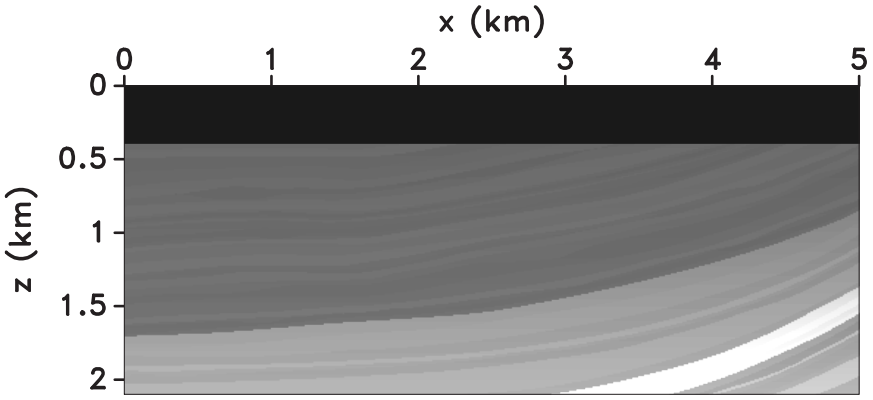

Figure 2.7: 2D synthetic density model with dipping layers.

We illustrate our method using three synthetic models. During the procedure for obtaining PS and SP images, we apply the filters to correct for the amplitude and phase distortion. In the first two examples, we also add a thin water layer to both of the models in order to generate PS conversion from a hard water bottom. The water layer is 0.4 km. The models are smoothed for source and receiver wavefield reconstruction. The first model (Figure 2.7) consists of semi-parallel gently dipping layers. We use 40 sources evenly distributed along the surface, and 500 receivers located at the surface of the model. The source function is a Ricker wavelet with a peak frequency of 35 Hz. Figures 2.8(a) and 2.8(b) are snapshots of the source P and receiver S wavefields, respectively, and Figures 2.9(a) and 2.9(b) are snapshots of the source S and receiver P wavefields, respectively. In both cases, we observe polarity flips in the S wavefield.

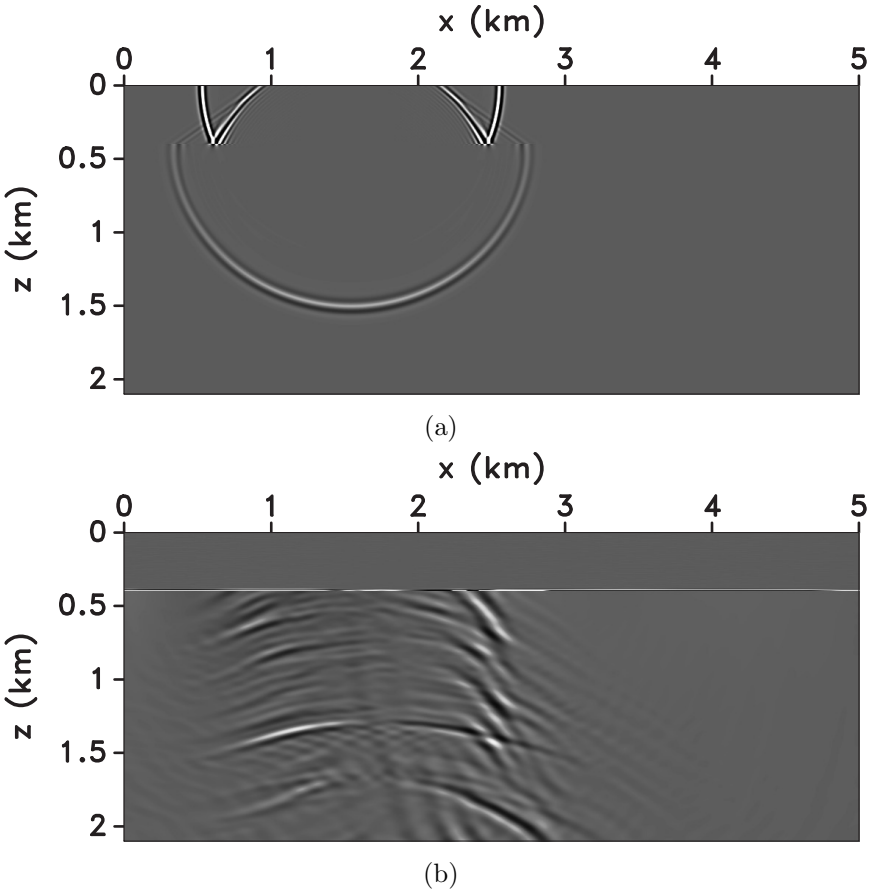

Figure 2.8: (a) Source P wavefield and (b) receiver S wavefield for a single shot. Both source and recievers are on the surface of the model.

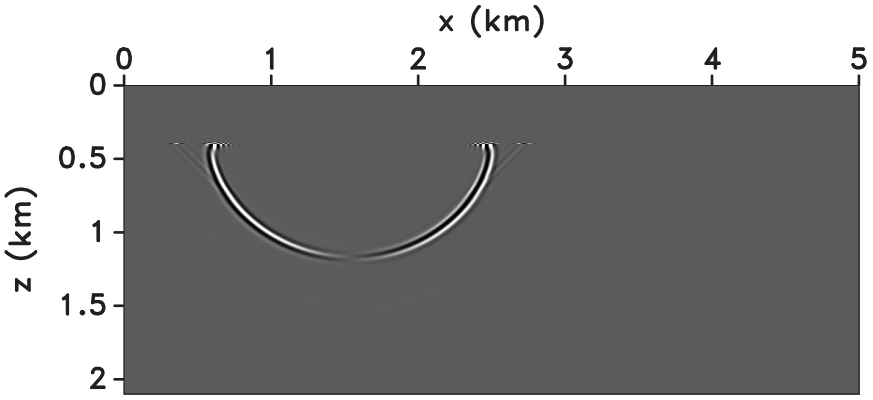

(a)

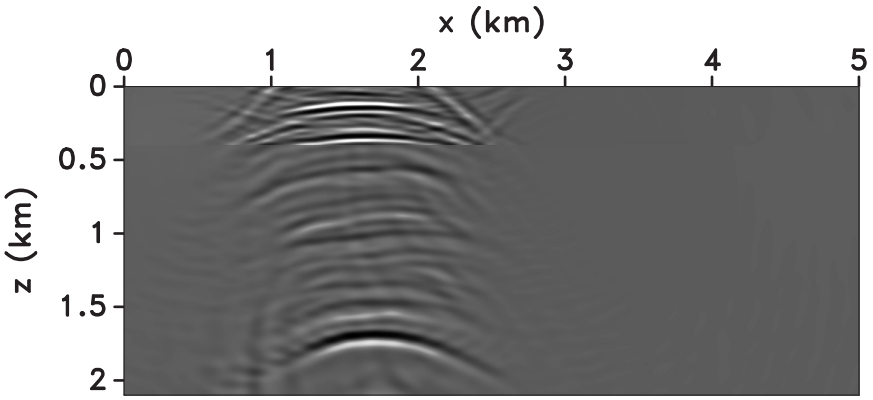

(b)

Figure 2.9: (a) Source S wavefield and (b) receiver P wavefield for a single shot. Both source and recievers are on the surface of the model.

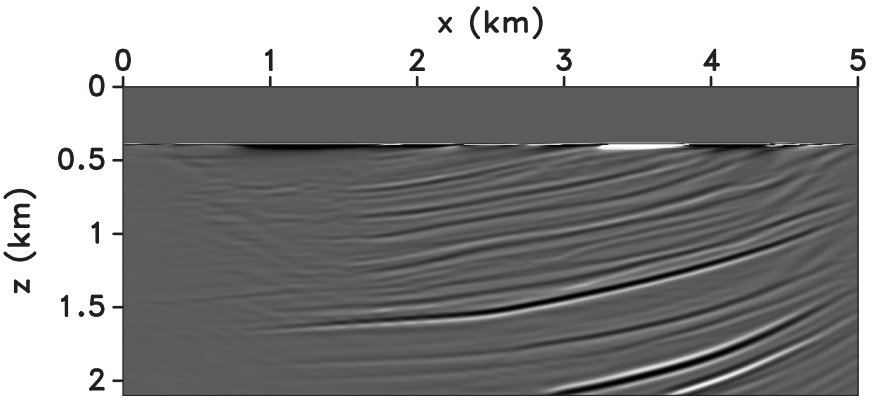

(a)

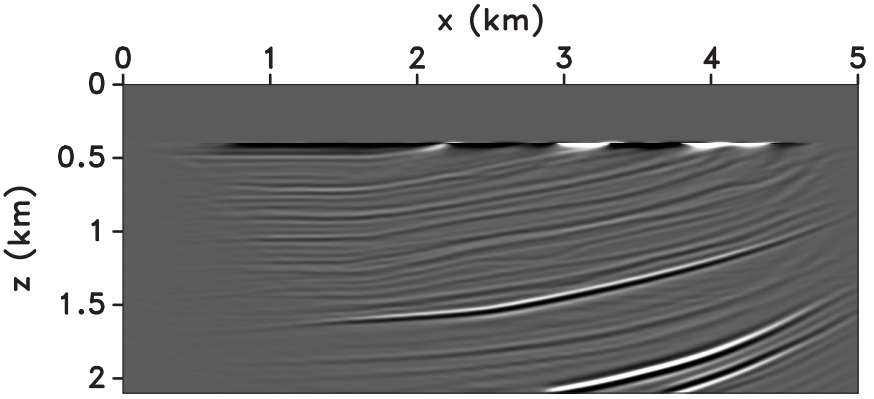

(b)

Figure 2.10: PS stacked images obtained using (a) the conventional imaging condition and (b) our new imaging condition. The image in panel (b) at $(1.0, 1.0)$ km is stronger, in contrast with the image in panel (a) which suffers from cancellation due to polarity reversal.

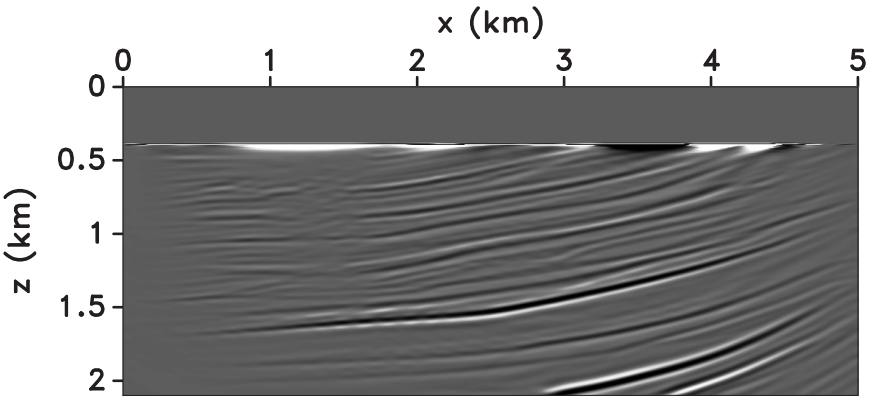

(a)

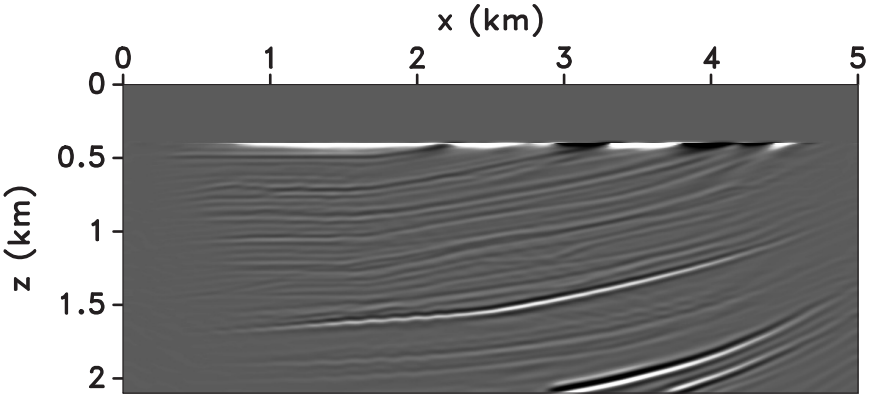

(b)

Figure 2.11: SP images obtained using (a) the conventional imaging condition and (b) our new imaging condition. The image in panel (b) at $(1.0, 0.7)$ km is stronger, in contrast with the image in panel (a) which suffers from cancellation due to polarity reversal.

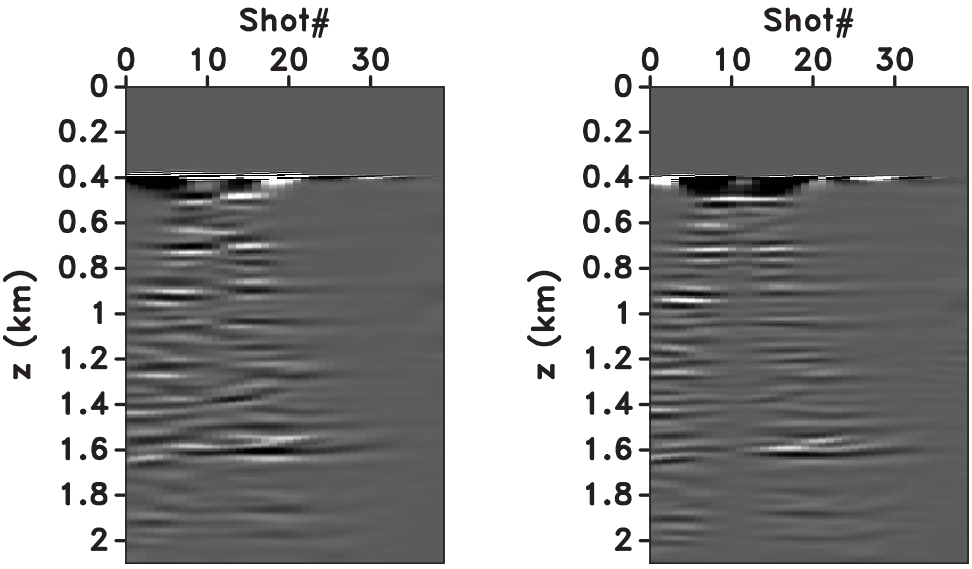

(a) (b)

Figure 2.12: PS common image gather at $x = 1.5$ km obtained from (a) the conventional imaging condition. From left to right, the horizontal events change sign at normal incidence. (b) Using the new imaging condition, we obtain the PS common image gather without polarity change.

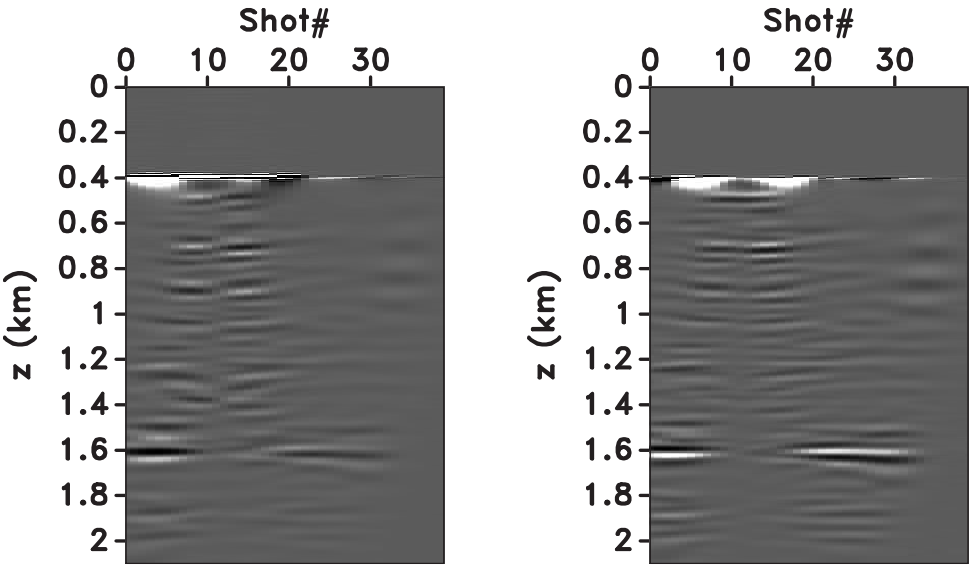

(a) (b)

Figure 2.13: SP common image gather at $x = 1.5$ km obtained from (a) the conventional imaging condition. From left to right, the horizontal events change sign at normal incidence. (b) Using the new imaging condition, we obtain the SP common image gather without polarity changes.

Using the conventional imaging condition (i.e., cross-correlation of the source and receiver wavefields), we obtain the PS and SP image shown in Figures 2.10(a) and 2.11(a). The reflectors on the left side of the model are not well imaged, due to the fact that the polarity of individual images change sign at normal incidence, thus causing destructive interference during summation over shots. The PS and SP common image gathers at $x = 1.5$ km (Figures 2.12(a) and 2.13(a)) show this polarity reversal causing image destruction.

In contrast, Figures 2.10(b) and 2.11(b) show PS and SP images using our new imaging condition, respectively. In this case, the interfaces are more continuous compared to the image constructed by the simple cross-correlation imaging condition. Moreover, the PS and SP common image gathers at $x = 1.5$ km (Figures 2.12(b) and 2.13(b)) confirm that there is no polarity change as a function of shot position.

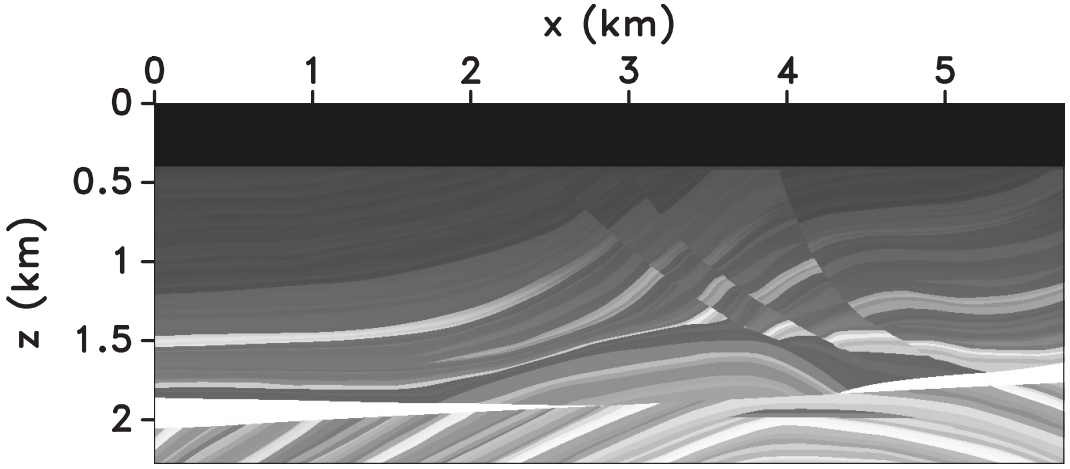

Figure 2.14: Marmousi model with density contrast.

The second example (Figure 2.14) is a modified Marmousi model (Versteeg, 1991, 1993). It contains several major faults and semi-parallel dipping layers. We use 60 explosive sources evenly distributed along the surface, and receivers are on a cable that moves with the source. The source-receiver offset ranges from -1.5 km to 1.5 km. The source function is a Ricker wavelet with a peak frequency of 35 Hz.

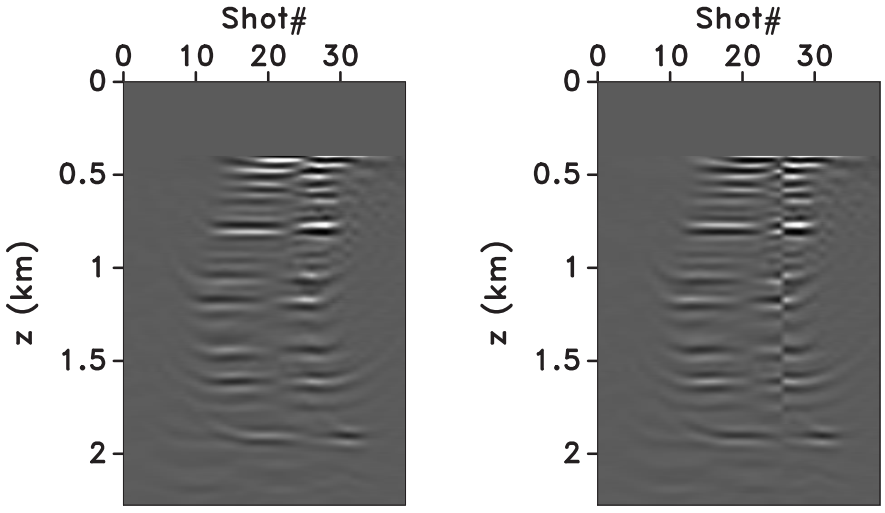

(a)

(b)

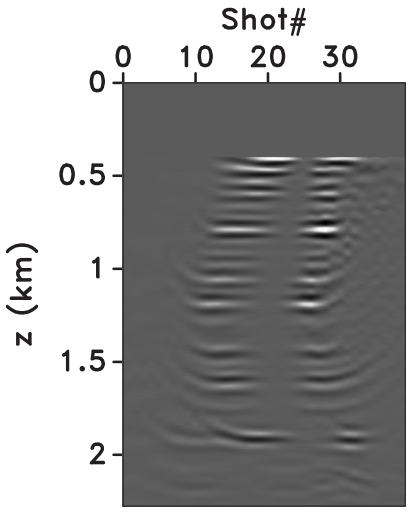

(c)

Figure 2.15: PS common image gather at $x = 2.5$ km obtained from (a) the conventional imaging condition, (b) the conventional imaging condition with the simple correction that flips the sign of the image at negative offset, and (c) the new imaging condition.

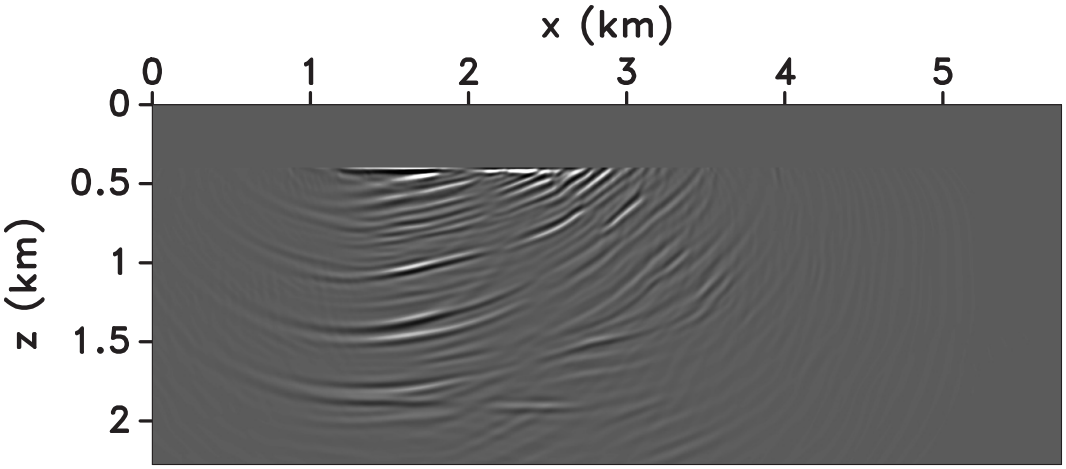

(a)

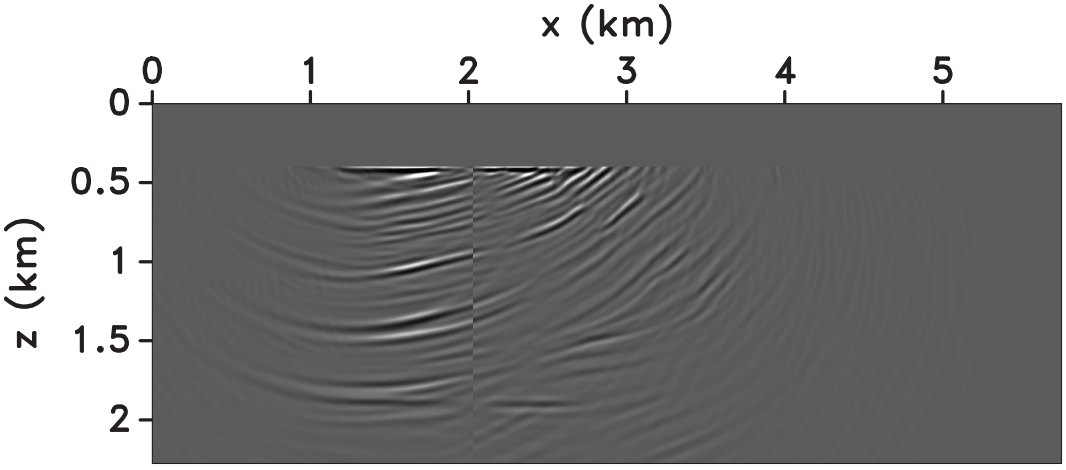

(b)

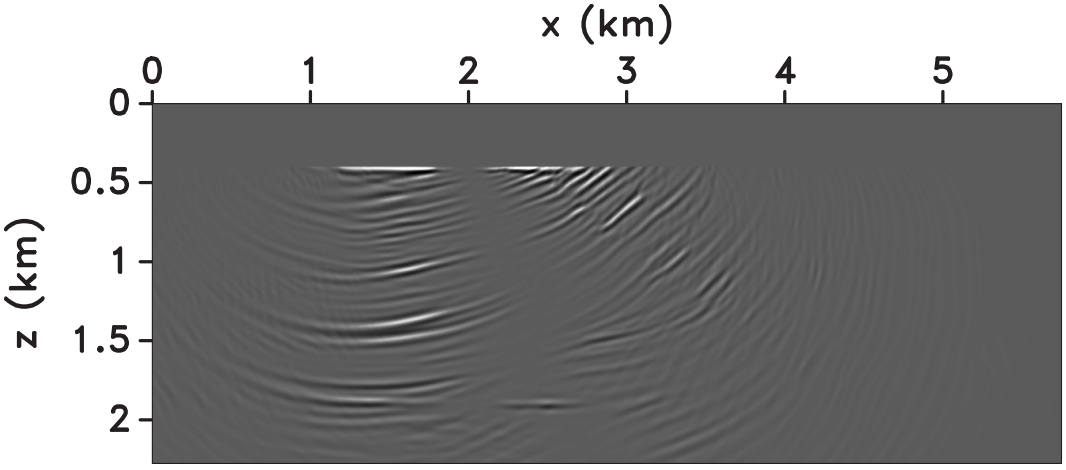

(c)

Figure 2.16: PS image from a single shot using (a) the conventional imaging condition, (b) the conventional imaging condition with simple correction that flips the sign of the image at negative offset, and (c) the new imaging condition. Source is located at $(1.85, 0)$ km.

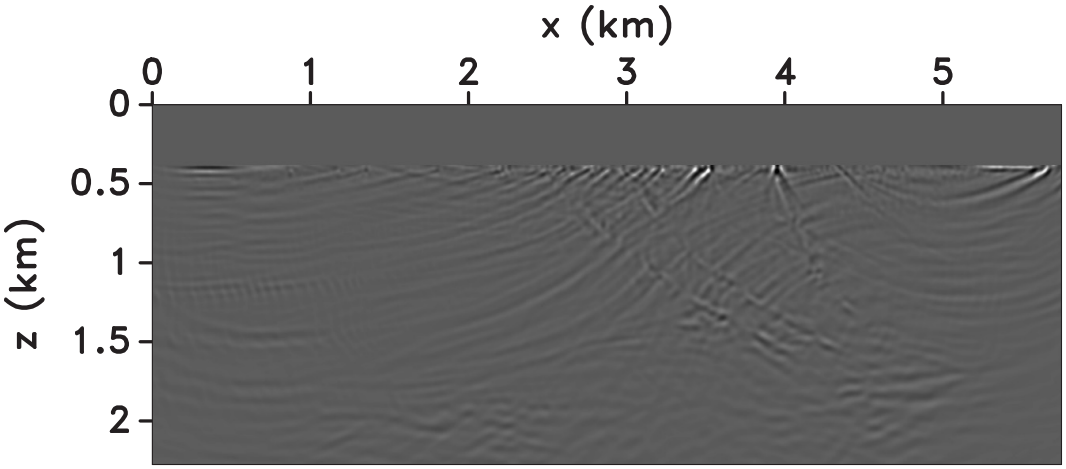

(a)

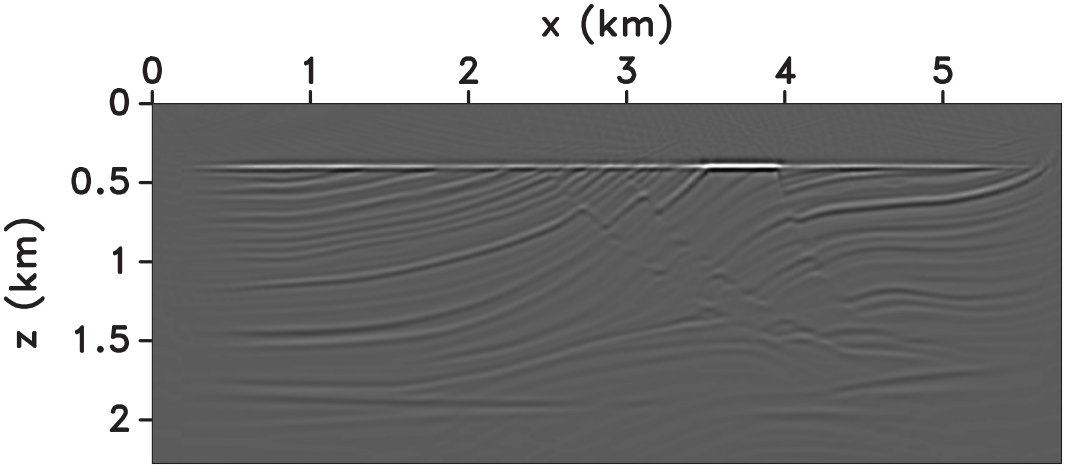

(b)

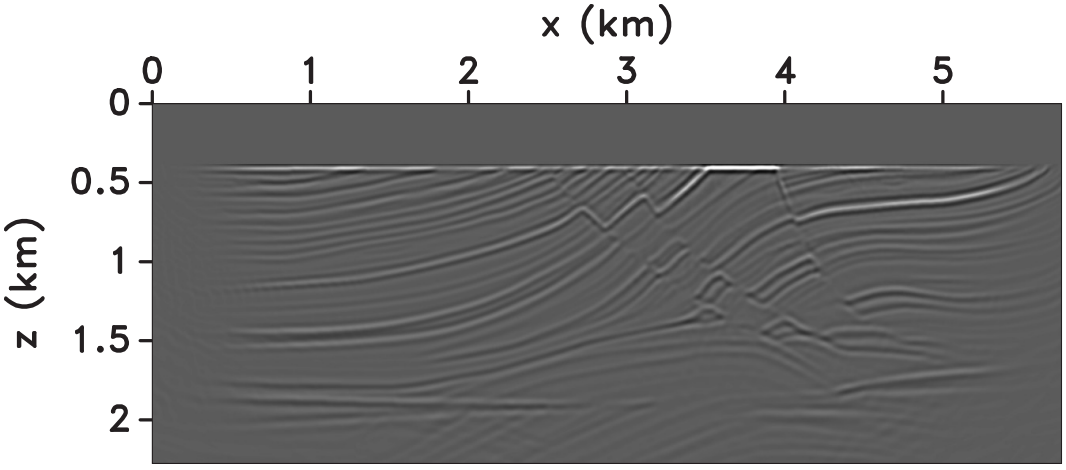

(c)

Figure 2.17: PS stacked image using (a) the conventional imaging condition, (b) the conventional imaging condition with simple correction that flips the sign of the image at negative offset, and (c) the new imaging condition.

The source S wavefield is weak because of the minor energy conversion at the top of the model; therefore the SP image is also weak. Consequently in the figures, we show only the PS image. Using the conventional imaging condition, we obtain an image from a single shot and the stacked PS image shown in Figure 2.16(a) and Figure 2.17(a), respectively. One common image gather (Figure 2.15(a)), is extracted from all 60 experiments at $x =$ 2.5 km. In Figure 2.17(a) and 2.15(a), the events change polarity at normal incidence, which leads to destructive interference in the stacked image. The simplest correction is to change the sign of the image where the offset is negetive. One common image gather at $x = 2.5$ km and one image from a single shot are shown in Figure 2.15(b) and Figure 2.16(b), respectively. This method corrects for polarity change at large offset, but does not work at small incidence angles. The stacked image seen in Figure 2.17(b) is better focused than the image in Figure 2.17(a); however, the middle part with complicated geological structures is not well-illuminated. By applying the new imaging condition, we obtain the common image gathers and the image from a single shot without polarity reversal shown in Figure 2.15(c) and 2.16(c), respectively. Notice that in the stacked image shown in Figure 2.17(c), events are well-focused.

The third model is the 3D SEG/EAGE salt model (Aminzadeh et al., 1997) and the density model is shown in Figure 2.18(a). The P and S velocity models are smoothed. We use 9 sources evenly distributed in a horizontal plane at $z = 0.02$ km and a dense network of receivers at $z = 0.03$ km. We simulate the data with constrasts in the density model and use displacement vectors at the receiver locations as recorded data. The source function is represented by a Ricker wavelet with a peak frequency of 40 Hz. Using the new imaging condition, we obtain the PS stacked image, Figure 2.18(b). In the PS image the salt boundary is continuous without polarity change, which shows that the new imaging condition works for 3D cases with complicated geological structures.

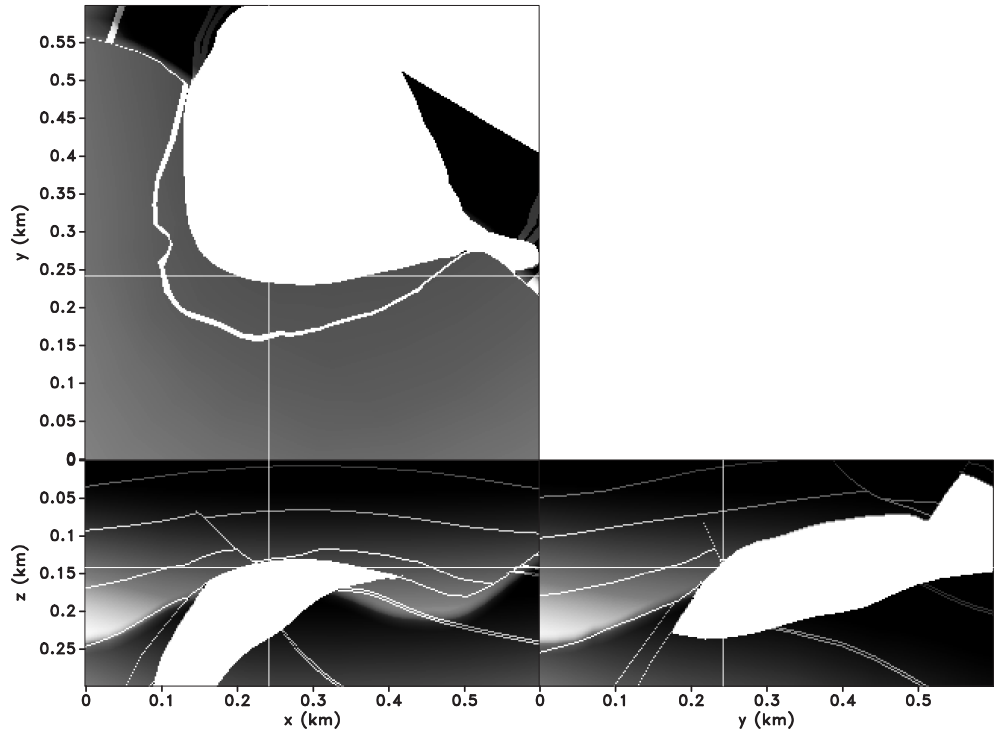

(a)

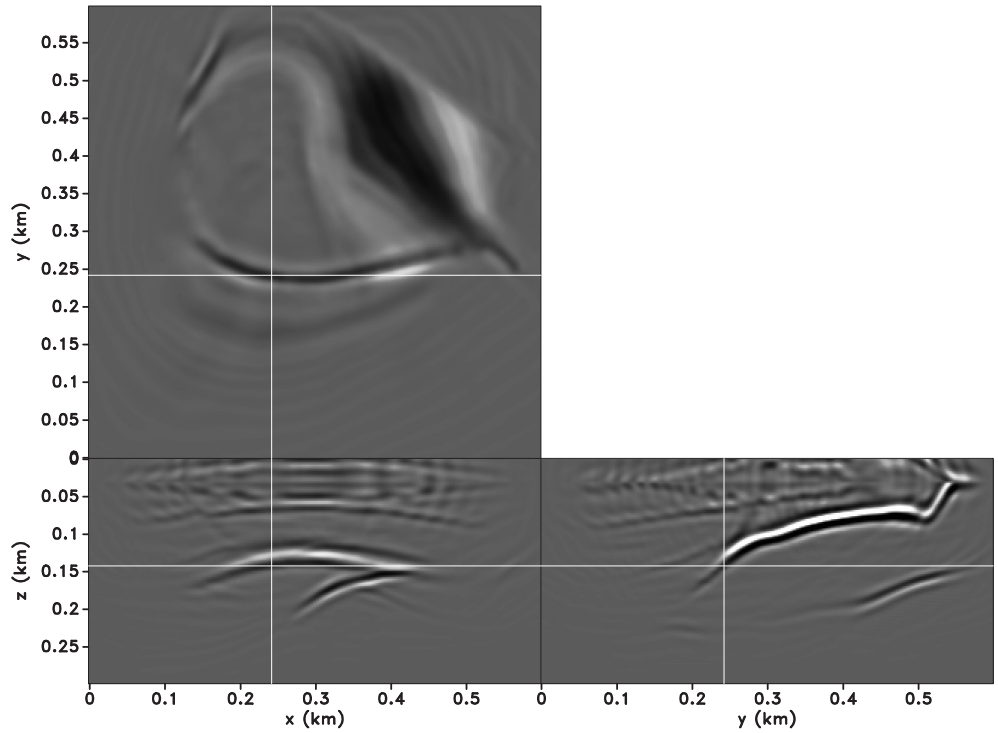

(b)

Figure 2.18: (a) 3D SEG/EAGE salt model, the density model. (b) The PS image obtained using the new imaging condition.

2.4 Discussions

This new imaging condition requires additional information that is not available in the extrapolated wavefield, specifically the reflector normal field. In this section, we investigate two practical problems associated with this imaging condition, including the estimation of the reflector normals when the reflectors are imaged at incorrect positions, and the imaging of a reflector by waves from opposite sides.

2.4.1 Estimation of the reflector normal

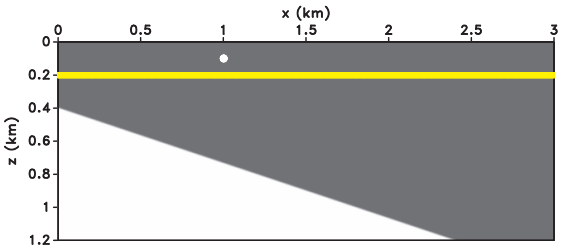

Figure 2.19: Synthetic model with one dipping reflector. The source, indicated by the dot, is located at $(0.1, 1.0)$ km. The receiver line, indicated by the line, is at $z = 0.2$ km.

The scalar imaging condition requires an estimate of the reflector normal $\mathbf{n}$. If the velocity is incorrect, reflectors in PP, PS, and SP images are incorrectly positioned and can cause inaccurate estimations of the normal for PS and SP imaging from the PP image. Reflector normals estimated from a PP image are inconsistent with those from a PS image and thus are unavailable for the scalar imaging condition. Therefore, instead of estimating reflector normals from a PP image, we choose to estimate the normal vectors from the PS image computed using the conventional imaging condition. Because the polarity reversal present in conventional PS images results in poor resolution of the stacked conventional PS image, we apply a simple correction for this polarity change, for example, by reversing the sign of the image at negative source-receiver offsets. Alternatively, we could estimate the reflector normal on individual images obtained with the conventional imaging condition which does not correct for polarity reversal, at higher overall computational cost.

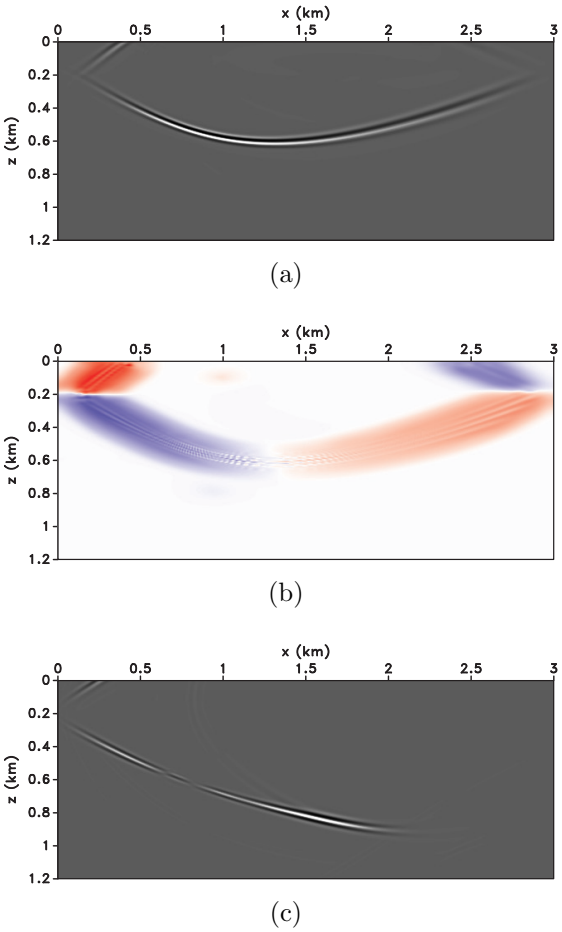

Figure 2.20: (a) The PP image computed by crosscorrelating P-waves in source and receiver wavefields. (b) The reflector normal estimated using the PP image. (c) The PS image computed using the dip field in panel (b). Note that the image of the reflector incorrectly changes polarity at around (0.7,0.6) km.

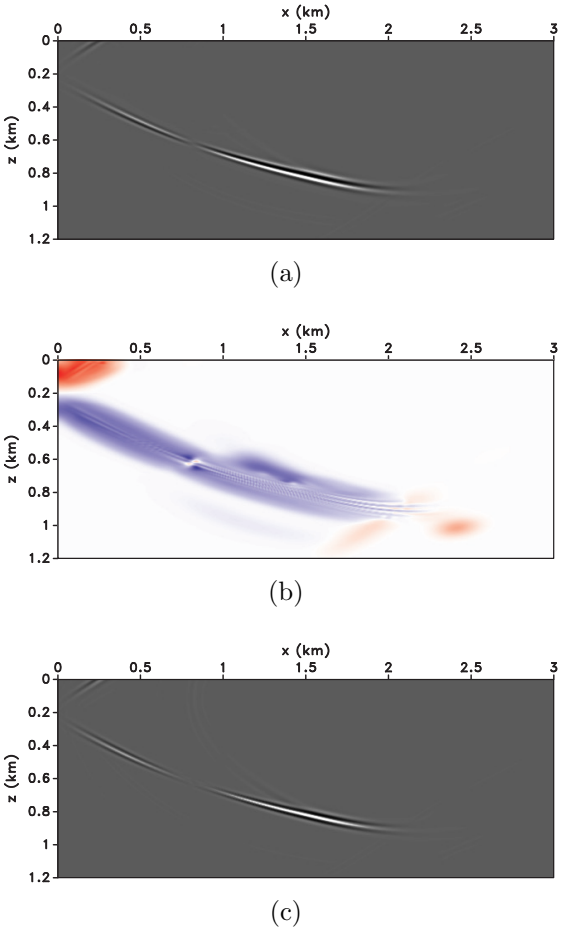

Figure 2.21: (a) The PS image obtained by crosscorrelating the source P wavefield and receiver S wavefield. (b) The reflector dip estimated using PS image. (c) The PS image computed using the dip field from panel (b). This PS image has no polarity change.

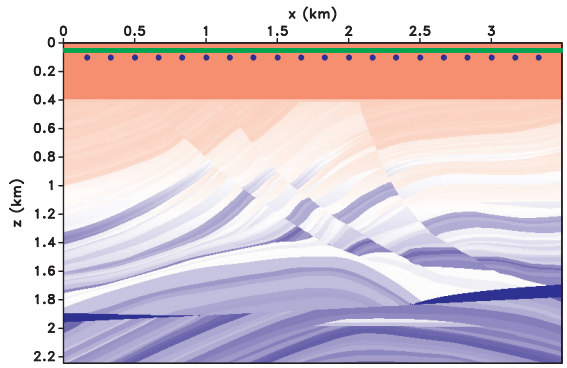

Figure 2.22: The Marmousi model. The 20 sources, indicated by the dots, are located at depth $z = 0.1$ km. The receiver line, indicated by the line, is at $z = 0.05$ km.

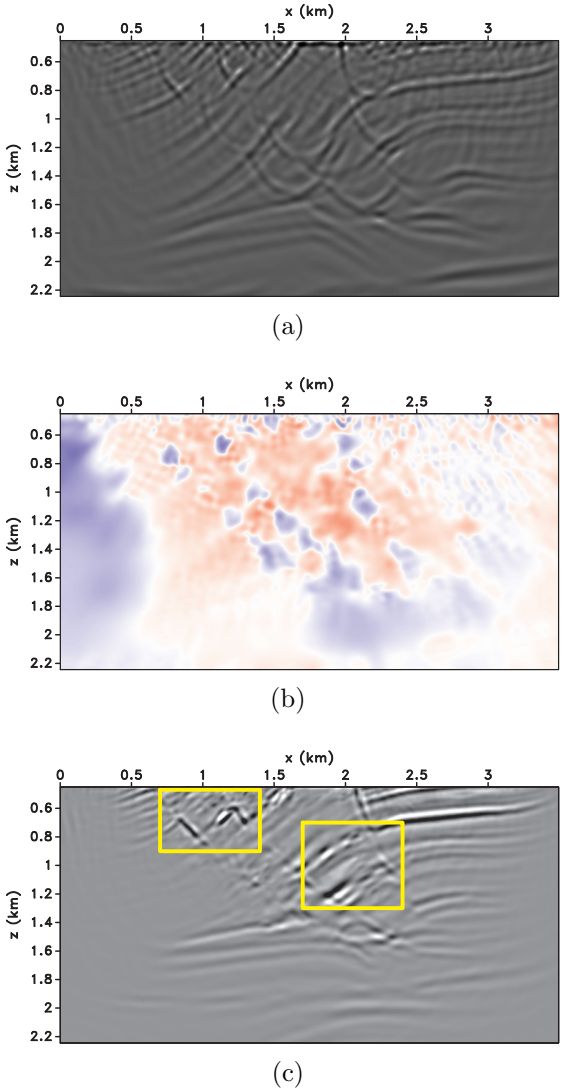

Figure 2.23: (a) The stacked PP image computed by crosscorrelating P-waves in source and receiver wavefields. (b) The reflector normal estimated using the PP image. (c) The PS image computed using the dip field from panel (b). The reflectors highlighted by the boxes are not continuous and poorly imaged.

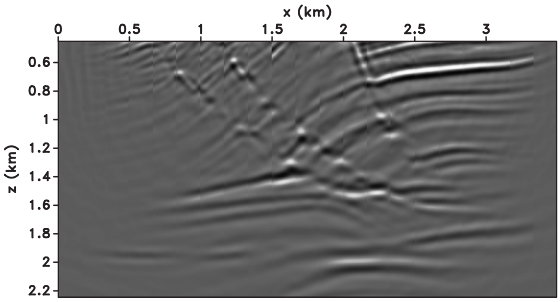

(a)

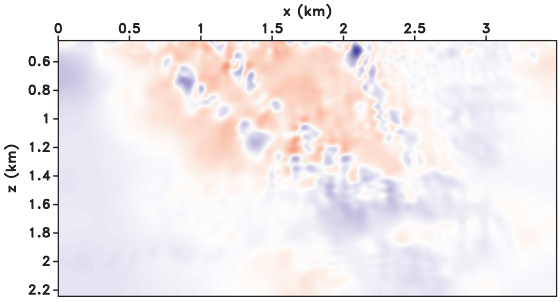

(b)

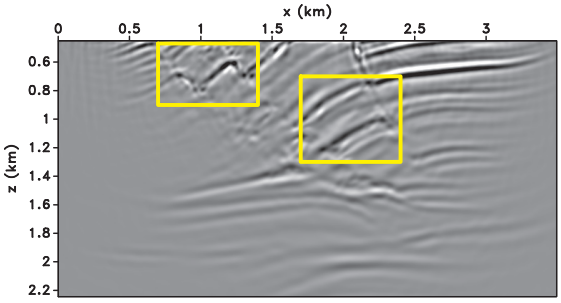

(c)

Figure 2.24: (a) The stacked PS image computed by crosscorrelating P-waves in the source wavefield and S-waves in the receiver wavefield. The PS image polarity for individual shots are corrected by reversing the image at negative offsets. (b) The reflector dip estimated using PS image. (c) The PS image computed using the dip field. The reflectors highlighted by the boxes are better imaged compared to the PS image in Figure 2.23(c).

We demonstrate our approach for estimating reflector normals using a model with a single dipping reflector, Figure 2.19. We use a displacement source located at $(1.0, 0.1)$ km, and we record the displacement wavefield with a line of receivers at depth $z = 0.2$ km. The source function is a Ricker wavelet with a peak frequency of 30 Hz. The P- and S-wave velocities of the true models are 2.6 and 1.5 km/s, respectively. For migration, we use incorrect constant P- and S-wave velocities of 2.0 and 1.6 km/s, respectively. Note in Figure 2.20(a) that the reflector in the PP image, computed using the incorrect velocity, is located above the position of the true reflector and also incorrectly exhibits curvature. Next, using the estimated normal vectors (Figure 2.20(b)) from the PP image, we obtain the PS image shown in Figure 2.20(c). Comparing Figure 2.20(a) to Figure 2.20(c), we observe that the position of the reflector in the PP image differs from that of the reflector in the PS image; thus, reflector normals computed from the PP image are not suitable for use in PS migration. This is further demonstrated by the fact that the PS image computed using the reflector normals from Figure 2.20(b) show polarity reversal at $(0.7, 0.6)$ km. We address this issue by using the conventional PS image (Figure 2.21(a)), instead of the PP image, to estimate the reflector normal vectors (Figure 2.21(b)). With the normal vectors shown in Figure 2.21(b), the resulting PS image shown in Figure 2.21(c) has no polarity change. The explanation for this behavior is that all vectors used in our imaging condition are consistent with one-another, although they are all distorted by the inaccurate migration velocity.

We illustrate our approach using a modified Marmousi model (Versteeg, 1991, 1993), as shown in Figure 2.22. Compared with the original model, the modified model has an increased depth of the water layer in order to generate PS conversion from a hard water bottom. Twenty explosive sources are evenly distributed along the surface, and 600 multicomponent receivers are located at depth $z = 0.05$ km. The source function is a Ricker wavelet with a peak frequency of 35 Hz. Crosscorrelating the source P wavefield with the receiver P and S wavefields, we obtain the PP (Figure 2.23(a)) and PS (Figure 2.24(a)) images, respectively. For the PS image in Figure 2.24(a), we apply a simple polarity correction by

reversing the sign of the pre-stacked PS images at negative source-receiver offsets. Because the P-velocity and S-velocity used for migration are 12% higher and 4% lower than the true model, respectively, the reflectors are at different positions in PP and PS images. With the reflector normal (Figure 2.23(b)) estimated from the PP image we compute the PS image using the scalar imaging condition (Figure 2.23(c)). Notice that a reflector changes polarity at $(1.1, 0.7)$ km. If we estimate the reflector normal (Figure 2.24(b)) using the conventional PS image, we obtain a stacked PS image, computed using the scalar imaging condition, without distortion caused by polarity reversals.

2.4.2 Imaging from opposite sides of a reflector

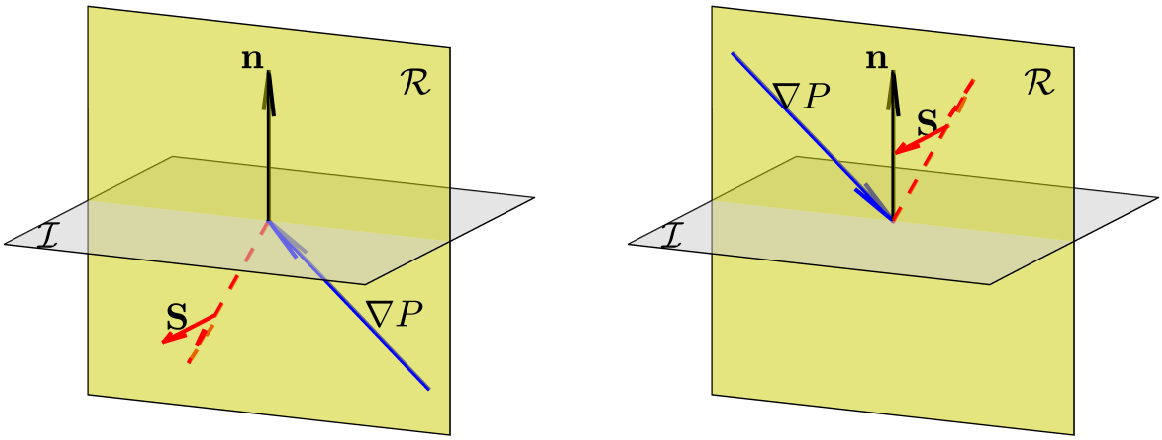

(a) (b)

Figure 2.25: Schematic representation of reflections at an interface for (a)down-going and (b)up-going PS converted-modes. Compared to (a), vector ∇P changes sign in (b), resulting in the sign change of $\nabla P \times \mathbf{n}$.

In complex subsurface models, reflectors are often illuminated by waves approaching from opposite sides; for example, a reflector might be imaged both from above by a down-going direct wave and from below by a diving wave. Consider the cases shown in Figures 2.25(a) and 2.25(b), depicting down-going and up-going PS converted waves, respectively. Assuming the incident P-modes in Figures 2.25(a) and 2.25(b) have the same polarity, then vectors ∇P point in opposite directions, and the reflected S-modes must have opposite polarities

because reflectivity changes sign for incident waves approaching a reflector from opposite sides (Aki and Richards, 2002). Therefore, conventional PS images computed by migrating waves reflected off opposite sides of a reflector also have opposite polarities.

In contrast, the polarities of PS images computed using our scalar imaging condition for the two cases shown in Figures 2.25(a) and 2.25(b) have the same polarity. This is because all reflector normal vectors are constructed to point toward only one side of the reflector (the vertical component of all normal vectors must have the same sign in order to avoid ambiguity). Thus, for the same type of incident P-modes, the signs of vector $\nabla P \times \mathbf{n}$ are opposite in the two cases depicted in Figures 2.25(a) and 2.25(b), because vectors ∇P points in opposite directions. The sign change of $\nabla P \times \mathbf{n}$ compensates for the difference in polarity of the reflected S-modes, and results in both SP images having the same polarity regardless of the direction of the incident P-mode. Similarly, for SP images, reflected P-modes on opposite sides of a reflector have different polarities due to the sign change in reflectivity; however, the reflector normal vector $\mathbf{n}$ corrects for the polarity difference in SP images computed from waves reflected from opposite sides.

To further explain how the scalar imaging condition generates PS images with the same polarity for both cases depicted in Figures 2.25(a) and 2.25(b), we consider another synthetic example with one horizontal reflector (Figures 2.26(a)-2.26(d)). The sources and receivers are positioned at the top of the first layer, and the reflector normal points upward. Using the scalar imaging condition, we obtain the PS image shown in Figure 2.26(a). If we switch the material properties of the top and bottom layers while keeping the acquisition geometry and the direction of the reflector normal vector unchanged, we obtain the PS image shown in Figure 2.26(b), which has opposite polarity compared to the image in Figure 2.26(a). Next, if we rotate the entire experiment shown in Figure 2.26(b) by 180 degrees or, equivalently, reverse the direction of the z-axis, we obtain the PS image shown in Figure 2.26(c) with the same polarity as the PS image shown in Figure 2.26(b). Finally, by simply reversing the direction of the reflector normal from Figure 2.26(c) to Figure 2.26(d), we obtain the

PS image in Figure 2.26(d) with the same polarity as the image shown in Figure 2.26(a). Notice that the only difference between the models shown in Figures 2.26(a) and 2.26(d) is that the incident P-modes illuminate the horizontal reflector from opposite sides. Therefore, using the scalar imaging condition, we obtain PS images of the same polarity for up- and down-going waves.

We illustrate migration with waves approaching reflectors from opposite sides using a model consisting of gently dipping layers (Figure 2.27). The sources and receivers are in two wells. We use 20 sources evenly distributed in the well at $x = 0.1$ km, and 500 receivers located at $x = 1.4$ km. Using the conventional imaging condition, we obtain the PS image shown in the left panel of Figure 2.28(a). The reflectors around $z = 1.2$ km are poorly imaged because they are illuminated by waves from opposite sides. In the common image gather at $x = 0.8$ km, the right panel of Figure 2.28(a), the polarities of the events in different experiments are inconsistent. In contrast, Figure 2.28(b) shows the PS image using the scalar imaging condition. In this case, the interfaces in the image around $x = 1.4$ km are stronger, and the events have consistent polarities in all experiments, which confirms that the PS images computed using waves reflected at opposite sides of the reflector have consistent polarities.

2.5 Conclusions

We derive a new 3D imaging condition for PS and SP images constructed by elastic reverse-time migration. In conventional methods, P- and S-modes are obtained using Helmholtz decomposition. However, our imaging condition does not correlate various components of the S wavefield with the P wavefield; instead, our method uses geometrical relationships between the wavefields, their propagation directions, and the reflector orientation and polarization directions to construct a single image characterizing the PS or SP reflectivity. Our method leads to accurate images without the need to decompose wavefields into directional components or to construct costlier extended images in the angle domain. However, our method is constructed based on the assumption that polarity changes at normal

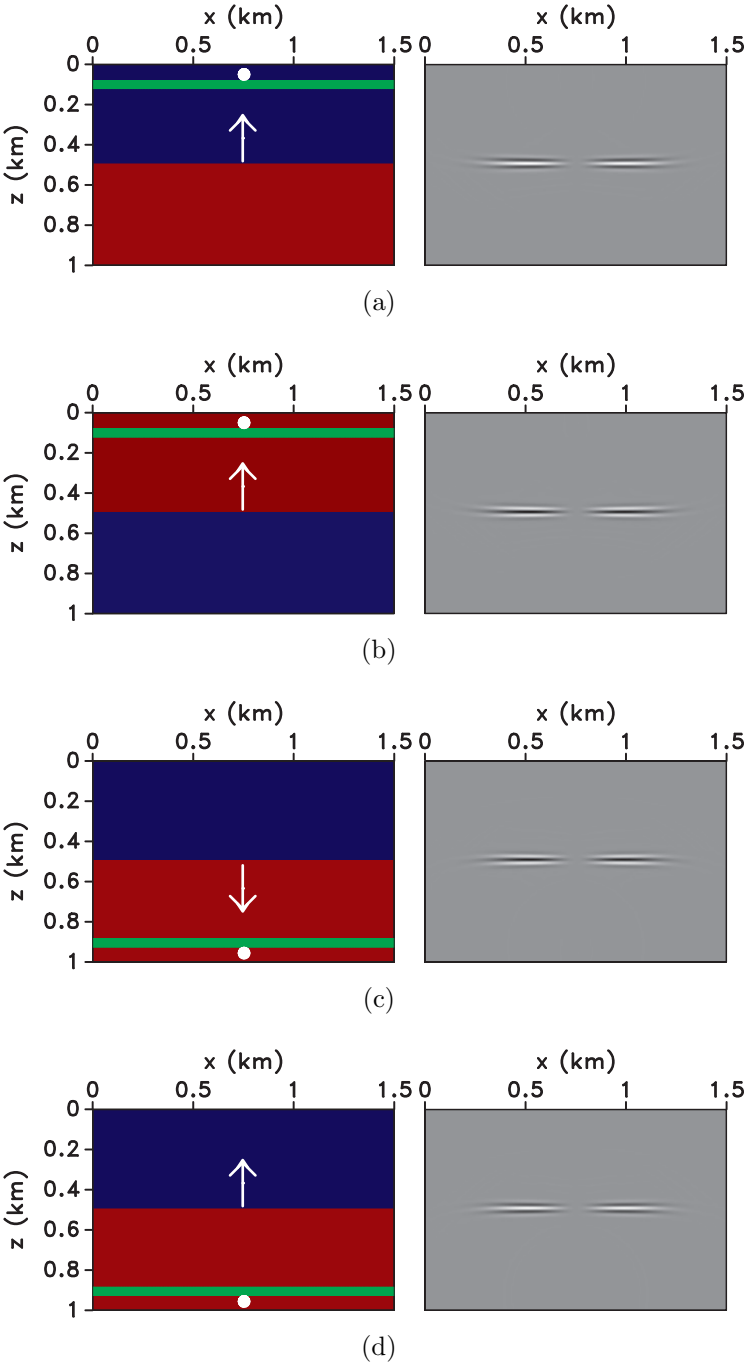

Figure 2.26: PS imaging of a horizontal interface for various source/receiver configurations. The left panels are the models with the acquisition geometry, and the right panels are the corresponding PS images. The dots are the locations of the sources and lines are the locations of the receivers. The arrow indicates the reflector normal for PS migration. Note that the polarities of the PS images are the same in experiments (a) and (d), but different from experiments (b) and (c).

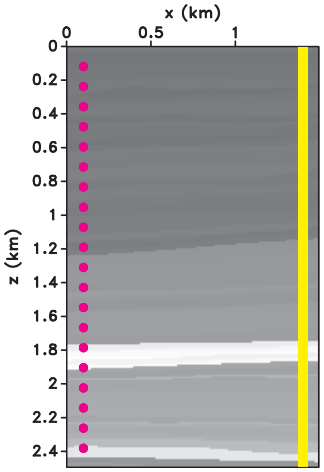

Figure 2.27: A crosswell example illustrating illumination for opposite sides of a reflector. The 20 sources, indicated by the dots, are in a well at $x = 0.1$ km. The receivers, indicated by the line, are at $x = 1.4$ km.

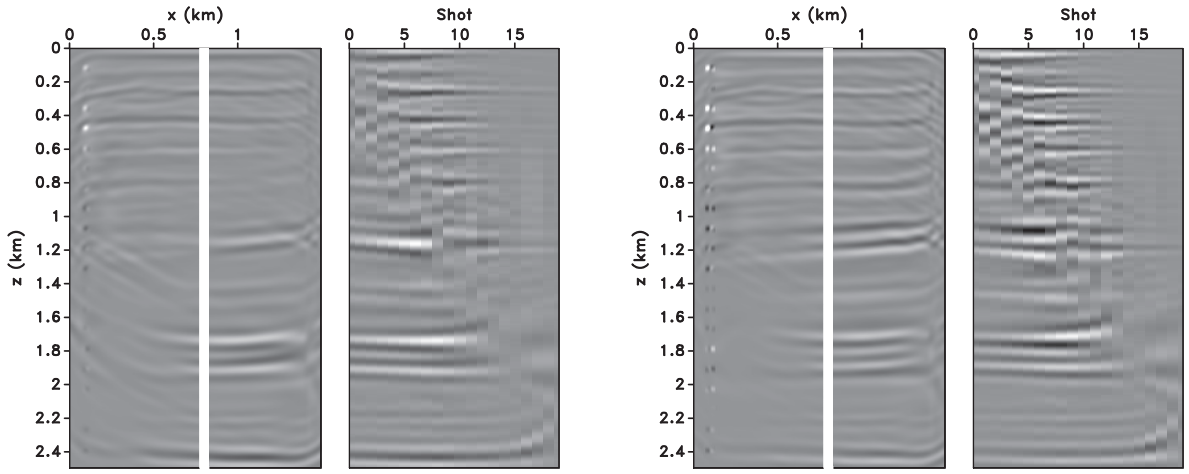

Figure 2.28: (a) The stacked PS image using conventional imaging condition. The reflectors around $z = 1.2$ km are not imaged. (b) The stacked PS image using the scalar imaging condition. The reflectors around $z = 1.2$ km are well-imaged. The left panels are the stacked PS images and the right panels are common image gathers at $x = 0.8$ km. Note that for Figure (a), the polarities of the events in the common image gather are inconsistent from left to right, while for Figure (b), the events have consistent polarities in all experiments.

incidence in isotropic media. In the case of anisotropy, polarity may change at non-zero incidence angle, in which case the imaging condition would need to be modified.

2.6 Acknowledgments

We thank the sponsors of the Center for Wave Phenomena, whose support made this research possible. The reproducible numeric examples in this paper use the Madagascar open-source software package (Fomel et al., 2013) freely available from http://www.ahay.org. The authors thank Tariq Alkhalifah for helpful discussions and valuable suggestions.

CHAPTER 3

3D ANGLE DECOMPOSITION FOR ELASTIC REVERSE TIME MIGRATION

A paper submitted to *Geophysics*

Yuting Duan[4,5] and Paul Sava[5]

Common reflection-angle gathers are important tools for migration velocity analysis and amplitude-versus-angle analysis. Angle gathers of acoustic (PP) and elastic (PS, SP, and SS) reflections provide information about different subsurface material properties. We propose 3D angle decomposition methods for elastic reverse time migration using three approaches. The first approach uses time- and space-lag common image point gathers computed from elastic wavefields. This method felicitates computing angle gathers at sparse and irregularly distributed points in the image, which is computationally cheaper compared to alternative methods based on common image gathers. The second approach uses time-lag common image gathers. This improved method transforms the extended time-lag images to the angle domain using slant-stacks along surfaces that connect neighboring positions, instead of using line slant-stacks for isolated common image gathers as is commonly done with common image gathers. The third approach uses space-lag common image gathers. We propose a new method based on a system of equations that handles dipping reflectors and generates angle gathers with improved accuracy compared to other existing methods. We demonstrate our methods using 2D and 3D synthetic and field data examples and show that our techniques provide accurate opening and azimuth angles, and that they can handle steeply dipping reflectors and converted wave modes.

[4]Author for correspondence.
[5]Center for Wave Phenomena, Colorado School of Mines, 924 16th Street, Golden, CO 80401.

3.1 Introduction

Common reflection-angle gathers are useful in migration velocity analysis and amplitude-versus-angle analysis. Angle decomposition techniques can be classified into two categories, depending on the type of migration used: ray-based methods and wavefield-based methods. Ray-based methods (Brandsberg-Dahl et al., 1999; Audebert et al., 2000; Xu et al., 2001) are convenient, as it is straightforward and efficient for obtaining angle information from ray-paths traced to an image point. However, the accuracy of ray-based algorithms suffers in areas where velocity contrasts are strong, for example, in the presence of salt bodies. Wavefield-based angle-decomposition methods rely on decomposition of the wavefield into its plane wave components (De Bruin et al., 1990; Wu and Xie, 2002; Sava and Fomel, 2003; Biondi and Symes, 2004; Yoon et al., 2004; Sava, 2007; Xu et al., 2011; Sava and Vlad, 2011). Although more computationally expensive compared to ray-based methods, the wavefield-based methods are superior because they accurately simulate wave propagation in complex geologic structures.

Wavefield-based methods generally fall into two categories: pre-migration and post-migration algorithms (Vyas et al., 2011). Pre-migration methods refer to techniques that decompose the wavefields prior to the imaging condition, for example, by $f-k$ domain decomposition (Xu et al., 2011), or by Poynting vector methods (Yoon and Marfurt, 2006; Yan and Ross, 2013). Because $f-k$ domain decomposition requires 4D Fourier transforms in 3D models, the computational cost can be high. Poynting vector methods are less computationally intensive but may yield inaccurate angle information when wavefields are complicated, e.g., by triplicated wavefronts (Patrikeeva and Sava, 2013). Post-migration methods, which decompose migrated images to angle gathers after the imaging condition, require two steps: computation of extended images as a function of space- or time-lag gathers followed by mapping of the images from the extended domain to the angle domain. The extended image gathers can be formed as a function of space-lag (λCIG)(Rickett and Sava, 2002; Sava and Fomel, 2003), time-lag (τCIG)(Sava and Fomel, 2006), or mixed time- and space-lag common

image point (CIP) gathers (Sava and Vlad, 2011). Angle gathers computed using λCIGs or τCIGs describe the reflectivity as a function of reflection angles and a space axis (typically the depth axis), while for CIPs, the angle-dependent reflectivity is evaluated at key selected points in the subsurface.

Wavefield-based angle-decomposition methods can be extended to elastic and anisotropic media. Sava and Alkhalifah (2013) propose a technique for mapping CIP gathers to angle gathers in 3D TI media, with wavefields constructed by solving a pseudo-acoustic wave equation. Algorithms for elastic wavefield-based angle decomposition have also been proposed (Yan and Sava, 2008; Yan and Xie, 2012). One important issue in angle decomposition using elastic wavefields is the choice of imaging condition. A proper imaging condition is needed to separate different wave modes. Yan and Sava (2008) propose an extended imaging condition that crosscorrelates decomposed P and S wavefields from the source and receiver. The amplitudes of computed CIGs for different types of reflections (PP, PS, SP, and SS) are related to their reflection coefficients, and these CIGs can be mapped to the angle domain through a process similar to that used in the acoustic case. However, the shear wavefield after Helmholtz decomposition has three non-zero components in 3D, which makes it challenging to include information from all components into PS angle gather. Duan and Sava (2015) propose a scalar imaging condition for converted waves, that generates 3D PS and SP scalar images. We extend this imaging condition to compute scalar PS and SP extended images without polarity reversal, which can then be used for 3D angle decomposition.

Most of the angle decomposition methods using extended images assume that the reflectors are horizontal and the incidence and reflection angles are equal. Therefore, the computed angles for dipping reflectors and converted waves using the existing methods lead to inaccurate angle gathers. In this paper, we present improved methods for opening and azimuth angle decomposition for elastic RTM. We develop an extended scalar imaging condition from the zero-lag scalar imaging condition introduced by Yan and Sava (2008). Our methods utilize local plane wave decompositions of extended images and exploit the rela-

tionships between the time-lag, space-lag, and image shift in space. These relationships lead to opening and azimuth angle decomposition for PP, PS, SP, and SS reflections using either time-lag common image gathers (τCIGs), space-lag common image gathers (λCIGs), or time- and space-lag common image point (CIP) gathers.

3.2 Elastic scalar imaging condition

Duan and Sava (2015) develop a scalar imaging condition using geometrical relationships between the P and S wave propagation directions, the reflector orientation, and the S wave polarization direction. The PS and SP images computed using this imaging condition are scalars without polarity reversal. Combining this scalar imaging condition for converted waves with the PP and SS imaging conditions proposed by Yan and Sava (2008), we obtain an elastic imaging condition defined by the following equations for PP, PS, SP, and SS reflectivity:

$$I^{PP}(\mathbf{x}) = \sum_{e,t} P_s(e,\mathbf{x},t)\, P_r(e,\mathbf{x},t) \ , \tag{3.1}$$

$$I^{PS}(\mathbf{x}) = \sum_{e,t} \left[\nabla P_s(e,\mathbf{x},t) \times \mathbf{n}(\mathbf{x})\right] \cdot \mathbf{S}_r(e,\mathbf{x},t) \ , \tag{3.2}$$

$$I^{SP}(\mathbf{x}) = \sum_{e,t} \left[(\nabla \times \mathbf{S}_s(e,\mathbf{x},t)) \cdot \mathbf{n}(\mathbf{x})\right] P_r(e,\mathbf{x},t) \ , \tag{3.3}$$

$$I^{SS}(\mathbf{x}) = \sum_{e,t} \mathbf{S}_s(e,\mathbf{x},t) \cdot \mathbf{S}_r(e,\mathbf{x},t) \ . \tag{3.4}$$

The vector $\mathbf{n}(\mathbf{x})$ represents the normal to the reflector plane. Quantities $P(e,\mathbf{x},t)$ and $\mathbf{S}(e,\mathbf{x},t)$ represent P and S wavefields obtained by wave-mode separation, as functions of experiment e, time t, and space $\mathbf{x}$. Subscripts s and r indicate the wavefield origins at the source or receivers, respectively. The P and S wavefields are obtained from displacement wavefields using Helmholtz decomposition (Dellinger and Etgen, 1990a; Yan and Sava, 2008):

$$P(e,\mathbf{x},t) = \nabla \cdot \mathbf{u}(e,\mathbf{x},t) \ , \tag{3.5}$$

$$\mathbf{S}(e,\mathbf{x},t) = \nabla \times \mathbf{u}(e,\mathbf{x},t) \ . \tag{3.6}$$

Equations 3.1-3.4 represent special cases of more general forms of extended imaging conditions (Rickett and Sava, 2002; Sava and Fomel, 2006; Sava and Vasconcelos, 2009). An extended imaging condition defines the image as a function of space and crosscorrelation lags, i.e., space-lag $\boldsymbol{\lambda}$ and time-lag τ:

$$I^{PP}(\mathbf{x},\boldsymbol{\lambda},\tau) = \sum_{e,t} P_s(\mathbf{x}-\boldsymbol{\lambda},t-\tau)\, P_r(\mathbf{x}+\boldsymbol{\lambda},t+\tau) \ , \tag{3.7}$$

$$I^{PS}(\mathbf{x},\boldsymbol{\lambda},\tau) = \sum_{e,t} [\nabla P_s(\mathbf{x}-\boldsymbol{\lambda},t-\tau)\times \mathbf{n}(\mathbf{x})]\cdot \mathbf{S}_r(\mathbf{x}+\boldsymbol{\lambda},t+\tau) \ , \tag{3.8}$$

$$I^{SP}(\mathbf{x},\boldsymbol{\lambda},\tau) = \sum_{e,t} [\nabla \times \mathbf{S}_s(\mathbf{x}-\boldsymbol{\lambda},t-\tau)\cdot \mathbf{n}(\mathbf{x})]\, P_r(\mathbf{x}+\boldsymbol{\lambda},t+\tau) \ , \tag{3.9}$$

$$I^{SS}(\mathbf{x},\boldsymbol{\lambda},\tau) = \sum_{e,t} \mathbf{S}_s(\mathbf{x}-\boldsymbol{\lambda},t-\tau)\cdot \mathbf{S}_r(\mathbf{x}+\boldsymbol{\lambda},t+\tau) \ . \tag{3.10}$$

Space-lag $\boldsymbol{\lambda} = [x_x, x_y, x_z)$ and time-lag τ describe the space shift and time shift, respectively, between the source and receiver wavefields prior to imaging.

Such extended images can be used in image post-processing for amplitude variation with angle analysis (Beretta et al., 2002), tomographic velocity analysis (Symes, 1993; Sava and Biondi, 2004a; Yang and Sava, 2015), and migration artifact attenuation (Zhang and Sun, 2009; Duan and Sava, 2014).

3.3 Moveout analysis

The extended imaging condition in equations 3.7-3.10 preserve necessary information for decomposing images in angle-dependent components, and these images can be used for velocity analysis. In 3D, the PP, PS, SP, and SS images generated using this imaging condition are scalars, which can be used directly to compute angle gathers. We formulate our method under the assumption that the reflector is locally a plane, and that the incident and reflected wavefields are also locally planar. However, the derived algorithms are not limited to cases where the wavefronts are planar because waves can always be decomposed to planar components, even in complex wavefields with triplicated waves.

We define the angle domain as the set of half-opening angle θ, and azimuth ϕ, and we use the following unit vectors to describe the angle decomposition procedure (Figure 3.1):

- $\mathbf{o}$: azimuth vector acting as a reference direction, e.g., North
- $\mathbf{n}$: reflector normal
- $\mathbf{a}$: projection of the azimuth vector in the interface plane:

$$\mathbf{a} = (\mathbf{n} \times \mathbf{o}) \times \mathbf{n} \tag{3.11}$$

- $\mathbf{n}_s$: propagation direction of the incident wave
- $\mathbf{n}_r$: propagation direction of the reflected wave
- $\mathbf{q}$: vector lying at the intersection of the interface and the reflection plane:

$$\mathbf{q} = Q\left(\mathbf{n}, \phi\right) \mathbf{a} \ , \tag{3.12}$$

where $Q\left(\mathbf{n}, \phi\right)$ is a rotation matrix defined by the axis $\mathbf{n}$ and the angle ϕ:

$$Q = \begin{bmatrix} n_x^2 + \left(n_y^2 + n_z^2\right)\cos\phi & n_x n_y (1-\cos\phi) - n_z \sin\phi & n_x n_z (1-\cos\phi) + n_y \sin\phi \\ n_y n_x (1-\cos\phi) + n_z \sin\phi & n_y^2 + (n_z^2 + n_x^2)\cos\phi & n_y n_z (1-\cos\phi) - n_x \sin\phi \\ n_z n_x (1-\cos\phi) - n_y \sin\phi & n_z n_y (1-\cos\phi) + n_x \sin\phi & n_z^2 + \left(n_x^2 + n_y^2\right)\cos\phi \end{bmatrix} . \tag{3.13}$$

The (locally planar) source wavefield propagates along the direction indicated by vector $\mathbf{n}_s$ with speed v_s, and the (locally planar) receiver wavefield propagates along the direction indicated by vector $\mathbf{n}_r$ with speed v_r. As shown in Figure 3.2(a), the point of coordinates $\mathbf{x}_o$ indicates the intersection of the two wavefronts and the reflection plane at time $t = t_o$:

$$\begin{cases} \mathbf{n}_s \cdot (\mathbf{x} - \mathbf{x}_o) = v_s \left(t - t_o\right) \ , & (3.14) \\ \mathbf{n}_r \cdot (\mathbf{x} - \mathbf{x}_o) = v_r \left(t - t_o\right) \ . & (3.15) \end{cases}$$

Introducing space-lag $\boldsymbol{\lambda}$ to equations 3.14 and 3.15 is equivalent to shifting the wavefronts in space, and introducing time-lag τ is equivalent to propagating the wavefronts in time. For

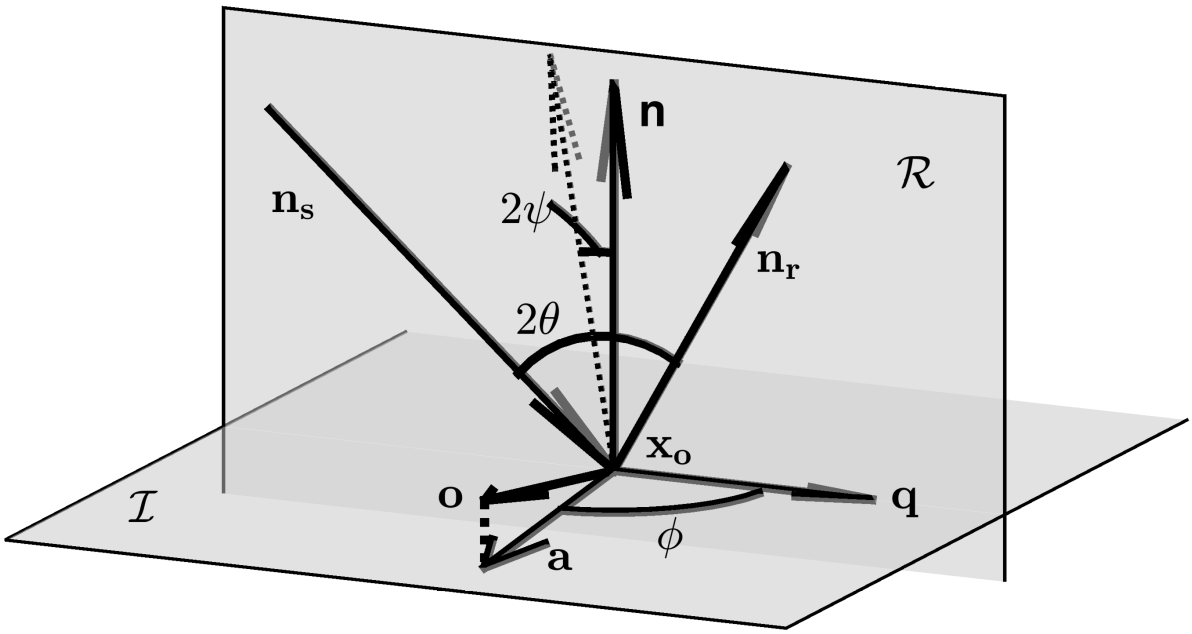

Figure 3.1: Schematic representation of the angles and vectors used in opening and azimuth angle decomposition for an image point $\mathbf{x}_o$. $\mathcal{I}$ and $\mathcal{R}$ are the interface plane and reflection planes, respectively. Vector $\mathbf{n}$ indicates the normal to the interface $\mathcal{I}$, vector $\mathbf{n}_s$ defines the propagation direction of the incident wave, vector $\mathbf{n}_r$ defines the propagation direction of the reflected wave, vector $\mathbf{a}$ is the projection of the azimuth vector in the interface plane, vector $\mathbf{o}$ is the reference direction, and vector $\mathbf{q}$ lies at the intersection of the interface and reflection planes. Angle 2θ is the sum of incidence and reflection angles, angle 2ψ is their difference, and angle ϕ is the azimuth.

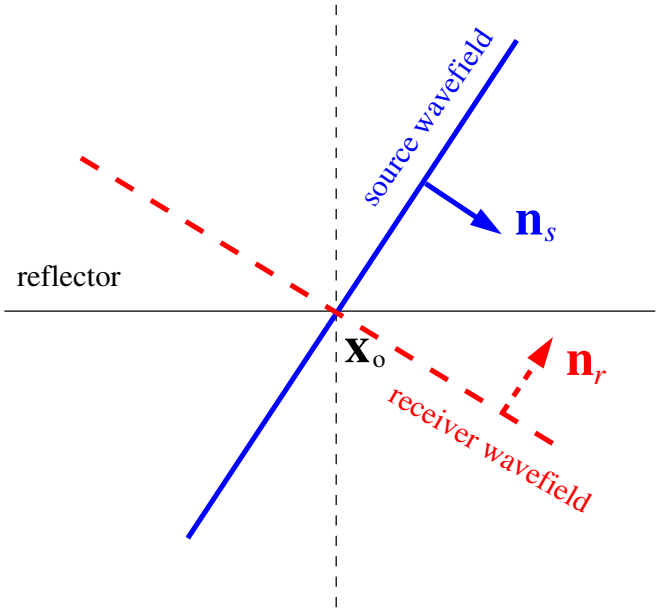

(a)

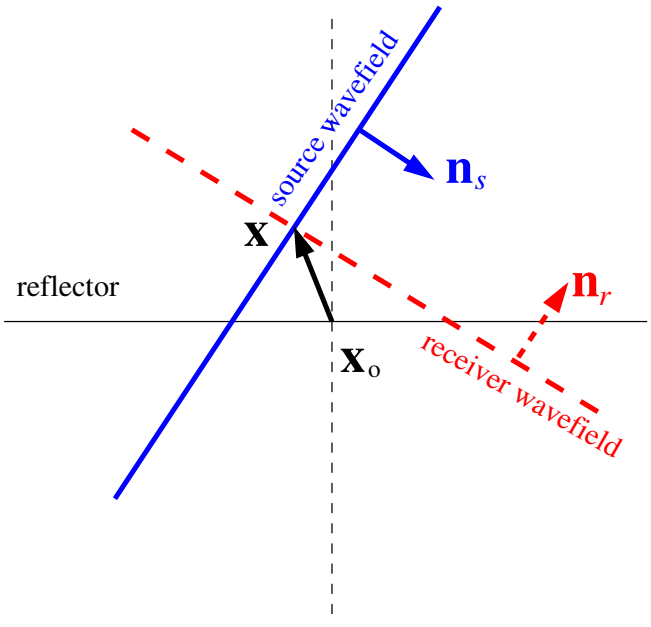

(b)

Figure 3.2: Cartoon describing source and receiver planes intersecting in the reflection plane (a) at location $\mathbf{x}_o$ at time t_o, and (b) at location $\mathbf{x}$ after moving both planes along time- and space-axises. Vectors $\mathbf{n}_s$ and $\mathbf{n}_r$ define the propogation directions of the incident and reflected waves in space, respectively.

equation 3.14, we shift the source wavefront in space by $+\boldsymbol{\lambda}$. At time $t = t_o - \tau$, the source wavefront is described by

$$\mathbf{n}_s \cdot (\mathbf{x} - \mathbf{x}_o - \boldsymbol{\lambda}) = v_s\,(-\tau) \ . \tag{3.16}$$

For equation 3.15, we shift the receiver wavefront in space by $-\boldsymbol{\lambda}$. At time $t = t_o + \tau$, the receiver wavefront is described by

$$\mathbf{n}_r \cdot (\mathbf{x} - \mathbf{x}_o + \boldsymbol{\lambda}) = v_r\,(+\tau) \ . \tag{3.17}$$

The intersection of the two wavefronts in the reflection plane is shifted to position $\mathbf{x}$, outside the local reflector plane as shown in Figure 3.2(b). The expressions relating the extended images using the locally planar source and receiver wavefields are

$$\begin{cases} \left(\dfrac{\mathbf{n}_s}{v_s} - \dfrac{\mathbf{n}_r}{v_r}\right) \cdot (\mathbf{x} - \mathbf{x}_o) - \left(\dfrac{\mathbf{n}_s}{v_s} + \dfrac{\mathbf{n}_r}{v_r}\right) \cdot \boldsymbol{\lambda} = -2\tau \ , & (3.18) \\ \left(\dfrac{\mathbf{n}_s}{v_s} + \dfrac{\mathbf{n}_r}{v_r}\right) \cdot (\mathbf{x} - \mathbf{x}_o) - \left(\dfrac{\mathbf{n}_s}{v_s} - \dfrac{\mathbf{n}_r}{v_r}\right) \cdot \boldsymbol{\lambda} = 0 \ , & (3.19) \end{cases}$$

which are obtained by the sum and difference of equations 3.16 and 3.17. The vector $(\mathbf{x} - \mathbf{x}_o)$ measures the spatial shift of the image point, corresponding to time-lag τ and space-lag $\boldsymbol{\lambda}$.

We consider three special cases of extended images: using both space- and time-lags, using time-lag, or using space-lags. For each extended image type, we derive the equations that link space- or time-lag with half-opening angle θ and azimuth ϕ from equations 3.18 and 3.19. One common step for the three approaches is to replace vectors $\mathbf{n}_s$ and $\mathbf{n}_r$ with functions of vectors $\mathbf{n}$ and $\mathbf{q}$:

$$\begin{cases} \mathbf{n}_s = \mathbf{q}\sin(\theta - \psi) - \mathbf{n}\cos(\theta - \psi) \ , & (3.20) \\ \mathbf{n}_r = \mathbf{q}\sin(\theta + \psi) + \mathbf{n}\cos(\theta + \psi) \ . & (3.21) \end{cases}$$

As shown in Figure 3.1, the angle 2θ is the sum of the incidence and reflection angles, and the angle 2ψ is their difference. Thus the incidence angle is $\theta - \psi$, and the reflection angle is $\theta + \psi$. With γ as the ratio of the source and receiver velocities, v_s and v_r, respectively, we use Snell's law and obtain the expression

$$\gamma = \frac{v_s}{v_r} = \frac{\sin(\theta - \psi)}{\sin(\theta + \psi)} , \tag{3.22}$$

or the expression for ψ using γ and θ:

$$\tan\psi = \frac{1-\gamma}{1+\gamma}\tan\theta . \tag{3.23}$$

By substituting equation 3.23 in equations 3.20 and 3.21, we can replace the angle ψ with a function of γ and θ:

$$\begin{cases} \mathbf{n}_s + \gamma\mathbf{n}_r = \dfrac{((\gamma^2-1)\,\mathbf{n} + 2\mathbf{q}\gamma\sin 2\theta)}{\sqrt{\gamma^2+1+2\gamma\cos 2\theta}} , & (3.24) \\ \mathbf{n}_s - \gamma\mathbf{n}_r = -\mathbf{n}\sqrt{\gamma^2+1+2\gamma\cos 2\theta} , & (3.25) \end{cases}$$

which can be substituted in equations 3.18 and 3.19 to form the system of equations for angle decomposition.

3.3.1 Angle decomposition using CIPs

For CIP gathers, we derive the relationships between time- and space-lags at point $\mathbf{x}_o$ from equations 3.18 and 3.19 by setting the image shift $(\mathbf{x} - \mathbf{x}_o)$ to zero:

$$\begin{cases} \left(\dfrac{\mathbf{n}_s}{v_s} + \dfrac{\mathbf{n}_r}{v_r}\right)\cdot\boldsymbol{\lambda} = 2\tau , & (3.26) \\ \left(\dfrac{\mathbf{n}_s}{v_s} - \dfrac{\mathbf{n}_r}{v_r}\right)\cdot\boldsymbol{\lambda} = 0 . & (3.27) \end{cases}$$

Substituting equations 3.24 and 3.25 in equations 3.26 and 3.27, we obtain the system of equations that describes the relationships between image shift $(\mathbf{x} - \mathbf{x}_o)$ and time-lag τ:

$$\begin{cases} \dfrac{\gamma\sin 2\theta}{\sqrt{\gamma^2+1+2\gamma\cos 2\theta}}\,(\mathbf{q}\cdot\boldsymbol{\lambda}) = v_s\tau , & (3.28) \\ \mathbf{n}\cdot\boldsymbol{\lambda} = 0 . & (3.29) \end{cases}$$

From equation 3.29, only space-lags that are orthogonal to the reflector normal vector $\mathbf{n}$ contribute to the extended image.

The pseudocode for the angle decomposition procedure using time- and space CIP gathers (equations 3.28 and 3.29) is shown in Algorithm 1. Given the normal vector $\mathbf{n}$ and the azimuth reference vector $\mathbf{o}$, we compute vector $\mathbf{a}$, which is the projection of the azimuth vector in the interface plane. Then, we loop over all possible values of the azimuth angle ϕ and construct the vector $\mathbf{q}$, which lies at the intersection of the interface and reflection planes. This step is a rotation of the azimuth reference vector $\mathbf{a}$ within the interface plane by the azimuth angle ϕ. Next, we loop over all possible values of the reflection angle θ and apply a slant-stack to $\mathbf{I}(\boldsymbol{\lambda}, \tau)$ using equations 3.28 and 3.29. The output image $\mathbf{I}(\phi, \theta)$ is a function of half-opening angle θ and azimuth angle ϕ.

Algorithm 1 Isotropic angle decomposition using time- and space-lag CIP gathers

```
for each CIP do
    input I(λ, τ)
    input n, o, γ, v_s
    {n, o} → a
    for φ = 0° ... 360° do
        {n, a, φ} → q
        for θ = 0° ... 90° do
            I(λ, τ) ⟹ I(φ, θ)
        end for
    end for
    return I(φ, θ)
end for
```

Equations 3.28 and 3.29 simplify for PP reflections, with velocity ratio $\gamma = 1$ (Sava and Fomel, 2003):

$$\begin{cases} \sin\theta\,(\mathbf{q}\cdot\boldsymbol{\lambda}) = v_s\tau\ , & (3.30) \\ \mathbf{n}\cdot\boldsymbol{\lambda} = 0\ . & (3.31) \end{cases}$$

Similar to equation 3.28, equation 3.30 describes a linear relationship between space-lag $\boldsymbol{\lambda}$ and time-lag τ.

We illustrate this angle decomposition method using a 3D homogeneous model with a horizontal reflector at depth $z = 0.2$ km, shown in Figure 3.3. The acquisition geometry consists of a 2D network of receivers at $z = 0.02$ km. We generate a three-component shot

gather using a vertical displacement source at coordinates $(0.4, 0.4, 0.02)$ km with a 110Hz peak frequency Ricker wavelet. Figures 3.4(a) and 3.4(b) show the PP and PS images, respectively, which are computed using the imaging condition shown in equations 3.1 and 3.2. Both the PP and PS images are scalars without polarity reversal. Figure 3.5(a) shows a PP CIP gather of a picked image point at coordinates $(0.33, 0.33, 0.2)$ km. Following Algorithm 1, we compute the corresponding angle gather shown in the top right panel of Figure 3.5(a). The dot overlain on the angle gather indicates the analytical estimation of the opening and azimuth angle using the acquisition geometry. We also compute PP angle gathers for eight different shots, shown in Figure 3.5(b). Because the migration velocity is correct, the summation of the eight extended PP images forms a focusing point at $\tau = 0$, $\boldsymbol{\lambda} = \mathbf{0}$. The top right panel of Figure 3.5(b) shows the combination of eight PP angle gathers at the center of the reflector, which match the analytical estimation shown as dots. Similarly, we compute the PS angle gather for the CIP gather (Figure 3.6(a)) of a picked image point at coordinates $(0.2, 0.2, 0.2)$ km. The computed PP and PS angle gathers match the analytical estimations, which demonstrates the accuracy of the angle decomposition algorithm.

3.3.2 Angle decomposition using τCIGs

For time-lag common image gathers (τCIGs), we set $\boldsymbol{\lambda} = \mathbf{0}$ in equations 3.18 and 3.19 and obtain

$$\begin{cases} \left(\dfrac{\mathbf{n}_s}{v_s} - \dfrac{\mathbf{n}_r}{v_r}\right) \cdot (\mathbf{x} - \mathbf{x}_o) + 2\tau = 0 \ , & (3.32) \\ \left(\dfrac{\mathbf{n}_s}{v_s} + \dfrac{\mathbf{n}_r}{v_r}\right) \cdot (\mathbf{x} - \mathbf{x}_o) = 0 \ . & (3.33) \end{cases}$$

This system of equations shows the relationships between image shift $(\mathbf{x} - \mathbf{x}_o)$ and time-lag τ.

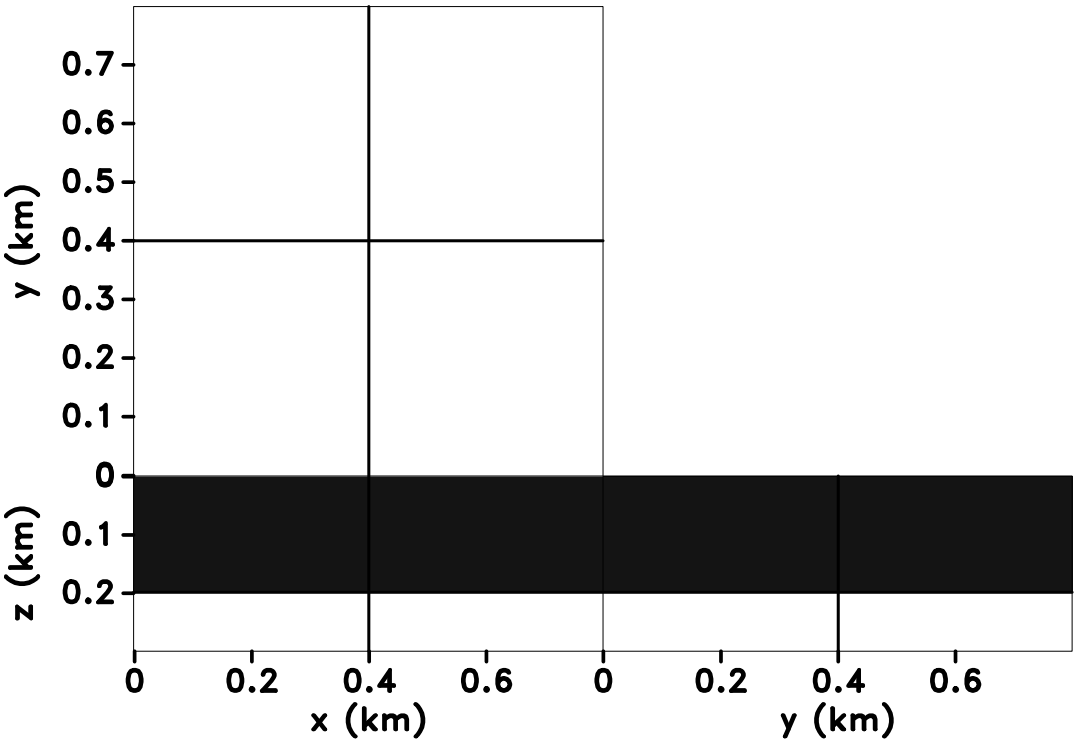

Figure 3.3: 3D P-velocity model with one horizontal reflector at $z = 0.2$ km in a homogeneous medium. The acquisition geometry consists of a vertical displacement source at $(0.4, 0.4, 0.02)$ km and a 2D network of receivers at $z = 0.02$ km.

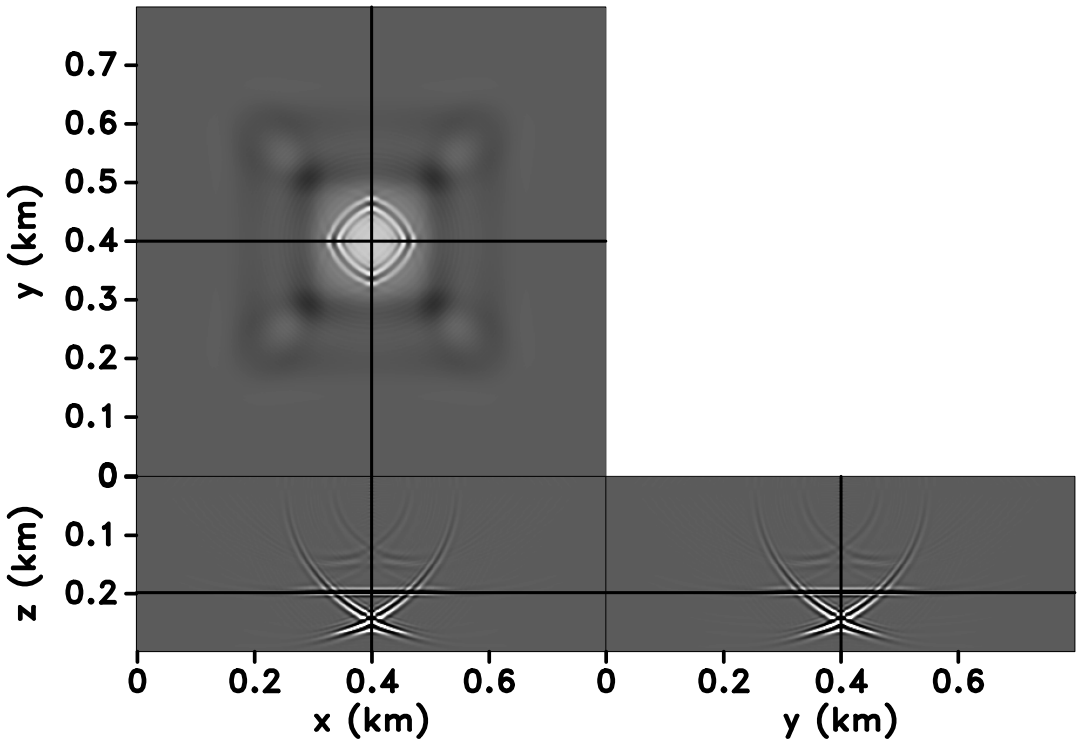

(a)

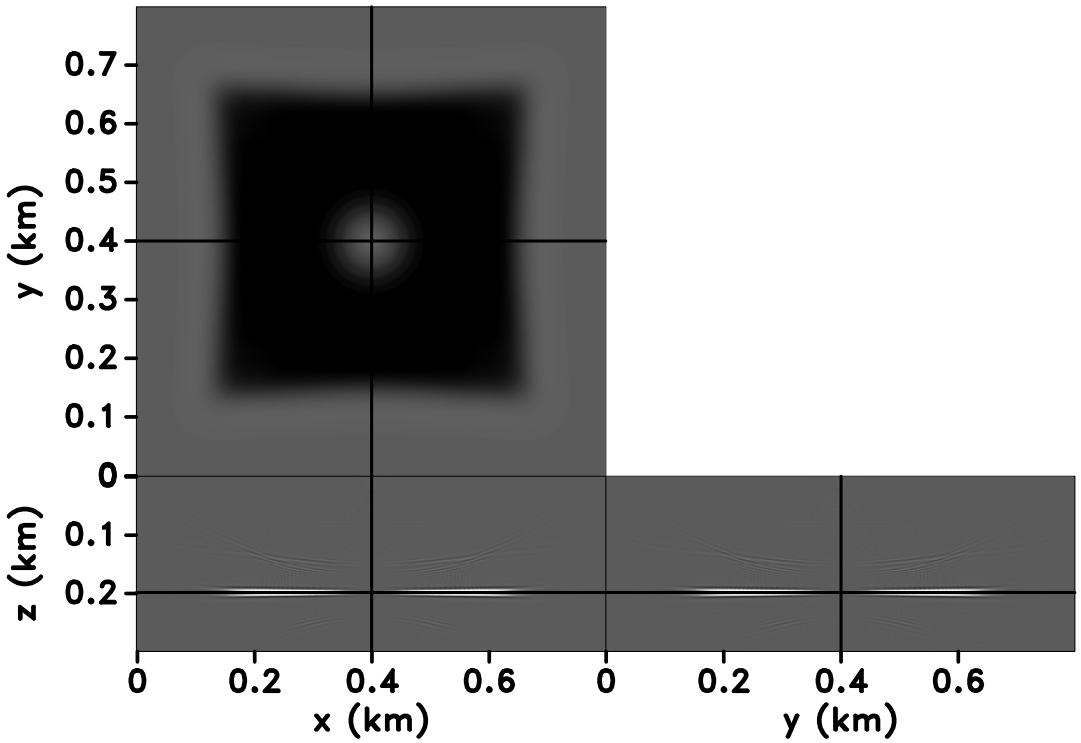

(b)

Figure 3.4: (a) PP and (b) PS images computed for one shot at $(0.4, 0.4, 0.02)$ km. The flat reflector is at $z = 0.2$ km.

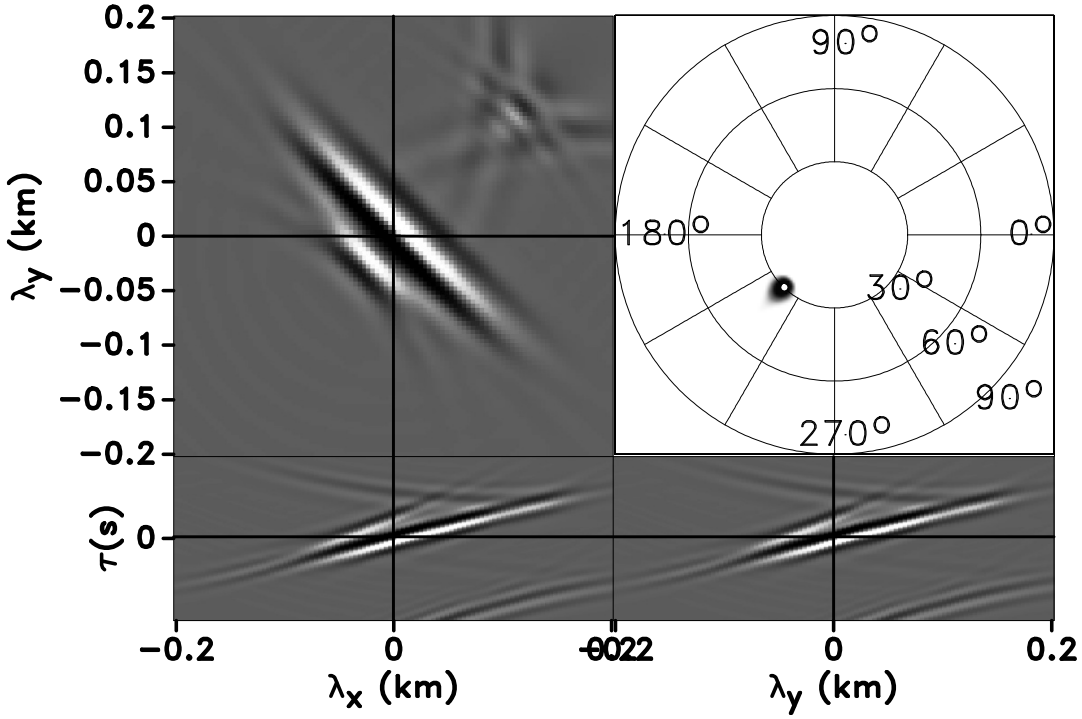

(a)

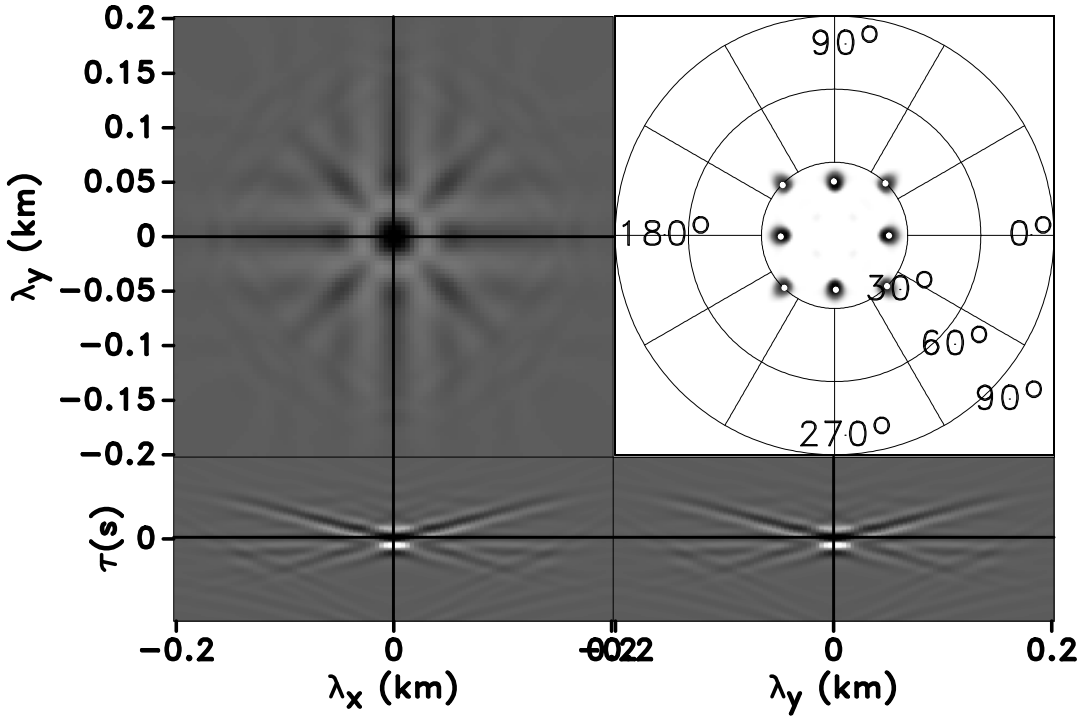

(b)

Figure 3.5: PP extended CIP and wide-azimuth angle gathers of (a) a picked image point at coordinates $(0.33, 0.33, 0.2)$ km for one shot at coordinates $(0.4, 0.4, 0.02)$ km and (b) a picked image point at coordinates $(0.4, 0.4, 0.2)$ km for eight shots. The dot represents the analytical estimation of the opening and azimuth angle using the acquisition geometry.

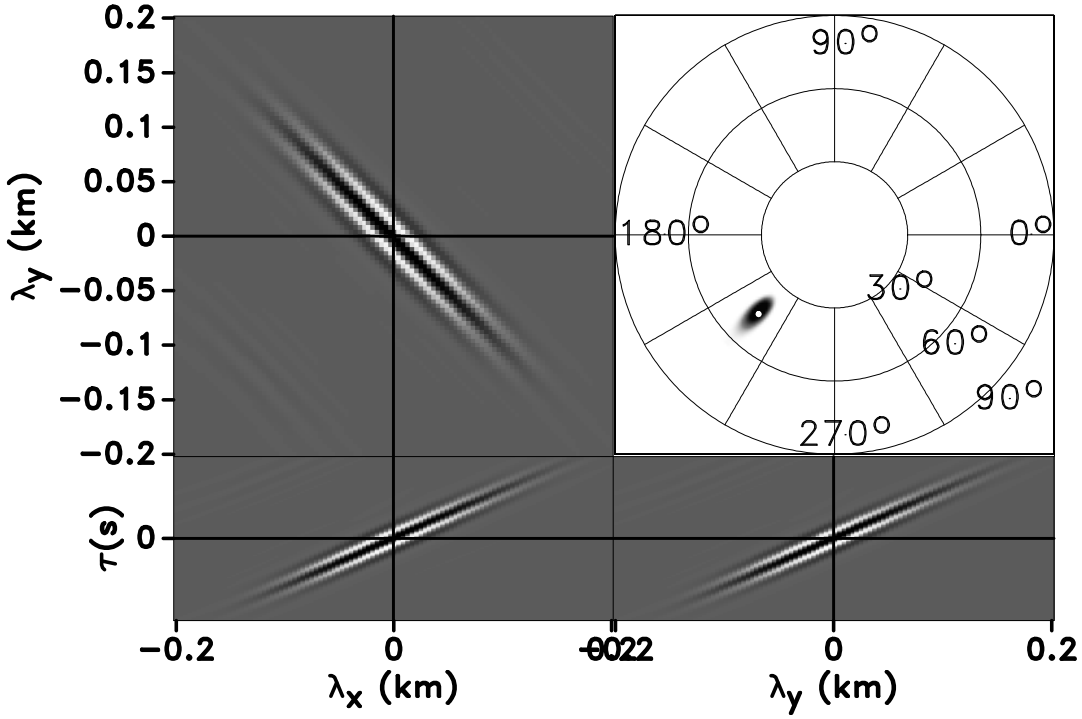

(a)

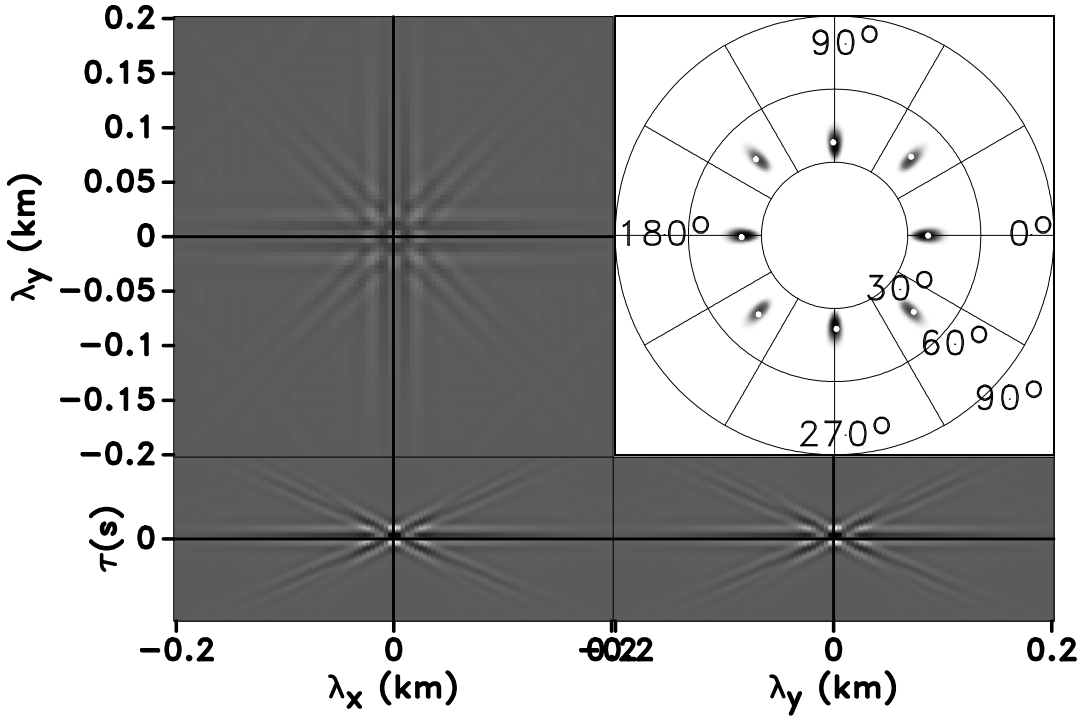

(b)

Figure 3.6: PS extended CIP and wide-azimuth angle gathers of (a) a picked image point at coordinates $(0.2, 0.2, 0.2)$ km for one shot at coordinates $(0.4, 0.4, 0.02)$ km and (b) a picked image point at coordinates $(0.4, 0.4, 0.2)$ km for eight shots. The dot represents the analytical estimation of the opening and azimuth angle using the acquisition geometry.

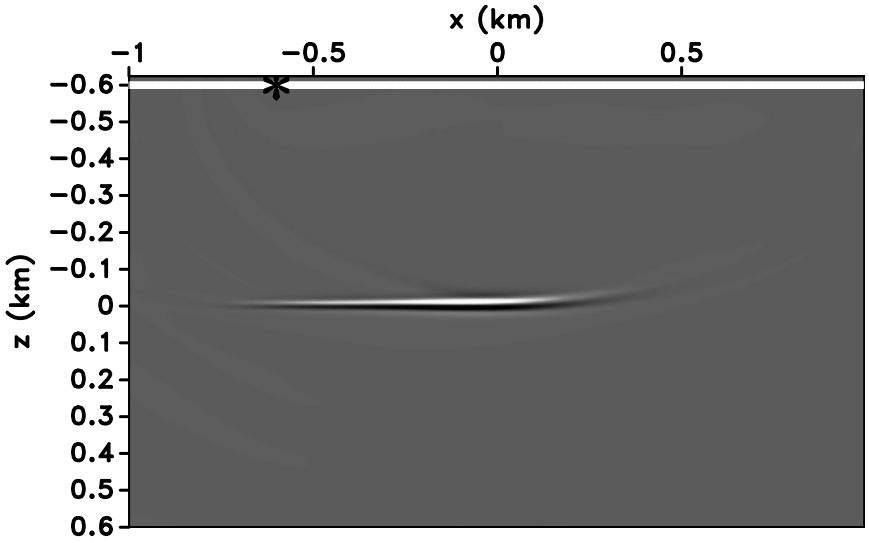

(a)

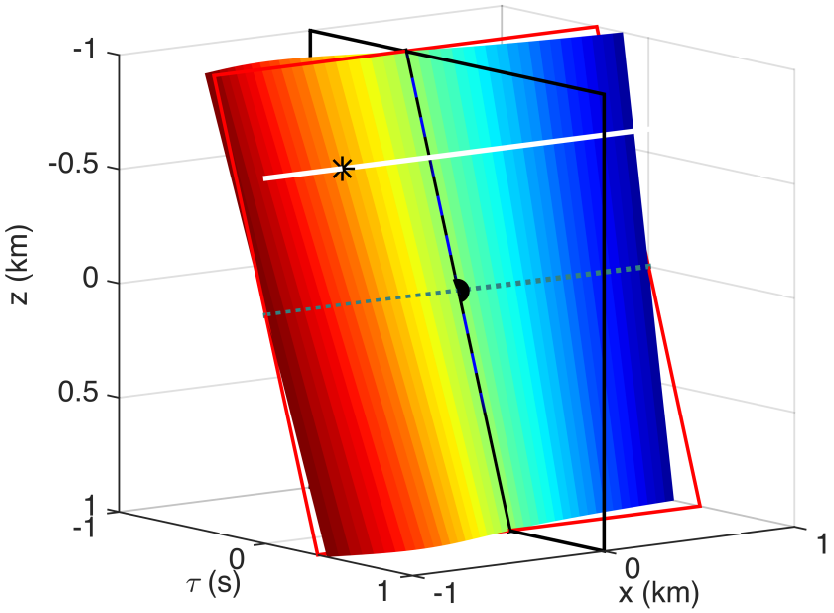

(b)

Figure 3.7: (a) PP image computed from one shot gather. The reflector is horizontal at $z = 0.0$ km. The star represents the source location, and the white line represents the receiver locations. (b) Predicted spatial shift of a horizontal reflector for $\gamma = 1$. The star at coordinates $x = -0.6$ km, $z = -0.6$ km, and $\tau = 0$ s represents the source location, and the white line at $z = -0.6$ km and $\tau = 0$ s represents the receiver locations. The dotted line at $z = 0.0$ km and $\tau = 0$ s shows the zero-lag image. The line at $x = 0.0$ km illustrates the spatial shift for the image point at $\{0.0, 0.0\}$ km. The colors on the surface indicate the contour of the spacial shifts for different image points.

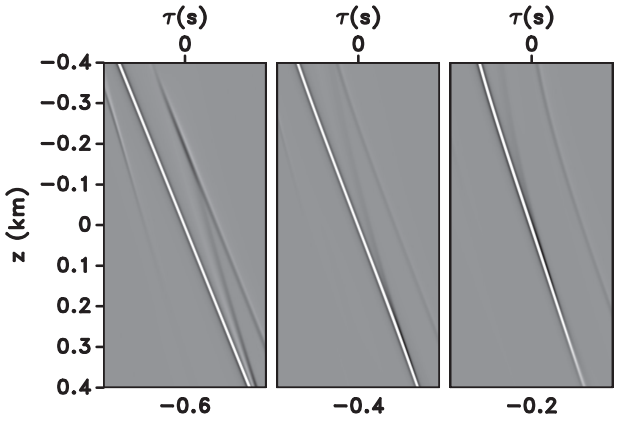

(a)

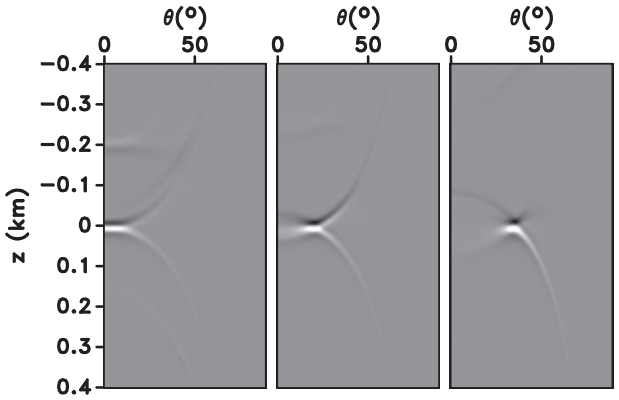

(b)

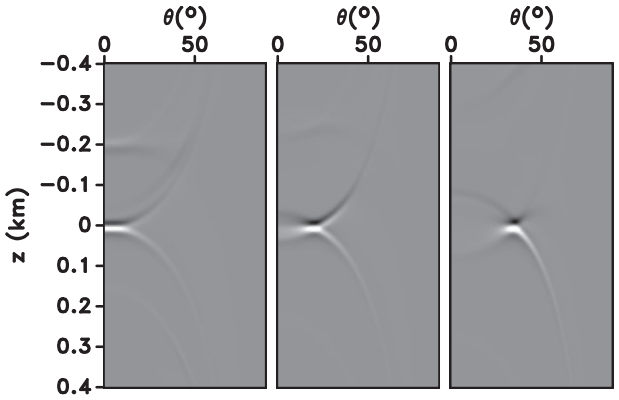

(c)

Figure 3.8: (a) Computed extended image gathers at several x-locations, indicated by the number below each image. The shape of the image in each panel matches the corresponding horizontal slice of the surface plot in Figure 3.7(b). Computed angles for all samples on the reflector by applying (b) a line slant-stack along the vertical trace, and (c) the method described in Algorithm 2, which applies a slant-stack along the surface shown in Figure 3.7(b). The two methods generate the same angle gathers, and they are the same for PP reflections with flat reflectors.

Substituting equations 3.24 and 3.25 in equations 3.32 and 3.33, we obtain the system for angle decomposition using time-lag extended images:

$$\begin{cases} \dfrac{\sqrt{\gamma^2+1+2\gamma\cos 2\theta}}{2}\left[\mathbf{n}\cdot(\mathbf{x}-\mathbf{x}_o)\right] = v_s\tau \ , & (3.34) \\ \sin 2\theta\sqrt{\gamma^2+1+2\gamma\cos 2\theta}\left[\mathbf{q}\cdot(\mathbf{x}-\mathbf{x}_o)\right] = v_s\tau\left(\dfrac{1}{\gamma}-\gamma\right) \ , & (3.35) \end{cases}$$

where equation 3.34 corresponds to the projection of the image shift $(\mathbf{x}-\mathbf{x}_o)$ on the reflector normal $\mathbf{n}$, and equation 3.35 corresponds to the projection of the image shift $(\mathbf{x}-\mathbf{x}_o)$ on vector $\mathbf{q}$. Algorithm 2 shows the pseudocode for the angle decomposition procedure using space-lag extended images. Given the normal vector $\mathbf{n}$, the velocity ratio γ, and the incident wave velocity v_s, we loop over all possible values of the azimuth angle ϕ and construct the vector $\mathbf{q}$, which lies at the intersection of the interface and the reflection plane. Next, we loop over all possible values of the opening angle θ and azimuth angle ϕ, and apply a slant-stack along the surface described in equations 3.34 and 3.35 to the extended image $\mathbf{I}(\mathbf{x},\tau)$. The output is image $\mathbf{I}(\mathbf{x},\phi,\theta)$ as a function of space location $\mathbf{x}$, angle θ, and angle ϕ.

Algorithm 2 Elastic angle decomposition using τCIGs

```
for each τCIG do
    input I(x, τ)
    input n, o, γ, v_s
    {n, o} → a
    for φ = 0° ... 360° do
        {n, a, φ} → q
        for θ = 0° ... 90° do
            I(x, τ) ⟹ I(x, φ, θ)
        end for
    end for
    return I(x, φ, θ)
end for
```

Equations 3.34 and 3.35 simplify to the acoustic case, with velocity ratio $\gamma = 1$ (Sava and Fomel, 2006):

$$\begin{cases} \cos\theta\,[\mathbf{n}\cdot(\mathbf{x}-\mathbf{x}_o)] = v_s\tau\ , & (3.36) \\ \mathbf{q}\cdot(\mathbf{x}-\mathbf{x}_o) = 0\ . & (3.37) \end{cases}$$

Note that in equation 3.37, the time-lag τ is not related to the azimuth vector $\mathbf{q}$, i.e., time-lag extended images do not contain azimuthal information for the acoustic case; however, for converted waves ($\gamma \neq 1$), time-lag extended images contain azimuthal information, according to equation 3.35. Although the resolution of the azimuth gather for converted waves depends on the velocity ratio γ, the possibility of obtaining the azimuth angle from the time-lag gathers is important, because computing time-lag gathers rather than space-lag gathers is much less computationally expensive.

We illustrate the time-lag algorithm with 2D examples. Figure 3.7(a) shows a PP image for the a two-layered model with a horizontal reflector in the P-velocity model. The acquisition geometry contains one source, at $(-0.6, -0.6)$ km, and one receiver line, at $z = -0.6$ km. Using equations 3.36 and 3.37, we can predict the spatial shift of the reflector as function of time-lag τ and space $\mathbf{x}$, shown in Figure 3.7(b). Because the opening angle for each image point on the reflector changes with its relative position to the source, the spatial shift for each image point also varies. Figure 3.8(a) shows the vertical common image gathers at several locations, indicated by the number below each image panel. The shapes of the extended images in each panel are supposed to be straight lines, which matches the corresponding vertical slice of the surface in Figure 3.7(b). We compare the angle gathers at these locations using a conventional method (Sava and Fomel, 2006) and our proposed method. The conventional method maps each vertical time-lag gather individually to a angle gather (Figure 3.8(b)), and the proposed method compute angle gathers (Figure 3.8(c)) by applying a slant-stack along the surface shown in Figure 3.7(b). Because in this example, the image shifts vertically in the time-lag gather, the two methods generate similar angle gathers.

Figure 3.9(a) shows a PP image for a model with a dipping reflector in the P velocity. Using equations 3.36 and 3.37, we can predict the spatial shift of the reflector as a function of time-lag τ, shown in Figure 3.9(b). The dashed line is the intersection of two planes (equations 3.36 and 3.37), which illustrates the spatial shift for the image point at $x = 0.0$ km and $z = 0.0$ km. The solid line through the image point represents the analytical moveout of the extended image in a vertical CIG. The dashed and solid lines do not coincide with each other, i.e., the method that applies a slant-stack to a CIG at a fixed location in space does not accurately measure the image shift $(\mathbf{x} - \mathbf{x}_o)$. The angle gathers computed using this method and the method using a slant-stack along the surface are shown in Figures 3.10(b) and 3.10(c), respectively. The surface slant-stack leads to more focused angle gathers, indicating significantly higher resolution.

For converted waves, the image does not only shift vertically, but also horizontally in the time-lag gather even for a horizontal reflector. Figure 3.11(a) is the PS image for a two-layered model with a horizontal reflector defined by a P-velocity contrast. The predicted spatial shift of the reflector is shown in Figure 3.11(b). Figure 3.12(a) shows the vertical image gathers at several locations in space. Note that the shape of the event in the extended image in each panel is curved. The angle gathers computed using a line slant-stack and a surface slant-stack are shown in Figures 3.12(b) and 3.12(c), respectively. As for the preceding example, we obtain more focused angle gathers using the surface slant-stack.

3.3.3 Angle decomposition using λCIG

For space-lag extended images (λCIGs), we set $\tau = 0$ in equations 3.18 and 3.19 and obtain the system:

$$\begin{cases} \left(\dfrac{\mathbf{n}_s}{v_s} - \dfrac{\mathbf{n}_r}{v_r}\right) \cdot (\mathbf{x} - \mathbf{x}_o) = \left(\dfrac{\mathbf{n}_s}{v_s} + \dfrac{\mathbf{n}_r}{v_r}\right) \cdot \boldsymbol{\lambda} \,, & (3.38) \\ \left(\dfrac{\mathbf{n}_s}{v_s} + \dfrac{\mathbf{n}_r}{v_r}\right) \cdot (\mathbf{x} - \mathbf{x}_o) = \left(\dfrac{\mathbf{n}_s}{v_s} - \dfrac{\mathbf{n}_r}{v_r}\right) \cdot \boldsymbol{\lambda} \,, & (3.39) \end{cases}$$

which indicates the relationships between image shifts $(\mathbf{x} - \mathbf{x}_o)$ and space-lag $\boldsymbol{\lambda}$.

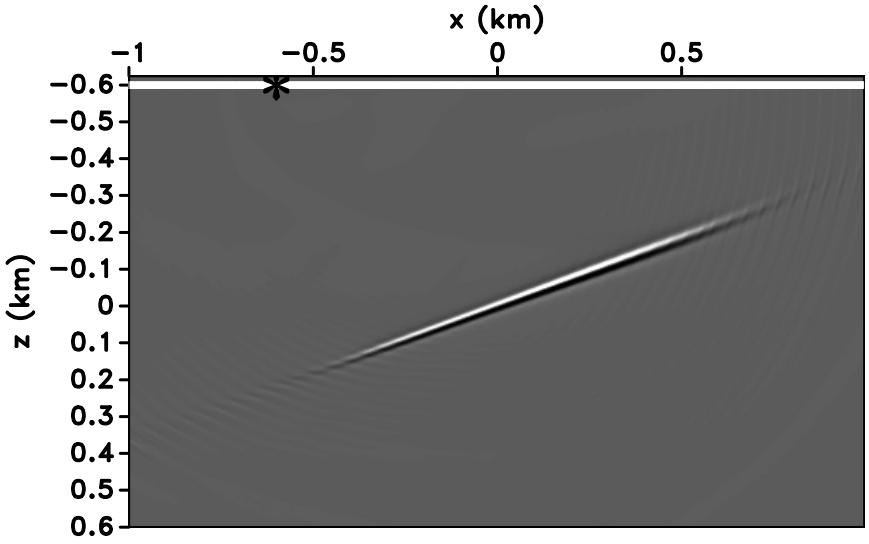

(a)

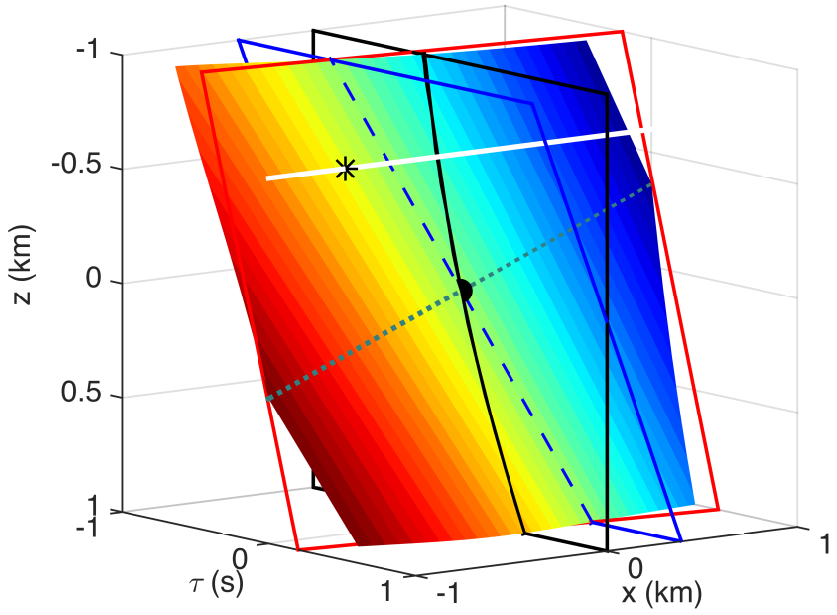

(b)

Figure 3.9: (a) PP image computed from one shot gather. The reflector is dipping. (b) Predicted spatial shift of a dipping reflector for $\gamma = 1$. The star at coordinates $x = -0.6$ km, $z = -0.6$ km, and $\tau = 0$ s represents the source location, and the white line at $z = -0.6$ km and $\tau = 0$ s represents the receiver locations. The dotted line at $\tau = 0$ s shows the zero-lag image. The dashed line illustrates the spatial shift for image point at $(0.0, -0.6)$ km. The solid line at $x = 0.0$ km illustrates the extended image for a time-lag gather at a fixed horizontal position. Note that these two lines do not overlay. The colors on the surface indicate the contour of the spacial shifts for different image points.

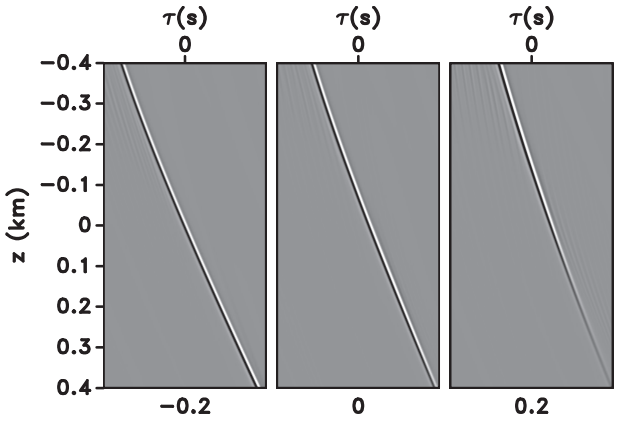

(a)

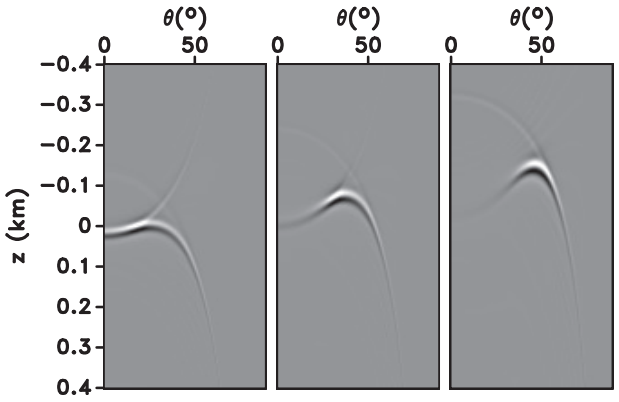

(b)

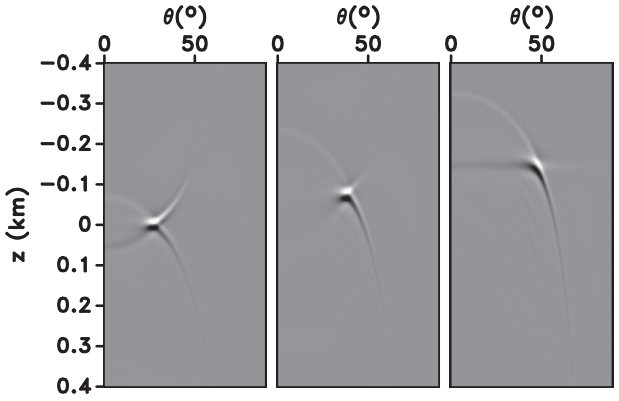

(c)

Figure 3.10: (a) Computed extended image gathers at several x-locations, indicated by the number below each image. The shape of the image in each panel matches the corresponding horizontal slice of the surface plot in Figure 3.9(b). Computed angles for all samples on the reflector by applying (b) a line slant-stack along the vertical trace and (c) the method described in Algorithm 2, which applies a slant-stack along the surface shown in Figure 3.9(b). The angle gathers in (c) are more focused and accurate than those in (b).

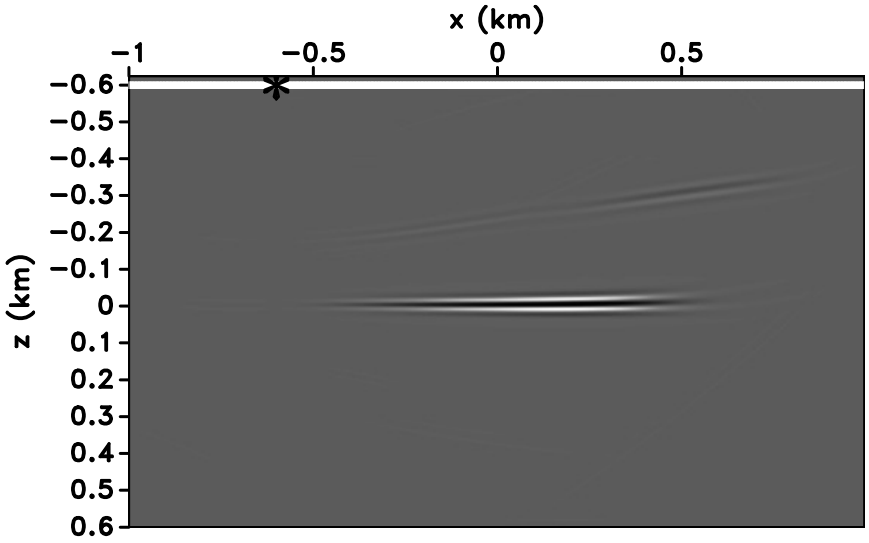

(a)

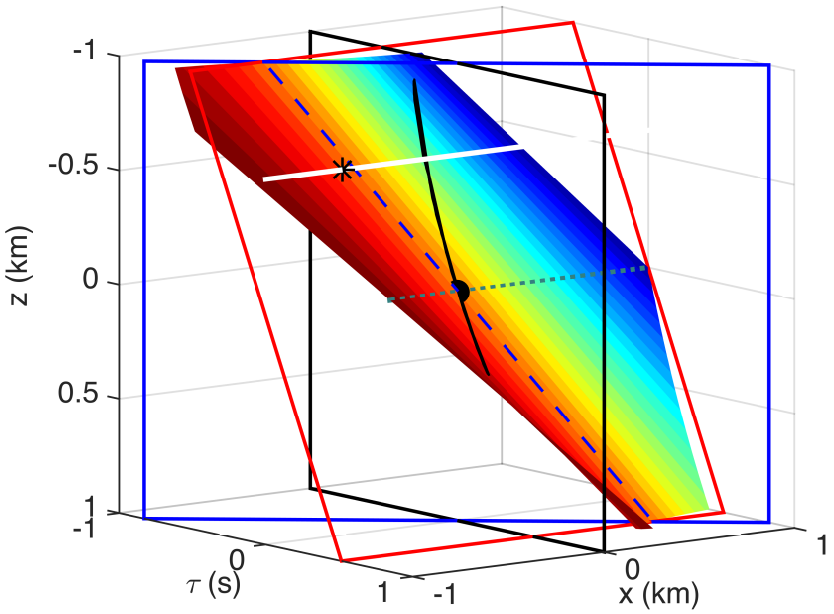

(b)

Figure 3.11: (a) PS image computed from one shot gather. The reflector is horizontal at $z = 0.0$ km. (b) Predicted spatial shift of a horizontal reflector for $\gamma = 1.8$. The star at coordinates $x = -0.6$ km, $z = -0.6$ km, and $\tau = 0$ s represents the source location, and the white line at $z = -0.6$ km and $\tau = 0$ s represents the receiver locations. The dotted line at $z = 0.0$ km and $\tau = 0$ s shows the zero-lag image. The dashed line illustrates the spatial shift for the image point at $(0.0, -0.6)$ km, The solid line illustrates the extended image for a time-lag gather at a fixed horizontal position ($x = 0.0$ km). Note that these two lines do not overlay. The colors on the surface indicate the contour of the spacial shifts for different image points.

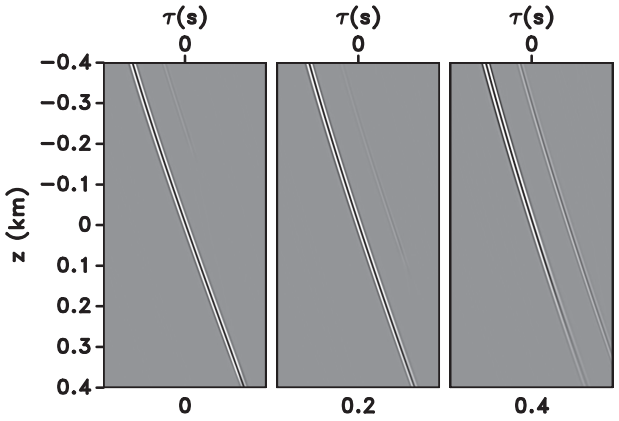

(a)

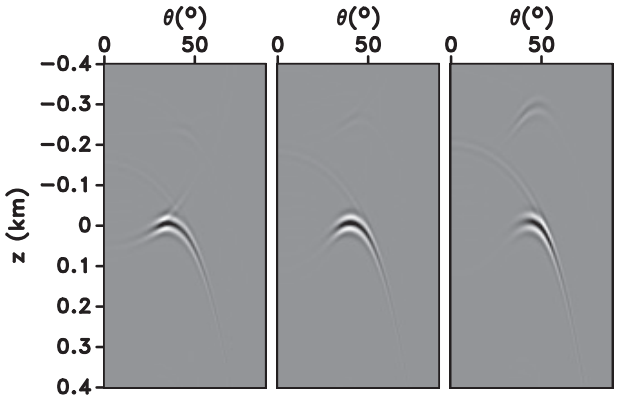

(b)

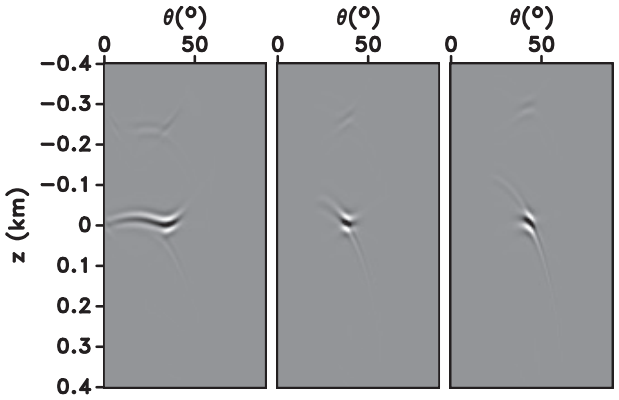

(c)

Figure 3.12: (a) Computed extended image gathers at several x-locations, indicated by the number below each image. The shape of image in each panel matches the corresponding horizontal slice of the surface plot in Figure 3.11(b). Computed angles for all samples on the reflector by applying (b) a line slant-stack along the vertical trace and (c) the method described in Algorithm 2, which applies a surface slant-stack along the surface shown in Figure 3.11(b). The angle gathers in (c) are more focused than those in (b), and they have higher resolutions at larger opening angles.

Substituting equations 3.24 and 3.25 in equations 3.38 and 3.39, we obtain

$$\begin{cases} \dfrac{\gamma^2+1+2\gamma\cos 2\theta}{2\gamma}\mathbf{n}\cdot(\mathbf{x}-\mathbf{x}_o)+\sin 2\theta\mathbf{q}\cdot\boldsymbol{\lambda}=\dfrac{1-\gamma^2}{2\gamma}\mathbf{n}\cdot\boldsymbol{\lambda}\ , & (3.40) \\ \dfrac{\gamma^2+1+2\gamma\cos 2\theta}{2\gamma}\mathbf{n}\cdot\boldsymbol{\lambda}+\sin 2\theta\mathbf{q}\cdot(\mathbf{x}-\mathbf{x}_o)=\dfrac{1-\gamma^2}{2\gamma}\mathbf{n}\cdot(\mathbf{x}-\mathbf{x}_o)\ . & (3.41) \end{cases}$$

The terms $\mathbf{n}\cdot(\mathbf{x}-\mathbf{x}_o)$ and $\mathbf{q}\cdot(\mathbf{x}-\mathbf{x}_o)$ are projections of vector $(\mathbf{x}-\mathbf{x}_o)$ to the normal vector $\mathbf{n}$ and azimuth vector $\mathbf{q}$, respectively. Algorithm 3 shows the pseudocode for the angle decomposition procedure using space-lag extended images. Given the normal vector $\mathbf{n}$ and the azimuth reference vector $\mathbf{o}$, we compute vector $\mathbf{a}$, which is the projection of vector $\mathbf{o}$ in the interface plane, and loop over all possible values of the azimuth angle ϕ and construct the vector $\mathbf{q}$, which lies at the intersection of the interface and reflection plane. This step is a rotation of the azimuth reference vector $\mathbf{a}$ within the interface plane by angle ϕ. Next, we loop over all possible values of the reflection angle θ and apply a slant-stack along the surface (described in equations 3.40 and 3.41) to the extended image $\mathbf{I}(\mathbf{x},\boldsymbol{\lambda})$. The output is image $\mathbf{I}(\mathbf{x},\phi,\theta)$ as a function of half-opening angle θ and azimuth angle ϕ.

Algorithm 3 Elastic angle decomposition using λCIGs

```
for each λCIG do
    input I(x, λ)
    input n, o, γ
    {n, o} → a
    for φ = 0° ... 360° do
        {n, a, φ} → q
        for θ = 0° ... 90° do
            I(x, λ) ⟹ I(x, φ, θ)
        end for
    end for
    return I(x, φ, θ)
end for
```

Equations 3.40 and 3.41 simplify to the acoustic case with velocity ratio $\gamma = 1$:

$$\begin{cases} \mathbf{n} \cdot (\mathbf{x} - \mathbf{x}_o) + \tan\theta\,(\mathbf{q} \cdot \boldsymbol{\lambda}) = 0\,, & (3.42) \\ \tan\theta\,[\mathbf{q} \cdot (\mathbf{x} - \mathbf{x}_o)] + (\mathbf{n} \cdot \boldsymbol{\lambda}) = 0\,, & (3.43) \end{cases}$$

where equation 3.42 is similar to the equation proposed by Sava and Fomel (2003). For PP reflections, if the space-lag is parallel to the normal vector $\mathbf{n}$, the image shift $(\mathbf{x} - \mathbf{x}_o)$ lies in the local interface plane. If the space-lag is orthogonal to the normal vector $\mathbf{n}$, the image shift $(\mathbf{x} - \mathbf{x}_o)$ is parallel to the normal vector $\mathbf{n}$.

3.4 Examples

3.4.1 SEG/EAGE example

For simple geologic models, subsurface illumination from different angles tends to be uniform. However, in areas with complex geologic structures such as salt bodies, severe wavefield distortions lead to irregular subsurface illumination patterns, even if acquisition distribution is uniform. Angle gathers can provide indication of subsalt illumination, which benefits reservoir characterization and acquisition design.

We show angle gathers computed using the proposed elastic angle decomposition methodologies for the synthetic SEG/EAGE salt model (Aminzadeh et al., 1996), shown in Figure 3.13(a). We add a horizontal reflector at $z = 0.3$ km, and compute the half-opening and azimuth angles for an image point on the horizontal reflector at coordinates $(0.3, 0.4, 0.3)$ km. The acquisition geometry consists of 99 sources (the black dots in Figure 3.13(a)) and a 2D network of receivers at z = 0.02 km. We generate three-component shot gathers using a vertical displacement source with a 100Hz peak frequency Ricker wavelet. As shown in Figure 3.13(b), due to the existence of the salt body above the horizontal reflector, it is difficult to illuminate the considered image point at coordinates $(0.3, 0.4, 0.3)$ km from certain azimuths. Figures 3.14 and 3.15 show the stacked angle gather at coordinates $(0.3, 0.4, 0.3)$ km, which are computed from PP and PS CIP gathers, respectively, using Algorithm 1. Both angle gathers show similar illumination patterns. We define azimuth $\phi = 0^\circ$ as east. For the

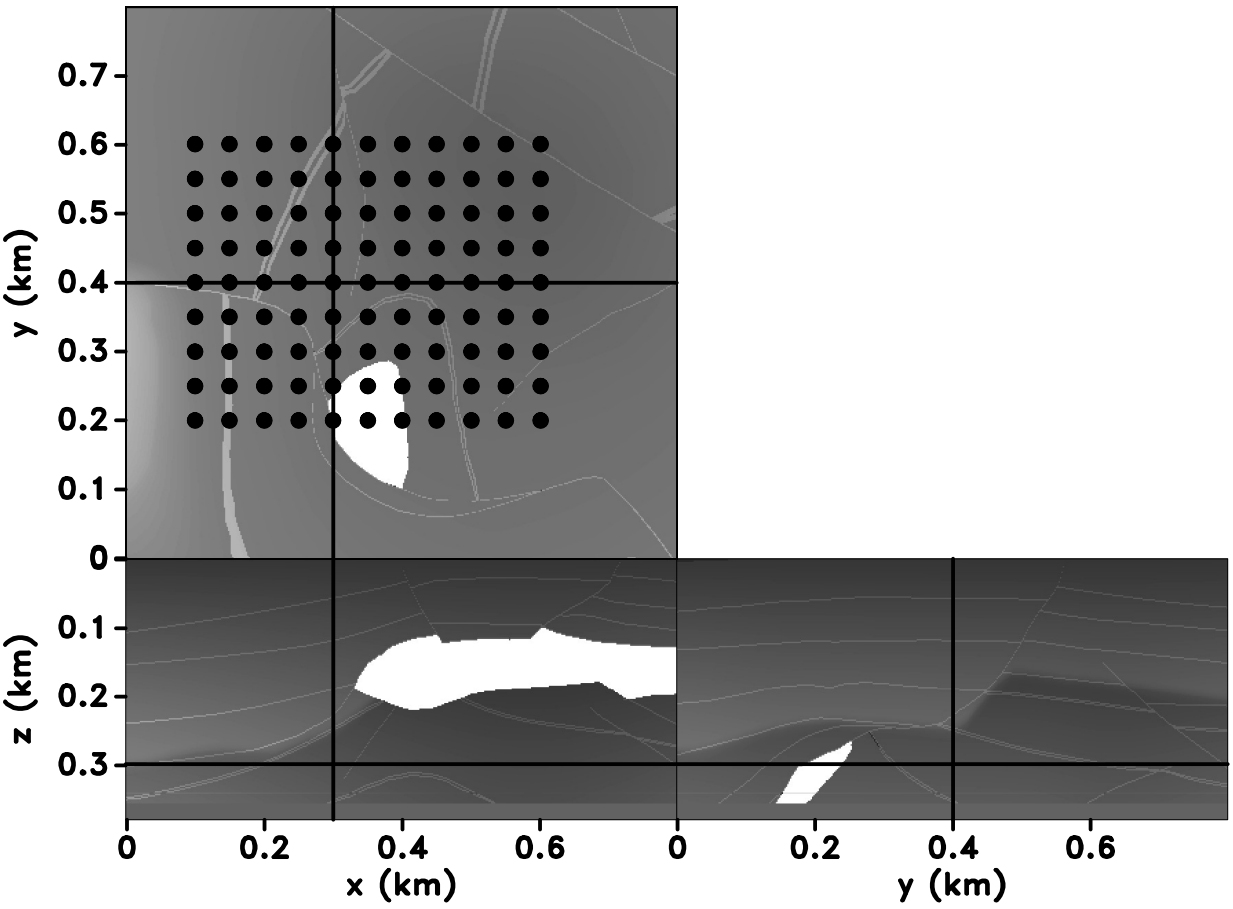

(a)

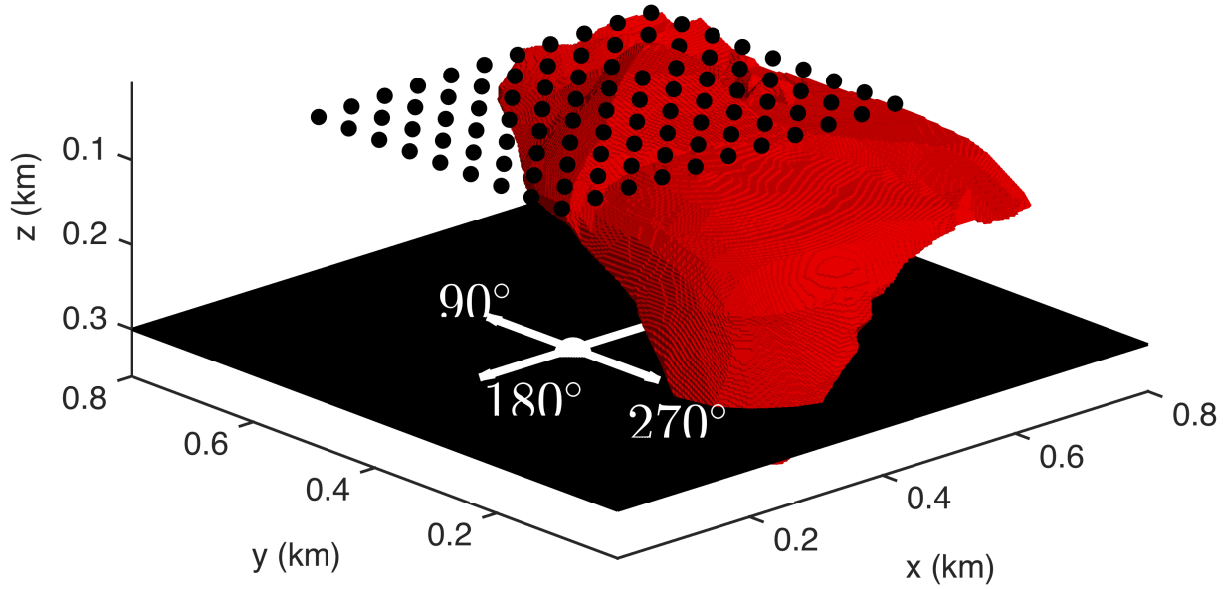

(b)

Figure 3.13: (a) SEG/EAGE model. The dots show the source locations. (b) Relative position of the image point at coordinates $(0.3, 0.4, 0.3)$ km and the salt body.

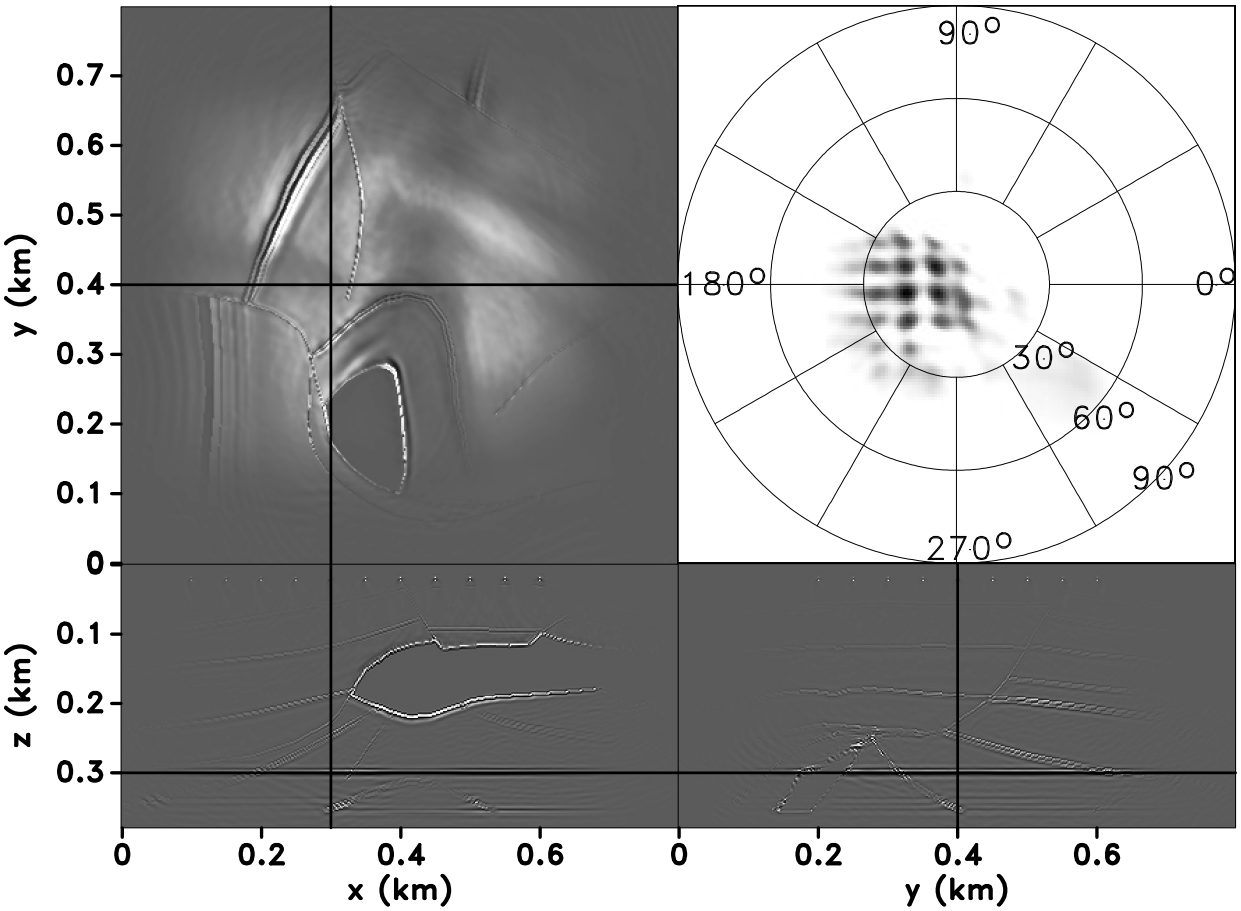

Figure 3.14: PP image and angle gathers at coordinates $(0.3, 0.4, 0.3)$ km, computed using the extended PP image. We define azimuth $\phi = 0°$ in the definition pointing East. This image point is mainly illuminated from the west direction.

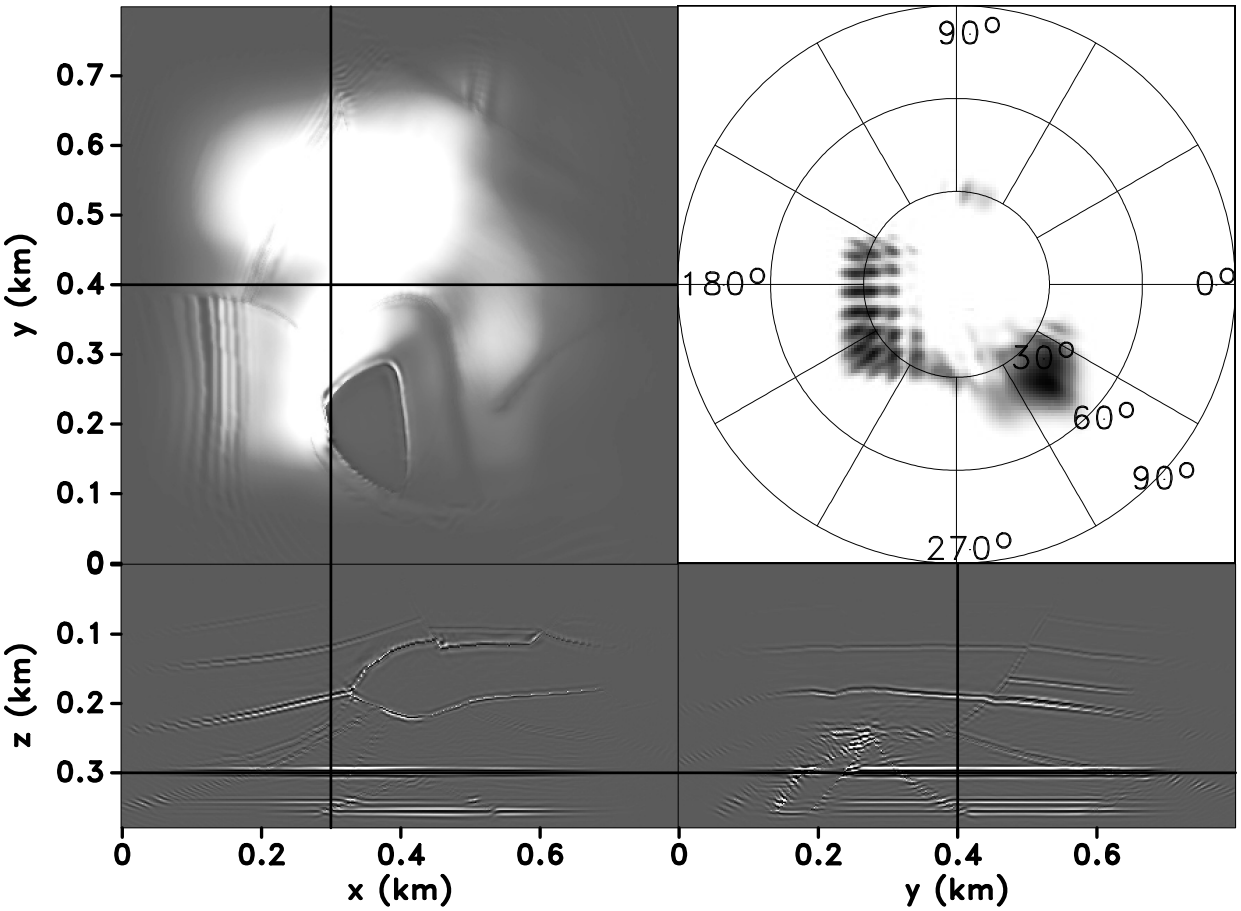

Figure 3.15: PS image and angle gathers at coordinates $(0.3, 0.4, 0.3)$ km, computed using the extended PS image. We define azimuth $\phi = 0°$ as east. This image point is illuminated from the west and the south directions.

PP image, this image point is mainly illuminated from the west direction, and for the PS image, this image point is illuminated from the west and south directions. Therefore, both PP and PS angle gathers show similar subsurface illumination patterns that are affected by the salt on the east.

3.4.2 Volve data example

The Volve field is located in the Norwegian North Sea and is characterized by a complex subchalk reservoir (Szydlik et al., 2007). The acquisition geometry consists of 12 parallel OBC receiver lines, and each line contains 240 receivers. The provided PP data are pre-processed for PP imaging, while the PS data are pre-processed for PS imaging. The PP data mainly contain up-going PP reflections, which are obtained from the hydrophone and vertical geophone components, using PZ summation (Hoffe et al., 1999). The PS dataset is obtained by rotating the horizontal inline and crossline geophone components into the source-receiver (radial) direction (Gaiser, 1999). We bandpass both datasets to 0-15 Hz to save computational cost by simulating wavefields using a relatively coarse grid. By using the provided P- and S-velocity models, we compute the PP and PS images above the chalk layer, using the PP and PS imaging conditions (equations 3.1 and 3.2), respectively. The reflector normal vector $\mathbf{n}$ from the PP image is almost vertical above the chalk layer throughout this field. Figure 3.16(a) shows the stacked PP image for 140 receiver gathers, and Figure 3.16(b) shows the stacked PS image. Because the wavelength of the S wave is in general shorter than that of the P wave, the PS image has higher resolution than the PP image. However, the PS data have a lower signal-to-noise ratio than the PP data; therefore, the reflectors in the PS image are less continuous than those in the PP image. We compute the extended CIP gathers at the image point $(6.461, 3.406, 2.106)$ km for four receiver gathers, whose locations are indicated by the dots in Figure 3.16(a) and Figure 3.16(b). Figures 3.17(a)-3.17(d) show the PP extended CIP gathers and angle gathers for these receiver gathers; Figures 3.18(a)-3.18(d) show the PS extended CIP gathers and angle gathers. The PS CIP and angle gathers are noisier than PP the gathers. The angle gathers show that this image point is illuminated

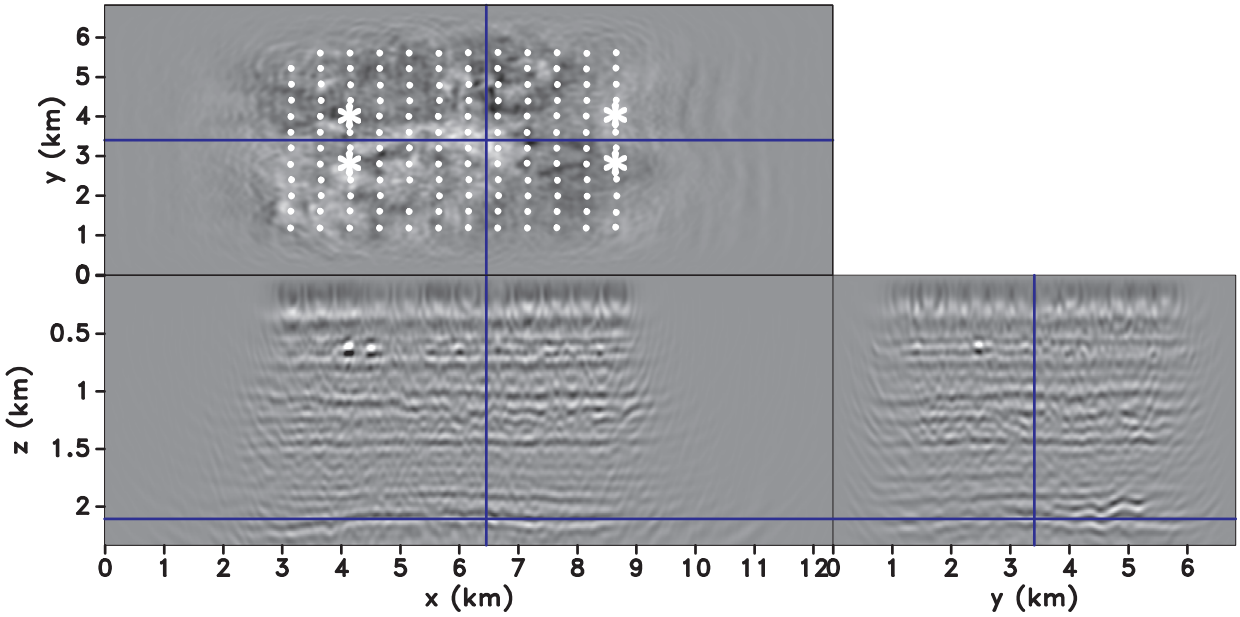

(a)

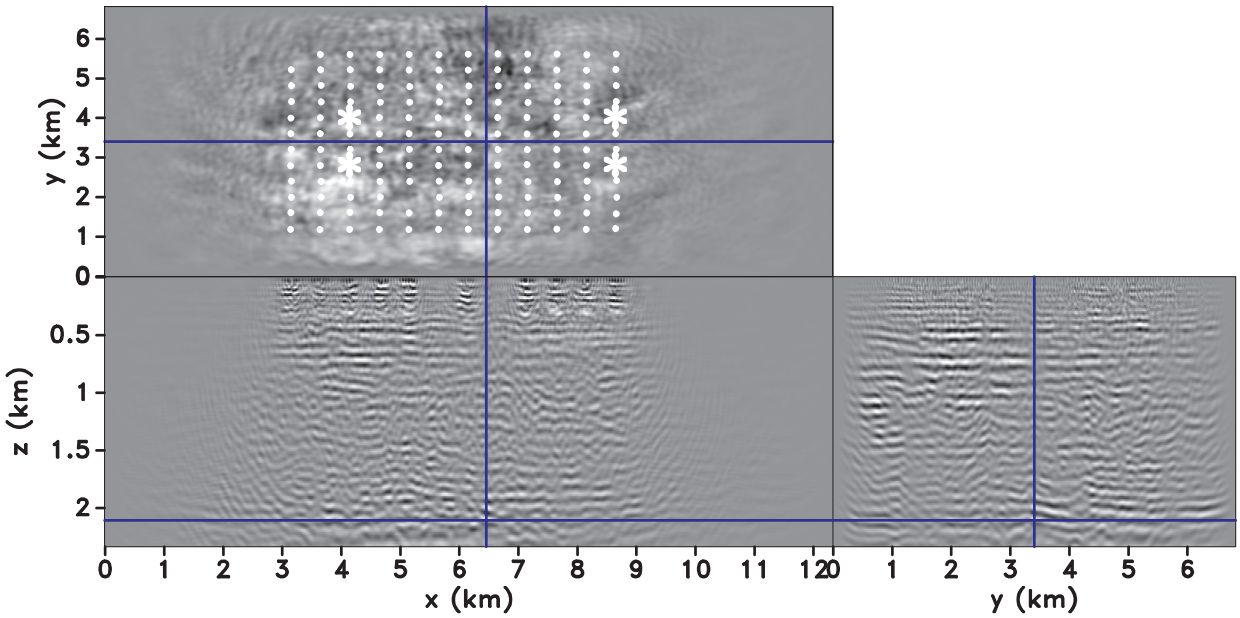

(b)

Figure 3.16: Volve data example. (a) PP and (b) PS images computed using 142 receiver gathers. The dots show locations of all the receivers, and the stars show locations of four receivers. The reflectors in the PS image are less continuous than those in the PP image.

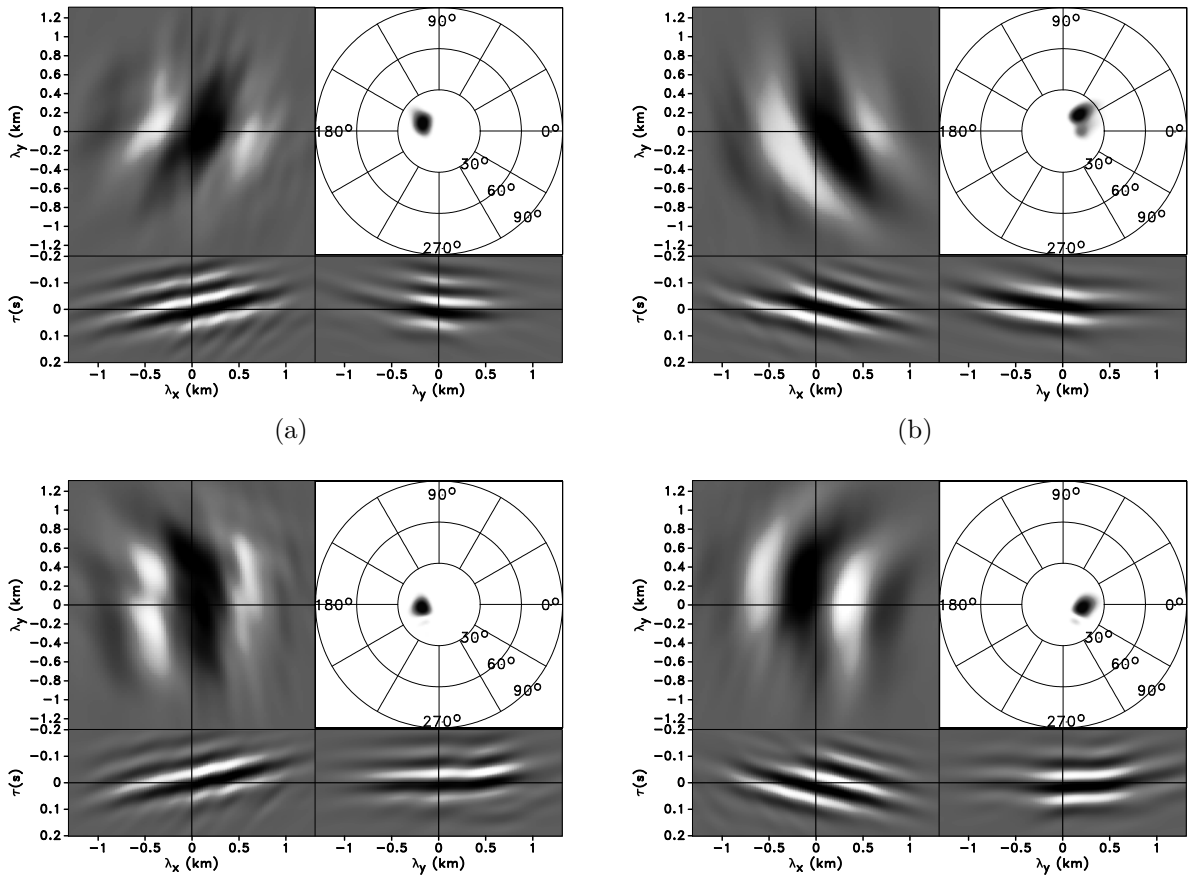

Figure 3.17: PP extended CIP and wide-azimuth angle gathers for four receiver gathers. The receivers are at (a) $(4.1, 4.0, 0.1)$, (b) $(8.6, 4.0, 0.1)$, (c) $(4.1, 2.8, 0.1)$, and (d) $(8.6, 2.8, 0.1)$ km. The angle gathers show that this image point is illuminated by the four receivers from various directions with PP reflections.

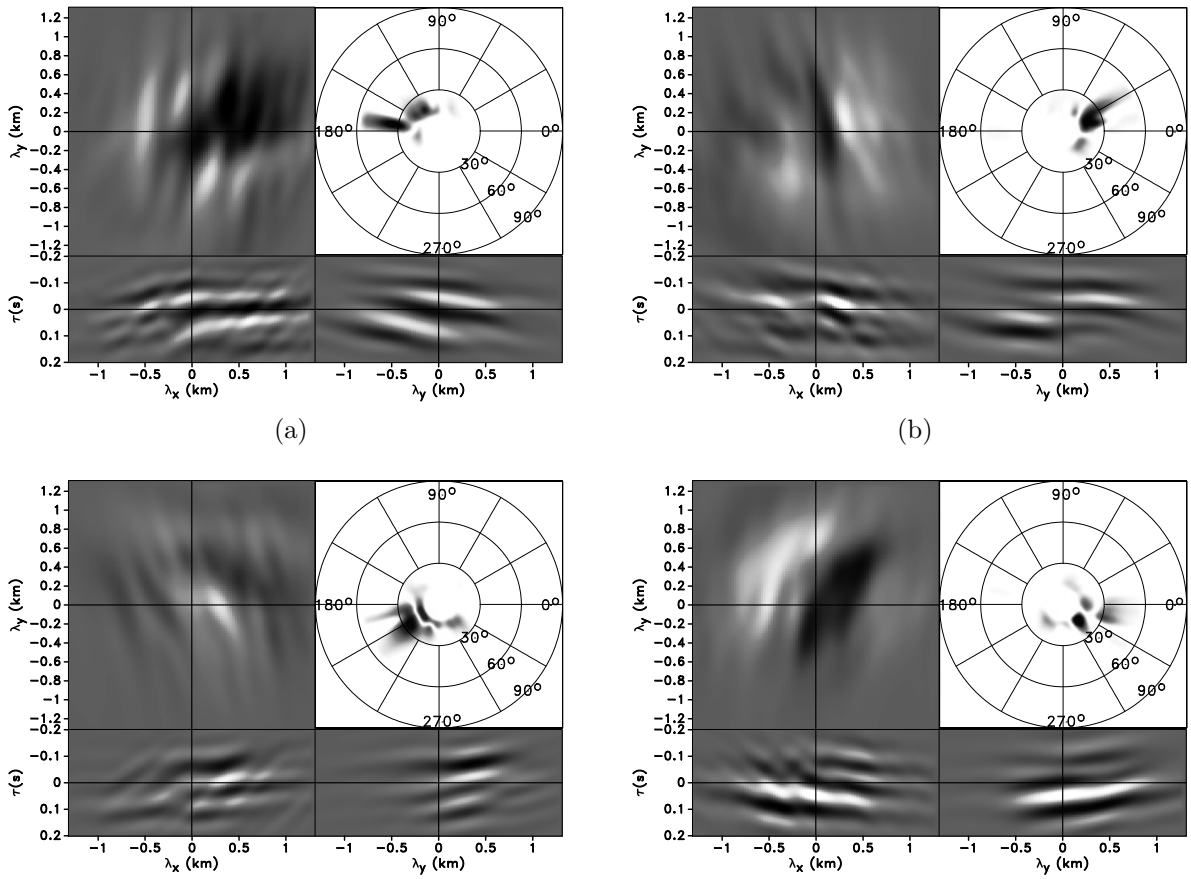

Figure 3.18: PS extended CIP and wide-azimuth angle gathers for four receiver gathers. The receivers are at (a) $(4.1, 4.0, 0.1)$, (b) $(8.6, 4.0, 0.1)$, (c) $(4.1, 2.8, 0.1)$, and (d) $(8.6, 2.8, 0.1)$ km. The angle gathers show that this image point is illuminated by the four receivers from various directions with PS reflections.

by receiver gathers from various directions, depending on the relative positions of receivers and the imaging point.

3.5 Conclusions

Elastic 3D angle gathers can be computed from time-lag or space-lag common image gathers, as well as from mixed time- and space-lag common image point gathers. We propose extended imaging conditions to compute scalar PP, PS, SP, and SS images, and develop three algorithms to compute opening and azimuth angle gathers. One algorithm uses combined time- and space-lag common image point gathers to compute angle gathers, and the other two algorithms use time-lag or space-lag common image gathers, mapping all image points simultaneously from the model space to the angle domain. Examples in both 2D and 3D demonstrate that our methods correctly handle dipping reflectors as well as converted wave images. The computed angle gathers correctly indicate the illumination pattern for subsurface image points, which is important for acquisition design, model building, and reservoir characterization.

3.6 Acknowledgments

We thank the sponsors of the Center for Wave Phenomena, whose support made this research possible. We also thank Statoil ASA and the Volve license partners ExxonMobil E & P Norway and Bayerngas Norge AS, for the release of the Volve data. The views expressed in this paper are the views of the authors and do not necessarily reflect the views of Statoil ASA and the Volve field license partners. The reproducible numeric examples in this paper use the Madagascar open-source software package (Fomel et al., 2013) freely available from http://www.ahay.org.

CHAPTER 4

ELASTIC LEAST-SQUARES REVERSE TIME MIGRATION

A paper submitted to *Geophysics*

Yuting Duan[6,7], Antoine Guitton[7], and Paul Sava[7]

Least-squares migration (LSM) can produce images with improved resolution and reduced migration artifacts, compared to conventional imaging. We propose a method for elastic least-squares reverse time migration (LSRTM) based on a new perturbation imaging condition that yields scalar images of squared P and S velocity perturbations. These perturbation images do not suffer from polarity reversals that are common for more conventional elastic imaging methods. We use 2D synthetic and field data examples to demonstrate the proposed LSRTM algorithm using the perturbation imaging condition. Results show that elastic LSRTM improves the energy focusing and illumination of the elastic images, and it attenuates artifacts resulting, for instance, from sparseness in the wavefield sampling and crosstalk of P and S modes. Compared to RTM images, the LSRTM images provide more accurate relative amplitude information that is useful for reservoir characterization.

4.1 Introduction

Seismic migration is a technique for obtaining structural images of the subsurface from recorded seismic data. Starting from a linearized forward operator which is based on assumptions about the wave equation and model parameters, seismic migration can be formulated as the adjoint operator that maps seismic data to a subsurface image (Claerbout, 1992). Migrated images not only can show geologic structures, but can also provide information about material properties, such as reflectivity, which is important for reservoir characterization. In practice, however, migration images often contain various undesirable artifacts, for example,

[6]Author for correspondence.
[7]Center for Wave Phenomena, Colorado School of Mines, 924 16th Street, Golden, CO 80401.

the artifacts caused by limited bandwidth and acquisition coverage. Also, migration images are usually computed under assumptions about wave propagation in the subsurface, e.g., that the earth is isotropic and acoustic; these assumptions are, to varying degrees, inaccurate. Taken together, these limitations and assumptions result in artifacts and thus degrade the resolution of the images.

Advances in seismic acquisition and ongoing improvements in computational capability make imaging using elastic waves increasingly feasible (Sun and McMechan, 1986; Hokstad et al., 1998; Sun et al., 2006; Yan and Sava, 2008; Denli and Huang, 2008; Artman et al., 2009; Wu et al., 2010; Du et al., 2012b; Duan and Sava, 2015; Rocha et al., 2016). Compared to acoustic images, elastic images can provide more information about the subsurface, e.g., fracture distributions and elastic properties. However, elastic migration also suffers from issues that negatively affect the quality of the images. Because it is in general difficult to separate all arrivals by wave mode in the recorded data, some arrivals are migrated using an incorrect velocity model. Such nonphysical modes lead to artifacts (i.e. cross-talk) in the image (Duan et al., 2014).

Least-squares migration (LSM) is an improved imaging algorithm that reduces these migration artifacts and also improves the resolution of migration images. LSM is a linearized waveform inversion that seeks to find the image that best predicts, in a least-squares sense, the recorded seismic data (Schuster et al., 1993; Nemeth et al., 1999; Kuehl et al., 2002; Kaplan et al., 2010). Schuster et al. (1993) propose LSM for cross-well data while Nemeth et al. (1999) apply this technique to surface data. Their studies show that LSM can significantly improve the spatial resolution of the images, and can also reduce migration artifacts arising from limited aperture, coarse sampling, and acquisition gaps.

LSM can be implemented using a Kirchhoff engine (Nemeth et al., 1999; Dai et al., 2011), one-way wave propagator (Kuehl et al., 2002; Kaplan et al., 2010; Huang and Schuster, 2012), or two-way wave propagator, i.e., least squares reverse-time migration (LSRTM) (Dong et al., 2012; Dai and Schuster, 2013; Wong et al., 2015; Hou and Symes, 2015). For elastic LSM,

Stanton and Sacchi (2015) propose elastic least-squares migration using a one-way wave equation, and they compute PP and PS images from two-component elastic data in isotropic media. Although computationally expensive, RTM is advantageous for velocity models with complicated geologic structures that result in wavefield multipathing.

A key component for elastic LSRTM is the imaging condition, and many different types of imaging conditions have been proposed for elastic media. For example, Yan and Sava (2008) propose a displacement imaging condition that crosscorrelates each component of source and receiver displacement wavefields. They also propose a potential imaging condition that crosscorrelates P- and S-wave modes derived from the source and receiver wavefields. One issue with this potential imaging condition is that the image components for converted waves change polarity at normal incidence. Therefore, they adopt an additional polarity correction in the angle domain, which is computationally expensive. Duan and Sava (2015) propose a scalar imaging condition for converted waves that produces scalar images without polarity reversal; however, this imaging condition requires knowledge of the geologic dip.

In this paper, we propose an elastic LSRTM method based on a new perturbation imaging condition, which is derived for squared P and S velocities. Images computed using this new imaging condition can be simply related to physical subsurface properties, and do not suffer from polarity changes; they can be stacked over experiments without an additional polarity correction thus reducing the computational cost of the algorithm. Using 2D synthetic and field data examples, we demonstrate that we are able to obtain elastic LSRTM images with higher resolution and reduced migration artifacts.

4.2 Theory

LSM aims to find the image that best predicts, in a least-squares sense, the recorded seismic data. For elastic migration, we consider a vector image $\mathbf{m}$ which contains both compressional and shear wave lithological information. We treat migration as an adjoint operator $\mathbf{F}^{\mathsf{T}}$ that transforms data $\mathbf{d}$ to image $\mathbf{m}$, and thus the forward process can be expressed as

$$\mathbf{Fm} = \mathbf{d} \ , \tag{4.1}$$

where $\mathbf{F}$ is the demigration operator. Data $\mathbf{d}\,(e, \mathbf{x}, t)$ is a vector, as a function of the experiment index e, spatial location $\mathbf{x}$, and time t.

For LSM, one typically updates the model iteratively by minimizing the objective function

$$\mathcal{J} = \sum_e \frac{1}{2} \| \mathbf{W}\,(\mathbf{Fm} - \mathbf{d}_r)\,\|^2 \ , \tag{4.2}$$

which evaluates the misfit between observed data $\mathbf{d}_r$ and predicted data ($\mathbf{Fm}$) for each experiment e. The operator $\mathbf{W}\,(e, \mathbf{x}, t)$ denotes a data weighting operator, which can be applied for various purposes. For example, Trad et al. (2015) use a matrix $\mathbf{W}$ to eliminate the impact of high-amplitude noise or missing traces on inversion; Wong et al. (2015) use $\mathbf{W}$ to weigh the salt reflection energy down. In this paper, we use the data weighting term to equalize the amplitudes of all arrivals in the recorded data, and thus to obtain balanced updates for all reflectors.

We derive perturbation models using the Born approximation (Hudson and Heritage, 1981; Jaramillo and Bleistein, 1999; Ribodetti et al., 2011). We consider the homogeneous elastic isotropic wave-equation to simplify the derivation:

$$\ddot{\mathbf{u}}_s - \alpha \nabla(\nabla \cdot \mathbf{u}_s) + \beta \nabla \times (\nabla \times \mathbf{u}_s) = \mathbf{d}_s \ . \tag{4.3}$$

The background elastic models are assumed to be slowly-varying. Vector $\mathbf{u}_s\,(e, \mathbf{x}, t) = [u_x \quad u_y \quad u_z]^T$ is the source displacement wavefield, which is a function of experiment e, space $\mathbf{x}$, and time t. The vector $\mathbf{d}_s\,(e, \mathbf{x}, t)$ is the source function, which we assume to be known. The parameters $\alpha\,(\mathbf{x}) = \dfrac{\lambda + 2\mu}{\rho}$ and $\beta\,(\mathbf{x}) = \dfrac{\mu}{\rho}$ are squared P- and S-wave velocities, respectively; λ and μ are Lamé parameters, and ρ is the density.

The perturbation $\mathbf{m} = [\delta\alpha \quad \delta\beta]^T$ added to the background model gives the perturbed model $[\alpha + \delta\alpha \quad \beta + \delta\beta]^T$. Under the Born approximation, the total wavefield $\mathbf{u}_s + \delta\mathbf{u}_s$ is computed using the same source term $\mathbf{d}_s$:

$$(\ddot{\mathbf{u}}_s + \delta\ddot{\mathbf{u}}_s) - (\alpha + \delta\alpha)\,\nabla[\nabla \cdot (\mathbf{u}_s + \delta\mathbf{u}_s)] + (\beta + \delta\beta)\,\nabla \times [\nabla \times (\mathbf{u}_s + \delta\mathbf{u}_s)] = \mathbf{d}_s\ , \qquad (4.4)$$

where $\delta\mathbf{u}_s$ is the perturbed wavefield:

By ignoring the high order terms $\delta\alpha\nabla(\nabla \cdot \delta\mathbf{u}_s)$ and $\delta\beta\nabla \times (\nabla \times \delta\mathbf{u}_s)$, and subtracting equation 4.3 from equation 4.4, we obtain a relation for the perturbed wavefield $\delta\mathbf{u}_s$ with respect to the model perturbations in α and β:

$$\delta\ddot{\mathbf{u}}_s - \alpha\nabla(\nabla \cdot \delta\mathbf{u}_s) + \beta\nabla \times (\nabla \times \delta\mathbf{u}_s) = [\nabla(\nabla \cdot \mathbf{u}_s) \quad -\nabla \times (\nabla \times \mathbf{u}_s)] \begin{bmatrix} \delta\alpha \\ \delta\beta \end{bmatrix}\ . \qquad (4.5)$$

The predicted data are extracted from the perturbed wavefield $\delta\mathbf{u}_s$ at the receiver locations.

We define a matrix $\mathbf{Q}$ that, at each time and space position, is given by

$$\mathbf{Q} = [\nabla(\nabla \cdot \mathbf{u}_s) \quad -\nabla \times (\nabla \times \mathbf{u}_s)]\ . \qquad (4.6)$$

Here, the first and second elements of $\mathbf{Q}$ are the decomposed P and S modes of the source wavefield $\mathbf{u}_s$, respectively. The demigration operator in equation 4.1 thus becomes

$$\mathbf{F} = \mathbf{KPQ}\ , \qquad (4.7)$$

where $\mathbf{P}$ represents an elastic forward modeling operator that computes the perturbed wavefield $\delta\mathbf{u}_s$ for a source term $\mathbf{Qm}$; $\mathbf{K}$ is an operator that restricts the perturbed wavefield $\delta\mathbf{u}_s$ to the known receiver positions. Equation 4.7 maps the image $\mathbf{m}$ to the data $\mathbf{d}_r$, and its adjoint operator

$$\mathbf{F}^\mathsf{T} = \mathbf{Q}^\mathsf{T}\mathbf{P}^\mathsf{T}\mathbf{K}^\mathsf{T} \qquad (4.8)$$

maps the data $\mathbf{d}_r$ to the image $\mathbf{m}$; the operator $\mathbf{K}^\mathsf{T}$ injects the recorded data $\mathbf{d}_r$ into the wavefield, and the adjoint wave propagation operator $\mathbf{P}^\mathsf{T}$ computes the receiver displacement wavefield $\mathbf{u}_r = \mathbf{P}^\mathsf{T}\mathbf{K}^\mathsf{T}\mathbf{d}_r$. Equation 4.8 describes a perturbation imaging condition for elastic RTM because the application of the adjoint operator $\mathbf{F}^\mathsf{T}$ to the recorded data $\mathbf{d}_r$ yields the images

$$\delta\alpha = \sum_{e,t} \nabla(\nabla \cdot \mathbf{u}_s) \cdot \mathbf{u}_r \ , \tag{4.9}$$

$$\delta\beta = \sum_{e,t} -\nabla \times (\nabla \times \mathbf{u}_s) \cdot \mathbf{u}_r \ , \tag{4.10}$$

for the α and β models, respectively. From equation 4.8, we see that images $\delta\alpha$ and $\delta\beta$ are computed by taking the zero-lag crosscorrelation of elements of the matrix $\mathbf{Q}$ with the displacement receiver wavefield $\mathbf{u}_r$. These images indicate the model perturbations, instead of the reflection coefficients; therefore they do not suffer from polarity reversal, which is a common issue for elastic images whose values are related to angle-dependent reflectivity. Because our inversion algorithm updates $\delta\alpha$ and $\delta\beta$ images simultaneously, we apply a scaling factor ϵ to the image $\delta\beta$ to balance the updates of the two images. For the following synthetic examples, we use $\epsilon = 1$; for the field data example, we estimate ϵ by comparing the RMS values of gradients in the first iteration of independent inversions for $\delta\alpha$ and $\delta\beta$.

4.3 Examples

We show the results of our elastic LSRTM method using three datasets. First, we run an inversion with a simple synthetic layered model, and we analyze the relationships of model perturbations and elastic reflections. Second, we test the method using a more complex model. We use the elastic Marmousi model to generate perturbation models, background models, and a two-component dataset. Finally, we apply our method to a real 2D OBC dataset and compare the elastic RTM and LSRTM images.

4.3.1 Layered model

We use a simple example to demonstrate the algorithms for elastic migration. Each of the α and β models contains one horizontal reflector, but the two reflectors are at different depths, as shown in Figures 4.1(a) and 4.1(b). We generate 30 two-component shot gathers using a vertical displacement source with a 30Hz peak frequency Ricker wavelet. Figures 4.2(a)–4.2(f) show the x- and z-component snapshots of a wavefield with the source

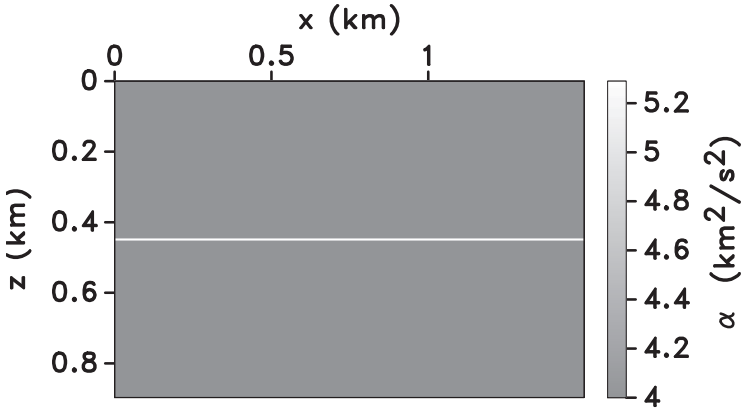

(a)

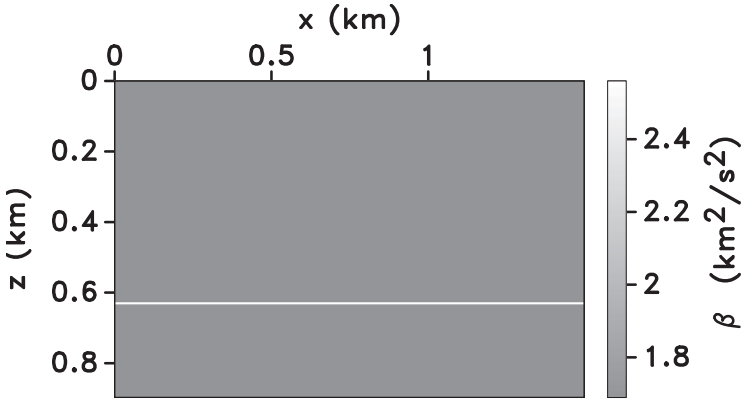

(b)

Figure 4.1: Synthetic layered model example. (a) α model with a horizontal reflector at $z = 0.45$ km, and (b) β model with a horizontal reflector at $z = 0.62$ km.

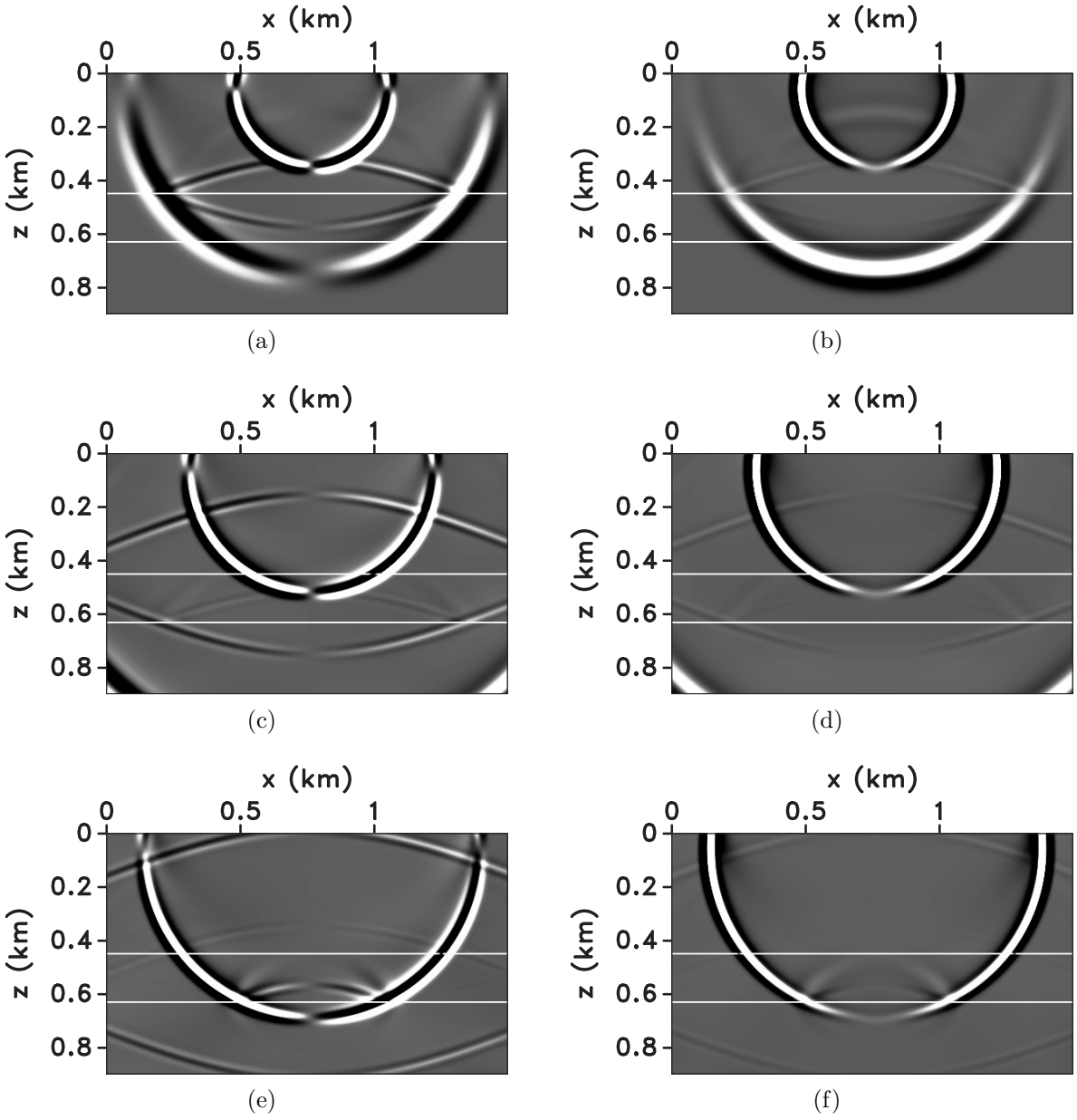

Figure 4.2: Synthetic layered model example. Snapshots of an elastic wavefield, for a source at coordinates $(0.76, 0.06)$ km: (a) x- and (b) z-components of the wavefield at $t = 0.2$ s; (c) x- and (d) z-components of the wavefield at $t = 0.3$ s; (e) x- and (f) z-components of the wavefield at $t = 0.4$ s. Two horizontal lines indicate the locations of reflectors in α and β models. P waves generate reflections only at the top reflector; S waves generate reflections only at the bottom reflector;

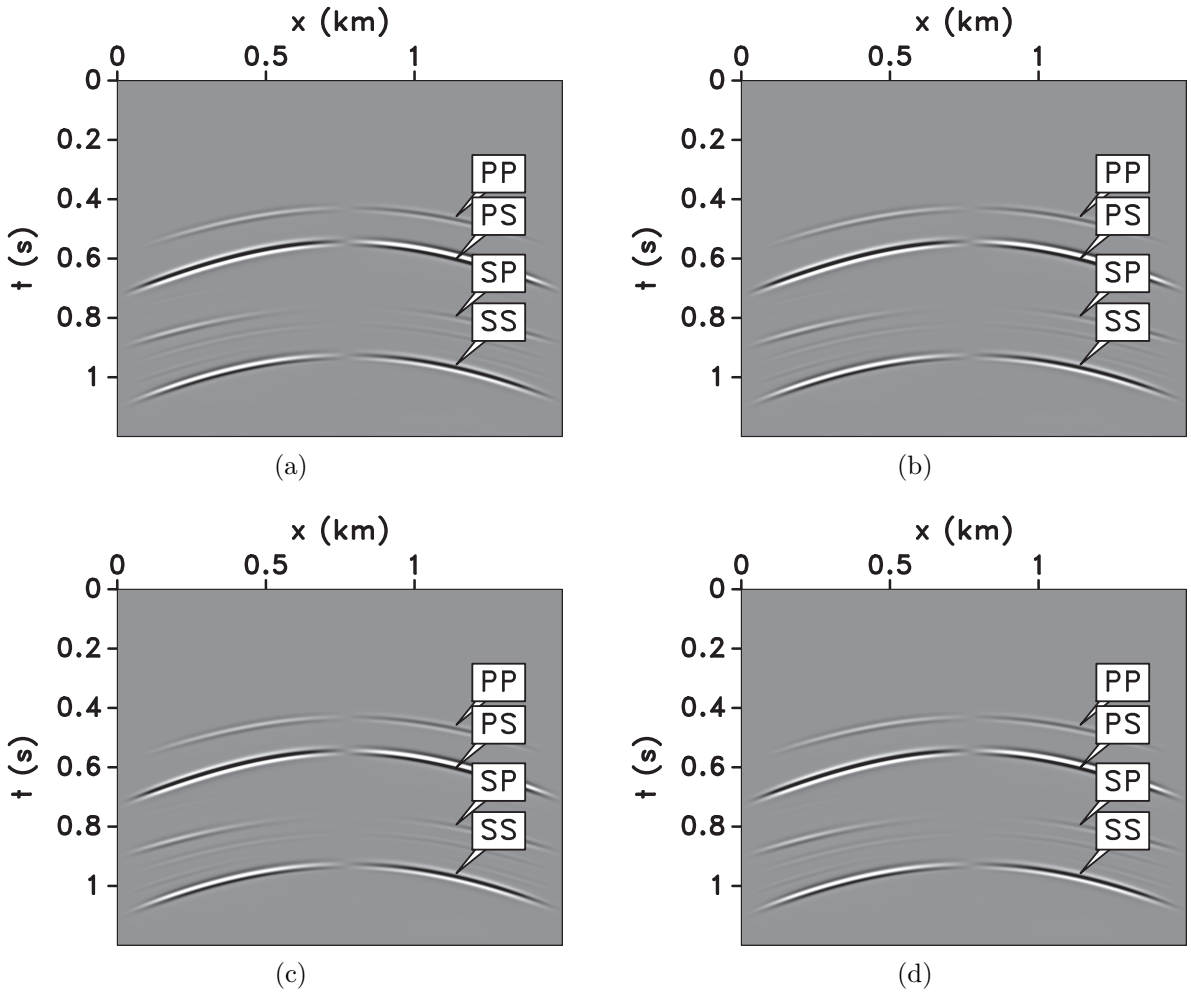

Figure 4.3: Synthetic layered model example. For the source at $(0.76, 0.06)$ km, (a) x- and (b) z-components of the recorded data (c) x- and (d) z-components of the predicted data using the inverted model. The direct arrivals are removed in the shot gathers. Note that the predicted data match the recorded data in both phase and amplitude.

at $(0.76, 0.06)$ km. The P wave generates reflections at the reflector in the α model, but not at the reflector in the β model. Similarly, the S wave generates reflections at the reflector in the β model, but not at the reflector in the α model. We also observe internal multiples that bounce between the two reflectors. The x- and z-components of this shot gather after direct wave removal are shown in Figures 4.3(a) and 4.3(b), respectively. Note the four strong arrivals which are, from top to bottom, PP, PS, SP, and SS reflections. Using the perturbation imaging condition (equation 4.7), we obtain the perturbation images for $\delta\alpha$ and $\delta\beta$ shown in Figures 4.4(a) and 4.4(b), respectively. Notice that additional reflectors appear in both $\delta\alpha$ and $\delta\beta$ images, and these reflectors are generated by fake modes in the constructed receiver wavefield.

Figures 4.4(c) and 4.4(d) are the LSRTM images after 10 iterations. Compared to the RTM images (Figures 4.4(a) and 4.4(b)), the artifacts in the LSRTM images are attenuated. Moreover, the peak values of the LSRTM images at $x = 0.6$ km are closer to the amplitudes of the true perturbation compared to the values of the RTM images. Therefore, LSRTM improves elastic imaging with true amplitude information and fewer artifacts, including artifacts caused by the nonphysical modes.

4.3.2 Marmousi model

The Marmousi-II model (Martin et al., 2006) is fully elastic, which supports not only compressional waves, but also shear waves and converted waves. The model simulates hydrocarbon reservoirs that dramatically decrease the value of α, but slightly increase the value of β . Figures 4.5(a) and 4.5(b) show the background model for α and β, respectively; both models contain a homogeneous layer at the top. Figures 4.6(a) and 4.6(b) show the corresponding true perturbation models for $\delta\alpha$ and $\delta\beta$, respectively, which are inconsistent in reservoir areas, e.g., only the $\delta\alpha$ model shows a reflector with a negative value at $(2, 0.4)$ km. This inconsistency poses a challenge for elastic LSRTM, e.g. if the inversion allows a leakage between model parameters.

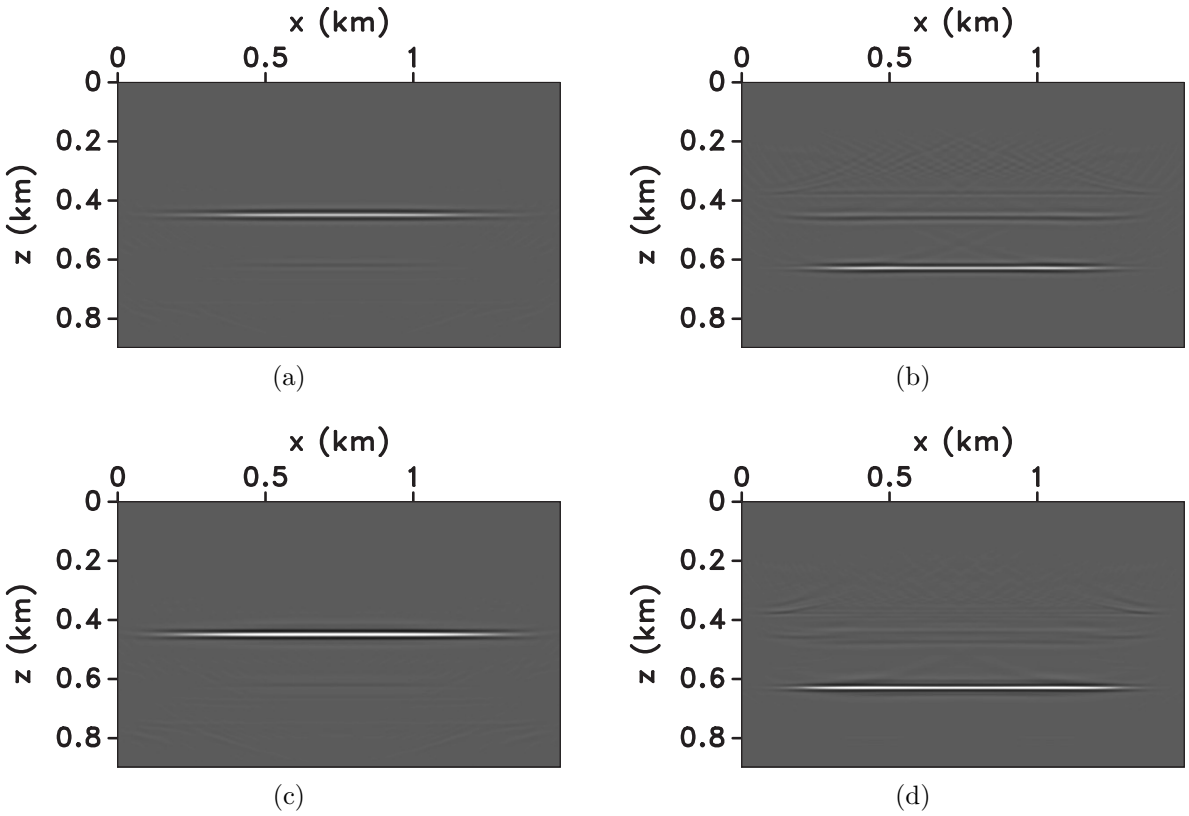

Figure 4.4: Synthetic layered model example. (a) $\delta\alpha$ and (b) $\delta\beta$ images after first iteration. In addition to the event at the correct depth, there are two strong horizontal events in the $\delta\beta$ image, which are crosstalk artifacts. (c) $\delta\alpha$ and (d) $\delta\beta$ images after 10 iterations. Compare to the $\delta\alpha$ and $\delta\beta$ images after the first iteration, the artifacts have been attenuated.

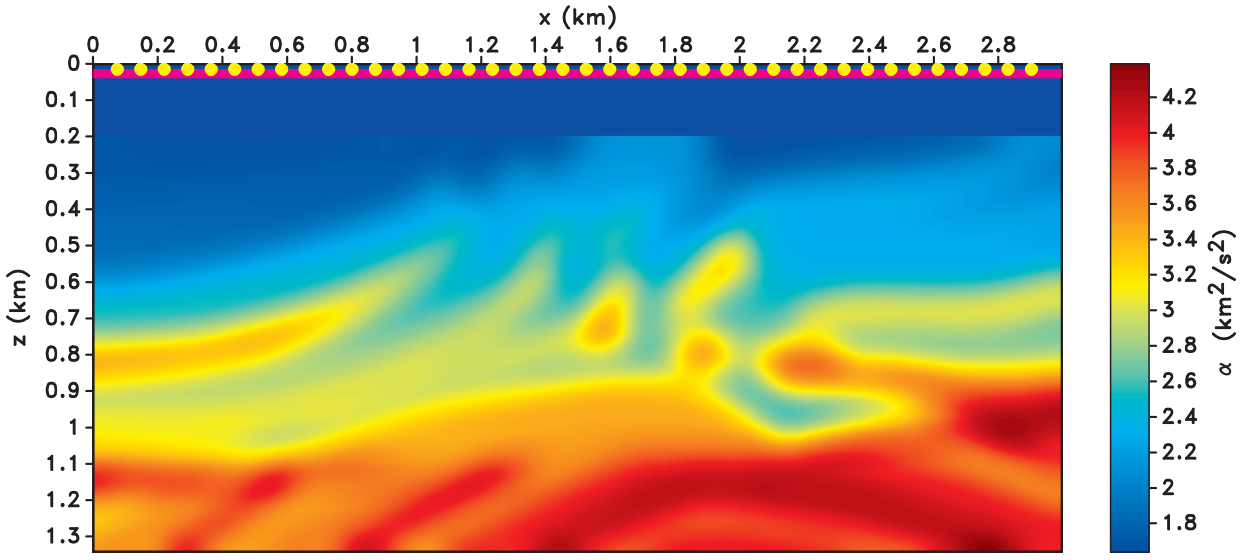

(a)

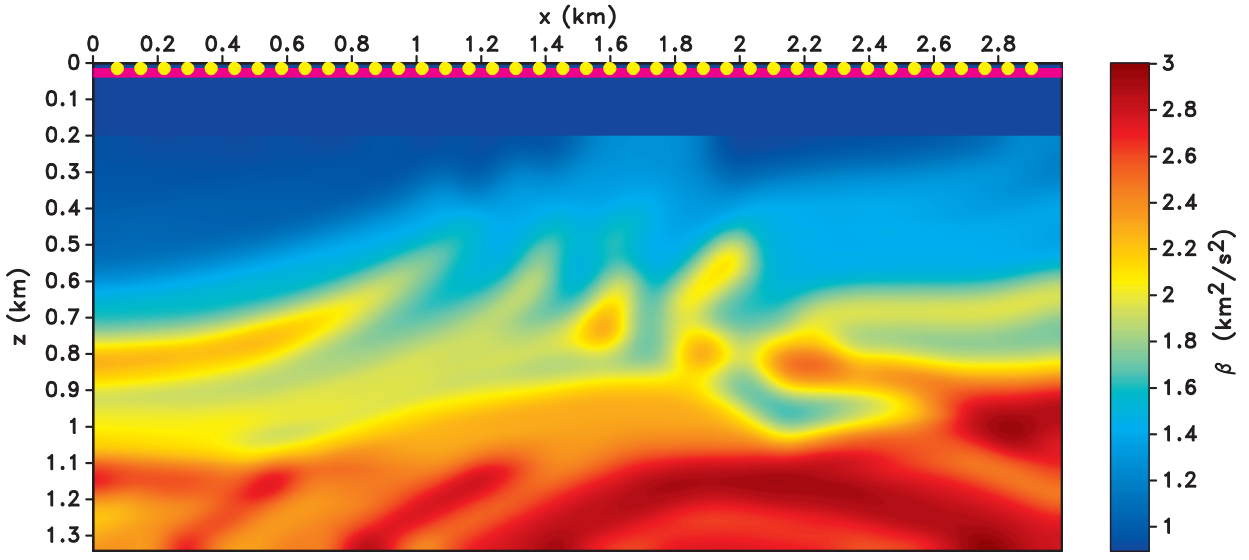

(b)

Figure 4.5: Synthetic Marmousi model example. Background (a) α and (b) β models. The receivers are at depth $z = 0.025$ km, and the sources are at depth $z = 0.013$ km. The top layer is homogeneous for both background models.

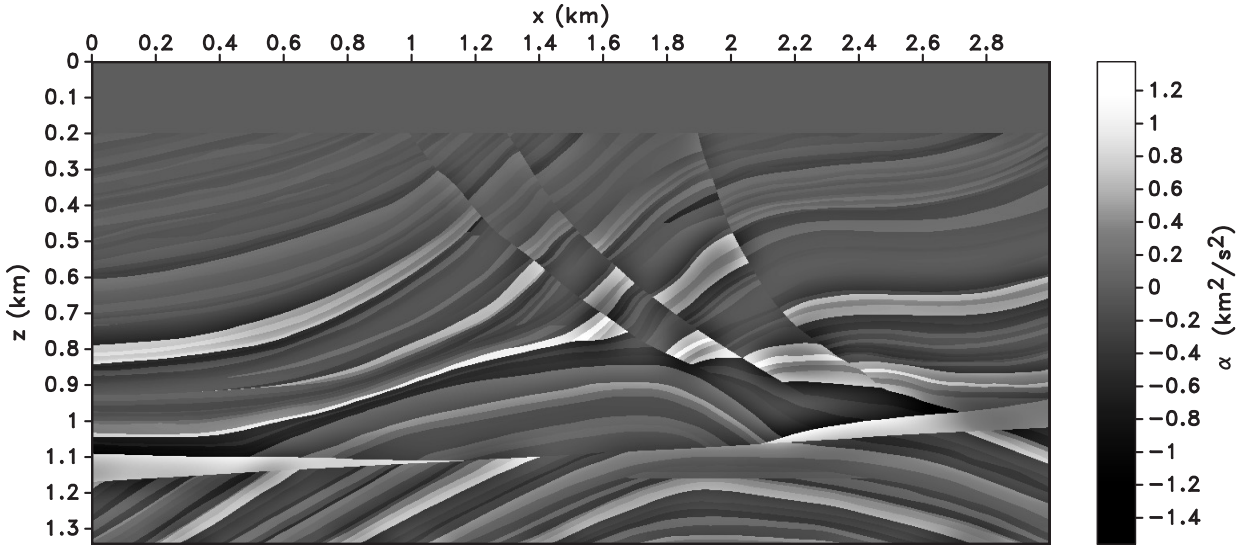

(a)

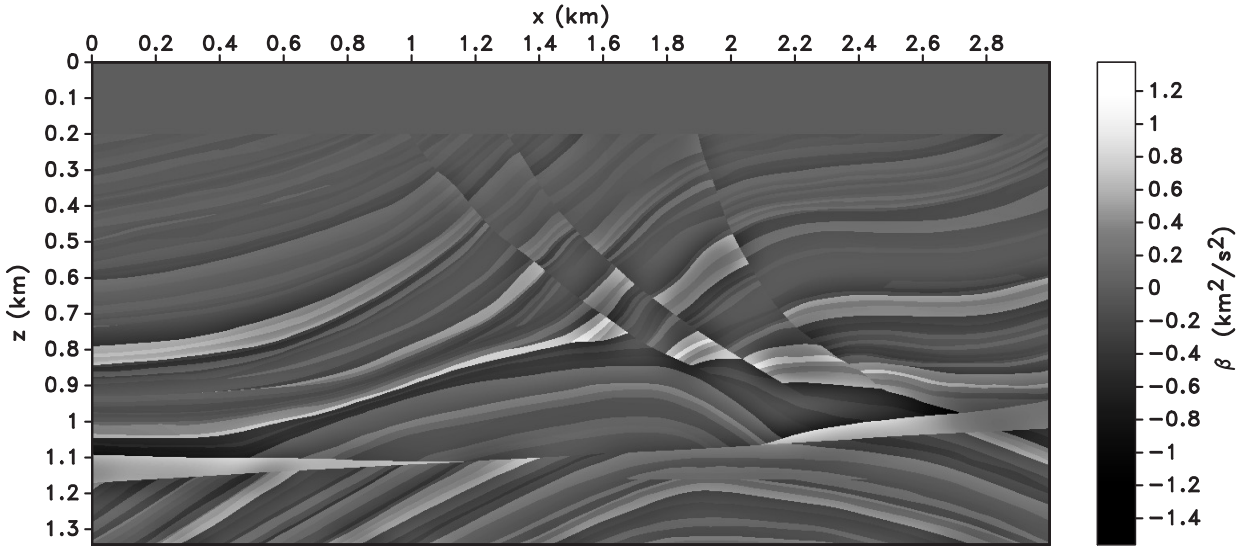

(b)

Figure 4.6: Synthetic Marmousi model example. True (a) $\delta\alpha$ and (b) $\delta\beta$ perturbation models. The perturbation models are not identical, e.g., a reflector with negative value at $(2, 0.4)$ km is presents only in the $\delta\alpha$ model.

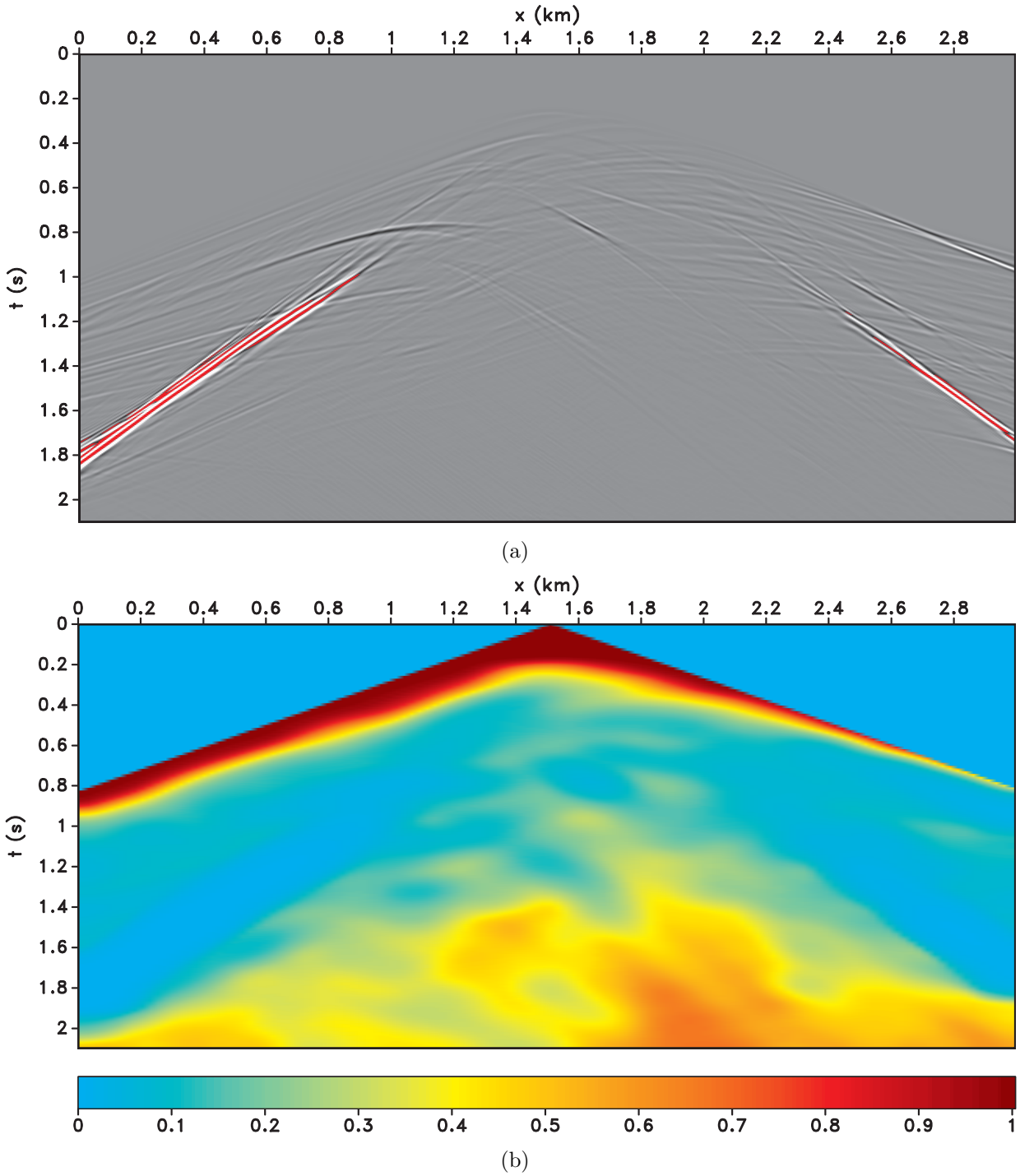

Figure 4.7: Synthetic Marmousi model example. For the source location at $(1.54, 0.013)$ km, (a) z-component of one shot gather. The highlighted arrival is the reflection from the bottom of the homogeneous layer, and its amplitude is much stronger than other arrivals in the recorded data. (b) The data weighting function generated from the recorded data. The same weighting function is applied to horizontal and vertical components of the shot gather.

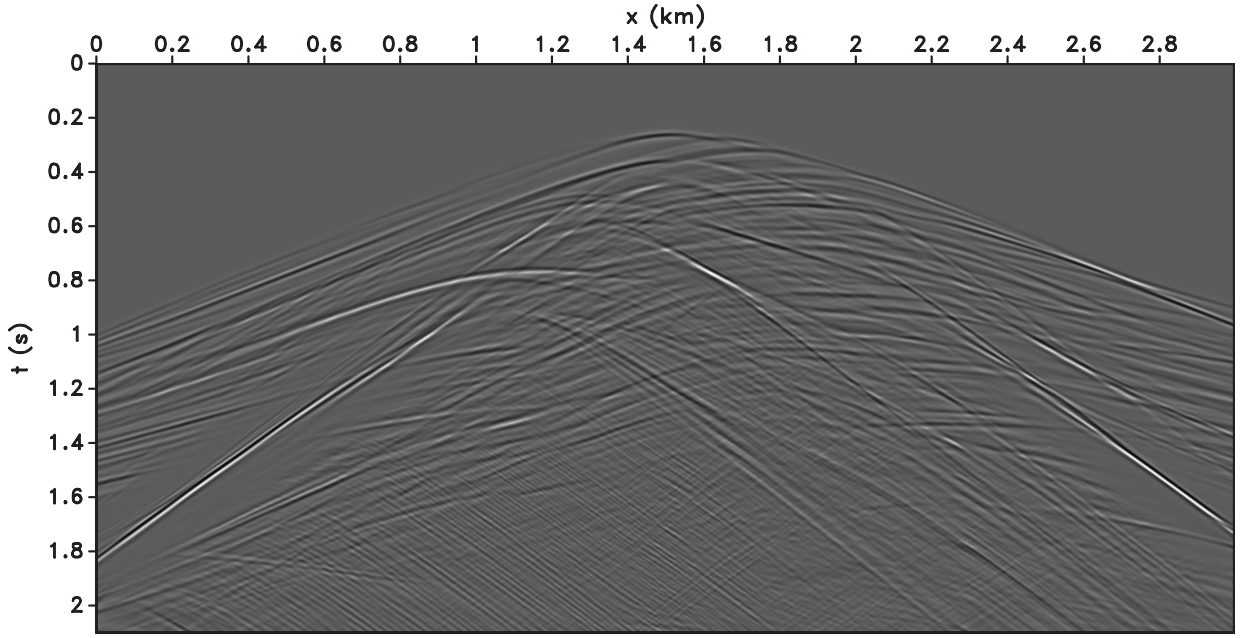

Figure 4.8: Synthetic Marmousi model example. For the source location at $(1.54, 0.013)$ km, z-components of the weighted shot gather. Note that the amplitudes of all arrivals are more balanced compared to Figure 4.7(a).

We model 40 shots evenly spaced on the surface using a displacement source with a 30Hz peak frequency Ricker wavelet. The horizontal and vertical components of the source function have the same amplitude in order to generate strong shear waves. The receiver spread is fixed for all shots and spans from 0 to 3.0 km with a 5 m sampling.

The recorded data are modeled according to equation 4.8. The z-component of one shot gather with the source location at $(1.54, 0.013)$ km is shown in Figure 4.7(a). The arrival with high amplitude is the reflection from the bottom of the homogeneous layer, and its amplitude is much stronger than other arrivals in the recorded data. Thus this arrival generates strong artifacts in the computed image, and the inversion mostly focuses on generating an image that best matches these strong arrivals, instead of the late arrivals with weaker amplitudes. In order to obtain a more uniform update using all arrivals, we use the data weighting term $\mathbf{W}$. The data weighting matrix is the inverse of the envelope of the recorded data, which weights down the strongest arrivals. We also apply a smoothing

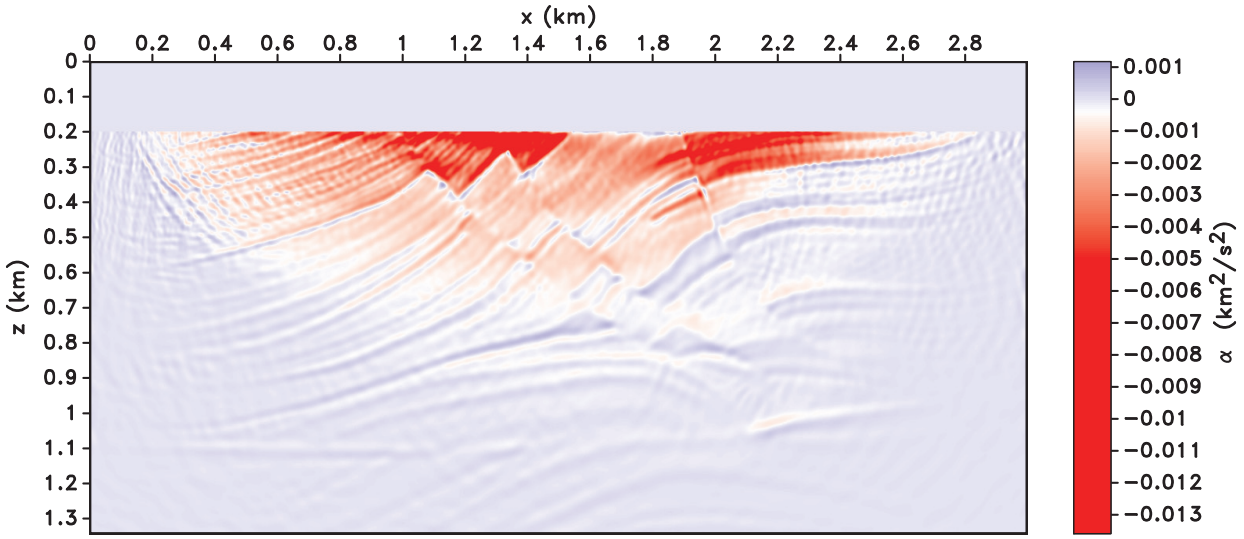

(a)

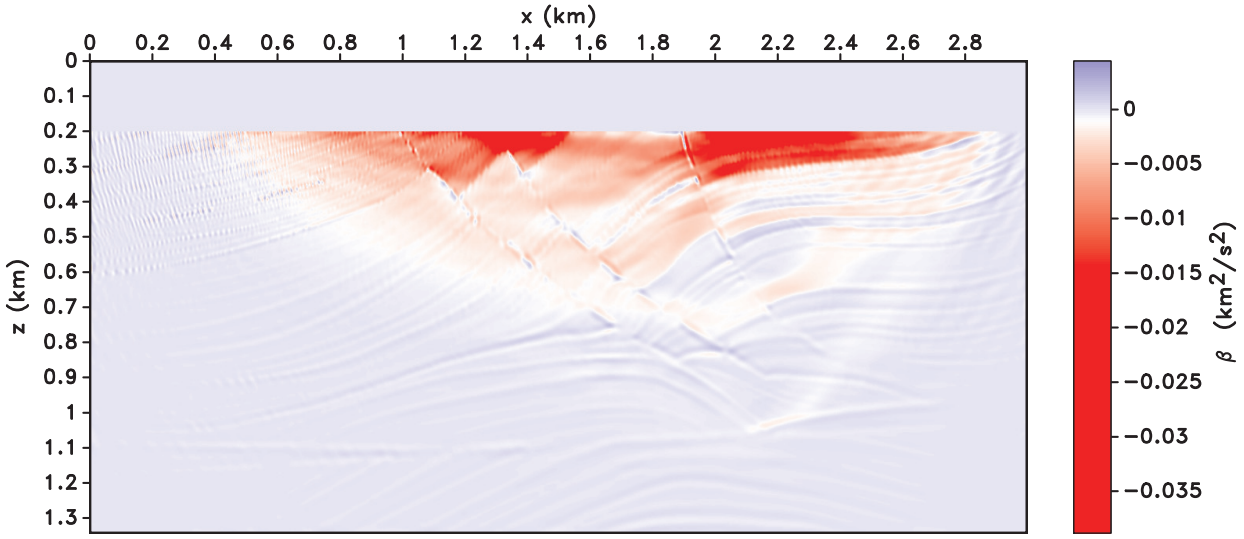

(b)

Figure 4.9: Synthetic Marmousi model example. (a) $\delta\alpha$ and (b) $\delta\beta$ RTM images with illumination compensation based on the source wavefield.

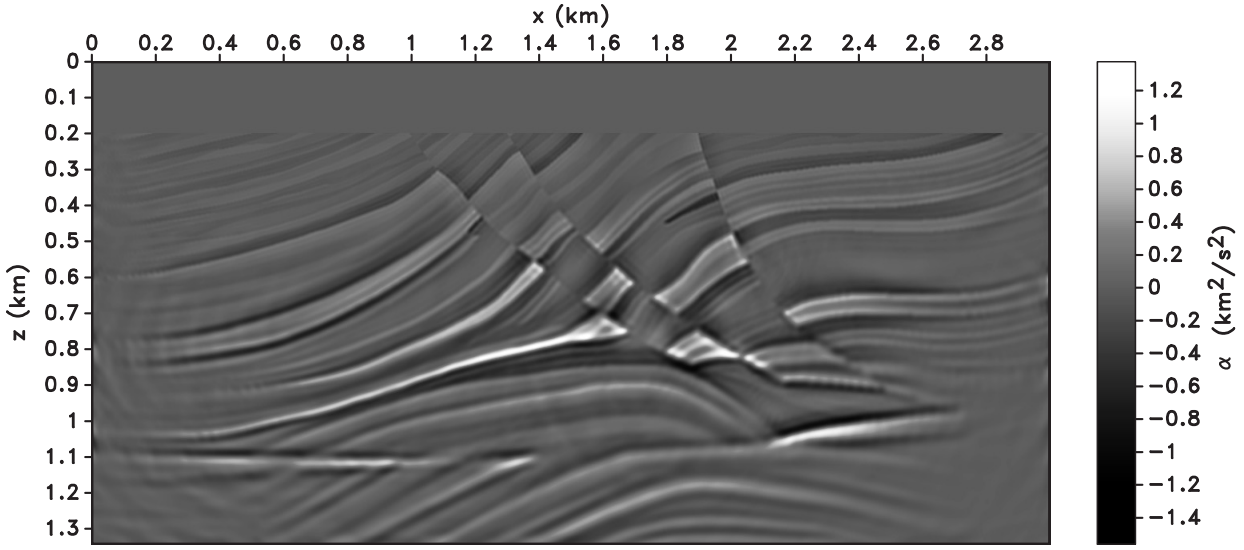

(a)

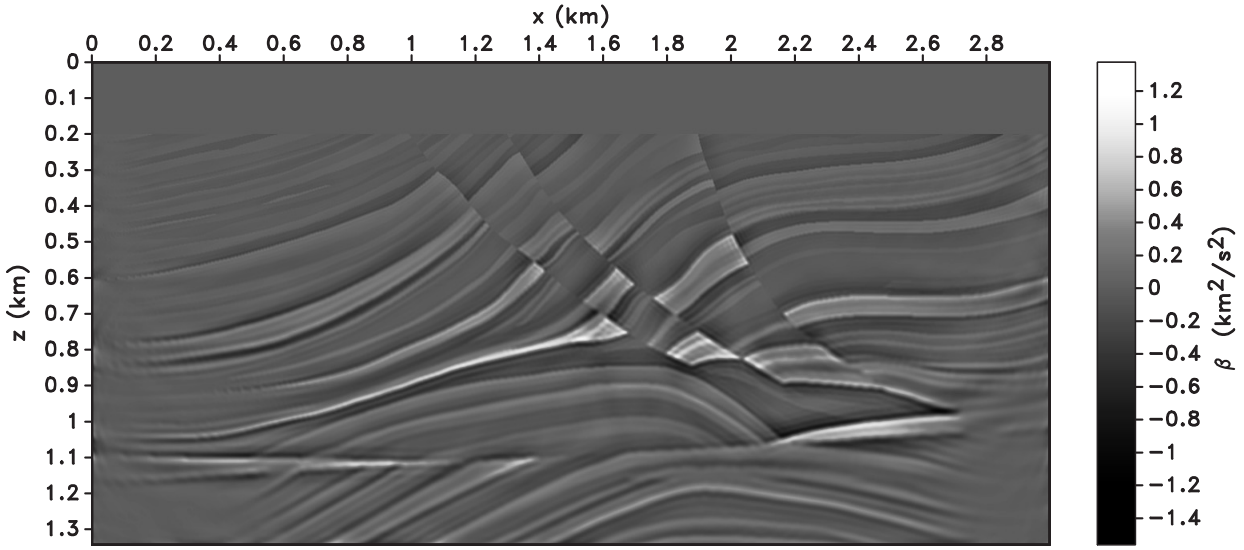

(b)

Figure 4.10: Synthetic Marmousi model example. Updated (a) $\delta\alpha$ and (b) $\delta\beta$ images after 100 iterations. Note that the reservoir near coordinates $(2.0, 0.4)$ km is correctly recovered in the updated $\delta\alpha$ image, without any leakage in the updated $\delta\beta$ image.

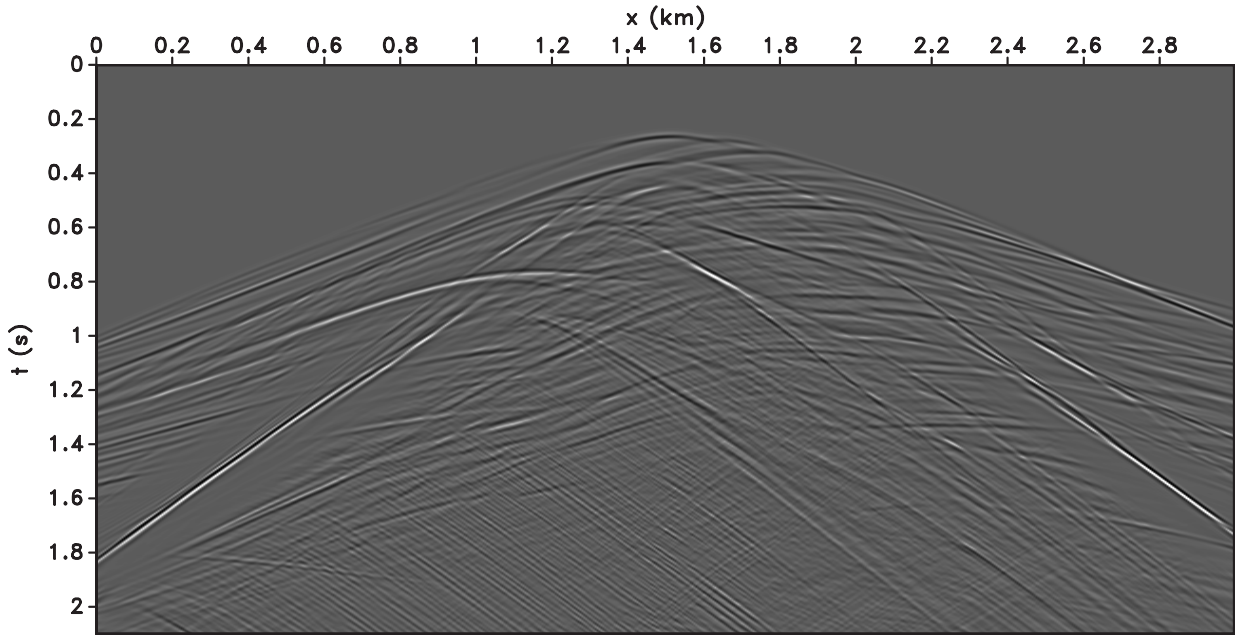

(a)

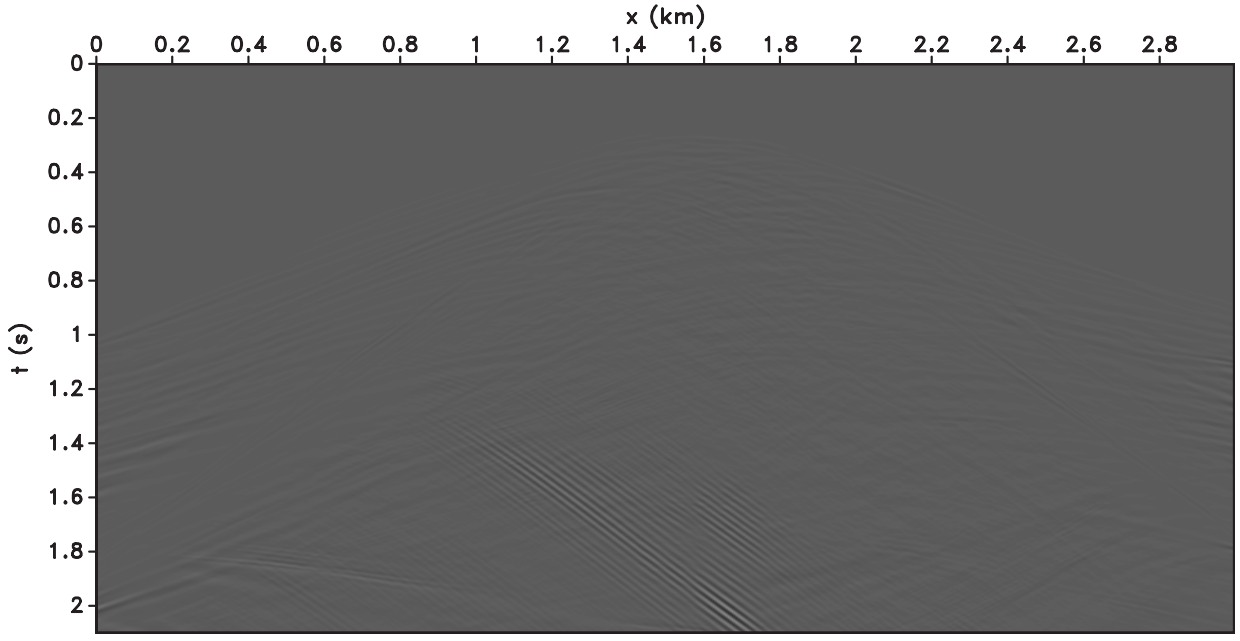

(b)

Figure 4.11: Synthetic Marmousi model example. The z component of (a) the predicted shot gather and (b) the data difference using the updated models (Figures 4.10(a) and 4.10(b)).

operator in the data space to the weighting function to avoid discontinuity along the time and space axes. Figure 4.7(b) shows the weighting function in the data domain, which we compute from the shot gather Figure 4.7(a). Figure 4.8 is the z-component of the weighted shot gather, and Figure 4.11(b) is the z-component of data difference. Compared to the original recorded data (Figure 4.7(a)), the amplitudes of the arrivals in the weighted data (Figure 4.8) are more balanced.

Figures 4.9(a) and 4.9(b) show the RTM images for $\delta\alpha$ and $\delta\beta$, respectively. We observe that the events for the shallow reflectors in both models have stronger amplitudes compared to those of the deeper reflectors, and strong backscattering is present due to the sharp interfaces in the background model. We apply an illumination compensation based on the source wavefield to the RTM images and LSRTM gradients, in order to balance nonuniform data coverage.

The LSRTM images after 100 iterations, when the convergence curve, representing the objective function, becomes flat, are shown in Figures 4.10(a) and 4.10(b). The updated image for $\delta\beta$ has higher resolution than $\delta\alpha$ because, in general, S waves have shorter wavelengths than P waves, and we do not consider attenuation in this experiment. The updated images are consistent with the true perturbation images (Figures 4.6(a) and 4.6(b)). For example, only the $\delta\alpha$ image (Figure 4.10(a)) contains the reflector with negative value at $(2, 0.4)$ km, which corresponds to a hydrocarbon reservoir in the true model that only decreases the value of α.

Figure 4.11(a) shows the z-component of the predicted shot gather after 100 iterations, respectively, using the updated images (Figures 4.10(a) and 4.10(b)). The same weighting functions are applied to the two gathers. The amplitudes of all arrivals in the data residual after inversion are small, i.e., for most arrivals, the predicted data match the recorded data in both phase and amplitude. Because we use Born data generated using the same wave equation as the recorded data, the amplitudes of the LSRTM images match well the true perturbation models. In practice, with errors in the background models and approximations

of the wave equation, we may not obtain true-amplitude LSRTM images; however, the relative amplitudes of the reflectors can still be estimated correctly, which is beneficial for reservoir characterization.

4.3.3 Volve OBC data

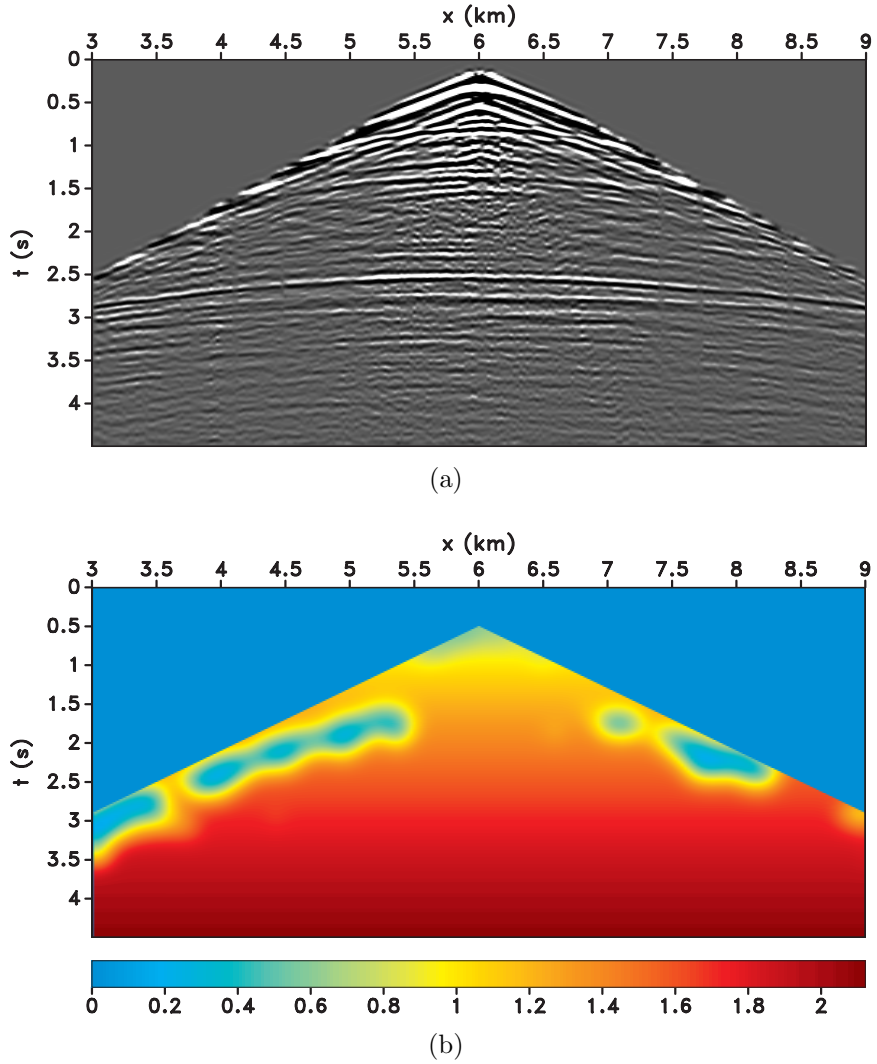

(a)

(b)

Figure 4.12: Volve data example. (a) one PP shot gather at $x = 6$ km, which is assumed to be a vertical displacement gather. (b) Weighting matrix for this shot gather. The weighting function mutes the direct arrivals, attenuates the predicted shear waves, and boosts later reflections.

We apply our elastic LSRTM method to data from the Volve field, located in the Norwegian North Sea. The Volve field has an average water depth of 90 m, and the field is

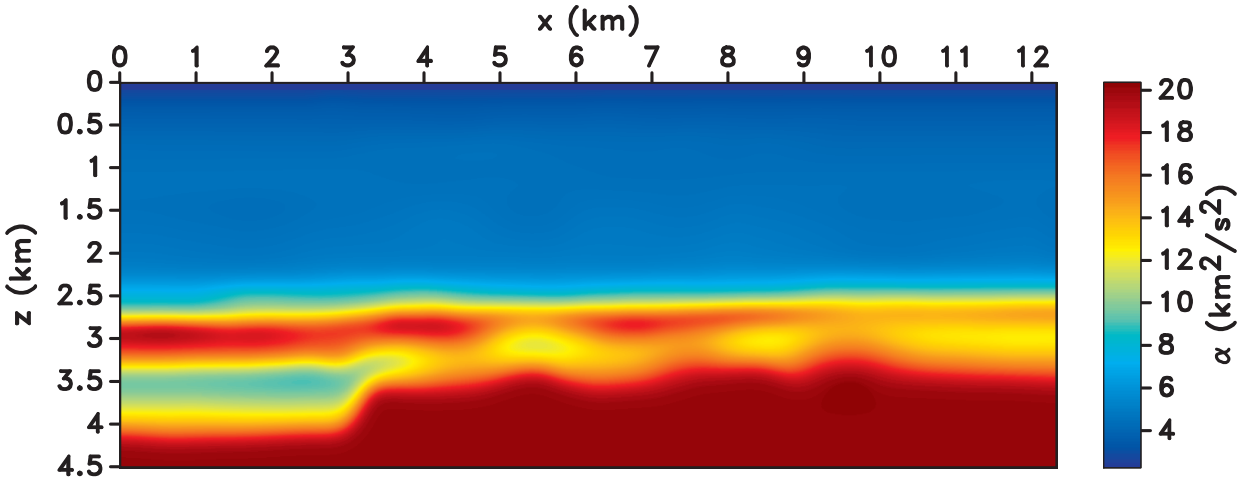

(a)

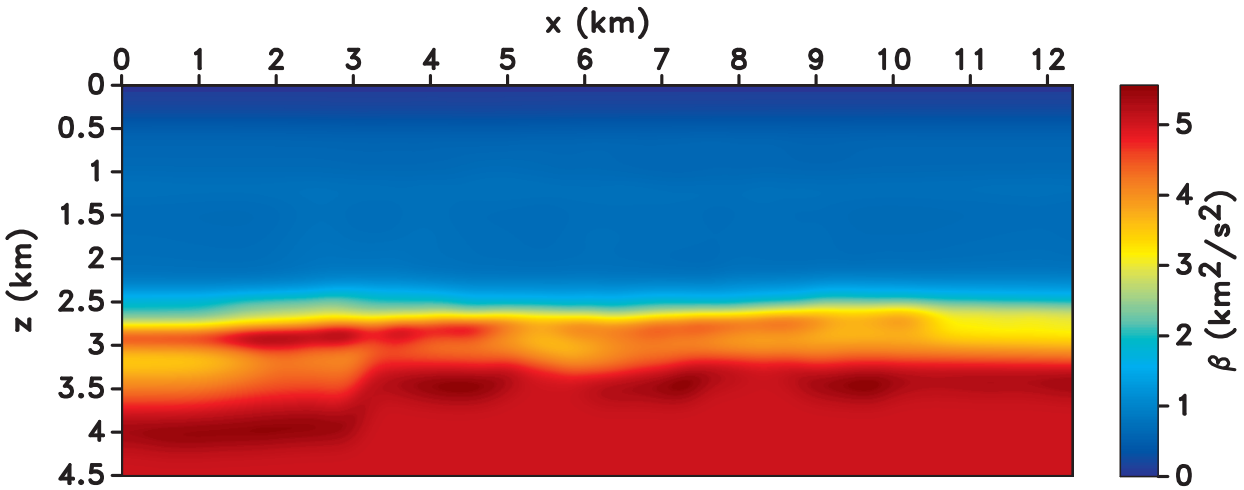

(b)

Figure 4.13: Volve data example. Background (a) α and (b) β models. The top water layer is from $z = 0$ to 90 m.

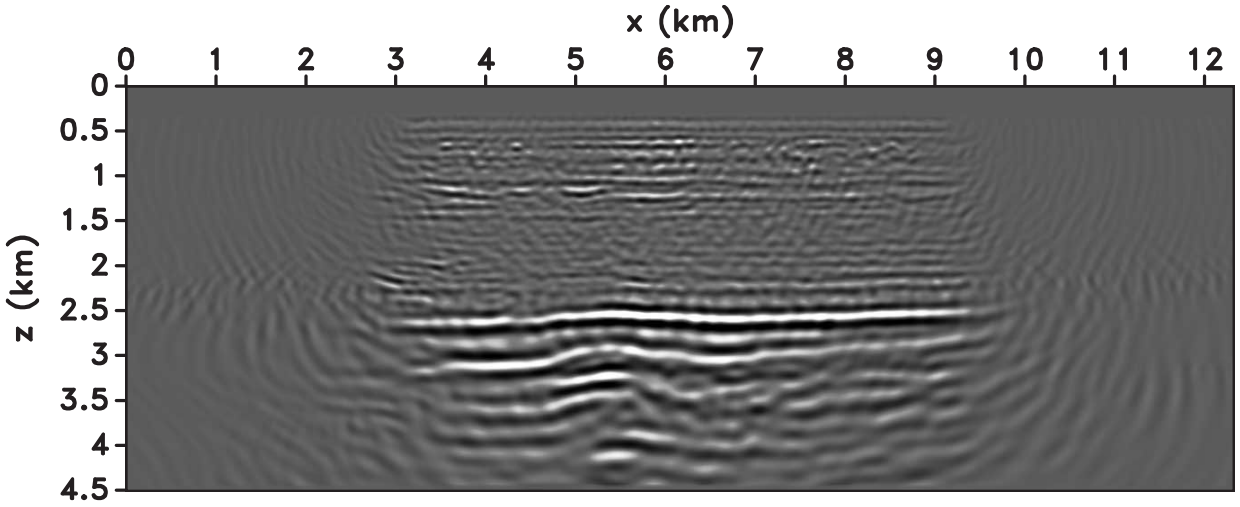

(a)

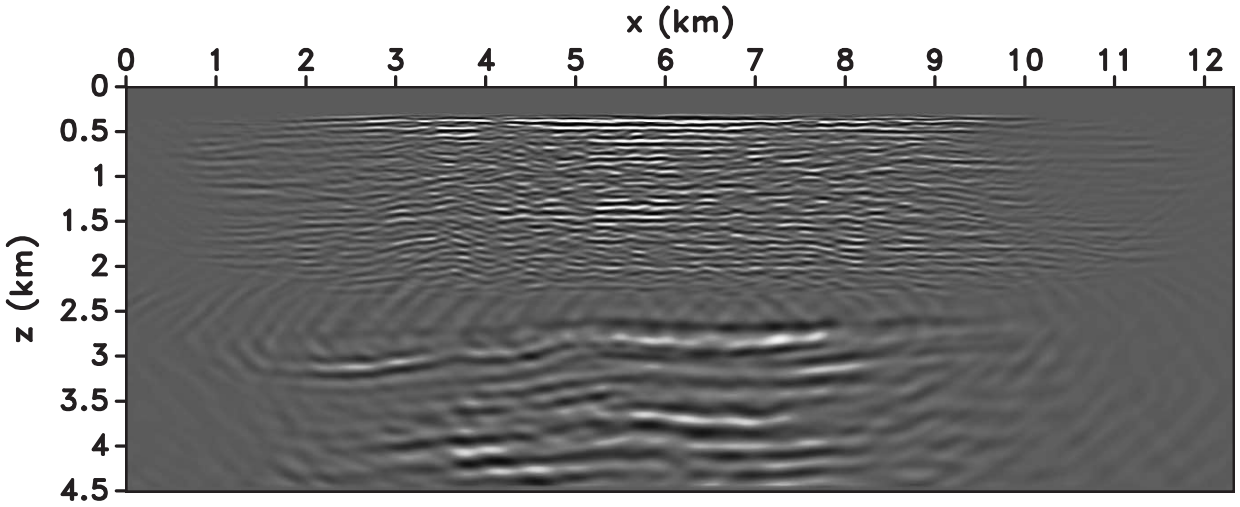

(b)

Figure 4.14: Volve data example. (a) $\delta\alpha$ and (b) $\delta\beta$ RTM images. The chalk layer is from $z = 2.5$ to 3.0 km. Note that the events above the chalk layer in the $\delta\beta$ are weak and discontinuous.

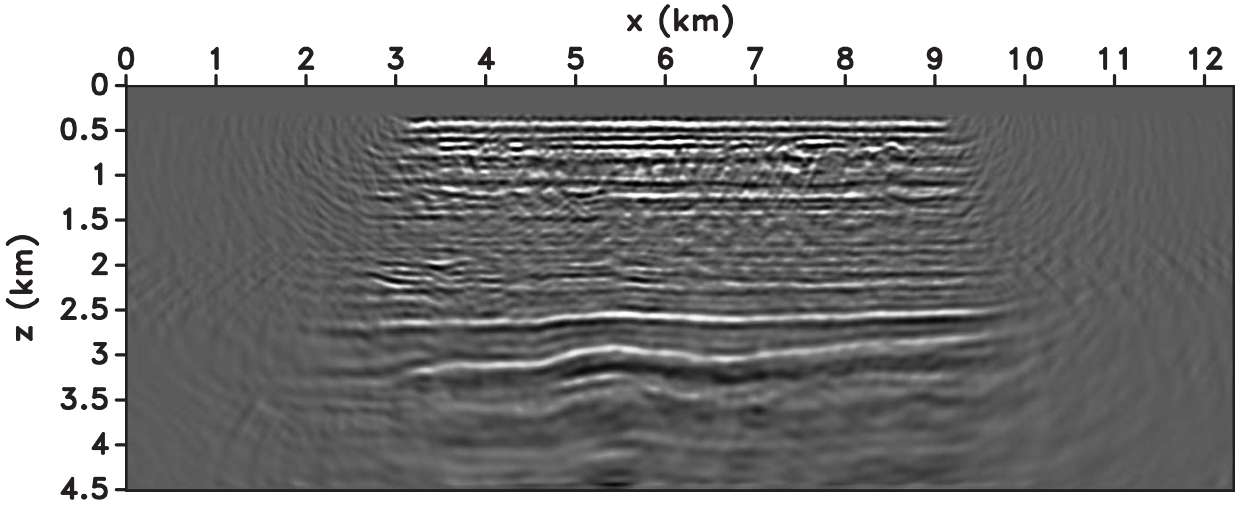

(a)

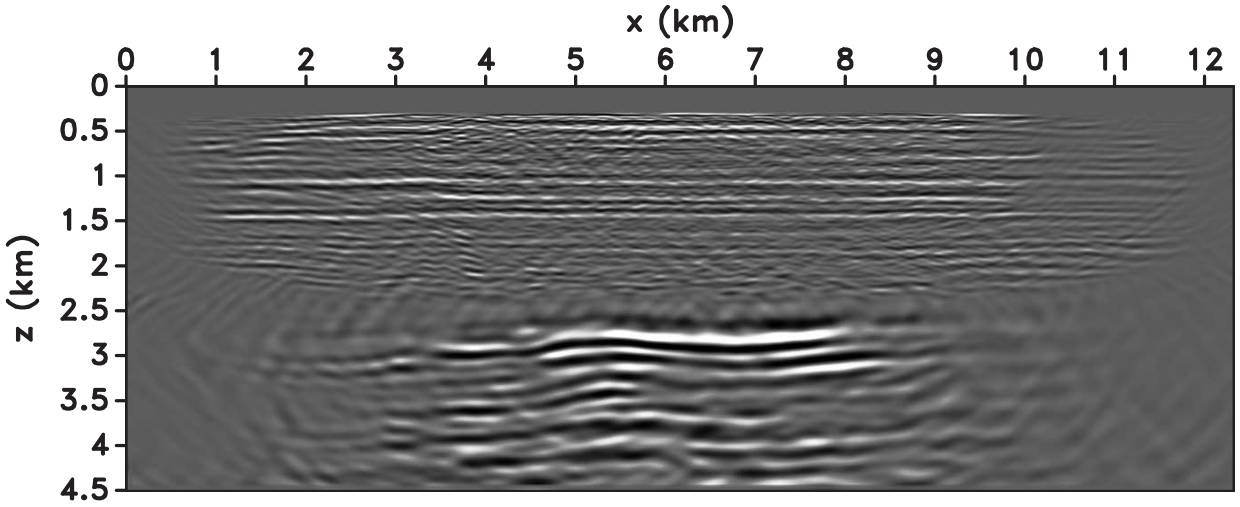

(b)

Figure 4.15: Volve data example. (a) $\delta\alpha$ and (b) $\delta\beta$ LSRTM images after 12 iterations. Compared to the RTM images (Figure 4.14(a) and 4.14(b)), the LSRTM images have higher resolution and better balanced amplitudes. The reflectors above 1.5 km appear in the $\delta\beta$ image after inversion with larger lateral extent along the x-direction than those in the $\delta\alpha$ image.

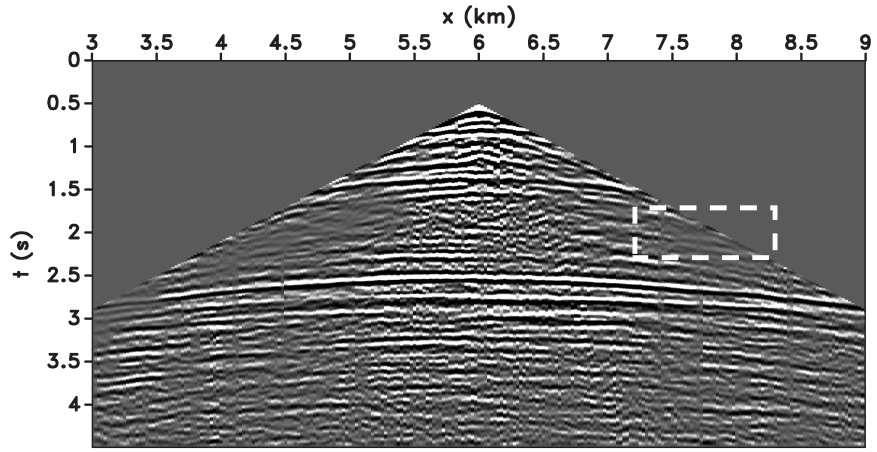

(a)

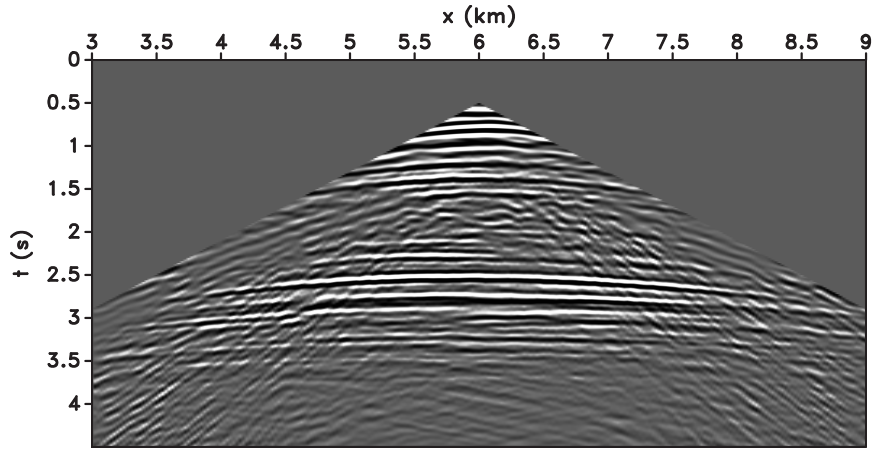

(b)

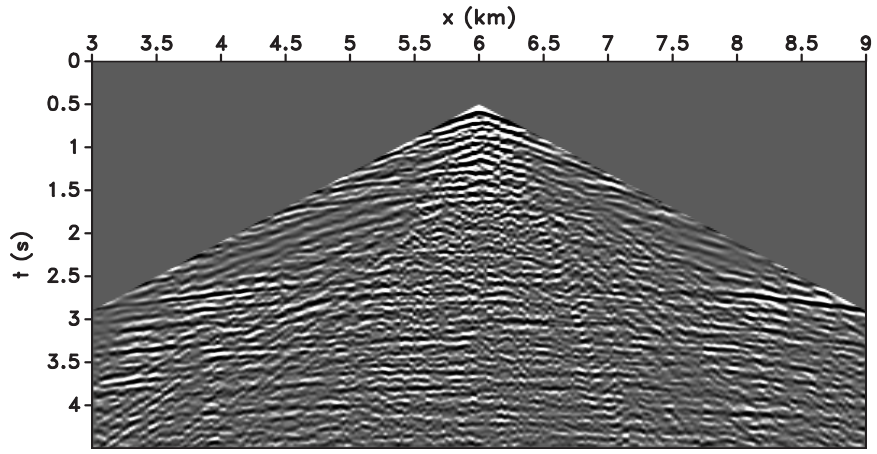

(c)

Figure 4.16: Volve data example. The weighted (a) observed data, (b) predicted data, and (c) data residual after 12 iterations. The predicted data accurately reproduces the dominant reflection energy seen in the observed data. The data residual contains mostly noise and some weaker reflection events.

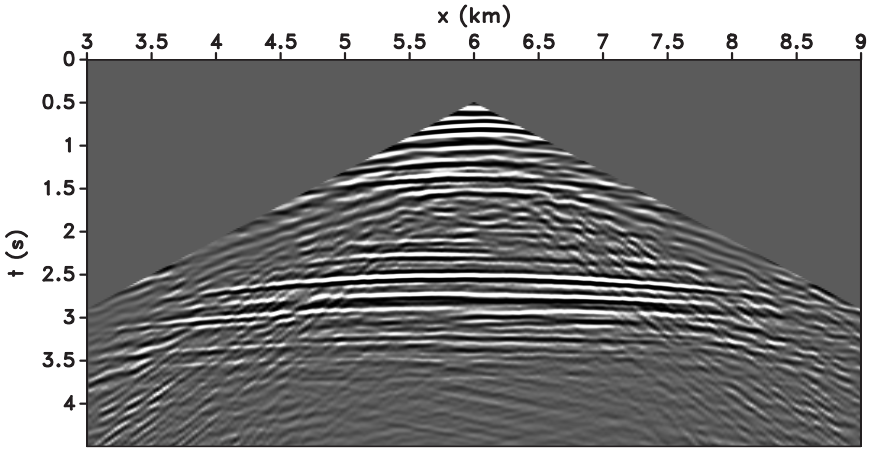

(a)

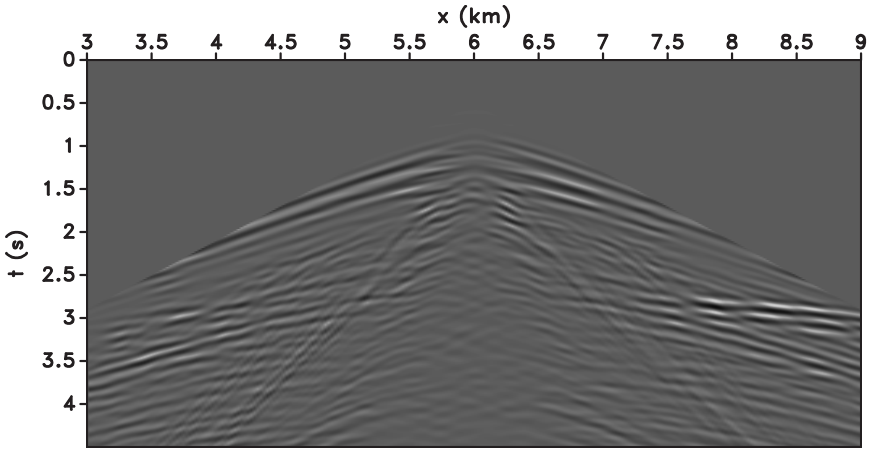

(b)

Figure 4.17: Volve data example. Predicted shot gathers using only (a) $\delta\alpha$ and (b) $\delta\beta$ LSRTM images. The $\delta\alpha$ image predicts most of the arrivals in the observation with correct amplitudes. The $\delta\beta$ image compensates for the AVO effect of the PP reflections at far offsets (e.g., $x = 8.5$ km, $t = 3.0$ s).

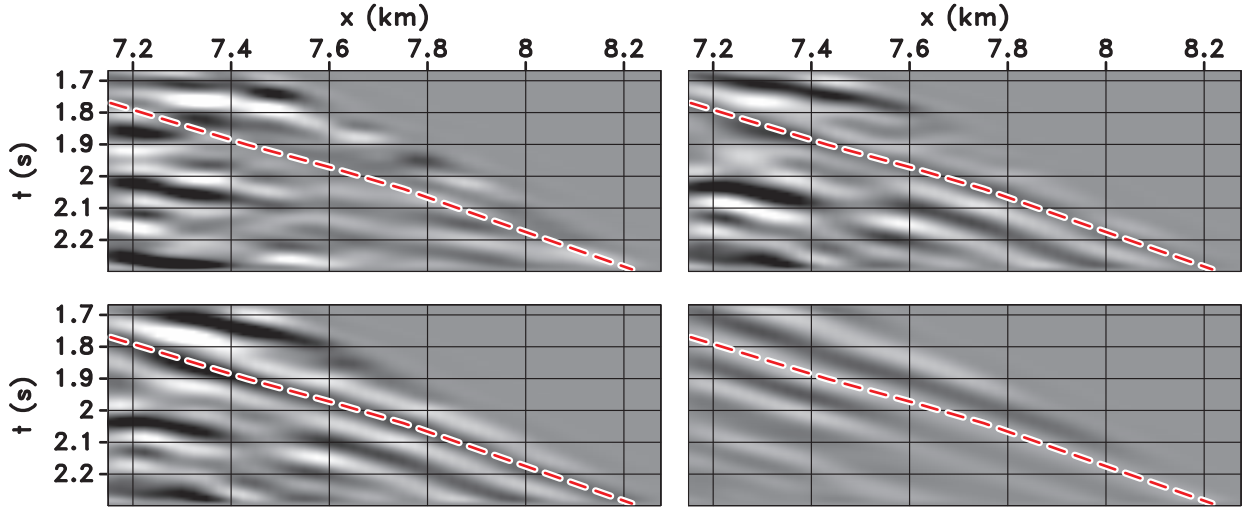

Figure 4.18: Volve data example. (b) Zoomed views of the weighted observation (top left panel), prediction computed using both $\delta\alpha$ and $\delta\beta$ images (top right panel), prediction computed using only $\delta\alpha$ image (bottom left), and prediction computed using only $\delta\beta$ image (bottom right) . A different clip from the previous plots (Figures 4.16(a)-4.17(b)) is applied to the zoomed-in panels for display. The box in Figure 4.16(a) indicates the zoomed in area. The dashed line highlights the same arrival in each panel. The $\delta\alpha$ and $\delta\beta$ images predict the same arrival with opposite polarities, so that the total prediction agrees with the observation.

characterized by a complex subchalk reservoir (Szydlik et al., 2007). We are provided with pre-processed PP and PS data, recorded in an acquisition geometry consisting of 12 parallel receiver lines each with 240 receivers. However, because PP and PS data typically are intended for independent PP and PS migrations, they are not well suited for our inversion algorithm, which requires recorded displacement data. For our test, we use a 2D line extracted from only the PP dataset, which we treat as the vertical component of the displacement vector. We bandpass the data between 0 and 15 Hz to attenuate high frequency noise and reduce the computational cost, and we apply a gain in time to compensate for 3D effects. Figure 4.12(a) shows one shot gather at $x = 6$ km, with the bandpass filter and 3D compensation applied. The arrivals at 2.5-3.0 s are PP reflections from the chalk layer.

Additional processing is required to condition the data for elastic LSRTM. Because shear waves were purposely attenuated in the provided PP data in preparation for acoustic imaging, we use a data weighting function (Figure 4.12(b)) for elastic imaging to attenuate predicted

shear wave arrivals that otherwise would result in a large data misfit. This data weighting function also incorporates a mask to mute direct arrivals, as well as an additional weight that boosts later arrivals in order to balance reflector amplitudes in the migration images.

The background α and β models are shown in Figures 4.13(a) and 4.13(b), respectively, and are computed from the provided P and S velocity models. We apply additional vertical and horizontal smoothing to the original models so that the background models follow our assumption of homogeneous or slowly-varying elastic media. A source wavelet for migration is estimated from the zero-offset data by matching the observed and predicted data using the background models. Using these models and an estimated source wavelet, we compute the RTM images shown in Figure 4.14(a) and 4.14(b), in which we observe reflectors, as well as the migration artifacts.

For elastic LSRTM, we invert for $\delta\alpha$ and $\delta\beta$ images simultaneously. The scaling factor ϵ is 0.5, which is applied to $\delta\beta$ image to balance the updates of the two images. Figures 4.15(a) and 4.15(b) show the LSRTM images after 12 iterations, at which point the convergence curve becomes flat. Compared to the RTM images, the LSRTM images have higher resolution and better balanced reflector amplitudes. In addition, shallow reflectors in the LSRTM image for $\delta\beta$ (Figure 4.15(b)) are much more continuous and have larger lateral extent along the x-direction, for example, at $z = 1.0$ km and $z = 1.5$ km. After the inversion converges, some reflectors below $z = 3.5$ km in the α image are eliminated; however, they appear as strong and continuous reflectors in the $\delta\beta$ image. Figures 4.16(a) are 4.16(b) show the observed and predicted shot gathers at $x = 6$ km, respectively, and Figure 4.16(c) shows the data difference plotted on the same scale. The predicted data accurately reproduces the dominant reflection energy seen in the observed data, and the remaining residual in the data difference contains mostly noise and some weaker reflection events. Some of these reflections with steep slopes are predicted shear waves which are missing in the observed data. Other weak reflections in the data residual may be due to anisotropy of the field, which is not considered in our current implementation of the algorithm.

In order to evaluate the reflectors in the $\delta\alpha$ and $\delta\beta$ images, we generate the predicted shot gathers using $\delta\alpha$ and $\delta\beta$ LSRTM images individually. By comparing these shot gathers with the observed data (Figure 4.16(a)), we notice that the inverted $\delta\alpha$ image predicts most of the arrivals in the observation with correct amplitudes (Figure 4.17(a)). The reflections predicted by the $\delta\beta$ image (Figure 4.17(b)) are relatively weaker than those predicted by the $\delta\alpha$ image. Figure 4.17(b) shows mainly two types of arrivals, PP reflections with gentle slopes and converted-wave reflections with steep slopes. The amplitudes of the predicted PP reflections are relatively strong at far offset. This is to be expected because, according to Zoeppritz equation, the β model in general affects the amplitudes of PP reflections, especially at far offsets. For example, the events at $z = 2.5$-3.5 km in the $\delta\beta$ image compensate for the amplitudes of PP reflections at $z = 2.5$-3.0 s to match the observed data at far offsets.

Figure 4.18 shows enlarged views of data from within the dashed box in Figure 4.16(a): the top left panel shows the observed data, the top right panel shows data predicted using both the $\delta\alpha$ and $\delta\beta$ images, the bottom left panel shows data predicted using only the $\delta\alpha$ image, and the bottom right panel shows data predicted using only the $\delta\beta$ image. The dashed line in each panel marks the same arrival, and this arrival is one that was attenuated during pre-processing of the PP data. Notice that because the $\delta\alpha$ image predicts this arrival (shown in the bottom left panel), the $\delta\beta$ image tries to predict the same arrival but with opposite polarity (shown in the bottom right panel), so that the total prediction agrees with the observation. Had this (and other) arrivals not been removed from the observed data, we would expect the data predicted from the $\delta\alpha$ and $\delta\beta$ images, as well as the corresponding reflector amplitudes, to change accordingly. This is an illustration of how pre-processing can negatively affect the LSRTM.

We also test the inversion algorithm by using both PP data and PS data, which were treated as the vertical and horizontal components of the displacement vector, respectively. However, we were not able to predict both components with correct phases and amplitudes. We attribute this outcome to the fact that the data were pre-processed for independent PP

and PS imaging, and thus the arrivals in the PP and PS gathers might not be consistent with each other, in terms of phase and amplitude; therefore, this dataset does not fit our elastic LSRTM algorithm underlying assumptions, which requires vertical and horizontal displacement data, instead of separated PP and PS gathers.

4.4 Conclusions

We propose a method for elastic least-squares reverse time migration using a perturbation imaging condition. The images computed using our method represent perturbations of squared P and S velocities, and they do not suffer from polarity reversals, which usually characterizes conventional elastic images for converted waves. Both synthetic and field data tests of the perturbation imaging condition demonstrate that elastic LSRTM produces images with fewer migration artifacts and higher resolution compared to the corresponding RTM image. The field data example also shows the importance of proper pre-processing of the recorded data, which should provide the LSRTM algorithm with data consistent with the output of the Born modeling operator.

4.5 Acknowledgments

We thank the sponsors of the Center for Wave Phenomena, whose support made this research possible. We also thank Statoil ASA and the Volve license partners ExxonMobil E & P Norway and Bayerngas Norge AS, for the release of the Volve data. The views expressed in this paper are the views of the authors and do not necessarily reflect the views of Statoil ASA and the Volve field license partners. The reproducible numeric examples in this paper use the Madagascar open-source software package (Fomel et al., 2013) freely available from http://www.ahay.org.

CHAPTER 5

ELASTIC WAVEFIELD TOMOGRAPHY WITH PHYSICAL MODEL CONSTRAINTS

A paper published[8] in *Geophysics*

Yuting Duan[9,10] and Paul Sava[10]

Data-domain elastic wavefield tomography is an effective method for updating multiparameter elastic models that exploits much of the information provided by observed multicomponent data. However, poor illumination of the subsurface by compressional (P) and shear (S) waves often prevents reliable updates of model parameters. Moreover, differences in illumination, amplitude, and wavelength between P and S waves can distort the intrinsic physical relationships between the reconstructed model parameters. We propose a method for elastic isotropic wavefield tomography which explicitly constrains the relationship between P- and S-wave velocities. By incorporating a model constraint term in the objective function, we confine P and S velocity updates to a physical area defined by prior information, for example, by laboratory measurements or well logs. Examples demonstrate that this physical constraint yields models that are more physically plausible, compared to models obtained using only the data misfit objective function.

5.1 Introduction

Seismic tomography is a commonly used tool for building models of subsurface parameters from recorded seismic data. The various approaches to seismic tomography generally fall into two categories. The first is traveltime tomography, which seeks to match the traveltimes of recorded seismic data with those of synthetic seismic data simulated in a trial model by using ray tracing (Zhu et al., 1992; Zelt et al., 2006; Taillandier et al., 2009) or by

[8]Reprinted with permission of *Geophysics*, 2016, 81, No. 6, R447-R456.
[9]Author for correspondence.
[10]Center for Wave Phenomena, Colorado School of Mines, 924 16th Street, Golden, CO 80401.

solving a wave equation (Woodward, 1992; Schuster and Quintus-Bosz, 1993). However, models computed with traveltime tomography tend to have lower resolution, and may be less accurate when the subsurface contains complicated geologic structures that result in wavefield multipathing. The second category consists of methods for wavefield tomography, which use both the amplitude and phase information of recorded seismic data to invert for the subsurface parameter model. Although more expensive than traveltime tomography, wavefield tomography is more effective in recovering model parameters that are sensitive to waveform amplitudes (Tarantola, 1986; Mora, 1988; Pratt, 1999; Prieux et al., 2013), and has the ability to recover parameters with higher resolution (Bae et al., 2012; McNeely et al., 2012).

However, one issue with wavefield tomography, including full waveform inversion and other similar methods, is that it has non-unique solutions, i.e., multiple models may fit the data equally well. Ivanov et al. (2005) summarize several factors that contribute to non-uniqueness including, for example, insufficient acquisition and the presence of noise in the data. Methods for regularization have been proposed to stabilize the results and reduce the number of possible solutions (Tikhonov and Arsenin, 1977; Sun and Schuster, 1992; Zhou et al., 2002). Regularization is usually defined in the model domain for the purpose of adding prior information to the model. Regularization can be formulated in many different, possibly complementary, ways. Tikhonov and Arsenin (1977) propose a regularization term that encourages smoothness in the computed model. Xiang and Zhang (2014) use an edge-preserving regularization term to preserve sharp interfaces within the model. Asnaashari et al. (2013) use an a priori model to constrain the inversion. These and other examples demonstrate that proper regularization or preconditioning can effectively reduce the number of non-unique solutions and, in many cases, improve the accuracy of the reconstructed models.

Wavefield tomography is well-developed under the acoustic assumption (Tarantola, 1984; Pratt, 1999; Operto et al., 2004; Biondi and Almomin, 2014); however, recorded seismic data

include shear waves in addition to compressional waves. Because all wave modes contain useful information about the subsurface, elastic wavefield tomography can allow for better characterization of the subsurface (Tarantola, 1986; Pratt, 1990; Guasch et al., 2012; Vigh et al., 2014). Though multi-parameter inversion can provide more physical information compared to single-parameter inversion, different parameters in the updated model may not be physically realistic (Plessix, 2006), i.e., inversion might not be able to resolve the model parameters while preserving their intrinsic physical relationships.

Such physical relationships need to be enforced explicitly because they provide constraints on the model parameters that cannot be achieved using data or shaping regularization terms. For example, Baumstein (2013) imposes rock-physics-based constraints on FWI using the Projection Onto Convex Sets (POCS) method, which clips the values of update model parameters or their relationships to be in the desired bounds and then performs a line search within the feasible region. Using this approach, Baumstein (2013) modifies the gradient and the line search without changing the objective function. Physical relationships between model parameters in elastic media can be derived from well logs, seismic data, and laboratory measurements, and they can also be derived based on first-principle physical relationships (Tsuneyama, 2006; Compton and Hale, 2013). Experiments have established the relationship between P and S velocities (Castagna et al., 1985; Katahara, 1999; Tsuneyama, 2006); therefore, enforcing a range of constant ratios between the two velocities could guide the model update, thus increasing the robustness of wavefield tomography.

In this paper, we perform wavefield tomography using the isotropic elastic wave equation, and invert for the squared velocities of P and S waves simultaneously. We propose an objective function for wavefield tomography that constraints the relationship between P- and S-wave velocities. Examples demonstrate that the model constraints enforce appropriate physical relationships between the model parameters.

5.2 Elastic wavefield modeling

We consider the elastic isotropic wave equation:

$$\ddot{\mathbf{u}} - \alpha\nabla(\nabla\cdot\mathbf{u}) + \beta\nabla\times(\nabla\times\mathbf{u}) = \mathbf{f}\ , \tag{5.1}$$

where $\mathbf{u}\left(e,\mathbf{x},t\right) = [u_x \quad u_y \quad u_z]^T$ is the displacement vector, and $\mathbf{f}\left(e,\mathbf{x},t\right)$ is the source function. Both vectors $\mathbf{u}$ and $\mathbf{f}$ are functions of the experiment index e, spatial location $\mathbf{x}$, and time t. Model parameters $\alpha\left(\mathbf{x}\right) = \frac{\lambda+2\mu}{\rho}$ and $\beta\left(\mathbf{x}\right) = \frac{\mu}{\rho}$ are squared P- and S-wave velocities, respectively. λ and μ are Lamé parameters, and ρ is the density. Equation 5.1 assumes slowly varying Lamé parameters (Lay and Wallace, 1995) and describes a linear relationship between the displacement vector $\mathbf{u}$ and the source function $\mathbf{f}$:

$$\mathbf{L}\mathbf{u} = \mathbf{f}\ , \tag{5.2}$$

where matrix $\mathbf{L}$ is the elastic wave operator corresponding to equation 5.1, with model parameters α and β, whose adjoint is written as $\mathbf{L}^{\mathsf{T}}$.

5.3 Objective function

For wavefield tomography, one typically updates a model by minimizing an objective function. We consider an objective function $\mathcal{J}\left(\mathbf{u}_s,\alpha,\beta\right)$ consisting of three terms: a data misfit term $\mathcal{J}_D\left(\mathbf{u}_s,\alpha,\beta\right)$, a regularization term $\mathcal{J}_M\left(\alpha,\beta\right)$ that allows for the use of prior models $\bar{\alpha}\left(\mathbf{x}\right)$ and $\bar{\beta}\left(\mathbf{x}\right)$ as well as model shaping, and a model constraint term $\mathcal{J}_C\left(\alpha,\beta\right)$ that restricts the relationship between α and β to a feasible region:

$$\mathcal{J}\left(\mathbf{u}_s,\alpha,\beta\right) = \mathcal{J}_D\left(\mathbf{u}_s,\alpha,\beta\right) + \mathcal{J}_M\left(\alpha,\beta\right) + \mathcal{J}_C\left(\alpha,\beta\right)\ . \tag{5.3}$$

We define the data misfit term using the difference between the predicted and observed data:

$$\mathcal{J}_D = \sum_e \frac{1}{2}\|\mathbf{W}_u\mathbf{u}_s - \mathbf{d}_o\|^2\ , \tag{5.4}$$

where $\mathbf{d}_o\left(e,\mathbf{x},t\right)$ are the observed data recorded at the receiver locations and weights $\mathbf{W}_u\left(e,\mathbf{x},t\right)$ restrict the source wavefield $\mathbf{u}_s\left(e,\mathbf{x},t\right)$ to the receiver locations.

The regularization term $\mathcal{J}_M$ in the objective function penalizes deviations from prior models $\bar{\alpha}\left(\mathbf{x}\right)$ and $\bar{\beta}\left(\mathbf{x}\right)$:

$$\mathcal{J}_M = \frac{1}{2}\|\mathbf{W}_\alpha\left(\alpha-\bar{\alpha}\right)\|^2 + \frac{1}{2}\|\mathbf{W}_\beta\left(\beta-\bar{\beta}\right)\|^2\ , \tag{5.5}$$

where $\mathbf{W}_\alpha(\mathbf{x})$ and $\mathbf{W}_\beta(\mathbf{x})$ are model shaping operators, whose inverses are related to the model covariance matrices. Such operators can be either simple space-invariant roughness operators, e.g., a Laplacian filter (Tarantola, 1987), or they can perform image-shaping with non-stationary filtering (Hale, 2007; Guitton et al., 2012).

Due to differences in illumination and amplitude between P and S modes, models α and β – computed using only the data misfit term – update independently, and this can lead to physically unrealistic solutions. Prieux et al. (2013) explain the differences in illumination and amplitude in terms of offset between PP, PS, SP, and SS reflections using diffraction patterns. Moreover, the undesired inconsistency in resolution between the recovered P and S velocity models is also due to the fact that the seismic wavelength for shear modes is shorter than that of P modes; therefore, the updated S velocity model could have higher resolution than the updated P velocity model. In order to eliminate the undesired solutions, one can constrain model updates using physical relationships between α and β, for example, using a region defined by an upper boundary $h_u(\alpha,\beta)=0$ and a lower boundary $h_l(\alpha,\beta)=0$:

$$h_u > 0\ , \tag{5.6}$$
$$h_l > 0\ . \tag{5.7}$$

In order to keep the updated model within these boundaries, we include in the objective function a constraint term $\mathcal{J}_C$ that uses a logarithmic penalty function (Peng et al., 2002; Nocedal and Wright, 2006; Gasso et al., 2009):

$$\mathcal{J}_C = -\eta \sum_{\mathbf{x}} \left[\log(h_u) + \log(h_l)\right]\ . \tag{5.8}$$

The constraint term $\mathcal{J}_C$ tends to $-\infty$ as h_u or h_l tends to 0, and thus penalizes violations of inequalities 5.6 and 5.7. This constraint term mainly contributes to model updating when the updated model approaches the boundaries. The parameter η weighs the constraint term $\mathcal{J}_C$ relative to other terms in the objective function $\mathcal{J}$. Note that the starting model for inversion must fall between the boundaries.

For elastic wavefield tomography, because the relationship of P and S velocities is generally linear (Castagna et al., 1985; Zimmer et al., 2002; Rojas et al., 2005), we set the boundaries to be

$$h_u = -\alpha + c_u\beta + b_u = 0 \ , \tag{5.9}$$
$$h_l = \quad \alpha - c_l\beta - b_l = 0 \ , \tag{5.10}$$

where the user-defined parameters c_l, c_u, b_l, and b_u characterize the slopes and α-intercepts of the specific boundaries. Notice that parameters c_l, c_u, b_l, and b_u are functions of spatial location $\mathbf{x}$, i.e., these parameters may vary with spatial location. For example, the ratios of P and S velocities for liquid and gas saturations have distinguishable differences (Gregory, 1976; Hamada, 2004). With prior physical information, one could apply proper constraints to liquid and gas zones. In areas of the model where the relationship between α and β has high uncertainty, one could set a broad physical constraint that allows for more variation between α and β.

5.4 Objective function gradient

We update the model iteratively using a steepest descent method (Lailly, 1983; Tarantola, 1984). For the wavefield tomography problem, one can directly apply the adjoint-state method to compute the gradient (Plessix, 2006):

$$\boldsymbol{\mathcal{F}}_s = \mathbf{L}\mathbf{u}_s - \mathbf{f}_s = \mathbf{0} \ . \tag{5.11}$$

Equation 5.11 simply indicates that we compute the source wavefield $\mathbf{u}_s$ from a given source function $\mathbf{f}_s$, i.e., $\mathbf{u}_s$ is a solution to the given wave equation.

The gradient of the objective function can be efficiently computed using the adjoint-state method (Plessix, 2006). The augmented functional $\mathcal{H}$ is defined as

$$\mathcal{H} = \mathcal{J} - \sum_e \boldsymbol{\mathcal{F}}^{\mathsf{T}}\mathbf{a}_s \ . \tag{5.12}$$

The gradient of $\mathcal{H}$ indicates the search direction toward the minimum of $\mathcal{J}$, constrained by $\boldsymbol{\mathcal{F}}_s = 0$. The adjoint variable, vector $\mathbf{a}_s\,(e, \mathbf{x}, t)$, is computed by solving the adjoint equations

obtained by setting the partial derivatives of the augmented functional relative to the state variables $\mathbf{u}_s$ to zero:

$$\mathbf{L}^{\mathsf{T}}\mathbf{a}_s = \mathbf{g}_s \;, \tag{5.13}$$

where $\mathbf{g}_s\,(e, \mathbf{x}, t)$ is the adjoint source given by

$$\mathbf{g}_s = \frac{\partial \mathcal{J}}{\partial \mathbf{u}_s} = \mathbf{W}_u^{\mathsf{T}}\left(\mathbf{W}_u\mathbf{u}_s - \mathbf{d}_o\right). \tag{5.14}$$

Note that because terms $\mathcal{J}_M$ and $\mathcal{J}_C$ are not functions of $\mathbf{u}_s$, they do not appear in the expression for the adjoint source.

The gradient of the augmented functional $\mathcal{H}$ is given by

$$\begin{bmatrix} \frac{\partial \mathcal{H}}{\partial \alpha} \\ \frac{\partial \mathcal{H}}{\partial \beta} \end{bmatrix} = \begin{bmatrix} \frac{\partial \mathcal{J}}{\partial \alpha} \\ \frac{\partial \mathcal{J}}{\partial \beta} \end{bmatrix} - \sum_e \begin{bmatrix} \frac{\partial \boldsymbol{\mathcal{F}}_s^{\mathsf{T}}}{\partial \alpha}\mathbf{a}_s \\ \frac{\partial \boldsymbol{\mathcal{F}}_s^{\mathsf{T}}}{\partial \beta}\mathbf{a}_s \end{bmatrix} \;. \tag{5.15}$$

We obtain the gradient of $\mathcal{J}_D$ by solving $\frac{\partial \mathcal{H}}{\partial \alpha} = 0$ and $\frac{\partial \mathcal{H}}{\partial \beta} = 0$:

$$\begin{bmatrix} \frac{\partial \mathcal{J}_D}{\partial \alpha} \\ \frac{\partial \mathcal{J}_D}{\partial \beta} \end{bmatrix} = \sum_e \begin{bmatrix} \frac{\partial \boldsymbol{\mathcal{F}}_s^{\mathsf{T}}}{\partial \alpha}\mathbf{a}_s \\ \frac{\partial \boldsymbol{\mathcal{F}}_s^{\mathsf{T}}}{\partial \beta}\mathbf{a}_s \end{bmatrix} = \sum_e \begin{bmatrix} -[\nabla(\nabla\cdot\mathbf{u}_s)]^T \star \mathbf{a}_s \\ [\nabla\times(\nabla\times\mathbf{u}_s)]^T \star \mathbf{a}_s \end{bmatrix} \;, \tag{5.16}$$

where the symbol $\star$ denotes zero-lag cross-correlation. In addition, we apply illumination compensation to the gradient for the data misfit term, by dividing the gradient with respect to α by $\sum_t [\nabla(\nabla\cdot\mathbf{u}_s)]^2$ and the gradient with respect to β by $\sum_t [\nabla\times(\nabla\times\mathbf{u}_s)]^2$. This compensation is an approximation for the diagonal of the inverse Hessian (Pratt et al., 1998).

The gradient of terms $\mathcal{J}_M$ and $\mathcal{J}_C$, with respect to the model parameters α and β, are

$$\begin{bmatrix} \frac{\partial \mathcal{J}_M}{\partial \alpha} \\ \frac{\partial \mathcal{J}_M}{\partial \beta} \end{bmatrix} = \begin{bmatrix} \mathbf{W}_\alpha^{\mathsf{T}}\mathbf{W}_\alpha\left(\alpha - \bar{\alpha}\right) \\ \mathbf{W}_\beta^{\mathsf{T}}\mathbf{W}_\beta\left(\beta - \bar{\beta}\right) \end{bmatrix} \;, \tag{5.17}$$

and

$$\begin{bmatrix} \frac{\partial \mathcal{J}_C}{\partial \alpha} \\ \frac{\partial \mathcal{J}_C}{\partial \beta} \end{bmatrix} = \begin{bmatrix} \frac{-\eta}{\alpha - c_u\beta - b_u} - \frac{\eta}{\alpha - c_l\beta - b_l} \\ \frac{\eta c_u}{\alpha - c_u\beta - b_u} + \frac{\eta c_l}{\alpha - c_l\beta - b_l} \end{bmatrix} \;, \tag{5.18}$$

respectively. When updated models approach the boundaries defined in $\mathcal{J}_C$, the gradient of $\mathcal{J}_C$ dominates the total gradient of the objective function $\mathcal{J}$, thus pushing the updated model away from the boundaries. When the updated models are distant from the boundaries

defined in $\mathcal{J}_C$, the gradient of $\mathcal{J}_C$ has less influence on the total gradient $\mathcal{J}$, and the data misfit term controls the inversion.

We update the model using a steepest-descent method in which we search for the step length via a quadratic line search in the direction opposite to the gradient of the objective function. This line search requires at least two additional evaluations of the objective function. In addition, when using logarithmic functions in the physical constraint term, one must ensure that the model remains in the predefined feasible region while performing the line search and model update.

5.5 Example

We illustrate our method for elastic wavefield tomography with two synthetic models, and compare inversion using only the data misfit term $\mathcal{J}_D$ to inversion using the data misfit with physical constraints $\mathcal{J}_D + \mathcal{J}_C$.

5.5.1 Borehole model

The first synthetic model contains two negative Gaussian anomalies centered at $(1.5, 2.0)$ and $(1.5, 5.0)$ km. There are 60 vertical displacement sources in a well at $x = 0.2$ km and a line of geophones at $x = 2.8$ km. The α and β models are shown in Figure 5.1. The vertical component of a shot gather is shown in Figure 5.2(a), which contains both P and S waves. To illustrate the influence of the physical constraint term $\mathcal{J}_C$ when the illumination of P and S waves differ, we mute the S waves in both observed and predicted data for receivers located between $z = 0$ and 3.5 km, and the P waves in both observed and predicted data for receivers located between $z = 3.5$ and 7 km, as shown in Figure 5.2(b). That is, for elastic wavefield tomography, we use primarily the P waves passing through the shallow Gaussian anomaly and the S waves passing through the deeper Gaussian anomaly. This is simply an artificial construction meant to simulate partial illumination and to highlight the influence of the model constraint.

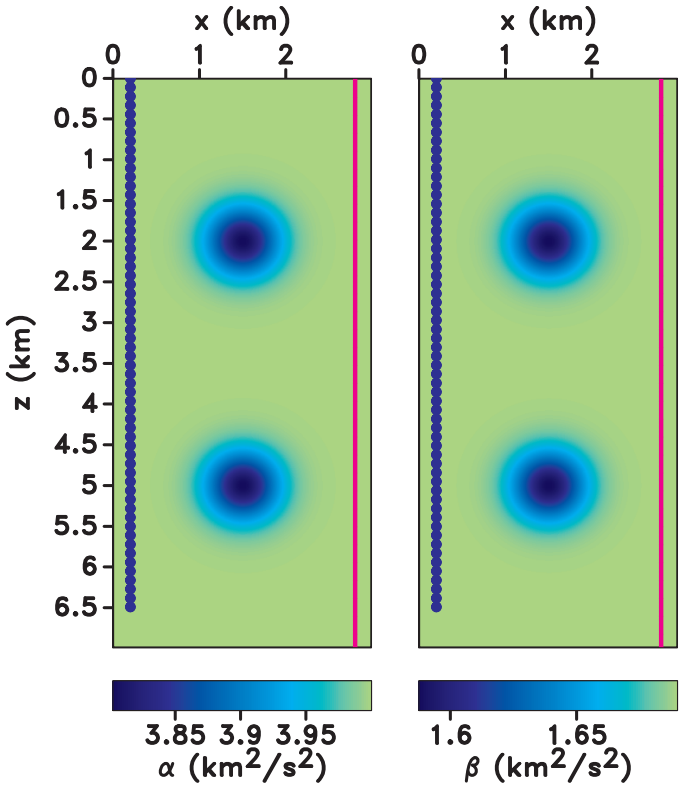

Figure 5.1: α (left panel) and β (right panel) models with two negative Gaussian anomalies. Dots are the source locations at $x = 0.2$ km, and the vertical line shows the receivers at $x = 2.8$ km.

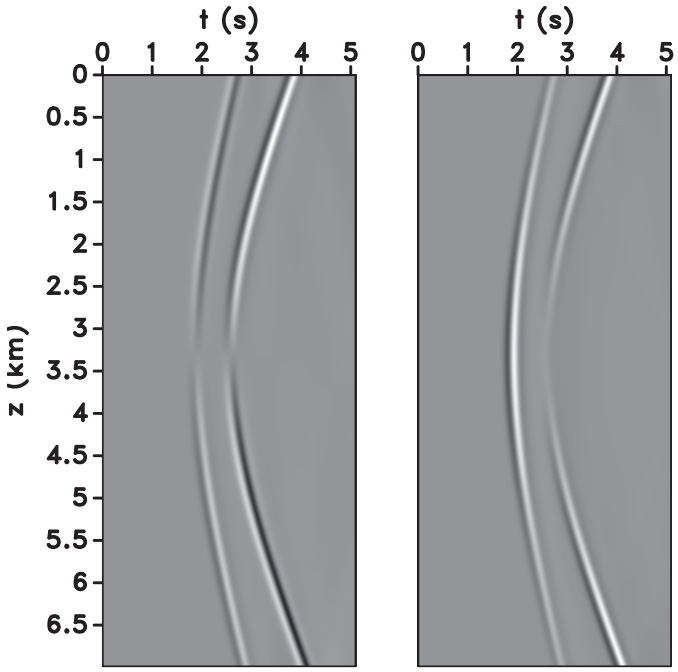

(a)

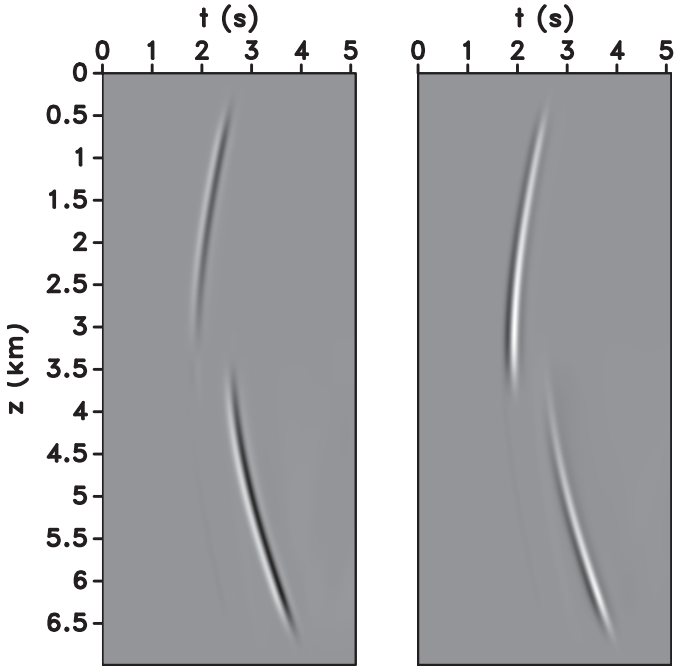

(b)

Figure 5.2: Horizontal (left panels) and vertical (right panels) components of a shot gather with the source at $z = 3.5$ km. First arrival is the P wave and second arrival is the S wave. (a) The original data. (b) Processed data for inversion with P waves only from $z = 0$ to 3.5 km and S waves only from $z = 3.5$ to 7 km. We window selected portions of the original data to simulate partial illumination for different wave modes.

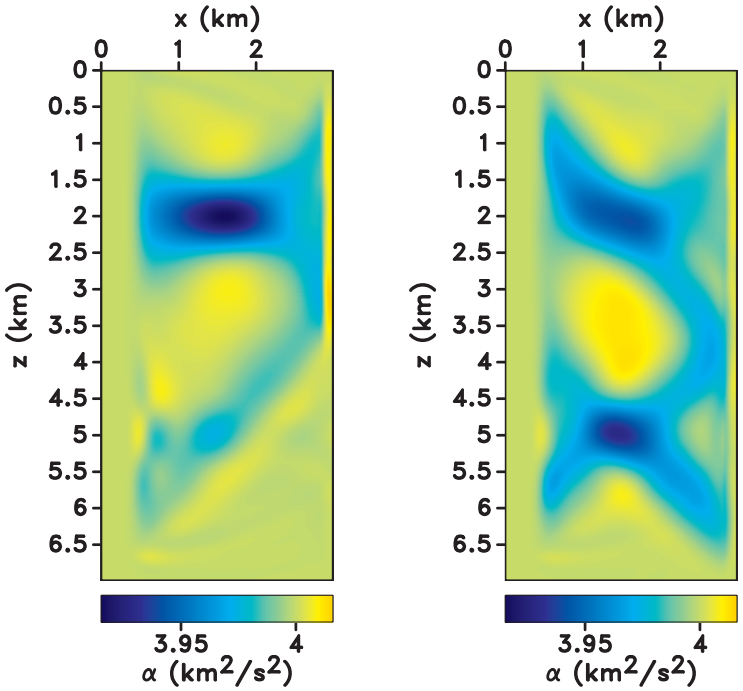

(a) (b)

Figure 5.3: Updated α models after 21 iterations using (a) objective function $\mathcal{J}_D$ and (b) $\mathcal{J}_D + \mathcal{J}_C$. Note that the Gaussian anomaly in (b) at $(1.5, 5)$ km is better recovered, and its amplitude and shape are closer to the true model compared to that in (a).

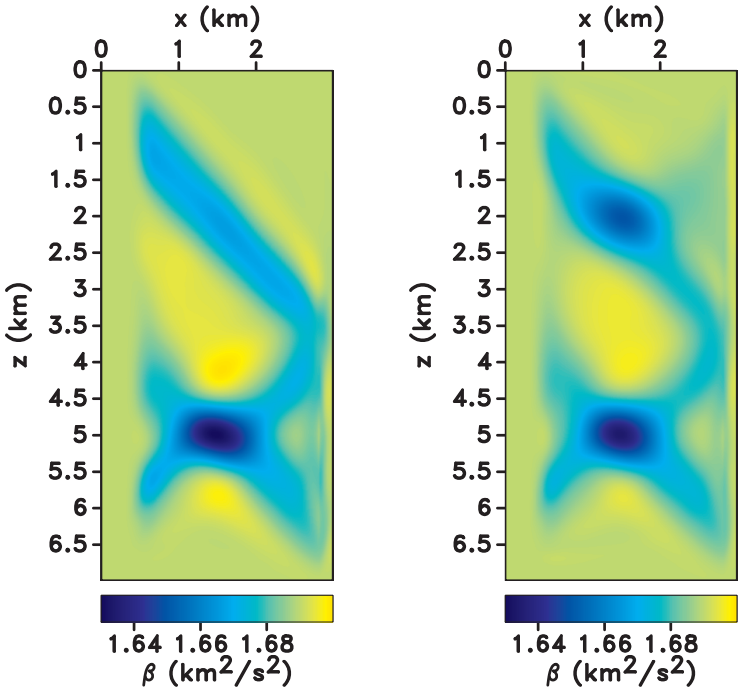

(a) (b)

Figure 5.4: Updated β models after 21 iterations using (a) objective function $\mathcal{J}_D$ and (b) $\mathcal{J}_D + \mathcal{J}_C$. Note that the Gaussian anomaly in (b) at $(1.5, 2)$ km is better recovered, and its amplitude and shape are closer to the true model compared to that in (a).

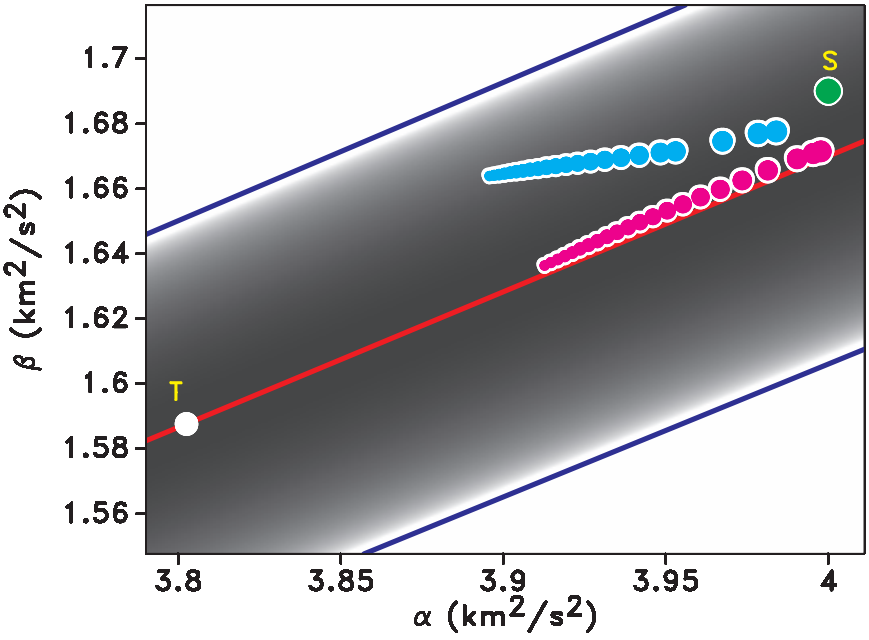

(a)

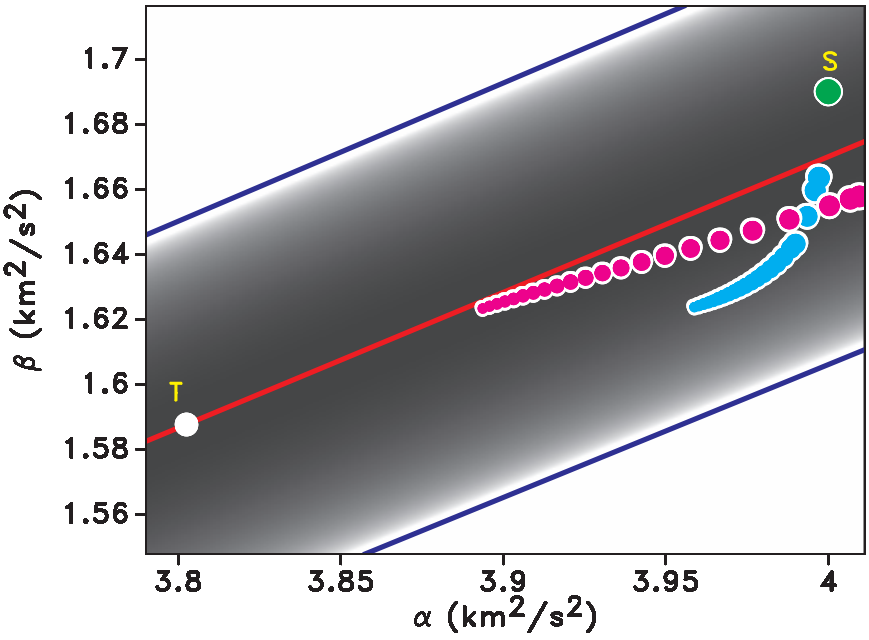

(b)

Figure 5.5: Model updates for the Gaussian model in Figure 5.1 as a function of iterations at (a) $(1.5, 2)$ km and (b) $(1.5, 5)$ km. Stars and dots are the updated models with and without constraints, respectively. Note that without constraints, the α and β models update toward the boundaries, while with constraints, the relationship of α and β models is enforced to be close to the true model indicated by the median line in the underlying physical constraint.

Using the data misfit term $\mathcal{J}_D$ as the objective function, we obtain the updated models for α and β after 21 iterations, shown in Figures 5.3(a) and 5.4(a), respectively. Notice that the model update of α focuses on the shallow Gaussian anomaly, while that of β focuses on the deeper Gaussian anomaly. By including the physical constraint term $\mathcal{J}_C$ in the objective function, we obtain the updated α and β models shown in Figures 5.3(b) and 5.4(b), respectively. We choose the weighting parameter η to be 0.6 in order to balance the gradients of $\mathcal{J}_D$ and $\mathcal{J}_C$. Observe that the Gaussian anomalies in α and β recovered using physical constraints (Figures 5.3(b) and 5.4(b)) are more accurate compared to those obtained without constraints (Figures 5.3(a) and 5.4(a)). Figures 5.5(a) and 5.5(b) show, respectively, the values of the updated models at $(1.5, 2)$ km and $(1.5, 5)$ km as a function of iteration number. In both figures, the stars represent the updated models with constraints, while the dots represent the updated models without constraints. Notice in Figure 5.5(a) that the recovered α and β models tend to move toward the lower constraint boundary in later iterations. In contrast, by including the physical constraint term $\mathcal{J}_C$ in the objective function, we preserve the ratio between α and β.

5.5.2 Marmousi model

The second example, shown in Figures 5.6(a) and 5.6(b), uses a modified Marmousi model (Versteeg, 1991, 1993). The top layer from 0 to 110 m is elastic and homogeneous. For this synthetic example, we assume that we know the values of α and β for the first layer. Figure 5.6(c) is the crossplot of α and β measured from three well logs at $x = 1.0, 2.0, 3.0$ km. The relationship between α and β in the well logs is approximately linear; therefore, we use two straight lines (Equations 5.9 and 5.10) to define the feasible region for the α-β relationships, which provides the prior physical constraints for inversion.

The starting α and β models (shown in Figures 5.7(a) and 5.7(b), respectively) are computed by smoothing the true model mainly along the horizontal axis. Note that in the crossplot of a and b models shown in Figure 5.7(c), all samples in the model space are within the predefined feasible range. We simulate 20 shots using displacement sources evenly

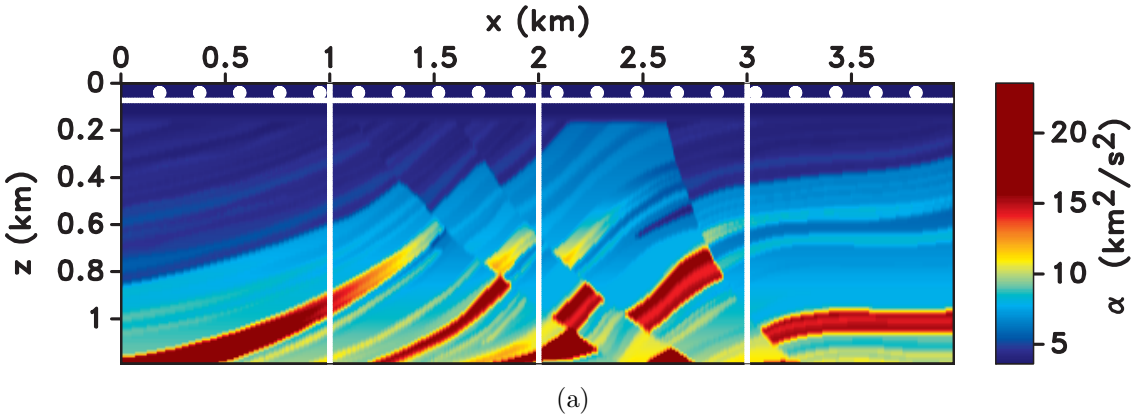

(a)

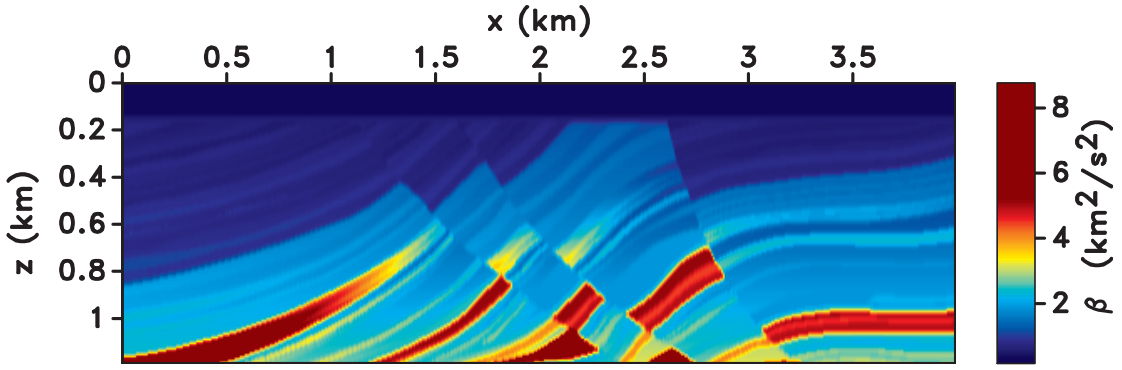

(b)

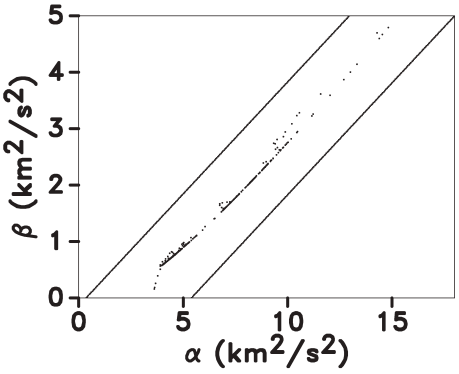

(c)

Figure 5.6: (a) True α model, (b) true β model, and (c) the crossplot of α and β models. The α and β models are computed from the original Marmousi P and S velocity models, respectively.

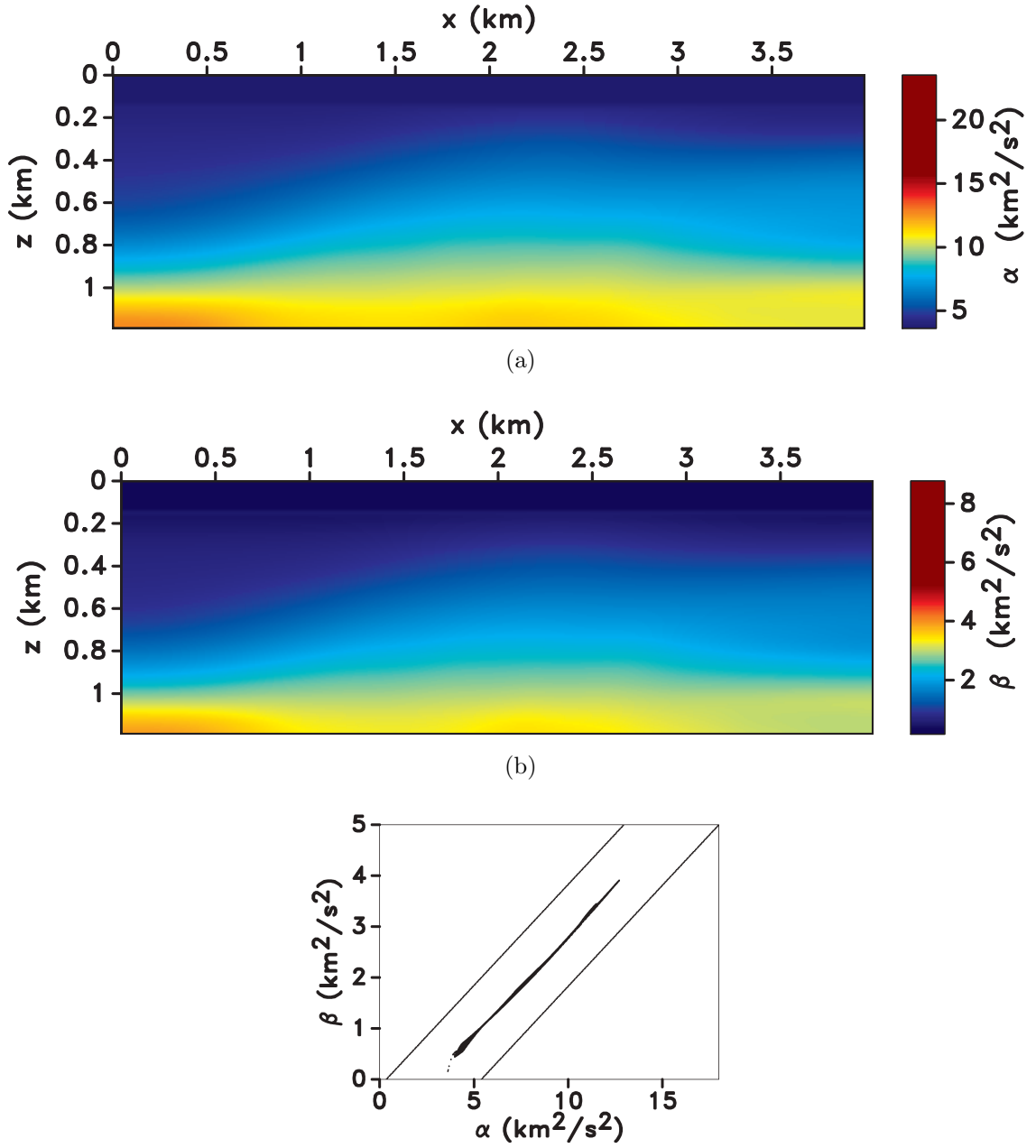

Figure 5.7: (a) Starting α model, (b) starting β model, and (c) crossplot of α and β models for Marmousi example. The α and β models are computed from the true model with smoothing mainly along the horizontal axis to eliminate detailed structures in the true model.

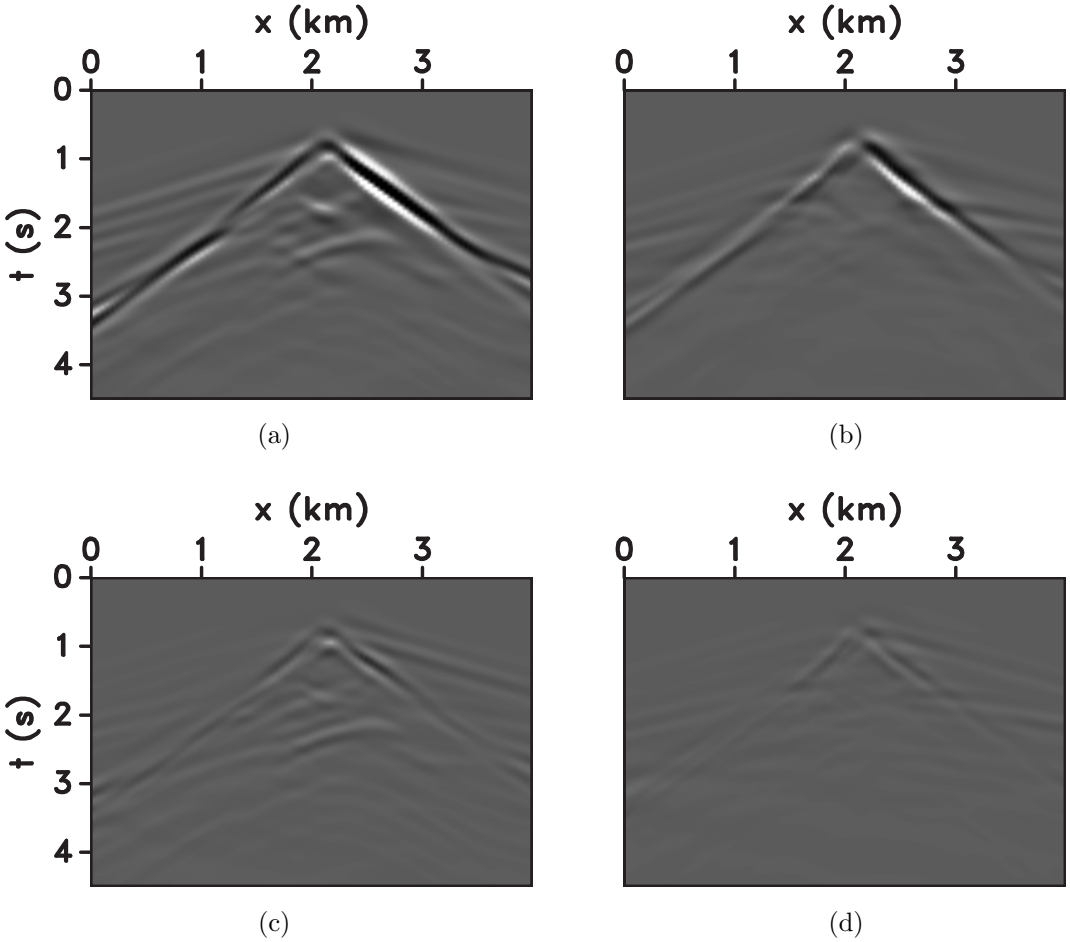

Figure 5.8: (a) Vertical and (b) horizontal components of the difference between a recorded shot gather and the corresponding predicted data for the first frequency band ($0-5$ Hz). The predicted data are computed using the initial model shown in Figures 5.7(a) and 5.7(b); (c) vertical and (d) horizontal components of the difference between the recorded and predicted data for the first frequency band. The predicted data are computed using the final model for the first frequency band.

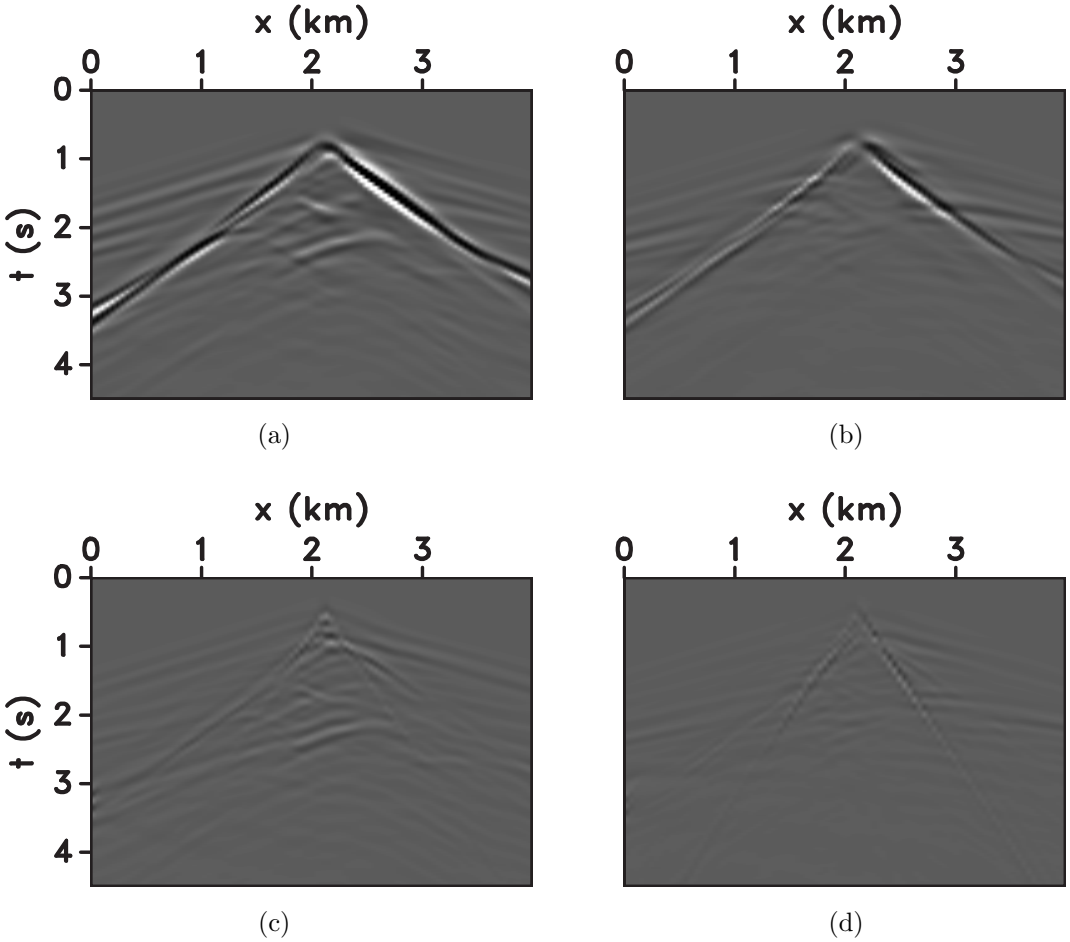

Figure 5.9: (a) Vertical and (b) horizontal components of the difference between a recorded shot gather and the corresponding predicted data for the second frequency band ($0 - 7$ Hz). The predicted data are computed using the final model from the first frequency band; (c) vertical and (d) horizontal components of the difference between the recorded and predicted data for the second frequency band. The predicted data are computed using the final model for the second frequency band.

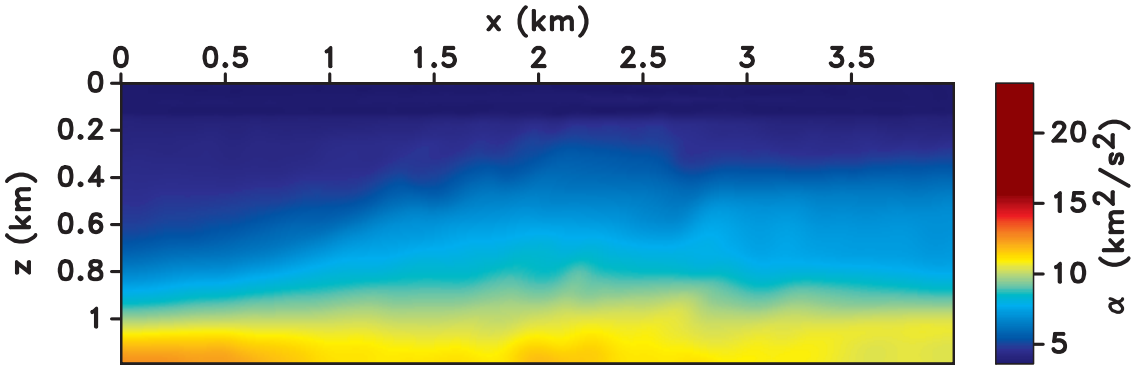

(a)

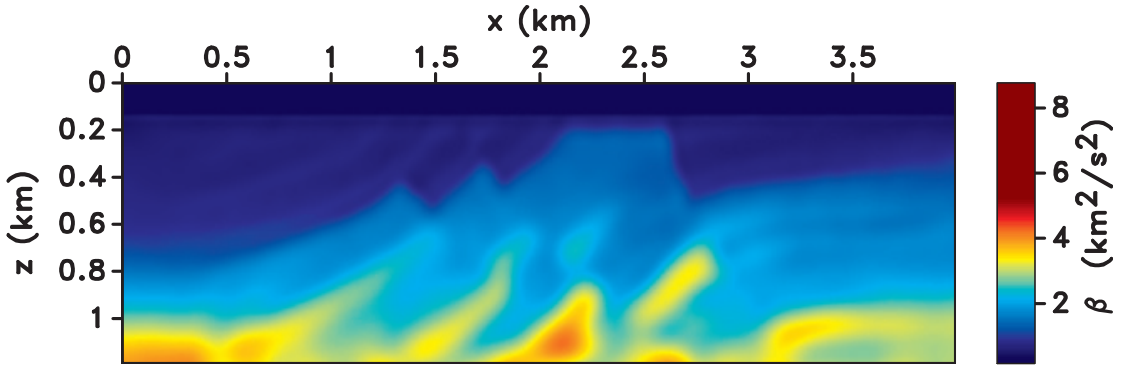

(b)

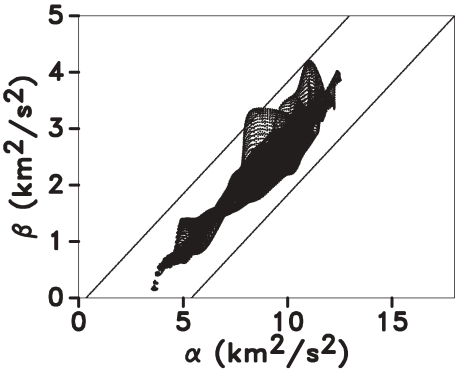

(c)

Figure 5.10: Recovered (a) α and (b) β models after the inversion of the second frequency band. (c) Crossplot of recovered α and β models using objective function $\mathcal{J}_D$. Note that the recovered β model contains more details than the α model.

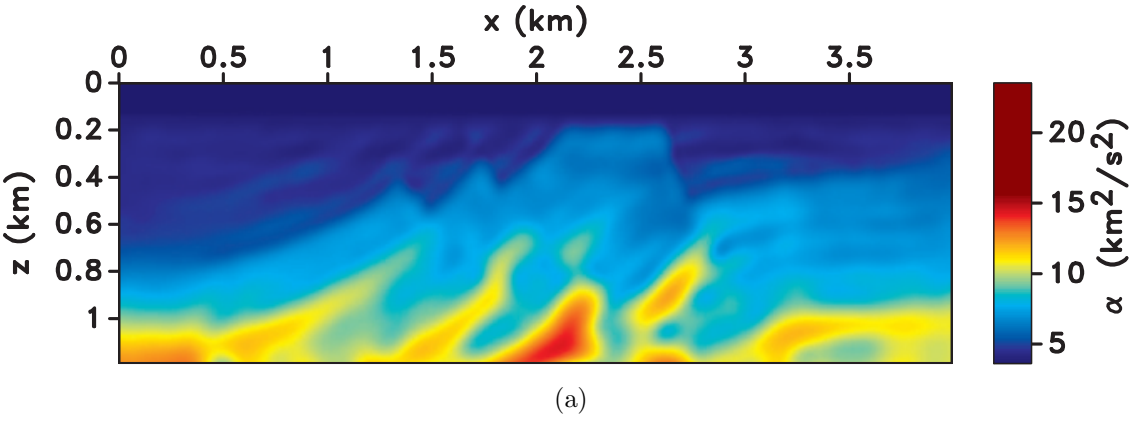

(a)

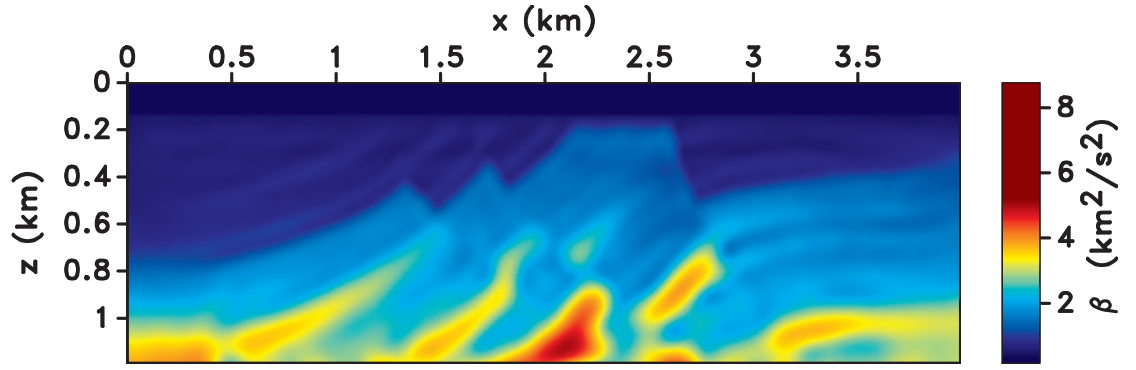

(b)

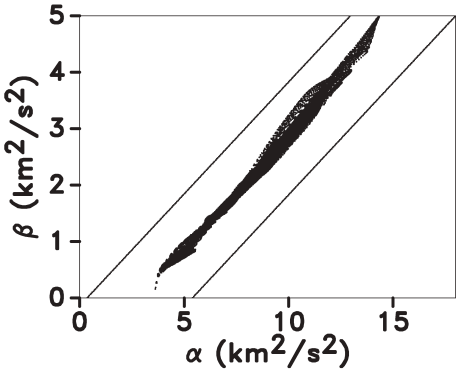

(c)

Figure 5.11: Recovered (a) α and (b) β models after the inversion of the second frequency band. (c) Crossplot of recovered α and β models using objective function $\mathcal{J}_D + \mathcal{J}_C$. The upper and lower boundaries are indicated by the two solid lines. Note that the recovered α and β models contain similar details.

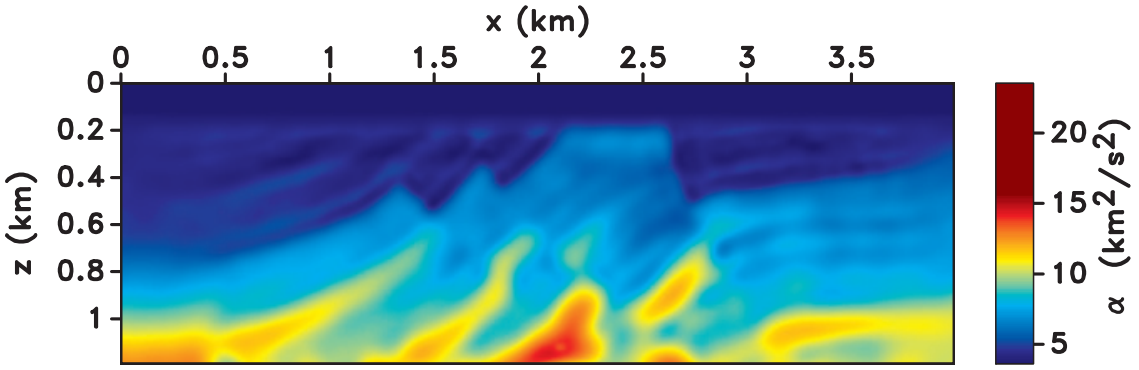

(a)

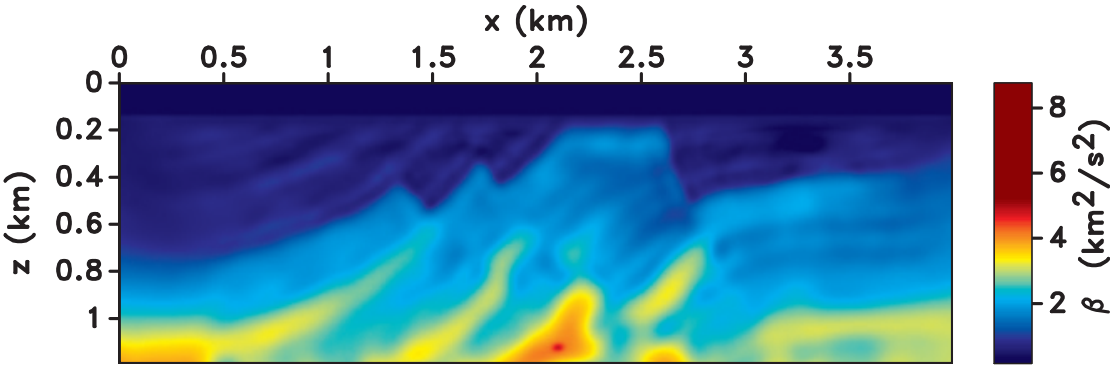

(b)

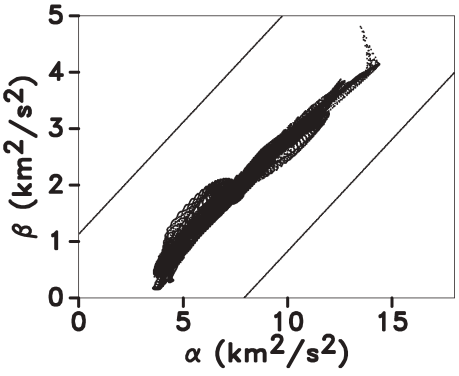

(c)

Figure 5.12: Recovered (a) α and (b) β models after the inversion of the second frequency band. (c) Crossplot of recovered α and β models using objective function $\mathcal{J}_D + \mathcal{J}_C$. The upper and lower boundaries are indicated by the two solid lines.

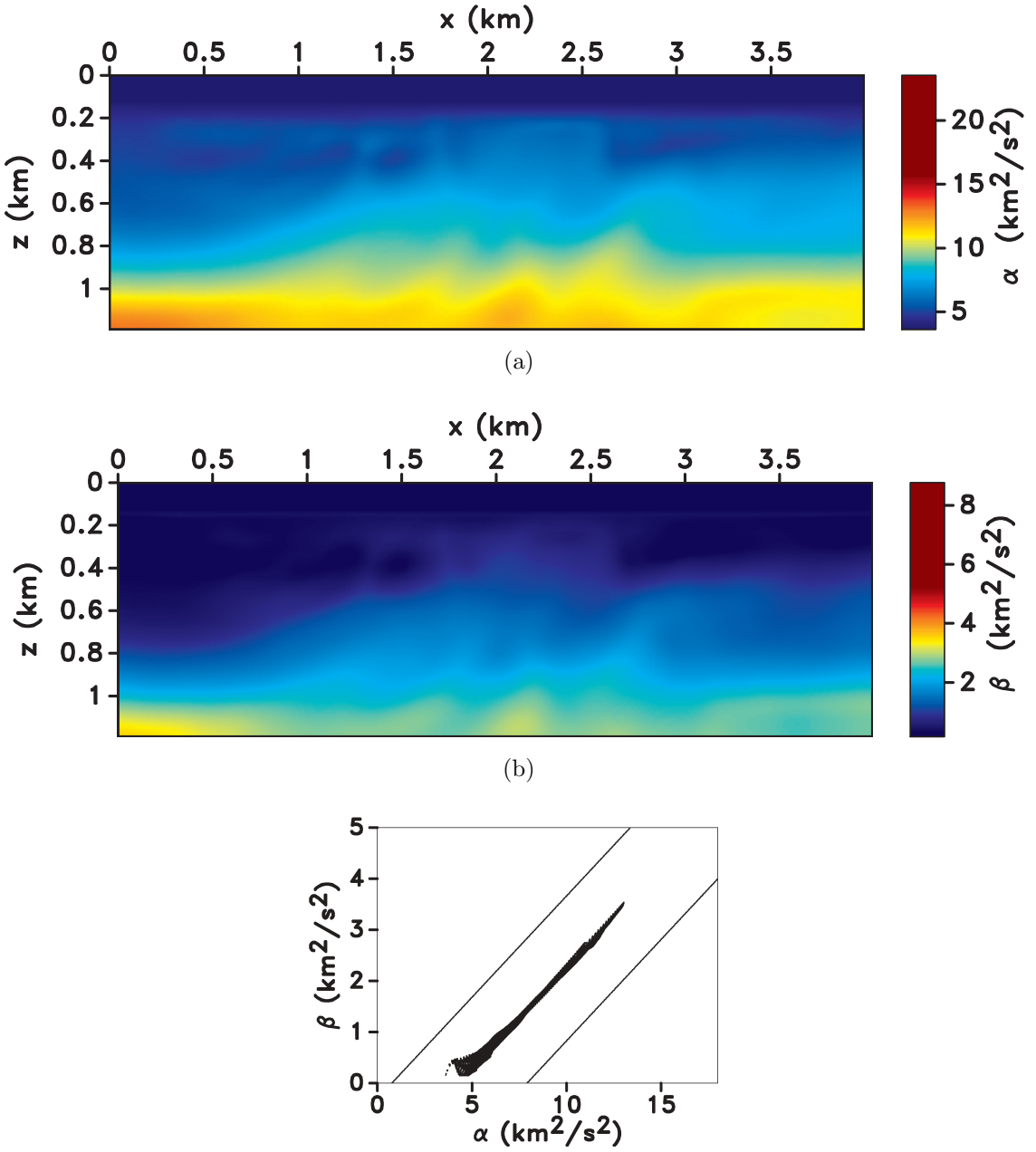

Figure 5.13: Recovered (a) α and (b) β models after the inversion of the second frequency band. (c) Crossplot of recovered α and β models using objective function $\mathcal{J}_D + \mathcal{J}_C$. The upper and lower boundaries are indicated by the two solid lines.

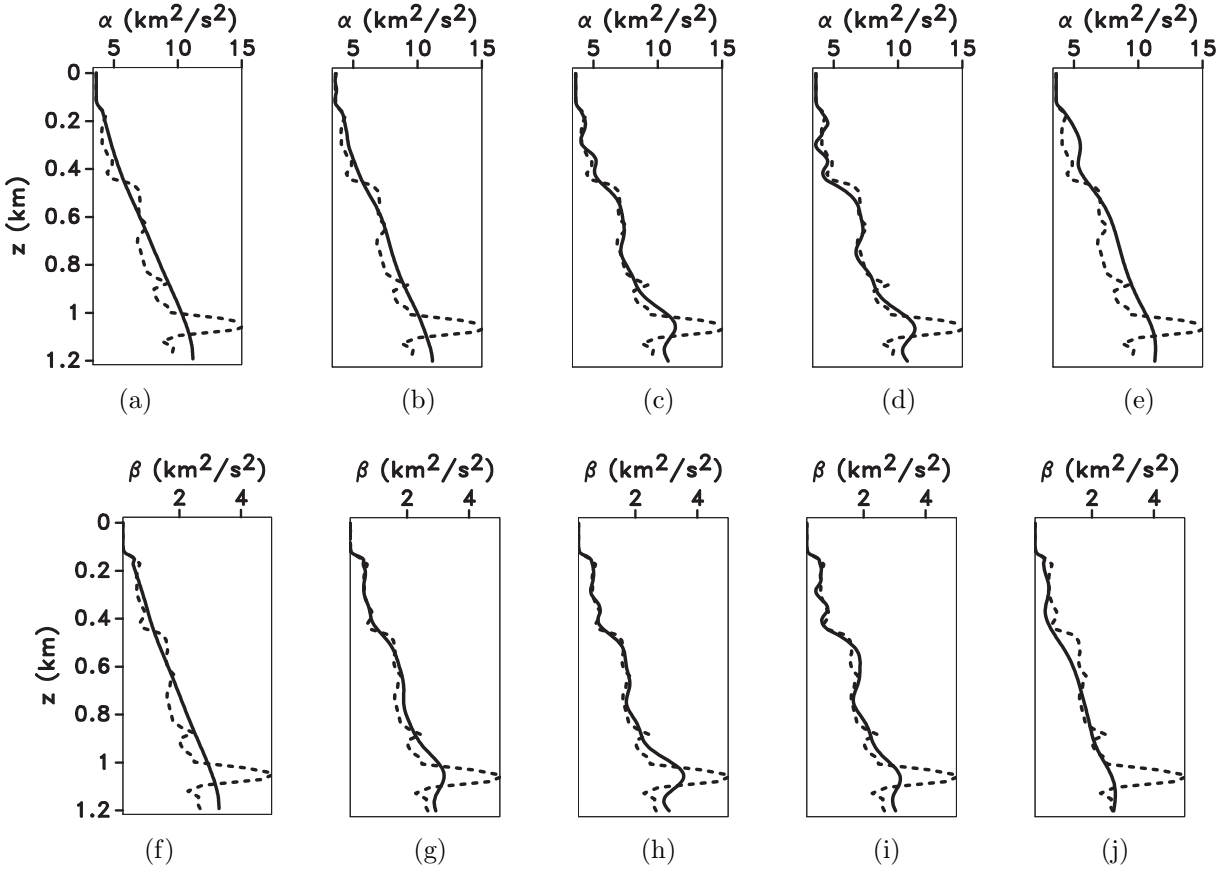

Figure 5.14: Comparison between initial or recovered models (solid lines) and true models (dashed lines) from the well at $x = 2.4$ km. Row one: Solid lines are the α profiles of (a) initial model; (b) updated models using objective function $\mathcal{J}_D$; (c) updated models using objective function $\mathcal{J}_D + \mathcal{J}_C$; (d) updated models using objective function $\mathcal{J}_D + \mathcal{J}_C$, where $\mathcal{J}_C$ is defined with a wider feasible region; (e) updated models using objective function $\mathcal{J}_D + \mathcal{J}_C$, where $\mathcal{J}_C$ is defined with a shifted feasible region. Row two: Solid lines are the β profiles of (f) initial model; (g) updated models using objective function $\mathcal{J}_D$; (h) updated models using objective function $\mathcal{J}_D + \mathcal{J}_C$; (i) updated models using objective function $\mathcal{J}_D + \mathcal{J}_C$, where $\mathcal{J}_C$ is defined with a wider feasible region; (j) updated models using objective function $\mathcal{J}_D + \mathcal{J}_C$, where $\mathcal{J}_C$ is defined with a shifted feasible region. In (c), (d), (g), (h), and (i), the recovered model profiles match the true models.

distributed along the x-axis, at depth $z = 0.04$ km, and record each shot with 500 receivers evenly distributed along the x-axis, at depth $z = 0.07$ km. The amplitude of the horizontal component of the displacement source is 5 times stronger than the vertical component so that the computed wavefields contain strong S waves. FWI is carried out using a multiscale approach with two frequency bands: $0 - 5$ Hz and $0 - 7$ Hz. The horizontal and vertical components of the data residual for the first frequency band, computed using the starting model, are shown in Figures 5.8(a) and 5.8(b), respectively. Notice that the data residual contains head waves, diving waves, and reflections.

We perform four different tests using the same starting models shown in Figures 5.7(a) and 5.7(b) in order to evaluate the constraint term $\mathcal{J}_C$. For the first test, we use only the data misfit term $\mathcal{J}_D$ as the objective function. Figures 5.8(a) and 5.8(b) show, respectively, the horizontal and vertical components of the data residual for the first frequency band before inversion. In comparison, Figures 5.8(c) and 5.8(d) show the data residual after inversion using only the first frequency band. The final model for the first frequency band is then used as the starting model for the second frequency band. The data residual for the second frequency band before inversion is shown in Figures 5.9(a) and 5.9(b), while Figures 5.9(c) and 5.9(d) show the data residual after inversion using the same frequency band. As expected, the magnitude of the data residual, in which we observe energy from all wave types, has decreased after inversion.

Figures 5.10(a) and 5.10(b) show the recovered α and β models after inversion using both frequency bands. Notice that the recovered β contains more structural details, for example, in the high velocity zones, while the recovered α model is smoother. The recovered α and β values are crossplotted in Figure 5.10(c). Without physical constraints, the α and β values deviate from the allowable region, resulting in recovered models that are inaccurate. One reason for the difference between the recovered α and β models is that the wavelengths of P and S waves differ significantly. Because there is no attenuation in this synthetic example, typical S wavelengths are shorter than P wavelengths for the same frequency band. This

results in the recovered β model having higher resolution than the α model, as seen in Figure 3.10. In reality, however, S waves experience more attenuation than P waves for the same frequency band, and the resolution of the recovered α and β models still differ in practice. This inconsistency in resolution between recovered α and β models does not reflect the true subsurface, and we address this inconsistency through physical constraints between the two model parameters.

For the remaining tests, we include both the data misfit term $\mathcal{J}_D$ and the physical constraint term $\mathcal{J}_C$ in the objective function. For the second test, we use upper and lower boundaries estimated from the three well logs shown in Figure 5.6(c). By including the physical constraint term in the objective function, the values of α and β are confined to the allowable range. Figures 5.11(a) and 5.11(b) show the updated α and β models after the inversion converges. Compared to the models obtained using only the data misfit term (Figure 3.10), both models seen in Figure 3.11 now have similar resolution. Figure 5.11(c) shows the crossplot of the recovered α and β models, and confirms that the α-β relationship is maintained within the allowable region as the models are updated. For this test and the following tests, the weighting parameter we use in the constraint term is $\eta = 4.0$.

For the third test, we increase the width of the feasible region, as indicated by the solid lines in the crossplot in Figure 5.12(c). The α and β models obtained with these less-restrictive constraints are shown in Figure 5.12(a) and Figure 5.12(b). Compared to the second test (Figure 3.11), the recovered α and β models exhibit larger differences in resolution and, as evidenced by the crossplot in Figure 5.12(c), more variation in the ratio between the values of α and β.

For the last test, we purposely select a feasible region, shown in Figure 5.13(c), whose center does not coincide with the best-fit line describing the relationship between α and β derived from the three well-logs. Using this constraint, the recovered α (Figure 5.13(a)) and β models (Figure 5.13(b)) are much smoother compared to those from the second (Figure 3.11) and third (Figure 3.12) tests. In this case, because the constraint term drives the relation

between α and β toward incorrect values, neither the α nor β models are updated correctly. Therefore, from the results of this test and the previous tests, we conclude that ideally one should choose a narrow constraint region that enforces an accurate relation between α and β but, when there is significant uncertainty in the estimated relation between α and β, choosing a broader constraint region is a preferable alternative to choosing a narrow constraint region that enforces an inaccurate relationship.

Vertical profiles extracted from α and β models at $x = 2.0$ km are shown in Figure 3.14. The solid line in Figure 3.14(a) is the initial α model, while the solid lines in Figures 3.14(b) to 3.14(e) are the recovered α models from the four tests. The dashed line in Figures 3.14(a) to Figure 3.14(e) indicates the true α model. Similarly, the solid line in Figure 3.14(f) is the initial β model, the solid lines in Figures 3.14(g) to 3.14(j) are the recovered β models from the four tests, and the dashed line in Figures 3.14(f) to 3.14(j) is the true β model. Using only the data misfit as the objective function, we obtain a reliable model update for β (Figure 5.14(b)), but only a limited model update for α (Figure 5.14(g)). When using constraints that enforce an accurate relationship between α and β, which are estimated from the three well logs, we obtain updated α and β models that both match the true model well. The recovered α (Figure 3.14(c)) and β (Figure 3.14(h)) models obtained with narrower constraints (Figure 3.11) are slightly more accurate than the α (Figure 3.14(d)) and β (Figure 3.14(i)) models obtained with broader constraints (Figure 3.12). Using narrow but inaccurate constraints (Figure 3.13) yields unsatisfactory results for both α (Figure 3.14(e)) and β (Figure 3.14(j)).

5.6 Conclusion

We demonstrate an elastic wavefield tomography method based on the isotropic elastic wave equation, formulated to reduce the misfit between observed and predicted data, and constrained in order to obtain models that are physically plausible. We invert for a model of multiple elastic material parameters, specifically the squared velocities of P and S waves. Due to differences in illumination, amplitude, and wavelength between P and S waves, the

model updates for the two parameters may differ in amplitude and location, thus leading to nonphysical models. To obtain a physically realistic model, we introduce physical constraints that force the updated models to satisfy known physical relations bounded within a certain feasible range. This constraint term only impacts model updating when the inverted model parameters are close to the boundaries of the constraints.

For multi-parameter wavefield tomography in general, another issue is the trade-off between model parameters, particularly in cases where data coverage is incomplete. The choice of model parameterization is an important aspect of multi-parameter wavefield tomography, and different parameterizations have been investigated in order to determine optimal combinations for inversion that result in minimal ambiguity between parameters. However, in general, this ambiguity cannot be completely avoided even with an optimal parameterization. By including a physical constraint term in the objective function, we limit the set of permissible solutions, and thereby we can potentially reduce the trade-off between parameters, and, more generally, the nonlinearity of the inverse problem. For example, we could use our knowledge of the fact that the P-wave velocity must be greater than S-wave velocity to constrain the inversion to yield only solutions that meet this criteria.

The use of a model constraint that links the model updates for multi-parameters could also be applied to other wavefield tomography problems. For example, for acoustic wavefield tomography in which one inverts for P-wave velocity and impedance, one could constrain the relationship between these two parameters to lie within a physically plausible range. Also, without imposing a hard relation between velocity and density, one could define arbitrary bounds on the feasible region, for example, by using experimental probability density functions established between the model parameters based on well log or other information.

5.7 Acknowledgments

We thank the sponsors of the Center for Wave Phenomena, whose support made this research possible. The reproducible numeric examples in this paper use the Madagascar open-source software package (Fomel et al., 2013) freely available from http://www.ahay.org.

CHAPTER 6
CONCLUSION

Wavefield migration and tomography are techniques for imaging the subsurface. In my thesis, I propose methods of migration and tomography based on the elastic wave-equation. The main results of this thesis and recommendations for further study are summarized below.

6.1 Scalar imaging condition for elastic reverse-time migration

In Chapter 2, I exploit geometrical relationships between the wavefields, their propagation directions, the reflector orientation, and polarization directions to derive a new 3D imaging condition for PS and SP reflectivities. This new method leads to accurate images without the need to decompose wavefields into directional components or to construct costlier extended images in the angle domain. This method is constructed based on the assumption that polarity changes at normal incidence in isotropic media.

In the case of anisotropy, polarity may change at non-zero incidence angle. With proper decomposition methods that separate the P and S waves, one can exploit the directionality of phase velocity, group velocity, and reflector normal and thus design an imaging condition for converted waves that corrects for polarity reversals at correct angles of incidence and reflection.

6.2 Angle decomposition

In Chapter 3, I show extended imaging conditions for PP, PS, SP, and SS images, and I present methods for computing opening and azimuth angle gathers from these images. These methods utilize local plane wave decompositions of extended images and exploit the relationships between the time-lag, space-lag, and image shift in space. These relationships lead to opening and azimuth angle decomposition methods using either time-lag common

image gathers, space-lag common image gathers, or time- and space-lag common image point gathers.

These angle decomposition relationships are derived for isotropic media. However, these methods can also be extended and applied to anisotropic media. For anisotropic media, e.g., arbitrary TTI media, the angle decomposition procedure is complicated by the fact that the velocities on the source and receiver sides depend on the angles of incidence. Sava and Alkhalifah (2013) propose the angle decomposition methods for PP reflections in the TI media. They reconstruct the wavefield using a pseudo-acoustic wave equation. By using the direction of symmetry axis, they derive the relationships between opening/azimuth angles and time-/space-lags. With proper methods that separate P and S waves, one could develop similar angle decomposition algorithms to obtain angle gathers for elastic reflections in anisotropic media.

6.3 Elastic least-squares reverse time migration

In Chapter 4, I propose a method for elastic least-squares reverse time migration using a perturbation imaging condition, which I derive for squared P and S velocities. Images computed using this new imaging condition can be simply related to physical subsurface properties, and in addition, these images do not suffer from polarity changes and thus can be stacked over experiments without an additional polarity correction. Compared to elastic RTM, elastic LSRTM produces high-resolution images that provide correct relative amplitudes, which makes this algorithm especially suitable for applications such as reservoir characterization.

LSRTM algorithms are developed based on the imaging conditions. We derive a new perturbation imaging condition for squared P and S velocity models. One can also used LSRTM algorithms for other elastic imaging conditions, for example, the potential imaging condition discussed in Chapter 2. The migration operator is defined by the imaging condition, which consists of the sequential operators. And the demigration operator can be obtained by using these operators contained in the migration operator. For anisotropic

media, one can also obtain the perturbation imaging conditions for individual model parameters using elastic anisotropic wave equation. The perturbation imaging condition can be derived based on various parameterizations, for example, images for V_{P0} and V_{S0}. Because of the trade-offs between parameters, it is important to choose a parameterization according to the acquisition.

6.4 Elastic wavefield tomography with physical model constraints

In Chapter 5, I demonstrate an elastic wavefield tomography method using the isotropic elastic wave equation formulated to reduce the misfit between observed and predicted data, and to obtain models that are physically plausible. I invert for a model of multiple elastic material parameters, i.e., the squared P and S velocities . Due to differences in illumination, amplitude, and wavelength between P and S waves, the model updates for the two parameters may differ in amplitude and location, thus leading to nonphysical models. To obtain a physically realistic model, I introduce physical constraints that force the updated models to satisfy known physical relations bounded within a certain feasible range.

This feasible range can be defined in various ways. In Chapter 5, we show constraints with upper and lower boundaries, which are estimated from the well-logs. One could define arbitrary bounds on the feasible region, for example, by using experimental probability density functions established between the model parameters. A similar idea could be applied to migration velocity analysis (MVA). MVA operates by establishing the relation between model perturbation and a corresponding image perturbation. The target of elastic MVA is to minimize such an image perturbation by optimizing the squared P and S velocity models. In my thesis, I show different imaging conditions, which can all be extended with space- and time-lags. These extended images can be used to construct the objective function for elastic MVA. One can use petrophysical constraints for MVA to eliminate the inconsistencies between recovered α and β models.

REFERENCES CITED

Aki, K., and P. Richards, 2002, Quantitative seismology (second edition): University Science Books.

Aminzadeh, F., J. Brac, and T. Kunz, 1997, 3-D salt and overthrust models: Society of Explorition Geophysicists.

Aminzadeh, F., N. Burkhard, J. Long, T. Kunz, and P. Duclos, 1996, Three dimensional SEG/EAEG models-an update: The Leading Edge, **15**, 131–134.

Aoki, N., and G. T. Schuster, 2009, Fast least-squares migration with a deblurring filter: Geophysics, **74**, WCA83–WCA93.

Artman, B., I. Podladtchikov, and A. Goertz, 2009, Elastic time-reverse modeling imaging conditions: SEG Technical Program Expanded Abstracts 2009, 1207–1211.

Asnaashari, A., R. Brossier, S. Garambois, F. Audebert, P. Thore, and J. Virieux, 2013, Regularized seismic full waveform inversion with prior model information: Geophysics, **78(2)**, R25–R36.

Audebert, F., P. Froidevaux, I. Huard, L. Nicoletis, and J. Svay-Lucas, 2000, A multi-angle toolbox for restored amplitude images and ava-gathers: 70th Ann. Internat. Mtg. Soc. of Expl. Geophys, **1023**.

Bae, H. S., S. Pyun, C. Shin, K. J. Marfurt, and W. Chung, 2012, Laplace-domain waveform inversion versus refraction-traveltime tomography: Geophysical Journal International, **190**, 595606.

Balch, A. H., and C. Erdemir, 1994, Sign-change correction for prestack migration of P-S converted wave reflections: Geophysical Prospecting, **42**, 637–663.

Baumstein, A., 2013, POCS-based geophysical constraints in multi-parameter Full Wavefield Inversion: Presented at the 75th EAGE Conference & Exhibition incorporating SPE EUROPEC 2013.

Baysal, E., D. D. Kosloff, and J. W. Sherwood, 1983, Reverse time migration: Geophysics, **48**, 1514–1524.

Beretta, M. M., G. Bernasconi, and G. Drufuca, 2002, AVO and AVA inversion for fractured reservoir characterization: Geophysics, **67**, 300–306.

Biondi, B., and A. Almomin, 2014, Efficient and robust waveform-inversion workflow: SEG Technical Program Expanded Abstracts, 917–921.

Biondi, B., and P. Sava, 1999, Wave-equation migration velocity analysis: 69th Annual International Meeting, SEG, Expanded Abstracts, 1723–1726.

Biondi, B., and W. W. Symes, 2004, Angle-domain common-image gathers for migration velocity analysis by wavefield-continuation imaging: Geophysics, **69**, 1283–1298.

Brandsberg-Dahl, S., M. V. de Hoop, and B. Ursin, 1999, Velocity analysis in the common scattering-angle/azimuth domain: 69th SEG meeting, Houston, USA, Expanded Abstracts, 1222–1223.

Bube, K., P. Lailly, P. Sacks, F. Santosa, and W. W. Symes, 1988, Simultaneous determination of source wavelet and velocity profile using impulsive point-source reflections from a layered fluid: Geophysical Journal International, **95**, 449–462.

Castagna, J. P., M. L. Batzle, and R. L. Eastwood, 1985, Relationships between compressional-wave and shear-wave velocities in elastic silicate rocks: Geophysics, **50(4)**, 571–581.

Červenỳ, V., M. M. Popov, and I. Pšenčík, 1982, Computation of wave fields in inhomogeneous mediaGaussian beam approach: Geophysical Journal International, **70**, 109–128.

Chang, W.-F., and G. A. McMechan, 1994, 3-d elastic prestack, reverse-time depth migration: Geophysics, **59**, 597–609.

Claerbout, J. F., 1971, Toward a unified theory of reflector mapping: Geophysics, **36(3)**, 467–481.

———, 1992, Earth soundings analysis: Processing versus inversion: Blackwell Scientific Publications Cambridge, Massachusetts, USA, **6**.

Claerbout, J. F., and S. M. Doherty, 1972, Downward continuation of moveout-corrected seismograms: Geophysics, **37**, 741–768.

Compton, S., and D. Hale, 2013, Estimating Vp/Vs rratio using smooth dynamic image warping: SEG Technical Program Expanded Abstracts, 1639–1643.

Dai, W., and G. T. Schuster, 2013, Plane-wave least-squares reverse-time migration: Geophysics, **78**, S165–S177.

Dai, W., X. Wang, and G. T. Schuster, 2011, Least-squares migration of multisource data with a deblurring filter: Geophysics, **76**, R135–R146.

De Bruin, C., C. Wapenaar, and A. Berkhout, 1990, Angle-dependent reflectivity by means of prestack migration: Geophysics, **55**, 1223–1234.

Dellinger, J., and J. Etgen, 1990a, Wave-field separation in two-dimensional anisotropic media: Geophysics, **55**, 914–919.

———, 1990b, Wavefield separation in two-dimensional anisotropic media: Geophysicas, **55(7)**, 914–919.

Denli, H., and L. Huang, 2008, Elastic-wave reverse-time migration with a wavefield-separation imaging condition: SEG Technical Program Expanded Abstracts 2008, 2346–2350.

Dickens, T. A., and G. A. Winbow, 2011, RTM angle gathers using Poynting vectors: SEG Technical Program Expanded Abstracts 2011, 3109–3113.

Dong, S., J. Cai, M. Guo, S. Suh, Z. Zhang, B. Wang, e. Z. Li, et al., 2012, Least-squares reverse time migration: Towards true amplitude imaging and improving the resolution: Presented at the 2012 SEG Annual Meeting, Society of Exploration Geophysicists.

Du, Q., X. Gong, Y. Zhu, G. Fang, and Q. Zhang, 2012a, PS wave imaging in 3D elastic reverse-time migration: SEG Technical Program Expanded Abstracts 2012, 1–4.

Du, Q., Y. Zhu, and J. Ba, 2012b, Polarity reversal correction for elastic reverse time migration: Geophysics, **77(2)**, S31–S41.

Duan, Y., and P. Sava, 2015, Scalar imaging condition for elastic reverse time migration: Geophysics, **80**, S127–S136.

Duan, Y., P. Sava, et al., 2014, Elastic reverse-time migration with OBS multiples: Presented at the 2014 SEG Annual Meeting, Society of Exploration Geophysicists.

Duan, Y., and P. C. Sava, 2014, Elastic reverse-time migration with obs multiples: SEG Technical Program Expanded Abstracts, 4071–4076.

Etgen, J., S. H. Gray, and Y. Zhang, 2009, An overview of depth imaging in exploration geophysics: Geophysics, **74**, WCA5–WCA17.

Fletcher, R., X. Du, P. J. Fowler, et al., 2008, A new pseudo-acoustic wave equation for TI media: Presented at the 2008 SEG Annual Meeting, Society of Exploration Geophysicists.

Fomel, S., P. Sava, I. Vlad, Y. Liu, and V. Bashkardin, 2013, Madagascar: open-source software project for multidimensional data analysis and reproducible computational experiments: Journal of Open Research Software, **1**, e8.

Gaiser, J., 1999, Applications for vector coordinate systems of 3-D converted-wave data: The Leading Edge, **18**, 1290–1300.

Gasso, G., A. Rakotomamonjy, and S. Canu, 2009, Recovering sparse signals with a certain family of non-convex penalties and DC programming: IEEE Transactions on Signal Processing, **57(12)**, 4686–4698.

Gregory, A., 1976, Fluid saturation effects on dynamic elastic properties of sedimentary rocks: Geophysics, **41(5)**, 895–921.

Guasch, L., M. Warner, T. Nangoo, J. Morgan, A. Umpleby, I. Stekl, and N. Shah, 2012, Elastic 3D full-waveform inversion: SEG Technical Program Expanded Abstracts, 1–5.

Guitton, A., G. Ayeni, and E. Díaz, 2012, Constrained full-waveform inversion by model reparameterization: Geophysics, **77(2)**, R117–R127.

Hale, D., 2007, Local dip filtering with directional laplacians: CWP Consortium Project on Seismic Inverse Methods for Complex Structures, 91–102.

Hamada, G., 2004, Reservoir fluids identification using Vp/Vs ratio: Oil & gas science and technology, **59(6)**, 649–654.

Hoffe, B. H., H. C. Bland, G. F. Margrave, P. M. Manning, D. S. Foltinek, et al., 1999, Analysis of the effectiveness of 3-C receiver arrays for converted wave imaging: Presented at the 1999 SEG Annual Meeting, Society of Exploration Geophysicists.

Hokstad, K., R. Mittet, and M. Landrø, 1998, Elastic reverse time migration of marine walkaway vertical seismic profiling data: Geophysics, **63**, 1685–1695.

Hou, J., and W. W. Symes, 2015, An approximate inverse to the extended Born modeling operator: Geophysics, **80**, R331–R349.

Huang, Y., and G. T. Schuster, 2012, Multisource least-squares migration of marine streamer and land data with frequency-division encoding: Geophysical Prospecting, **60**, 663–680.

Hudson, J., and J. Heritage, 1981, The use of the Born approximation in seismic scattering problems: Geophysical Journal International, **66**, 221–240.

Ivanov, J., R. D. Miller, J. Xia, D. Steeples, and C. B. Park, 2005, The Inverse Problem of Refraction Travel Times, Part i: Types of Geophysical Nonuniqueness Through Minimization: Pure and applied geophysics, **162(3)**, 447–459.

Jaramillo, H. H., and N. Bleistein, 1999, The link of Kirchhoff migration and demigration to Kirchhoff and Born modeling: Geophysics, **64**, 1793–1805.

Kaplan, S. T., P. S. Routh, and M. D. Sacchi, 2010, Derivation of forward and adjoint operators for least-squares shot-profile split-step migration: Geophysics, **75**, S225–S235.

Katahara, K. W., 1999, Effect of mineral Vp/Vs on rock Vp/Vs: SEG Technical Program Expanded Abstracts, 1029–1032.

Kuehl, H., M. Sacchi, et al., 2002, Robust AVP estimation using least-squares wave-equation migration: Presented at the 2002 SEG Annual Meeting, Society of Exploration Geophysicists.

Lailly, P., 1983, The seismic inverse problem as a sequence of before stack migrations: Conference on Inverse Scattering: Theory and Application, Society of Industrial and Applied Mathematics, Expanded Abstracts, 206–220.

Lay, T., and T. Wallace, 1995, Modern global seismology: Academic Press, San Diego.

Lee, K. H., and H. J. Kim, 2003, Source-independent full-waveform inversion of seismic data: Geophysics, **68**, 2010–2015.

Martin, G. S., R. Wiley, and K. J. Marfurt, 2006, Marmousi2: An elastic upgrade for Marmousi: The Leading Edge, **25**, 156–166.

McMechan, G. A., 1983, Migration by extrapolation of time-dependent boundary values: Geophysical Prospecting, **31**, 413–420.

McNeely, J., T. Keho, T. Tonellot, R. Ley, and J. Chen, 2012, 3D acoustic waveform inversion of land data: a case study from saudi arabia: SEG Technical Program Expanded Abstracts, 1–5.

Mora, P., 1988, Inversion of Seismic Wavefield Data for P- and S-wave Velocity: Exploration Geophysics, **19(1/2)**, 312–316.

Mulder, W., and A. Ten Kroode, 2002, Automatic velocity analysis by differential semblance optimization: Geophysics, **67**, 1184–1191.

Nemeth, T., C. Wu, and G. T. Schuster, 1999, Least-squares migration of incomplete reflection data: Geophysics, **64**, 208–221.

Nocedal, J., and S. J. Wright, 2006, Numerical optimization: Springer.

Operto, S., C. Ravaut, L. Improta, J. Virieux, A. Herrero, and P. Dell'Aversana, 2004, Quantitative imaging of complex structures from dense wide-aperturesseismic data by multiscale traveltime and waveform inversions: a case study: Geophysical Prospecting, **52**, 625–651.

Patrikeeva, N., and P. Sava, 2013, Comparison of angle decomposition methods for wave-equation migration: SEG Technical Program Expanded Abstracts 2013, 3773–3778.

Peng, J., C. Roos, and T. Terlaky, 2002, Self-regular functions and new search directions for linear and semidefinite optimization: Mathematical Programming, **93**, 129–171.

Plessix, R. E., 2006, A review of the adjoint-state method for computing the gradient of a functional with geophysical applications: Geophysics Journal International, **167**, 495–503.

Pratt, R. G., 1990, Inverse theory applied to multi-source cross-hole tomography: Geophysical Prospecting, **38**, 311–329.

———, 1999, Seismic waveform inversion in the frequency domain, Part 1: Theory and verification in a physical scale model: Geophysics, **64(3)**, 888–901.

Pratt, R. G., C. Shin, and G. Hick, 1998, Gauss-Newton and full Newton methods in frequency-space seismic waveform inversion: Geophysical Journal International, **133(2)**, 341–362.

Prieux, V., R. Brossier, S. Operto, and J. Virieux, 2013, Multiparameter full waveform inversion of multicomponent ocean-bottom-cable data from the Valhall field. part 2: imaging compressive-wave and shear-wave velocities: Geophysical Journal International, **194(3)**, 1665–1681.

Prieux, V., S. Operto, R. Brossier, J. Virieux, J. Kommendal, and O. Barkved, 2010, Application of 2D acoustic frequency-domain full-waveform inversion to obc wide-aperture data from the valhall field: SEG Technical Program Expanded Abstracts, 920–924.

Ribodetti, A., S. Operto, W. Agudelo, J.-Y. Collot, and J. Virieux, 2011, Joint ray + Born least-squares migration and simulated annealing optimization for target-oriented quantitative seismic imaging: Geophysics, **76**, R23–R42.

Rickett, J. E., and P. C. Sava, 2002, Offset and angle-domain common image-point gathers for shot-profile migration: Geophysics, **67(3)**, 883–889.

Rocha, D., N. Tanushev, and P. Sava, 2016, Isotropic elastic wavefield imaging using the energy norm: Geophysics, **81**, S207–S219.

Rojas, E., T. L. Davis, M. Batzle, M. Prasad, and R. J. Michelena, 2005, Vp-Vs ratio sensitivity to pressure, fluid, and lithology changes in tight gas sandstones: SEG Technical Program Expanded Abstracts, 1401–1404.

Rosales, D. A., S. Fomel, B. L. Biondi, and P. C. Sava, 2008, Wave-equation angle-domain common-image gathers for converted waves: Geophysics, **73(1)**, S17–S26.

Sava, P., 2007, Stereographic imaging condition for wave-equation migration: Geophysics, **72**, A87–A91.

Sava, P., and T. Alkhalifah, 2013, Wide-azimuth angle gathers for anisotropic wave-equation migration: Geophysical Prospecting, **61**, 75–91.

Sava, P., and B. Biondi, 2004a, Wave-equation migration velocity analysis. I. Theory: Geophysical Prospecting, **52**, 593–606.

———, 2004b, Wave-equation migration velocity analysis. II. Subsalt imaging examples: Geophysical Prospecting, **52**, 607–623.

Sava, P., and S. Fomel, 2006, Time-shift imaging condition in seismic migration: Geophysics, **71**, S209–S217.

Sava, P., S. Fomel, et al., 2005, Coordinate-independent angle-gathers for wave equation migration: Presented at the 2005 SEG Annual Meeting, Society of Exploration Geophysicists.

Sava, P., and I. Vlad, 2011, Wide-azimuth angle gathers for wave-equation migration: Geophysics, **76**, S131–S141.

Sava, P. C., and S. Fomel, 2003, Angle-domain common-image gathers by wavefield continuation methods: Geophysics, **68**, 1065–1074.

Sava, P. C., and I. Vasconcelos, 2009, Efficient computation of extended images by wavefield-based migration: SEG Technical Program Expanded Abstracts 2009, 2824–2828.

Schneider, W. A., 1978, Integral formulation for migration in two and three dimensions: Geophysics, **43**, 49–76.

Schuster, G. T., et al., 1993, Least-squares cross-well migration: 63rd Annual International Meeting, SEG, Expanded Abstracts, 110–113.

Schuster, G. T., and A. Quintus-Bosz, 1993, Wavepath eikonal traveltime inversion: Theory: Geophysics, **58(9)**, 1314–1323.

Shen, P., W. W. Symes, C. C. Stolk, et al., 2003, Differential semblance velocity analysis by wave-equation migration: Presented at the 2003 SEG Annual Meeting, Society of Exploration Geophysicists.

Stanton, A., and M. Sacchi, 2015, Least squares wave equation migration of elastic data: Presented at the 77th EAGE Conference and Exhibition 2015.

Sun, R., and G. A. McMechan, 1986, Pre-stack reverse-time migration for elastic waves with application to synthetic offset vertical seismic profiles: Proceedings of the IEEE, **74**, 457–465.

Sun, R., G. A. McMechan, C. Lee, J. Chow, and C. Chen, 2006, Prestack scalar reverse-time depth migration of 3D elastic seismic data: Geophysics, **71(5)**, S199–S207.

Sun, Y., and G. Schuster, 1992, Hierarchic optimizations for smoothing and cooperative inversion: SEG Technical Program Expanded Abstracts, 745–748.

Symes, W. W., 1993, A differential semblance criterion for inversion of multioffset seismic reflection data: Journal of Geophysical Research: Solid Earth, **98**, 2061–2073.

Szydlik, T., P. Smith, S. Way, L. Aamodt, and C. Friedrich, 2007, 3D PP/PS prestack depth migration on the Volve field: First Break, **25**.

Taillandier, C., M. Noble, H. Chauris, and H. Calandra, 2009, First-arrival traveltime tomography based on the adjoint-state method: Geophysics, **74(6)**, WCB1–WCB10.

Tarantola, A., 1984, Inversion of seismic reflection data in the acoustic approximation: Geophysics, **49(8)**, 1259–1266.

———, 1986, A strategy for nonlinear elastic inversion of seismic reflection data: Geophysics, **51(10)**, 1893–1903.

———, 1987, Inverse problem theory: Methods for data fitting and model parameter estimation: Elsevier Science Publishing Company, Inc.

Tikhonov, A., and V. Arsenin, 1977, Solution of ill-posed problems: Winston & Sons.

Trad, D., et al., 2015, Least squares Kirchhoff depth migration: implementation, challenges, and opportunities: Presented at the 2015 SEG Annual Meeting, Society of Exploration Geophysicists.

Tsuneyama, F., 2006, Exploring Vp-Vs relations: Approach from effective medium theories: Proceedings of the 8th SEGJ International Symposium, Kyoto, Japan, 1–6.

Versteeg, R., 1991, Analysis of the problem of the velocity model determination for seismic imaging: PhD thesis, University of Paris VII.

———, 1993, Sensitivity of prestack depth migration to the velocity model: Geophysics, **58**, 873–882.

Vigh, D., K. Jiao, and D. Watts, 2012, Elastic full-waveform inversion using 4C data acquisition: SEG Technical Program Expanded Abstracts, 1–6.

Vigh, D., K. Jiao, D. Watts, and D. Sun, 2014, Elastic full-waveform inversion application using multicomponent measurements of seismic data collection: Geophysics, **79(2)**, R63–R77.

Vyas, M., X. Du, E. Mobley, and R. Fletcher, 2011, Methods for computing angle gathers using RTM: Presented at the 73rd EAGE Conference & Exhibition.

Whitmore, N., et al., 1983, Iterative depth migration by backward time propagation: Presented at the 1983 SEG Annual Meeting, Society of Exploration Geophysicists.

Wong, M., B. L. Biondi, and S. Ronen, 2015, Imaging with primaries and free-surface multiples by joint least-squares reverse time migration: Geophysics, **80**, S223–S235.

Woodward, M. J., 1992, Wave-equation tomography: Geophysics, **57(1)**, 15–26.

Wu, R., and X. Xie, 2002, Extracting angle domain information from migrated wavefield: Presented at the 2002 SEG Annual Meeting, Society of Exploration Geophysicists.

Wu, R., R. Yan, and X, 2010, Elastic converted-wave path migration for subsalt imaging: SEG Technical Program Expanded Abstracts 2010, 3176–3180.

Xiang, S., and H. Zhang, 2014, A new adaptive edge-preserving regularization scheme for seismic full waveform inversion: SEG Technical Program Expanded Abstracts, 1238–1242.

Xu, S., H. Chauris, G. Lambaré, and M. Noble, 2001, Common-angle migration: A strategy for imaging complex media: Geophysics, **66**, 1877–1894.

Xu, S., Y. Zhang, and B. Tang, 2011, 3D angle gathers from reverse time migration: Geophysics, **76(2)**, S77–S92.

Yan, J., and W. Ross, 2013, Improving the stability of angle gather computation using Poynting vectors: Presented at the 2013 SEG Annual Meeting, Society of Exploration Geophysicists.

Yan, J., and P. Sava, 2008, Isotropic angle-domain elastic reverse-time migration: Geophysics, **73(6)**, S229–S239.

Yan, J., P. Sava, et al., 2010, Analysis of converted-wave extended images for migration velocity analysis: Presented at the 2010 SEG Annual Meeting, Society of Exploration Geophysicists.

Yan, R., and X. Xie, 2012, An angle-domain imaging condition for elastic reverse time migration and its application to angle gather extraction: Geophysics, **77(5)**, S105–S115.

Yang, T., and P. Sava, 2015, Image-domain wavefield tomography with extended common-image-point gathers: Geophysical Prospecting, **63**, 1086–1096.

Yang, T., P. Sava, et al., 2010, Wave-equation migration velocity analysis with extended common-image-point gathers: Presented at the 2010 SEG Annual Meeting, Society of Exploration Geophysicists.

Yoon, K., K. Marfurt, and E. W. Starr, 2004, Challenges in reverse-time migration: SEG Technical Program Expanded Abstracts 2004, 1057–1060.

Yoon, K., and K. J. Marfurt, 2006, Reverse-time migration using the poynting vector: Exploration Geophysics, **37**, 102–107.

Zelt, C. A., A. Azaria, and A. Levander, 2006, 3D seismic refraction traveltime tomography at a groundwater contamination site: Geophysics, **71(5)**, H67–H78.

Zhang, Y., and J. Sun, 2009, Practical issues in reverse time migration: true amplitude gathers, noise removal and harmonic source encoding: First Break, **27, No 1**, 29–35.

Zhou, H., R. Bloor, G. Zhang, et al., 2006, An anisotropic acoustic wave equation for modeling and migration in 2D TTI media: Presented at the 2006 SEG Annual Meeting, Society of Exploration Geophysicists.

Zhou, H., Y. Zhang, and S. Gray, 2002, Regularization algorithms for seismic inverse problems: SEG Technical Program Expanded Abstracts, 942–945.

Zhu, X., D. Sixta, and B. Angstman, 1992, Tomostatics: Turning-ray tomography + tatics corrections: The Leading Edge, **11**, 15–23.

Zimmer, M., M. Prasad, and G. Mavko, 2002, Pressure and porosity influences on Vp-Vs ratio in unconsolidated sands: The Leading Edge, **21**, 178–183.

APPENDIX - PERMISSION OF PAPERS

This appendix includes permission to use the papers submitted for publication in the dissertation and permission to publish the results obtained using the Volve data. Chapter 4 is co-authored by Antoine Guitton from Colorado School of Mines.

A.1 Permission from publisher

The screenshot below shows that permission is granted for use in thesis.

Traditional publication (including green open access)

- No author publication charge (APC) is levied, although payment of mandatory page charges are assessed and payment of voluntary charges is requested. Relief from mandatory charges may be requested under SEG's hardship relief policy.
- Copyright is transferred to SEG.
- Authors/employers retain proprietary rights such as the right to patentable subject matter and the right to make oral presentation of the work with full citation and proper copyright acknowledgment.
- Authors/employers enjoy the right to prepare and hold copyright in derivative publications based on the paper provided that the derivative work is published subsequent to the official date of the original paper's publication by SEG.
- Authors/employers may post a final accepted version of the manuscript or the final SEG-formatted version (book chapters excluded) on authors' personal websites, employers' websites, or in institutional repositories operated and controlled exclusively by authors' employers provided that:
  1. the SEG-prepared version is presented without modification;
  2. copyright notice and a full citation appear with the paper;
  3. a link to the SEG version of record in the SEG Digital Library using Digital Object Identifier (DOI) permalinks is provided;
  4. the posting is noncommercial in nature, and the paper is made available to users without charge; and
  5. that notice be provided that use is subject to SEG terms of use and conditions.
- Authors/employers may not post their articles in an institutional repository or other site in which the content is required to carry or is implied as carrying a license contrary to SEG copyright and terms of use and terms of this policy.
- Authors/employers may post to their own websites a preprint (a version prior to SEG peer review) of a submitted manuscript provided that the posting is accompanied by prominent notice that the paper is under review for publication by SEG and the publication to which the manuscript has been submitted is identified. Upon publication of the paper by SEG, the author must replace any previously posted electronic versions of the paper with either (a) a full citation to the SEG-published work with a DOI permalink to the paper's abstract or (b) the final version of the manuscript or SEG-formatted version (book chapters excluded) subject to SEG conditions for such posting.
- Authors may reuse all or part of their papers published with SEG in a thesis or dissertation that authors write and are required to submit to satisfy criteria of degree-granting institutions.

Figure A.1: Permission from Geophysics

A.2 Permission from co-author

I include a copy of the emails exchanged between myself and my co-author, who granted permission to include the papers in the dissertation.

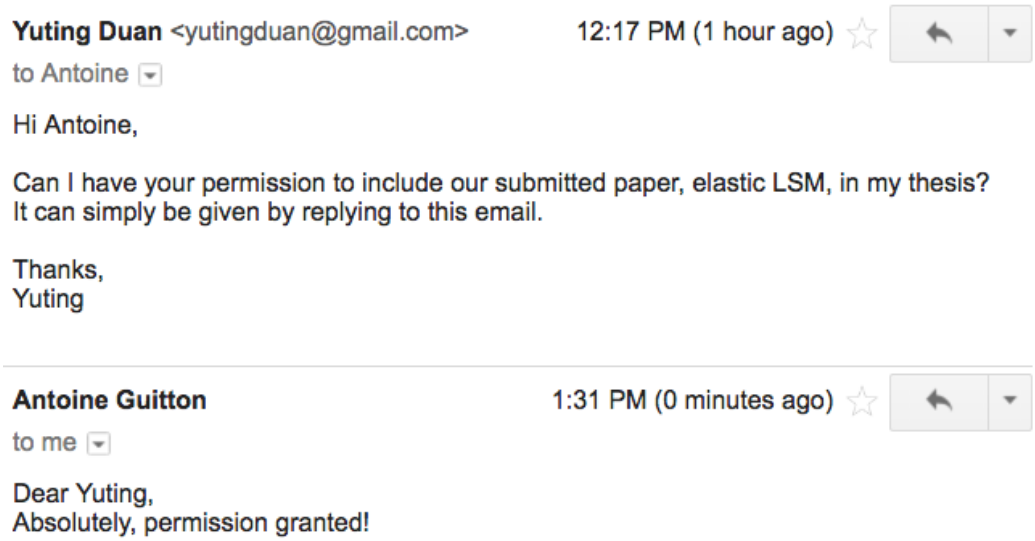

Yuting Duan <yutingduan@gmail.com> 12:17 PM (1 hour ago)

to Antoine

Hi Antoine,

Can I have your permission to include our submitted paper, elastic LSM, in my thesis? It can simply be given by replying to this email.

Thanks,
Yuting

Antoine Guitton 1:31 PM (0 minutes ago)

to me

Dear Yuting,
Absolutely, permission granted!

Figure A.2: Permission from co-author, Antoine Guitton.

A.3 Permission for field data

I include a copy of the emails exchanged between myself and Marianne Houbiers from Statoil, who granted permission to include the field data example in the dissertation.

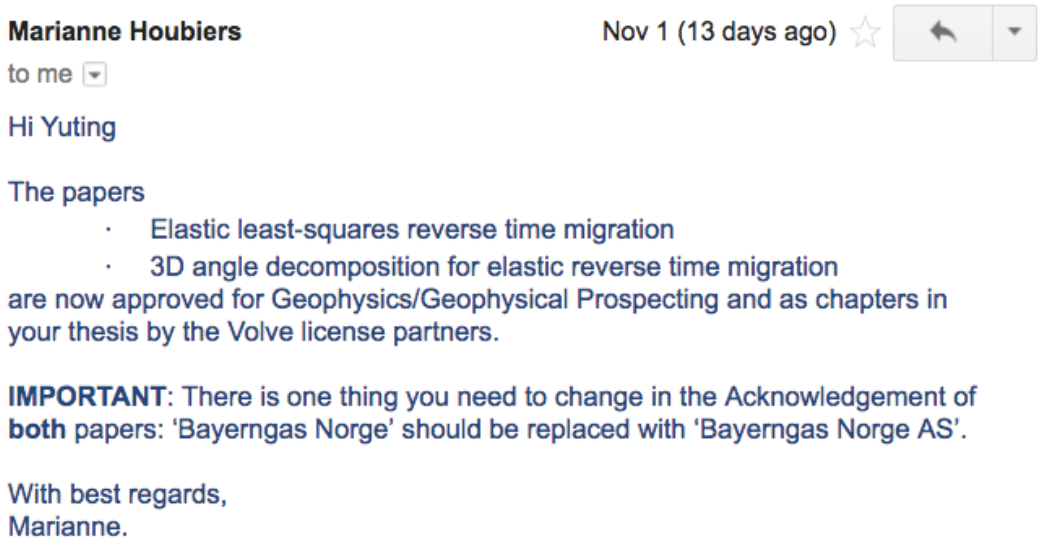

Marianne Houbiers Nov 1 (13 days ago)

to me

Hi Yuting

The papers

- Elastic least-squares reverse time migration
- 3D angle decomposition for elastic reverse time migration

are now approved for Geophysics/Geophysical Prospecting and as chapters in your thesis by the Volve license partners.

IMPORTANT: There is one thing you need to change in the Acknowledgement of **both** papers: 'Bayerngas Norge' should be replaced with 'Bayerngas Norge AS'.

With best regards,
Marianne.

Figure A.3: Permission for field data.